UNIVERSIDADE FEDERAL DE SANTA CATARINA

CENTRO TECNOLÓGICO DA UFSC

PROGRAMA DE PÓS-GRADUAÇÃO EM ENGENHARIA MECÂNICA

Danilo de Souza Braga

Fan noise prediction of aero-engines based on a modal approach in the presence of acoustic treatment and inviscid sheared flows

Florianópolis - SC

2019

Danilo de Souza Braga

Fan noise prediction of aero-engines based on a modal approach in the presence of acoustic treatment and inviscid sheared flows

Tese submetida ao Programa de Pós-Graduação em Engenharia Mecânica da Universidade Federal de Santa Catarina para a obtenção do título de Doutor em Engenharia Mecânica na sub-área Acústica e Vibrações.

Orientador: Prof. Júlio A. Cordioli, Dr. Eng.

Co-orientador: Prof. Andrey R. da Silva, Ph.D.

Florianópolis - SC

2019

Ficha de identificação da obra elaborada pelo autor,
através do Programa de Geração Automática da Biblioteca Universitária da UFSC.

Braga, Danilo de Souza
Fan noise prediction of aero-engines based on a modalapproach in the presence of acoustic treatment andinviscid sheared flows / Danilo de Souza Braga ; orientador, Julio Apolinário Cordioli, coorientador, Andrey Ricardo da Silva, 2019.
170 p.

Tese (doutorado) - Universidade Federal de Santa Catarina, Centro Tecnológico, Programa de Pós-Graduação em Engenharia Mecânica, Florianópolis, 2019.

Inclui referências.

1. Engenharia Mecânica. 2. Aeroacústica. 3. Turbofan. 4. Ruído de fan. 5. Liner. I. Cordioli, Julio Apolinário. II. da Silva, Andrey Ricardo. III. Universidade Federal de Santa Catarina. Programa de Pós-Graduação em Engenharia Mecânica. IV. Título.

Danilo de Souza Braga

Fan noise prediction of aero-engines based on a modal approach in the presence of acoustic treatment and inviscid sheared flows

O presente trabalho em nível de doutorado foi avaliado e aprovado por banca examinadora composta pelos seguintes membros:

Prof. Prof. Paulo Celso Greco Júnior, Dr. Eng.
Universidade Estadual de Campinas, Brasil

Victor Henrique Pereira da Rosa, Ph.D.
Universidade Federal de Santa Catarina, Brasil

Prof. Arcanjo Lenzi, Ph.D.
Universidade Federal de Santa Catarina, Brasil

Certificamos que esta é a **versão original e final** do trabalho de conclusão que foi julgado adequado para obtenção do título de doutor em Engenharia Mecânica.

Assinado de forma digital por Jonny Carlos da Silva:51451506449
Dados: 2019.11.27 09:55:58 -03'00'

Prof. Jonny Carlos da Silva, Dr.
Coordenador do Programa

Julio Apolinario Cordioli:00427698928
Digitally signed by Julio Apolinario Cordioli:00427698928
Date: 2019.11.26 10:34:04 -03'00'

Prof. Júlio A. Cordioli, Dr. Eng.
Orientador

Florianópolis - SC, 18 de outubro de 2019.

Ao meu filho Dante e minha esposa Raísa.

Ao meu saudoso avô e professor Edésio Lobato (In memorian).

ACKNOWLEDGEMENTS

Firstly, a special and sincere thanks to my wife Raísa and my son Dante for comprehending my absences and all the support over the past years. I am thankful for their aspiring support, which makes me a better father/man every day.

I would like to thank my parents, Antonio, and Edenice, and my brothers, Diego and David, and my sister Danielle for their priceless love and support during my studies. Even though they were 4000 km apart, I felt that they were always with me here in Florianopolis. Also, I would like to thank my big family from Amapá, my grandparents, uncles and aunts, and cousins for making my days happier when I go back home.

I am very grateful to my academic supervisors, Prof. Júlio Cordioli and Andrey da Silva, for their advice and immense support in my research. Under their guidance and attention to details, I gained invaluable experience both academically and personally. Moreover, I would also like to thank professor Júlio for providing me an opportunity to work on the aeronautical industry and to increase my learning curve in the field of aero-acoustics. It has been a pleasure to learn and discuss with you, especially when accompanied by some coffee (and beers sometimes!). I would also like to thank Professor Arcanjo Lenzi for professional, academic, and personal discusses over these four years.

The research was greatly benefited from useful interactions with many individuals. In particular, I would like to thank: Danillo Reis and Eduardo Lobão (Embraer) for their advice and support in this research; André Spillere for actively participating in the development of this work, for the friendship and fruitful discussions about science and other subjects.

Also, during the course of four years, I had an opportunity to meet many friendly people. Here are a few to list: André Loch, Zargos, Eduardo, Lucas Bonomo, Bernardo "phi", Lucas Lobato, Matheus "Monstrão", Amanda, Henrique "Alegrete", Wagner (my old friend!), Pedro ("Pedrão"!), Gil "Tubão", Guillerme Zanoteli, Nivaldo, Felipe "chamber", Victor "doctor", Sergio (Serjão!), José Pedro ("Gepeto"), Leonardo, Vinicius ("Drone guy"), Airton "Senna", and the list goes on... Thanks everyone for the memorable moments' and coffees, "cucas" and cakes, "açaís," beers, "cachaças de jambu" etc.

Last but not the least, I would gratefully acknowledge the financial support for my Ph.D. study provided jointly by CNPQ, FINEP and Embraer S.A. through the SILENCE Project. I am thankful to Acoustic and Vibration Laboratory (LVA) at UFSC to provide me an opportunity to contribute to industrially focused research, something which I always wanted to do.

"Everything owes its existence solely and completely to sound. Sound is a factor which holds it together, sound is the basis for form and shape."

(Dr. Peter Guy Manners, 1960)

RESUMO EXPANDIDO

Introdução

Em motores turbofan com grandes razões de passagem (*High bypass ratio* – HBR) de aeronaves modernas, o *fan* constitui uma das principais fontes de ruído, a qual é dependente da condição de operação da aeronave. A geração aeroacústica da componente de *fan* vem sendo amplamente investigada ao longo das últimas décadas, e a redução de suas fontes de ruído depende principalmente do projeto das pás, estatores, nacele e o material aplicado para tratamento acústico. Assim, o projeto de materiais de tratamento acústico aplicado a entrada de motores aeronáuticos, chamados de *liners* acústicos, têm recebido grande atenção, onde sua modelagem é complexa e envolve importantes variáveis como a presença de escoamento e elevados níveis de pressão sonora. Desta forma, suas propriedades acústicas e atenuação sonora proporcionada variam com as condições de voo e sua geometria. Para avaliar a efetividade desses dispositivos em termos de propagação a longo da nacele e a radiação sonora para exterior do motor, diferentes níveis de modelagem e técnicas de predição já foram propostos. Efeitos de convecção, reflexão e refração sonora gerados pelo escoamento interno e externo e pela terminação da nacele são comumente incorporados em ferramentas de modelagem, as quais são necessárias para esboçar o ruído gerado pela componente do *fan* na fase de projeto conceitual da aeronave ou do motor.

Objetivos

O principal objetivo da pesquisa nesta tese foi desenvolver uma ferramenta de modelagem analítica e de baixo custo para o projeto de *liner* aplicado na entrada de motores aeronáuticos objetivando mitigar o ruído de *fan*. Com base na abordagem modal, o presente trabalho também abordou o efeito da atenuação do liner na previsão da diretividade de radiação sonora e ao longo da nacele, assumindo escoamento invíscido uniforme e não-uniforme.

Revisão da literatura e fundamentação teórica

As ferramentas preditivas de ruído de *fan* na presença de *liners* acústicos são baseados na soma de diversos efeitos e dependem da modelo analítica ou numérica utilizado. Tradicionalmente, os modelos são utilizados para prever o impacto do ruído do *fan* no ruído global de uma aeronave. Nesse caso, a abordagem modal pode ser assumida, onde a geração, propagação e radiação sonora podem ser representadas analiticamente. Observa-se que os termos relacionados a efeitos de escoamento nas condições de voo tem forte influência na predição da propagação e radiação modal, e portanto, devem ser melhor investigados.

Modelos analíticos

Algumas formulações analíticas, como a técnica *mode matching* e modelos radiação, assumindo diferentes efeitos dentro e fora da nacele de motores foram discutidas em detalhes. Os modelos baseados na integral de Rayleigh/Kirchorff e no método de Wiener-Hopf são utilizados para solução da radiação em campo próximo e distante. Enquanto, a técnica *mode matching* possui duas condições de coincidência nas interfaces com *liner* e dois modelos segmentação de *liner*: uniforme e segmentado. A estrutura dos códigos computacionais criado para resolver tais modelos analíticos é detalhado (descrevendo dados de entrada e saída e o consumo de tempo

da rotina), onde as principais características de ambos os códigos e condições de contorno implementadas são apresentadas. Os modelos foram implementados para que sejam facilmente integrados entre si e utilizam um*solver* para determinar o número de onda adequado para paredes rígida e com impedância.

Avaliação e validação dos modelos analíticos

A investigação da precisão dos modelos preditivos é feita a partir de um *software* de elementos finitos especializado em propagação sonora de motores aeronáuticos. Desta forma, um estudo paramétrico baseado nos principais parâmetros de motor UHBR, em condições de voo, é examinado em detalhes. Os modelos implementados são analizados separadamente e discutidos em relação às suas limitações. Seis modelos numéricos com diferentes características são considerados para avaliar modelos analíticos implementados. Como principais resultados, é observado que a variação de seção e de velocidade do escoamento ao longo da nacele, espessura e forma da borda da entrada da nacele modificam a solução interna e externa do duto de entrada. Embora essas variações sejam esperadas, é possivel observar que os erros encontrados são pequenos quando comparados com os níveis globais previstos.

Efeitos do escoamento não-uniforme na transmissão sonora

Os efeitos do escoamento não-uniforme sobre a propagação sonora considerando a discontinuidade das transições *liner*-parede rigida são explorados em termos da espessura de camada limite e impedância acústica. O principal ponto desta análise é entender o comportamento do *liner* na presença de diferentes condições de voo e como a propagação sonora é afetada por tais efeitos. Com base na equação de Pridmore-Brown, investiga-se os efeitos de velocidade de escoamento e espessura de camada limite com ênfase para atenuação de modos de alta ordem (por serem as componentes dominantes do ruído de *fan* na condição de decolagem e cruzeiro). É observado que a espessura de camada limite é de grande importância na predição da atenuação sonora, levando a diferença significativas quando comparada com a modelagem usando escoamento uniforme. Essas variações também foram confirmadas para outras configurações de *liner* por meio de uma análise parametrica de impedância.

Efeitos do escoamento no ruído radiado em campo distante

As condições operacionais consideradas no capítulo anterior são investigados com relação os efeitos do escoamento interno e externo na nacele, em termos de campo distante. Assim, os efeitos convectivos fora e dentro do motor são investigados assumindo velocidade igual ($M_0 = M_\infty$) e diferentes ($M_0 > M_\infty$). É observado que a diferença de velocidades modifica o padrão de diretividade, especialmente na região do lóbulo principal de radiação sonora que depende da condição de operação. Além disso, na condição de teste estático ($M_\infty = 0$), o aumento de escoamento interno desloca o lóbulo principal de radiação sonora para o eixo de entrada da nacele, isto é, com $\theta^{\wedge}_{m,n} \to 0°$. Em contraste, se a velocidade no campo distante aumenta, nas mesmas condições, o lobulo principal tende a ser ortogonal a entrada do motor ($\theta^{\wedge}_{m,n} \to 90°$). Em seguida, a atenção é mudada para o equacionamento que permite a integração direta entre um modelo de radiação e a técnica *mode matching*. Esse modelo analítico híbrido "*mode matching* + modelo de radiação" fornece uma ferramenta prática para a previsão de padrões de radiação de campo distante para dutos assimétricos em freqüências e condições de escoamento de interesse prático para aplicação em motores aeronauticos, incluindo os efeitos de refração

gerados pela presença de escoamento interno não uniforme. O efeitos de redução de atenuação do *liner* com aumento da espessura de camada limite do escoamento e de impedância do *liner* observados no capitulo anterior, também são confirmados em termos de radiação sonora para o campo distante.

Considerações finais

Todas as ferramentas para predição do ruido de *fan* e para o projeto de *liners* desenvolvidas neste trabalho possuem suas limitações que devem ser posteriormente investigadas. A integração direta entre os modelos de radiação e as técnicas *mode matching* se mostra robusta o suficiente para entregar uma primeira estimativa do ruido em termos de campo sonoro interno e externo a nacele. O modelo analítico de atenuação sonora demonstra a importância de incluir a espessura de camada limite no projeto do *liner*. Entretanto, a análise está limitada para dutos de seção constante e sem reflexão na saída do duto, condições que podem não ser genérica para todas as condições de fonte sonora e de voo de motores aeronáuticos. De forma geral, este trabalho engloba a construção de uma metodologia baseada na propagação e radiação de modos acusticos para representar as fontes de motores reais. Tais ferramentas são necessárias na fase conceitual do projeto para projetar a atenuação adequada para essas fontes. Se todos os resultados e as discussões alcançados a partir dos capitulos são analisados em conjunto, conclui-se que a ferramenta proposta possui grande potencial para análise da redução do ruido de *fan* em condições realista de voo (em alta frequência e com camada limite) e que possui versatilidade suficiente para inserção de melhorias nos modelos atuais ou novos modelos.

Palavras-chave: Ruído de fan. Liner acústico. Motor turbofan. Modelo de radiação. Técnica mode-matching. Escoamento não-uniforme.

RESUMO

A previsão do ruído gerado por motores aeronáuticos, em condição de voo, é uma ferramenta importante para o projeto de uma aeronave ou um motor. Tais ferramentas possibilitam investigar o ruído de diferentes componentes desses motores, dentre os quais o ruído proveniente do *fan* pode ser mais significativo em determinadas condições de voo. Em geral, o campo sonoro gerado pelo *fan* dentro da nacele pode ser computado por meio de uma representação modal, a qual pode ser correlacionada com os diferentes mecanismos de geração sonora como ruído tonal (devido ao movimento periódico) e de banda larga (associado com escoamento turbulento). Para reduzir o ruído de tais mecanismos, *liners* acústicos são comumente utilizados, os quais, em geral, são modelados como uma impedância acústica localmente reativa. No entanto, sob condições realistas de escoamento, as propriedades de absorção acústica dos *liners* e a mitigação de ruído resultante podem ser afetadas, o que pode levar a uma redução na sua eficiência e a modificação da direcionalidade do ruído resultante em campo distante. Desta forma, o principal objetivo do presente estudo pode ser dividido em duas partes. O primeiro é dedicado ao desenvolvimento de uma ferramenta analítica para estimar a atenuação do ruído do *fan* provocada pelo *liner* em termos de propagação interna e radiação em campo distante. Em outras palavras, desenvolver uma ferramenta de predição que possa ser utilizada no projeto do tratamento acústico de naceles na presença de escoamento realístico ainda na fase de projeto conceitual. A segunda parte é comparar o efeito da atenuação do *liner* no campo distante para diferentes condições de contorno que representam os *liners*, envolvendo escoamentos médios uniforme e não-uniforme. Neste caso, as condições de contorno de Ingard-Myers e Brambley, bem como a solução de Pridmore-Brown são usadas para estimar os efeitos de atenuação do *liner* na presença de uma camada limite com espessura finita. Para o som irradiado para fora do duto foram implementadas as formulações de Rayleigh, Kirchhorff e Wiener-Hopf para campo próximo e distante. O estudo foi conduzido considerando parâmetros típicos da geometria de naceles e as condições de operação de motores turbofan modernos. Para os casos de escoamento uniforme, uma solução de referência foi obtida a partir de um código baseado no método de elementos finitos e usada para validar os modelos analíticos, os quais são baseados na técnica de *mode-matching* e em modelo de radiação. Os resultados dentro do duto, em termos de perda de transmissão e taxa de decaimento modal sugerem que uma espessura de camada limite crescente implica na redução direta da atenuação sonora do *liner* aplicado ao *intake* do motor. Além disso, a interação entre os efeitos de refração e a resistência e reatância do *liner* pode ser de natureza complexa, onde o efeito da camada limite depende fortemente da impedância do liner, e os dois não podem ser separados. Por outro lado, os modos transmitidos podem ser acoplados a um modelo de radiação analítica para computar a solução em todo o domínio. Os resultados sugerem que a espessura da camada limite influencia diretamente no espalhamento modal produzido pelas descontinuidades do *liner*, o que pode resultar em um comportamento complexo (com uma redistribuição da energia acústica em outros modos propagantes) em termos de radiação de ruído. A partir da integração destas abordagens estudadas, é possível obter uma ferramenta de engenharia simples e rápida para investigar diretamente como as variáveis relacionadas à impedância do *liner* influenciam o ruído do *fan* nas etapas de propagação e radiação.

Palavras-chave: Ruído de fan. Liner acústico. Motor turbofan. Modelo de radiação. Técnica mode-matching. Escoamento não-uniforme.

ABSTRACT

The prediction of noise generated by aero-engine components and their mutual interaction for in-flight condition is an important tool for the aircraft design. Such tools make it possible to investigate the noise of different elements of these engines, in which fan noise may be the most significant under certain flight conditions. In general, the sound field generated by the fan within the nacelle can be computed employing a modal representation, which can be correlated with different sound generation mechanisms such as tonal (due to periodic movement) and broad-band noise (associated with turbulent flow). In order to reduce these noise sources, acoustic liners are commonly used for noise control, which are frequently modeled as a locally reacting acoustic impedance. However, under realistic flow conditions, the acoustic absorbing properties of liners and the resulting noise mitigation can be affected, which may lead to a reduction in their efficiency and modification of the far-field sound directivity. The main goal of the present study can be divided into two parts. The first is dedicated to develop an analytical tool regarding fan noise attenuation by the acoustic liner in terms of in-duct propagation and far-field radiation. In other words, it relates to the development of a prediction tool to design intake nacelles with acoustic liner in the presence of realistic flow for the conceptual design phase. The second part is to compare the effect of liner attenuation in the far-field for different boundary conditions representing the liners, involving uniform and non-uniform mean flows. In this case, Ingard-Myers and Brambley boundary conditions, as well as the Pridmore-Brown solution, are used to estimate the liner attenuation effects in the presence of a boundary layer with a given thickness. For radiated sound, the Rayleigh, Kirchhoff, and Wiener-Hopf formulations for near- and far-field were implemented. The study was conducted considering typical geometry and operating conditions of modern turbofan engines. For uniform flow cases, a reference solution was obtained from a finite element method code and used to validate the analytical models, which are based on the mode-matching technique and analytic radiation model. In-duct results in terms of the power transmission and modal decay rate along the duct suggested that the influence of the boundary layer thickness can lead to a significant reduction on intake liner attenuation. Besides, the interaction between refractive effects and liner resistance and reactance can be complex, where the boundary layer effect strongly depends on the liner impedance, and the two cannot be separated. On the other hand, the transmitted modes were coupled to an analytic radiation model for the entire solution. Moreover, the results suggested that modal scattering produced by liner discontinuities results in a complex behavior (in terms of the redistribution of the acoustic energy onto cut-on modes) in terms of noise radiation. By integrating the analytical approaches, it is possible to obtain a fast and straightforward engineering tool for investigating directly how the liner impedance quantities influence the fan noise in propagation and radiation modeling.

Keywords: Fan noise. Acoustic liner. Turbofan. Radiation models. Mode-matching scheme. Shear flow.

LIST OF FIGURES

LIST OF TABLES

LIST OF ACRONYMS

ADP	Advanced Ducted Propulsion fan rig
ADS	Acoustic Data Surfaces
ANoPP	Aircraft Noise Prediction Program
ANOTEC	European Aero-Noise Consulting
APU	Auxiliar Power Unit
BEM	Boundary Element Method
BPF	Blade-Passing Frequency
BPR	By-Pass Ratio
CAA	Computational Aeroacoustics
CAE	Computer-Aided Engineering
CARMEN	Acoustic module in IESTA platform
CDuct-LaRC	Ducted Fan Noise Propagation and Radiation Code
CFD	Computational Fluid Dynamics
CHE	Convective Helmholz Equation
DFD	Data-Flow Diagram
DGM	Discontinuous Galerkin Method
DLR	Deutsches Zentrum für Luft und Raumfahrt (German Aerospace Center)
DNS	Direct Numerical Simulation
elsA	Unsteady compressible CFD solver
EMPA	Swiss Federal Laboratories for Materials Science and Technology, Laboratory for Acoustics/Noise Control
EO	Engine Orders
FDM	Finite Difference method
FEM	Finite Element Method

FVM	Finite Volume Method
FW-H	Ffwocs Willians and Hawkings
GTD	Geometric Theory of Diffraction
ICAO	International Civil Aviation Organization
IE	Infinite Element
IESTA	Infrastructure for Evaluating Air Transport Systems
ISVR	Institute of Sound and Vibration Research
LBM	Lattice Boltzmann Method
LEE	Linearized Euler Equation
LES	Large Eddy Simulation
LINFLUX	Unsteady threedimensional linearized code of the R/S interaction
LNSE	Linearized Navier-Stokes Equation
MDOF	Multiple Degrees of Freedom
M-M	Mass and momentum
NASA	National Aeronautics and Space Administration
OAPWL	Overall Sound power level
OASPL	Nível de pressão sonora global
OGV	Outlet Guide Vane or stator
ONERA	Office National d'Etudes et de Recherches Aérospatiales (French aerospace agency)
PW	Pratt and Whitney company
PWL	Sound power level
PANAN	Parametric Aircraft Noise Analysis Module
PHOENIX	Parametric mesHing and analysis of aerOENgine In-takes and eXhausts
PPW	Points Per Wavelength

PropNoise	Propulsion Noise code
P-V	Pressure and axial acoustic velocity
RANS	Reynolds-averaged Navier-Stokes
RSM	Response Surface Modelling
sAbrinA	LEE solver
SDOF	Single Degree of Freedom
SDT	Source Diagnostic Test fan rig
SE	Semi-Empirical
SPL	Sound pressure level
SonAIR	Swiss Aircraft Noise Calculation Procedure
TBIEM3D	Thin duct, Boundary Integral Equation Method, 3 Dimensional
TFaNS	Tone Fan Noise Design/Prediction System
TPP	Triple Plane Pressure
TURBO	Unsteady Flows in Turbomachinery solver
URANS	Unsteady Reynolds-averaged Navier-Stokes

LIST OF SYMBOLS

Latin Symbols

a^*	Duct radius, m
a_c	Dimensionless lip radius
$A_{m,n}$	Dimensionless mode amplitude
$\mathbf{A}, \mathbf{B}$	Incident and transmitted amplitude vectors
B	Number of fan blades
c_0^*	Speed of sound, $\mathrm{m\,s^{-1}}$
d	Diameter of the liner holes, m
D^*	Distance from the duct termination, m
E, H, T	Liner characteristic dimensions, m
$\mathcal{E}$	Dimensionless end correction of liner holes
f^*	Acoustic frequency, Hz
$F_{m,n}$	Directivity function
$\mathcal{H}$	Element size, m
J_m	Bessel function of the first kind
k	Helmholtz number
$k_{m,n}$	Dimensionless axial wavenumber
l^*, L^*	Hard-walled and lined ducts length, m
M, M_0	Mach number and uniform Mach number
m	Azimuthal mode order
M_t, M_{rel}	Tip and relative Mach number
n	Radial mode order

n_c	Highest radial order mode
p	Dimensionless pressure
$P(r)$	Pridmore-Brown mode shape in radial direction
p^*	Acoustic pressure, Pa
$\tilde{p}$	Dimensionless harmonic pressure perturbation
$\mathbf{P}$	Far-field pressure vector
$\mathcal{P}$	Acoustic power
r	Radial coordinate
R	Real part of the acoustic impedance
S	Duct cross section, m^2
s	Duct segment
$\mathcal{S}(\theta)$	Convective factor in the far-field radiation
t	Dimensionless time
t^*	Time, s
$\mathbf{T}, \mathbf{R}, \mathbf{S}$	Trasmission, reflection and scattering matrices
u_0	Axial flow velocity, $\mathrm{m\,s^{-1}}$
V	Number of stators
v, u, w	Dimensionless acoustic particle velocity in radial, axial and tangential directions
$\tilde{v}, \tilde{u}, \tilde{w}$	Dimensionless harmonic acoustic particle velocity perturbation radial, axial and tangential directions
W	Test function for mode
x	Axial coordinate
Y_m	Bessel function of the second kind

Z	Dimensionless impedance
Z^*	Wall impedance, $\mathrm{Pa\,s/m^{-1}}$
$\mathbf{x}$	Coordinate vector, (r, θ, x)

Greek Symbols

$\alpha_{m,n}$	Dimensionless radial wavenumber
β	Prandtl-Glauert factor
χ, σ	Incident wave and the wedge angles
δ	Boundary layer thickness
$\Delta_{\mathrm{PWL}}, \Delta_{\mathrm{SPL}}$	Transmission loss (acoustic power and pressure), dB
$\eta_{m,n}$	Cut-off ratio
Γ	Boundary of the computational domain
γ	Ratio of specific heats at constant pressure and volume
Λ	Control surface of the computational domain
λ	Dimensionless local wavelength
∇	Nabla operator
Ω, Ω_0	Actual and maximum rotational speed, RPM
ω^*	Angular frequency, $\mathrm{rad\,s^{-1}}$
Ψ	Mode shape function
ψ	Modal phase, rad
ρ_0^*	Density, $\mathrm{kg\,m^{-3}}$
θ	Polar coordinate in far-field, $^\circ$
$\theta_{m,n}^{\vee}$	Zeroes angles in radiation pattern, $^\circ$
$\theta_{m,n}^{\wedge}$	Main lobe angle in radiation pattern, $^\circ$

$\tilde{\phi}$	Harmonic velocity potential
ε	Dimensionless duct thickness
φ	Azimuthal coordinate, $^\circ$
$\varphi_{m,n}$	Azimuthal propagation angle, $^\circ$
ϖ	Mass of the liner facing sheet
ϱ	Liner porosity (or the percentage open area), $\%$
Ξ	Computational domain
$\xi_{m,n}$	Cut-off parameter

Other Symbols

$(\cdot)^{\pm}$	Downstream and upstream propagation directions, respectively
$\hat{(\cdot)}$	Harmonic variable
D_0/Dt	Material derivative
$\mathrm{Im}(\cdot)$	Imaginary part of a variable
$\mathrm{Re}(\cdot)$	Real part of a variable
$\tilde{(\cdot)}$	Fluctuation variable
i	Imaginary unit, $\sqrt{-1}$

CONTENTS

1 INTRODUCTION

1.1 CONTEXT

The use of single-jet turbojet engines became the predominant form of aeronautical propulsion after the World War II. In the 1960s, this type of propulsion was extended to turboprop engines. Later, a large fan was introduced in the engines, which allowed it to drive the inflow to pass only partially through the compression stages (and in the additional duct named by-pass). The proportion between flows through the by-pass and compression stages defines the ratio of the mass flow, which is related to the efficiency and consumption of the turbomachine. The ratio of the mass flow of air by-passing the engine core divided by the mass-flow of air passing through the core is referred to as the by-pass ratio (BPR).

In order to increase performance and reduce fuel consumption, new architectures tend to turbofan engines with high BPR, and consequently, with higher diameters (SMITH, 2004). In addition, to reduce the weight brought by these geometries, it is necessary to reduce the length of the nacelle in order to gain compactness. This architecture has improved the performance of the new generation of engines while reducing jet noise, which was the dominant engine noise source for aircraft, as shown in Figure 1. Most of the airflow through a high-bypass turbofan has a lower velocity: even when combined with a much higher velocity engine core exhaust, the average exhaust velocity is considerably lower than in a pure turbojet. For this very reason, turbofan engines are significantly quieter than a pure-jet engine of the same thrust, and jet noise is no longer the predominant source.

The noise of the fan has become one of the major contributions of modern turbofan and aircraft noise in general. The International Civil Aviation Organization (ICAO) and airport regulations are becoming increasingly restrictive, and, therefore, the reduction of this noise component is essential for both engine and aircraft manufacturers (see Figure 2). The international standards define three certification points to evaluate the aircraft community noise: two points at takeoff known as sideline and flyover (or flyover cutback), and one point at approach. The percentages in Fig. 2 are defined in terms of the Effective Perceived Noise Level (EPNL)[1], which is the metric defined by the standards to evaluate the noise impact.

The fan stage is composed of two main elements, which are the fan (rotor) and the out-

[1] The EPNL is an indicator of airplane noise at a certification point, integrated over time and filtered from the maximum level to account for psychological factors related to the human ear, which is measured in EPNdB.

Figure 1 – Evolution of the directivity and the relative levels of the different sources as a function of engine architecture (or ratio of the mass flow): (a) low BPR (single flow turbojet). (b) High BPR (turbofan engine).

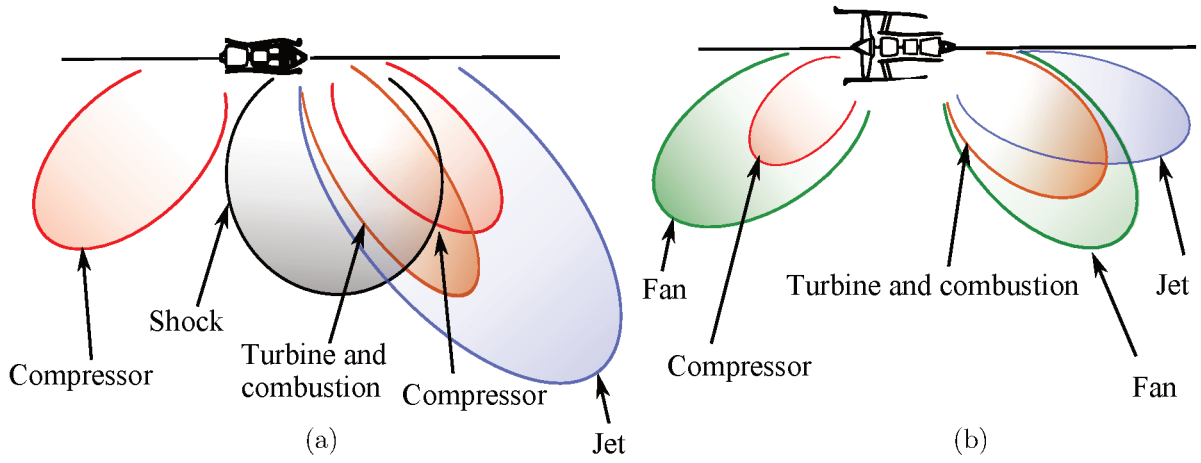

Source – Adapted from Smith (2004).

Figure 2 – Relative importance of the noise source on a commercial aircraft for the three control points of the ICAO certification.

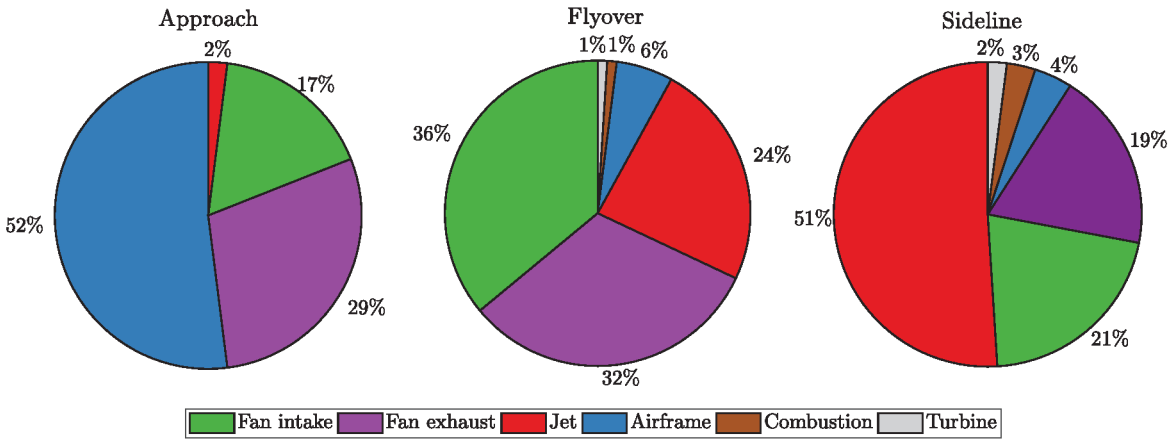

Source – Adapted from Cadot-Burillet et al. (2007).

let guide vanes (OGV) or stator, both placed inside the nacelle, as shown in Figure 3. In the primary circuit (red arrow), the airflow is compressed by the compressor and expanded by fuel burning in the combustion chamber, passing through the turbine stages, which powers the fan and compressor. The rest of the flow (blue arrow) is directed to the OGV where it is straightened to increase the thrust.

Figure 3 – Representation of a turbofan engine with a high BPR. (1): nacelle; (2): fan; (3): stator (or OGV); (4): engine section stator; (5): low-pressure compressor; (6): high-pressure compressor; (7): combustion chamber; (8): high-pressure turbine; (9): low-pressure turbine; (10): nozzle; (11): acoustic treatment. The red and blue arrows represent the primary and secondary flows, respectively.

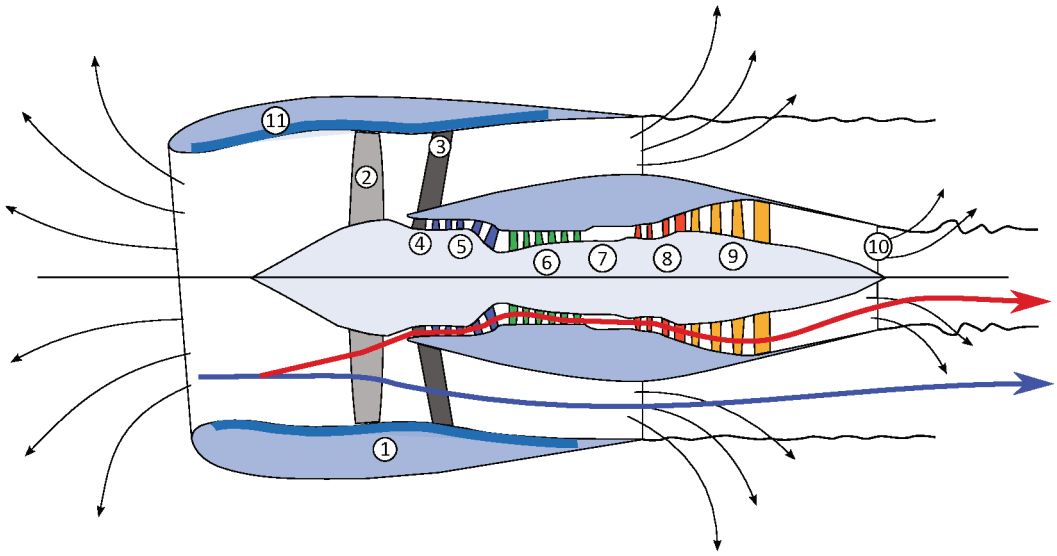

Source – Adapted from Rienstra (2016a).

An essential aspect for the design of the nacelle is the presence of the acoustic treatment (element 11 in Fig. 3) known as liner. Commonly, the structure of the liners is composed of three constructive elements: perforated plate, honeycomb structure, and rigid plate, as shown in Figure 4. These coupled elements act as Helmholtz resonators that are designed to operate in the frequency range of interest. In the most common variations, the liners may have a metal mesh covering the perforated plate (wire mesh liner), two or more liner layers (multiple degrees of freedom – MDOF – liner), axially segmented configuration, etc (LEYLEKIAN; LEBRUN; LEMPEREUR, 2014). In general, the liners are located inside the nacelle, in the inlet ducts and/or by-pass (see Figure 3), where the perforated plate is subjected to the tangential flow and the acoustic field generated by the different sources inside the engine (fan, core, compressor, etc.). The sound attenuation produced by a liner is an interplay between thermo-viscous dissipation inside its holes and the interaction with the grazing flow (EATON, 1999).

Figure 4 – Representation of typical liners applied to the aeronautical industry: (a) Single DOF liner; (b) Wiremesh liner; (c) Double DOF liner.

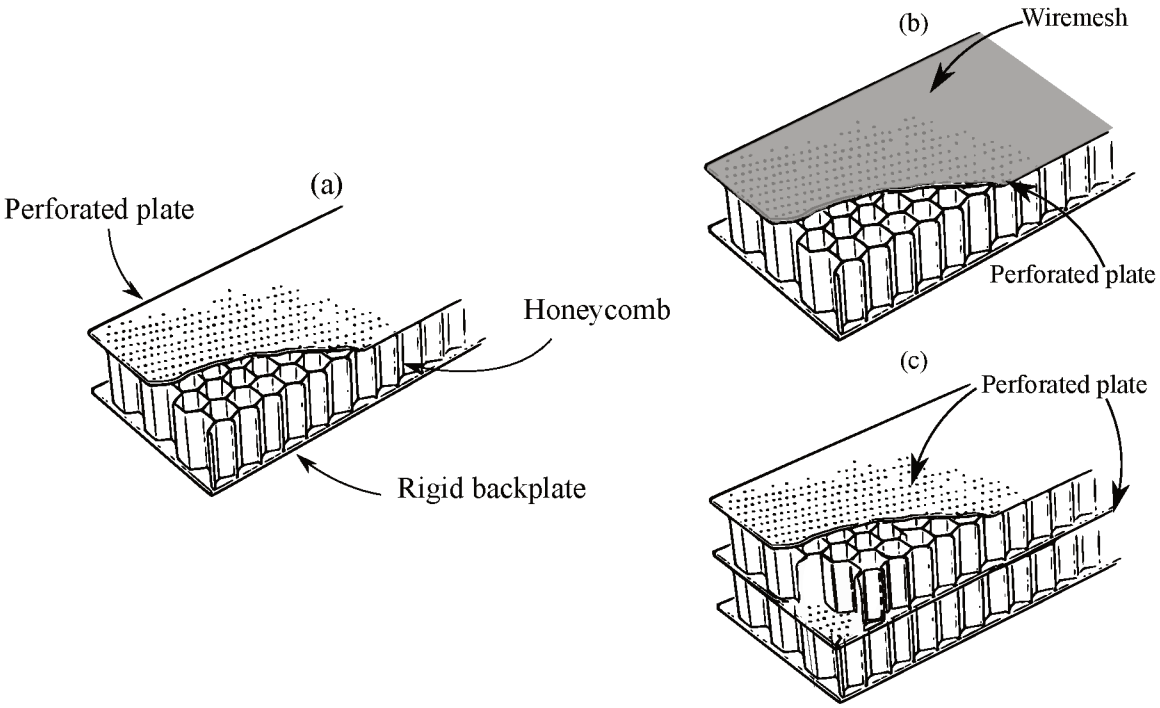

Source – Adapted from Smith (2004).

The prediction of fan noise can be a complex task due to its interaction with the liners, affecting the sound propagation and radiation to the far field. In addition, fan noise sources at different operating condition may also behave differently and need to be properly accounted for. One of the major sources of fan noise is the fan tone at the blade-passing frequency (BPF) caused by the periodic loading of the air mass closer to rotor blades. On the OGV interaction, it is responsible for the excitation of high and low order propagation modes along the engine duct. Besides, the interaction between turbulent flow and the edges of the rotor blades and OGV greatly contributes to the overall broadband noise (BB) level radiated to the far field (see Figure 5). Moreover, if the Mach number measured at the blade tip (and relative Mach number[2]), is supersonic (two bottom spectra in Fig. 5), shock waves attached to the blades generate multiple pure tones, harmonics of the rotation frequency, also called buzz-saw noise (BS).

The behavior of tonal and broadband noise was investigated experimentally by Tyler and Sofrin (1962) using a modal decomposition of the in-duct acoustic field, and the conditions under which the excited modes propagate or decay was verified. The study demonstrated the critical relationship between in-duct modal content and the far-field directivity patterns. In this sense, the prediction of far-field fan noise by means of a modal representation involves three key

[2] Absolute value with respect to axial and blade tip Mach number values in front of the fan plane.

Figure 5 – Example of narrowband spectra in the inlet duct of a turbofan for different relative Mach number. Ω and Ω_0 are actual and maximum speed rotation, respectively.

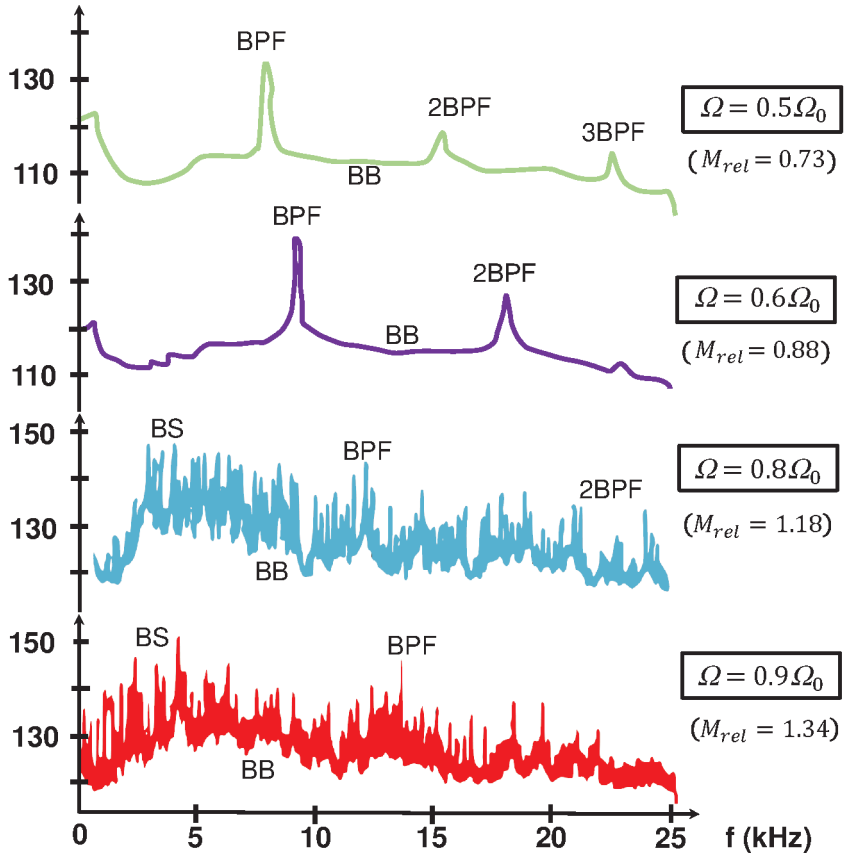

Source – Adapted from Lewy (2002).

elements: modal content generated at the fan plane, the in-duct propagation and the modal radiation efficiency. Thus, the complexity in the prediction of this noise component usually leads to a segmentation of the problem by modeling separatly the source, in-duct propagation and radiation to the far-field as shown in Figure 6. Black arrows represent the sound transmitted between the interfaces. In terms of the modal approach, the sound generation caused by unsteady flow fluctuations excite propagating modes, which propagate inside the inlet or exhaust duct and then are radiated to the free field. Each region is modeled based on their physical particularities (boundary conditions, physical characteristics, etc.) and may consider different prediction approaches (numerical, analytical, semi-empirical, etc.).

The importance of advanced simulation capabilities for fan noise prediction is demonstrated by the fact that most organizations and institutions have their own in-house software for fan noise predictions. An important step to further improve the overall noise prediction is the combination of different methods with different levels of accuracy. The most prominent examples of tools to investigate sound radiated from the aircraft and aero-engines were developed

Figure 6 – Typical divided regions used to predict fan noise in engines: sources generation, propagation and radiation.

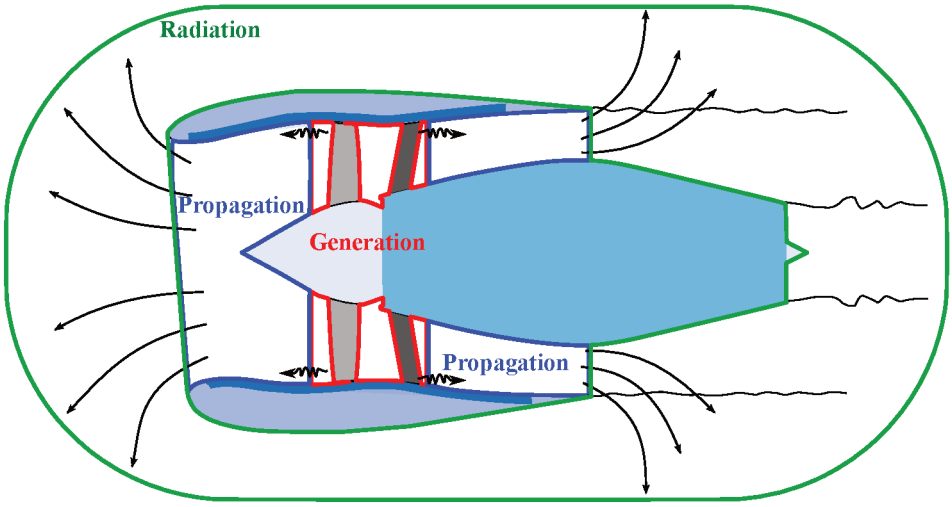

Source – Adapted from Rienstra (2016a).

by the main research institutions and aerospace agencies. These tools are developed to address overall aircraft/engine noise at the conceptual design stage, where available input data is limited in quantity and complexity. One may cite some prediction tool examples such as Aircraft Noise Prediction Program (ANoPP and ANoPP 2.0) (GILLIAN, 1982; LOPES; BURLEY, 2016), Silencer Common Platform for Aircraft Noise calculations (SOPRANO) (OOSTEN; COLLIN, 2014), Infrastructure for Evaluating Air Transport Systems (IESTA) (MALBÉQUI; ROZENBERG; BULTÉ, 2011) and Parametric Aircraft Noise Analysis Module (PANAN) (BERTSCH; GUERIN, et al., 2011), which were developed by NASA (American aerospace agency), ANOTEC (European aero-noise consulting), ONERA (French aerospace agency) and DLR (Germany aerospace agency), respectively. These prediction tools focus mainly on the low-cost, overall noise and physics–based approaches such as analytical and semi-empirical models.

In contrast, numerical simulations must allow to precisely model the mechanisms of generation, propagation, and radiation of noise. However, the differences between aerodynamic and acoustic fluctuations require sufficiently mesh sizes and small time steps to capture the physics of the problem. The mesh domain must also be large enough in order to contain all the sources and receivers. In such cases, the direct methods (DNS, Direct Numerical Simulation (ZHANG; BODONY, 2016), LES, Large-Eddy Simulation (LEONARD et al., 2016), LBM, and Lattice Boltzmann Method (CASALINO; HAZIR; MANN, 2016)) are very appealing but also costly in terms of computing time and can currently be applied to simplified configurations. Thus, hybrid methods in computational aeroacoustics (CAA) context provide less expensive meth-

ods that consist of decoupling computational fluid dynamics (CFD) and acoustic calculations. For the acoustic part, the boundary element method (BEM) for homogeneous (DUNN, 1997) and non-homogeneous (MANCINI et al., 2016) propagation media, finite-difference method (FDM) (GABARD; BRAMBLEY, 2014), discontinuous Galerkin method (DGM) (RARATA, 2014; GABARD; DAZEL, 2015) and finite element method (FEM) (ASTLEY, 2009; ASTLEY; SUGIMOTO; MUSTAFI, 2011; OZYORUK; ALPMAN, et al., 2004; MUSTAFI, 2013) represent the most common approaches. These numerical methods may be applied to solve the Euler and Navier-Stokes equations, in the complete or linearized form, considering the presence of the mean flow. For the aerodynamic part, in general, the simulation accuracy and computational cost applied to the region of the engine being studied depends on the flow characteristics being considered (inviscid, irrotational, etc.). In studies considering some arbitrary mean flows for intake regions (RARATA, 2014; MUSTAFI, 2013), it is observed that the temperature gradient and the turbulent flow intensity are small and, the adiabatic and irrotational flow hypothesis can be generally assumed.

These methods are excellent tools to study, in depth, the noise mechanisms and propagation conditions that arise from the source in the ducted fan stage. However, it remains particularly expensive to solve a propagation problem such as the fan inlet with a fully three-dimensional geometry. On the other hand, the calculation cost is currently too great to be used as pre-design tools, especially during preliminary parametric studies. This is why the analytical approaches remain quite useful and will be detailed in the continuation of this work.

The analytical modeling of the transmission and radiation of sound in ducts is reviewed by several authors (RIENSTRA, 2016a; EVERSMAN; HUBBARD, 1991; SHUR et al., 2016) in terms of modal approach. Some works focus on an infinite straight, circular duct (assuming most inlets are nearly circular), where the reflections and mode radiation are neglected, and the duct has a smooth geometry so that the aerodynamic flow is stable and total pressure losses are small. At typical BPF, the acoustic wavelength is of the order of one-tenth of the inlet duct diameter (MCALPINE; ASTLEY, et al., 2006), so changes in the duct diameter and the mean flow are generally assumed small, at least over an acoustic wavelength. For practical purposes, some of these approaches are also used to investigate the modal absorption rate due to the liner presence employing parametric studies (GABARD, 2016) (e.g., for a given frequency, mode order and Mach number) or considered an optimized noise reduction study for broadband and tone components (MCALPINE; ASTLEY, et al., 2006; LAFRONZA et al., 2006; SPILLERE; CORDIOLI, 2019). Moreover, other studies assuming the sound transmission in slowly varying

ducts were carried out for the same purposes for different flow cases and liner configurations (RIENSTRA, 1999; OVENDEN; RIENSTRA, 2004; RIENSTRA, 2016b).

In general, the noise reduction depends on the characteristics of the mean flow and other parameters such as liner geometry and acoustic sound pressure level (SPL) (SPILLERE, 2017). Usually, acoustic liners are represented as a locally reacting wall impedance, leading to different wavenumbers and mode shapes in the lined section, as opposed to a hard-walled duct. If the flow profile is taken as uniform, the acoustic particle displacement is assumed to be continuous across a thin vortex sheet over the liner surface. This set of assumptions constitute the basis of the Ingard-Myers boundary condition (INGARD, 1959; MYERS, 1980), which has been thoroughly used to represent the interplay between the flow and the acoustic impedance that represents the liner within the duct.

Over the past years, many studies have shown that this assumption may lead to erroneous predictions in modal attenuation (GABARD, 2016), which in turn can yield inaccurate far-field predictions (MUSTAFI, 2013). Other issues related to the Ingard-Myers boundary condition include time domain instabilities (BRAMBLEY, 2009) and differences between educed impedances using downstream and upstream propagating waves (RENOU; AURÉGAN, 2011; BODEN et al., 2017). These studies show that the design of acoustic linings for inlet applications must include careful consideration of boundary layer effects.

When predictions of the radiated noise are required, recourse usually is made to a simplified model of a cylindrical axisymmetrical duct with mean flow. Most of the proposed solutions are based on strong assumptions (for very long wavelength (LEVINE; SCHWINGER, 1948)) or strongly idealized situations, such as a zero thickness duct wall (HOMICZ; LORDI, 1975; RIENSTRA, 1984; MUNT, 1990) or an infinite flange (TYLER; SOFRIN, 1962; MORFEY, 1969). Numerical simulations with finite or boundary elements (MUSTAFI, 2013; DUNN; TWEED; FARASSAT, 1999; LIDOINE et al., 2001) can also be used, but they are not very conducive to physical insight or the implementation of optimization methods.

An important aspect addressed in the present work, but not dealt with in previous studies, is the effect of the boundary layer and flow profile on the intake duct that include the liner interfaces. As far as we know, no previous research has investigated this issue for turbofan intake applications where the liner section has a significant effect on the noise radiated from the exit duct. Also, the use of an in-duct model coupled to a radiation model has the advantage of shorter computational times as well as providing the possibility of gaining some physical understanding of the problem separately.

Despite the fact that the numerical and analytical methods are well developed for predicting the propagation of sound on subsonic flow regimes, some limitations have been observed. Most of them are based on a convective theory and cannot capture the propagation within a non-uniform flow, which is strongly influenced by the operating conditions. Moreover, the effect of refraction is inappreciably exploited when the liner discontinuities and far-field modeling are considered.

1.2 AIM AND OBJECTIVES

The main objective of the research in this thesis is to develop a semi-analytical tool to predict the far-field fan noise based on a modal approach. As a essential requirement, the tool must capture the effects caused by the interplay between liners and different flow conditions on the noise calculations. Moreover, this study aims at verifing the extent to which typical modeling assumptions, such as an uniform flow can affect the far-field prediction. Other contributions can be structured in the specific objectives, which are listed below:

- Develop a computational tool for calculation of the sound propagation and radiation from the inlet duct of a turbofan engine, considering the modal approach, which should allow to assess the effectiveness of different liner configurations.
- Evaluate the relevance and the limitations of numerical and asymptotic methods used on the problem of the intake configuration. In this case, the acoustic field in the duct should be simulated to assess the accuracy of the analytical methods by means of a FEM commercial code.
- Use different approaches to analyze the physical phenomena governing acoustic propagation and radiation of the inlet ducts and isolate the influence of the different parameters of the problem such as acoustic treatments, geometry and shear flow for tone (single mode analysis) components.
- Investigate the boundary layer effects on the liner attenuation and, consequently, its influence on the radiation directivity, considering uniform and shear flows.

1.3 DOCUMENT STRUCTURE

This thesis consists of 7 chapters organized as follows:

Chapter 2 provides a literature review. First, the basic equations of duct acoustics are reviewed. This is important for two reasons: (i) the methods and techniques implemented in this thesis are based on the fundamentals of duct acoustics; and (ii) the key concept of a prediction tool for fan noise reduction is based on the duct acoustics formulation and its relationship with the non-uniform mean flow and acoustic impedance. On the following, details about modeling approaches in fan noise context regarding the main characteristics of prediction tools, specialized methods and techniques, and acoustic liner representation are given. Moreover, a brief explanation is given about the noise source representations by means of the modal approach.

Chapter 3 describes the predictive semi-analytical models implemented in this thesis. Two mode matching schemes (for uniform and segmented liners) and two matching conditions are shown in details. Additionally, the radiation models for different duct ends are also briefly presented and their main characteristics are discussed. On the following, the basic structure of the code is provided, where the inputs of these models are mainly linked to (i) air properties, (ii) liner geometry and (iii) operating conditions.

Chapter 4 investigates the accuracy of these predictive models by using a finite element (FE) specialized software. A compressible parametric study based on typical engine parameters is explored in detail. Both in-duct and radiation models are also examined separately and discussed regarding their limitations in the present work. Six numerical models with different characteristics are considered to evaluate these analytical models.

Chapter 5 concentrates on the effect of the boundary layer thickness applied to circular lined ducts with discontinuities, with emphasis on the sideline, cutback, and approach operating conditions. This chapter aims at including the impact of non-uniform flow on the liner attenuation performance. More specifically, this is done considering typical parameters of the inlet duct and applying different boundary conditions (described in Chapter 2), which are compared in terms of the modal decay rate along the duct and sound power transmission. Also, an impedance parametric study is conducted in order to verify if the effects observed previously in the course of the chapter are also presented in other conditions.

Chapter 6 investigates sound attenuation prediction in the far-field noise, due to the presence of shear flow in the in-duct propagation. Details about the numerical formulation to couple the analytic radiation model to a mode-matching scheme are given. On the following, effects of mean flow velocity and boundary layer thickness are investigated for a typical turbofan engine, which is presented in terms of the radiated far-field sound. Moreover, employing the impedance parametric study investigated in Chapter 5, the attenuation and scattering effects are also anal-

ysed in the far-field predictions.

Chapter 7 presents the overall conclusions and recommendations for future works.

2 LITERATURE REVIEW AND THEORETICAL BACKGROUND

This chapter describes the literature review and theoretical modeling used in this thesis to describe the propagation of sound in the engine intake ducts and radiation to the far-field. This chapter starts with a review of duct acoustics in the presence of flow and a lined surface. Subsequently, a description of typical modeling tools used in aeronautical applications is given. These tools provide a basic understanding of the modeling capabilities of the different approaches. Also, the main methods and techniques in fan noise modeling are described, followed by a review of the most recent studies related to impedance models for the representation of acoustic liners.

2.1 DUCT ACOUSTICS

In this section, the governing equations and boundary conditions are presented. Initially, we seek the wavenumbers and mode shapes at the rigid and lined sections in the presence of uniform and shear flows. On the following, we introduce some important concepts related to the eigenvalue problem for hard-walled and lined duct assumed in the next chapters.

2.1.1 Governing equations

Consider a duct of radius a^* with a lined section of length L^*, locally reacting impedance Z^* and cylindrical coordinates, as shown in Figure 7. In the presence of an inviscid compressible flow, the governing equations are given by the Euler equations

Figure 7 – Straight duct with a lined segment and shear flow.

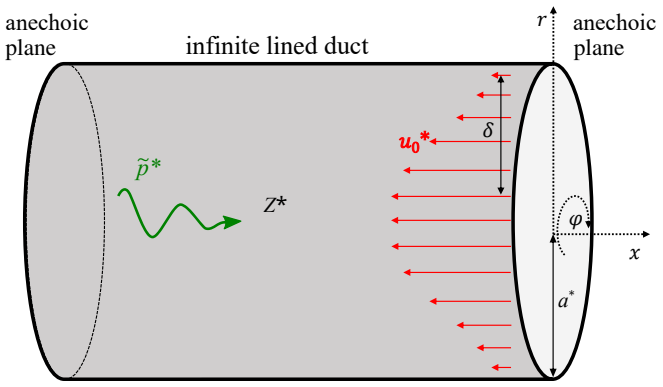

Source – Own authorship.

$$\frac{\partial \rho^*}{\partial t^*} + \nabla \cdot (\rho^* \mathbf{u}^*) = 0, \tag{2.1}$$

$$\rho^* \frac{\mathrm{D}_0 \mathbf{u}^*}{\mathrm{D}t^*} + \nabla p^* = 0, \tag{2.2}$$

$$\frac{\mathrm{D}_0 p^*}{\mathrm{D}t^*} - c_0^{*2} \frac{\mathrm{D}_0 \rho^*}{\mathrm{D}t^*} = 0, \tag{2.3}$$

where ρ^* is the fluid density, t^* is the time, $\mathbf{u}^*$ is the velocity vector, p^* is the pressure and c_0^* is the speed of sound and $\mathrm{D}_0/\mathrm{D}t = \partial/\partial t + u_0 \partial/\partial x$ is the material derivative in the non-stationary fluid (or in the frequency domain $\mathrm{D}_0/\mathrm{D}t = \mathrm{i}\omega + u_0 \partial/\partial x$). The superscript * denotes physical variables. At this point, it is convenient to introduce the non-dimensional variables:

$$\begin{gathered} \rho = \rho^*/\rho_0^*, \quad t = t^* c_0^*/a^*, \quad \mathbf{x} = \mathbf{x}^*/a^*, \quad p = p^*/\rho_0^* c_0^{*2}, \\ \mathbf{u} = \mathbf{u}^*/c_0^*, \quad Z = Z^*/\rho_0^* c_0^*, \quad M = u_0^*/c_0^*, \end{gathered} \tag{2.4}$$

where ρ_0^* is a reference density, $\mathbf{x}$ is the coordinate vector, M is the flow Mach number and Z is the liner impedance. The linearization of the equation can be performed by introducing a steady mean flow and small unsteady acoustic pressure $\tilde{p}$ of angular frequency ω, so that

$$\mathbf{u} = \mathbf{u_0} + \tilde{\mathbf{u}}, \tag{2.5}$$

$$p = p_0 + \tilde{p}, \tag{2.6}$$

$$\rho = \rho_0 + \tilde{\rho}. \tag{2.7}$$

Assuming a modal solution, the in-duct pressure field can be described as the sum of acoustic modes of the form of

$$[\tilde{p}, \tilde{\mathbf{u}}, \tilde{\rho}] = [\hat{p}, \hat{\mathbf{u}}, \hat{\rho}] \exp(i\omega t - \mathrm{i} k_{m,n} x - \mathrm{i} m \varphi), \tag{2.8}$$

where m is the azimuthal mode order, $\hat{\cdot}$ denotes the harmonic variable, and $k_{m,n}$ is the axial wavenumber. Assuming a homoentropic relation and that the sound speed is radially uniform (i.e. $\tilde{\rho} = \tilde{p}$), the linearized Euler equations can be written in cylindrical coordinates as

$$\mathrm{i}(k - M k_{m,n})\hat{p} - \mathrm{i} k_{m,n} \hat{u} + \left(\frac{d}{dr} + \frac{1}{r}\right)\hat{v} - \frac{\mathrm{i}m}{r}\hat{w} = 0, \tag{2.9}$$

$$-\mathrm{i} k_{m,n} \hat{p} + \mathrm{i}(k - M k_{m,n})\hat{u} + \frac{dM}{dr}\hat{v} = 0, \tag{2.10}$$

$$\frac{d\hat{p}}{dr} + \mathrm{i}(k - M k_{m,n})\hat{v} = 0, \tag{2.11}$$

$$-\frac{\mathrm{i}m}{r}\hat{p} + \mathrm{i}(k - M k_{m,n})\hat{w} = 0 \tag{2.12}$$

where $k = \omega^* a^*/c_0^*$ is the non-dimensional wavenumber and $\hat{u}$, $\hat{v}$ and $\hat{w}$ are the acoustic velocity components in axial, radial, and azimuthal directions, respectively. Equations (2.9) to (2.12) can be combined to form the Pridmore-Brown (PRIDMORE-BROWN, 1958) equation

$$\begin{aligned} \frac{d^2\hat{p}}{dr^2} + \left(\frac{1}{r} + \frac{2k_{m,n}}{k - Mk_{m,n}}\frac{dM}{dr}\right)\frac{d\hat{p}}{dr} + \\ \left((k - Mk_{m,n})^2 - k_{m,n}^2 - \frac{m^2}{r^2}\right)\hat{p} = 0, \end{aligned} \tag{2.13}$$

although the system of equations is preferred when solving it numerically by means of finite difference or spectral methods. In the case of uniform flow, the Mach number M becomes M_0, and $dM/dr = 0$, such that the Pridmore-Brown equation is simplified to the convected Helmholtz equation (CHE)[1],

$$\frac{d^2\hat{p}}{dr^2} + \frac{1}{r}\frac{d\hat{p}}{dr} + \left((k - M_0 k_{m,n})^2 - k_{m,n}^2 - \frac{m^2}{r^2}\right)\hat{p} = 0, \tag{2.14}$$

which satisfies the dispersion relation

$$\alpha_{m,n}^2 + k_{m,n}^2 = (k - M_0 k_{m,n})^2, \tag{2.15}$$

for each pair of modes (m, n) and radial wavenumber $\alpha_{m,n}$ value. The solution of the pressure field in Eq. (2.14) is given in the form of Bessel functions of the first kind and azimuthal dependence $J_m(\alpha_{m,n}r)\exp(-\mathrm{i}m\varphi)$ for both right- and left-running modes (or downstream and upstream propagation, respectively). In Eq. (2.13), the Pridmore-Brown modes are generically written as $\Psi_{m,n}(r)\exp(-\mathrm{i}m\varphi)$ for both directions as well. For each acoustic velocity component or pressure we can assume modal shape solutions of the form $\Psi_{m,n}(r)\exp(-\mathrm{i}m\varphi) = [P(r), U(r), V(r), W(r)]\exp(-\mathrm{i}m\varphi)$.

The expressions of the general solution in terms of pressure and axial acoustic velocity[2] on any section of duct, for both Eqs. (2.13) and (2.14), are given by

$$\begin{aligned} \hat{p}(x,r,\varphi) = \sum_{m=-\infty}^{\infty}\sum_{n=1}^{\infty}[\hat{p}_{m,n}^{+}(x,r,\varphi) + \hat{p}_{m,n}^{-}(x,r,\varphi)], \quad \text{with} \\ p_{m,n}^{\pm}(x,r,\varphi) = A_{m,n}^{\pm}\Psi_{m,n}(r)e^{-\mathrm{i}m\varphi - \mathrm{i}k_{m,n}^{\pm}x} \end{aligned} \tag{2.16}$$

and

$$\begin{aligned} \hat{u}(x,r,\varphi) = \sum_{m=-\infty}^{\infty}\sum_{n=1}^{\infty}[\hat{u}_{m,n}^{+}(x,r,\varphi) + \hat{u}_{m,n}^{-}(x,r,\varphi)], \quad \text{with} \\ u_{m,n}^{\pm}(x,r,\varphi) = \frac{k_{m,n}^{\pm}}{k - k_{m,n}^{\pm}M}A_{m,n}^{\pm}\Psi_{m,n}(r)e^{-\mathrm{i}m\varphi - \mathrm{i}k_{m,n}^{\pm}x} \end{aligned} \tag{2.17}$$

[1] Note that M_0 is also the centerline Mach number for shear flow case.

[2] It is not demonstrated here but it is straightforward to find pressure and acoustic velocity relation from the momentum conservation equation (Eq. (2.2)).

where $A_{m,n}$ is the pressure modal amplitude. For Eq. (2.14) (i.e. corresponding to uniform flow solution) $\Psi_{m,n}(r) = J_m(\alpha_{m,n}r)$ and for Eq. (2.13) the pressure modal form is used $\Psi_{m,n}(r) = P_{m,n}(r)$. The sign $\pm$ denotes the propagation directions along the duct, which is assumed as positive direction for wave in the same direction of the mean flow (or downstream propagation), otherwise when it is against the mean flow (or upstream propagation) the propagation is negative.

2.1.2 Boundary conditions

In the presence of mean flow, in order to address the the wall boundary condition that representing the acoustic liner, this Section is divided into: uniform and shear flows. For slipping mean flow or uniform flow, it is introduce the boundary conditions in the context of the CHE in Eq. 2.14. On the following, in the case of shear flow, we assume that there is no mean flow at the duct wall, such that the standard relation of hard-walled and lined duct is used.

2.1.2.1 Uniform flow

In hard-walled ducts, the normal acoustic velocity at the wall is zero, or

$$\hat{\mathbf{u}} \cdot \mathbf{n} = 0, \tag{2.18}$$

where $\mathbf{n}$ is a unit vector normal to the wall. Therefore, the derivative of pressure must vanish (i.e., by means of the momentum conservation equation), and the radial wavenumbers $\alpha_{m,n}$ must satisfy

$$J'_m(\alpha_{m,n}) = 0. \tag{2.19}$$

The spatial distribution of the normalized acoustic pressure is illustrated in Figure 8 for four different modes (and four Bessel roots of the Eq. (2.19)). In our notation, the circumferential order is assumed $-\infty \leq m \leq \infty$ and radial order $n \geq 1$. Note that the nodal lines of higher modal patterns (i.e., $|m| > 1$ or $n > 2$) are visible in the duct cross-section and the transversal pattern is rotating along the duct for higher circumferential modes ($|m| > 0$), which are usually called spinning modes. The radial acoustic pressure distribution of the spinning modes is concentrated at the duct wall with increasing circumferential order, which spirals around the x-axis with a constant spin pitch $2\pi m/|\mathrm{Re}(k^{\pm}_{m,n})|$. For uniform flow cases, these Fourier-Bessel modes still are solutions that satisfy the Eq. (2.19).

Figure 8 – Modal form and propagation pattern of acoustic modes in cylindrical ducts.

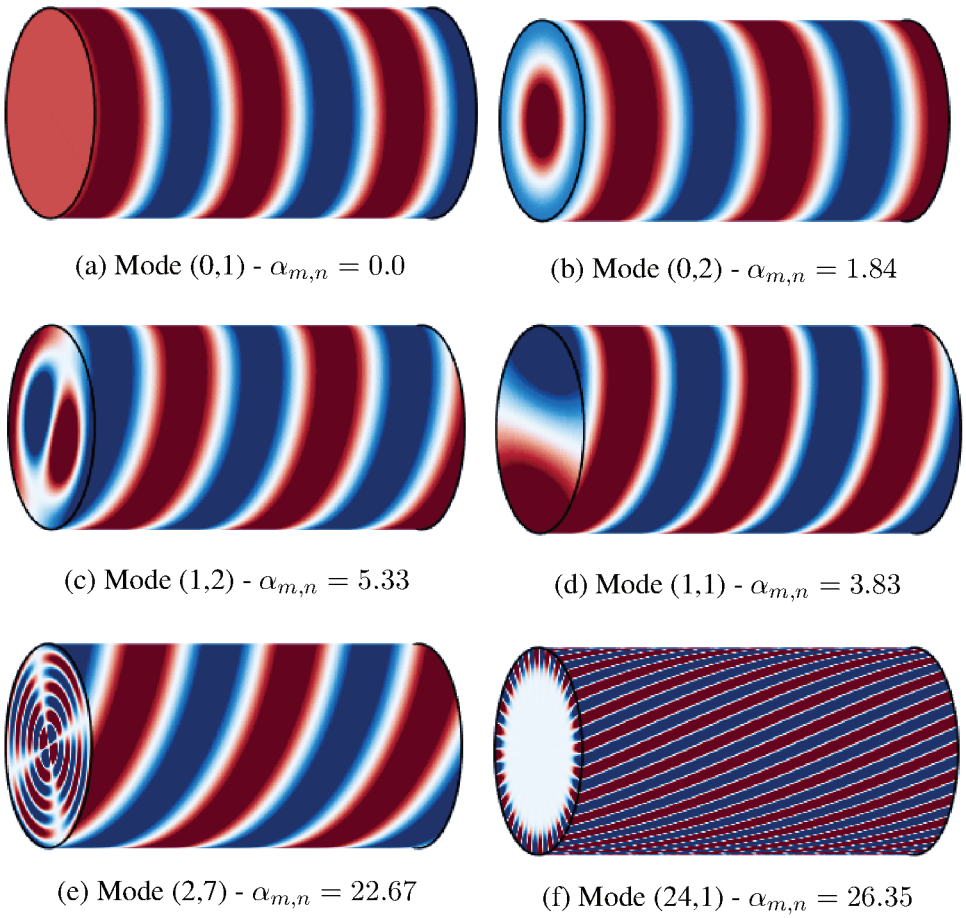

(a) Mode (0,1) - $\alpha_{m,n} = 0.0$ (b) Mode (0,2) - $\alpha_{m,n} = 1.84$

(c) Mode (1,2) - $\alpha_{m,n} = 5.33$ (d) Mode (1,1) - $\alpha_{m,n} = 3.83$

(e) Mode (2,7) - $\alpha_{m,n} = 22.67$ (f) Mode (24,1) - $\alpha_{m,n} = 26.35$

Source – Own authorship.

From Eq. (2.15), the axial wavenumber can be calculated as

$$k^{\pm}_{m,n} = \frac{k}{1 - M_0^2}\left[-M_0 \pm \sqrt{1 - (1 - M_0^2)\left(\frac{\alpha_{m,n}}{k}\right)^2}\right], \tag{2.20}$$

with $\mathrm{Im}\left\{\pm\sqrt{1 - (1 - M_0^2)\,(\alpha_{m,n}/k)^2}\right\} \leq 0$. In a rigid-wall duct, only a finite number of modes can propagate and transmit acoustic energy. These modes are called cut-on modes and can be found by using the following definition (also called cut-off ratio):

$$\eta_{m,n} = \frac{k}{\alpha_{m,n}\sqrt{1 - M_0^2}}, \tag{2.21}$$

where $\eta_{m,n} \geq 1$ means that mode is cut-on, otherwise it is cut-off (also called evanescent mode). Later, a similar cut-off parameter will be necessary to identify general trends in the modes (e.g. in terms of absorption rate or the influence of the boundary layer[3]) defined by Rice (1978) as follows

[3] These both cut-off definitions are derived for uniform flow, it is also useful for sheared flows to order the acoustic modes.

Figure 9 – Illustration of cut-on phenomena of a higher-order mode (without mean flow) and the influence cut-off ratio on its propagation.

(a) $\eta_{m,n} = 2$ ($\xi_{m,n} = 0.25$) (b) $\eta_{m,n} = 1$ ($\xi_{m,n} = 1$) (c) $\eta_{m,n} = 0.8$ ($\xi_{m,n} = 1.7$)

Source – Own authorship.

$$\xi_{m,n} = \frac{1}{\eta_{m,n}^2} = \frac{\alpha_{m,n}^2(1 - M_0^2)}{k^2}. \tag{2.22}$$

The propagation pattern of a higher order mode as a function of the cut-off parameters is illustrated in Figure 9. The well cut-on modes (as seen in Fig. 9a) have a higher cut-off ratio, which is commonly assumed as $\eta_{m,n} \geq 2$. If $\eta_{m,n} \cong 1$, the mode is defined as nearly cut-off, and in the absence of mean flow, the mode can be understood as at resonance and the axial wavelength ($2\pi/k_{m,n}$) is infinite (see Fig. 9b)[4]. Once the wavenumber is reduced to below the cut-off frequency of the mode (defined as $\alpha_{m,n}\sqrt{1 - M_0^2}$), the amplitude decays exponentially, which is determined by the imaginary part of axial wavenumber $k_{m,n}$ (see Fig. 9c). In general, for higher-order modes, it is reasonable to neglect all evanescent modes, especially far from the noise source. On the other hand, the cut-off modes might become important if the cut-off ratio is too close to 1.

The convective effect due to the uniform mean flow is also important on the modal propagation. It is interesting to note that in the Eq. (2.20), due to the uniform mean flow, the axial modal wavenumbers are shifted to the left ($M_0 > 0$), or right ($M_0 < 0$), by a fixed amount of $-kM_0/\sqrt{1 - M_0^2}$, while the cut-off ratio limit is lowered from $k/\alpha_{m,n} = 1$ for no flow to $k/\alpha_{m,n} = \sqrt{1 - M_0^2}$ with flow (it can be seen in the Eq. (2.21)). It implies that with mean uniform flow more modes are possibly cut-on than in the absence of flow. Figure 10 illustrates the convective effect in a higher order mode propagating in the same direction and against the mean flow. The effect of the flow for hard wall is more simple, which is to stretch the wavelength of waves travelling in the direction of the flow by a factor of $1 + M_0$, corresponding

[4] When the uniform mean flow is present and $\eta_{m,n} \approx 1$, the propagation mode only depends on the Mach number and duct mode eigenvalue or wavenumber (i.e. Eq. (2.20) becomes $k_{m,n}^{\pm} = -kM_0/(1 - M_0^2) = -\alpha_{m,n}M_0/\sqrt{1 - M_0^2}$). Therefore, the axial wavelength becomes finite.

Figure 10 – Uniform mean flow effects on the downstream (top) and upstream (bottom) propagation of higher-order modes.

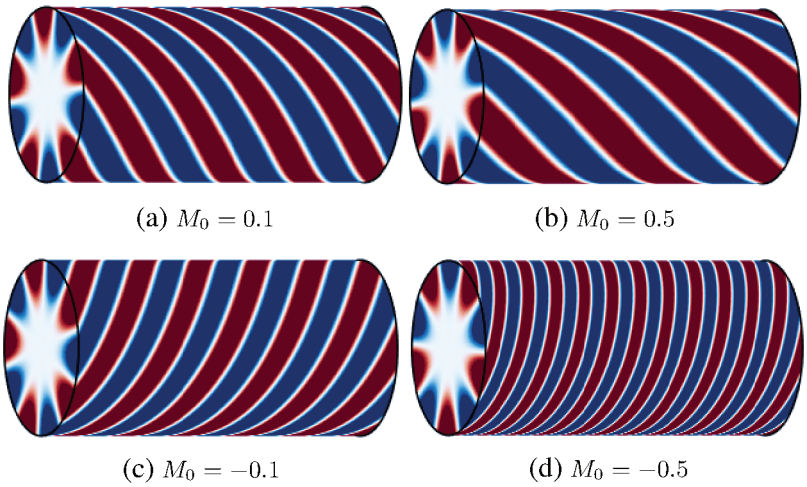

(a) $M_0 = 0.1$ (b) $M_0 = 0.5$

(c) $M_0 = -0.1$ (d) $M_0 = -0.5$

Source – Own authorship.

to an increase of the speed of sound and to contract the wavelength of waves travelling in the opposite direction by a factor of $1 - M_0$, corresponding to a decrease of the speed of sound.

Another physical insight of the modal propagation is the point of view of the acoustic field as the result of the interference of plane waves propagating at an angle to the duct axis and therefore reflecting from the duct walls. This approach follows the definitions of geometric acoustics or ray acoustics (GTD), as described in Section 2.2.2. Note that it is exact in a two-dimensional duct with parallel walls and approximate in a circular duct. The angle of propagation is directly related to the cutoff ratio, and the duct modes can be expressed exactly as the superposition of two plane waves (see in (HOCTER, 1999; CHAPMAN, 1994) for more details). For example, without flow, the structure of propagation angles is given as $\sin\theta_{m,n} = 1/\eta_{m,n}$ and $\sin\varphi_{m,n} = m/\alpha_{m,n}$, as shown in Figure 11. Therefore, modes nearly cut-off have mode angles close to $90°$, whereas modes that are well cut-on have smaller angles and have a prominent upstream directivity closer to the axial duct line. For instance, when high order modes propagate in a lined duct close to its cut-off frequency, a large axial absorption rate is expected (EVERSMAN; HUBBARD, 1991). Conversely, well cut-on modes will have small axial decay rates, due to the acoustic lining proprieties and the radial profile of the acoustic pressure inside the duct, generally concentrated far from the wall. Moreover, even though the cut-off ratio is derived for uniform flow, it is also useful for sheared flows and lined duct and may be used to order the acoustic modes. Several authors used these definitions to obtain an advantage in correlating attenuation in lined ducts (RICE, 1971; MOREAU; GUERIN; BUSSE, 2009; GABARD,

2013) and in estimating the direction of the major lobe of the radiation from a duct termination (HOMICZ; LORDI, 1975; HOCTER, 1999).

Figure 11 – Propagation angles in cylindrical ducts: a ray to be piecewise linear helix of higher-order modes.

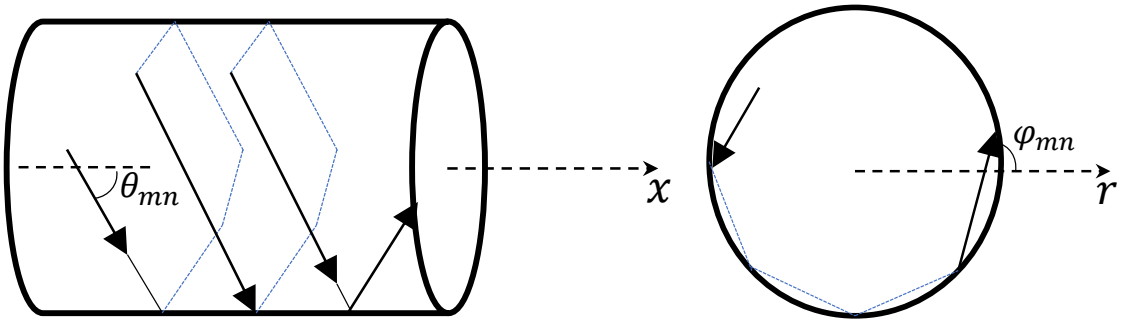

(a) Side view of duct

(b) Front view of the duct.

Source – Adapted from Chapman (1994).

In contrast to the rigid wall, the soft wall (prescribed by a locally reactive impedance Z) is much more sensitive to the details of the flow, especially in the region close to the wall. If uniform flow is assumed, the non-zero flow velocity is present at the duct wall (corresponding to a slip condition). Ingard (1959) derived a boundary condition assuming continuity of the normal component of acoustic particle displacement, for a planar boundary, across an infinitely thin boundary layer (also called vortex sheet) as shown in Figure 12. This boundary condition was generalized to curved surfaces by Myers (1980), leading to the Ingard-Myers boundary condition, given by

Figure 12 – Illustration of the Ingard-Myers boundary condition implications at wall.

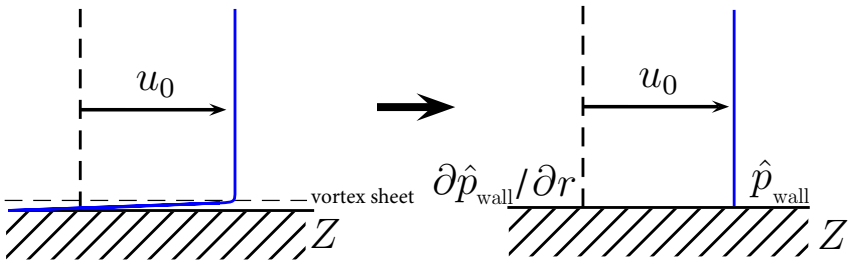

Source – Adapted from Rienstra and Hirschberg (2015).

$$\frac{\partial\hat{p}(1)}{\partial r} = \hat{v}(1)\cdot\mathbf{n} = \mathrm{i}(\omega - u_0 k_{m,n})\frac{\hat{p}(1)}{\mathrm{i}\omega Z}, \tag{2.23}$$

and which leads to the eigenvalue equation

$$-\frac{\mathrm{i}k}{Z}\left(1-M_0\frac{k_{m,n}}{k}\right)^2=\alpha_{m,n}\frac{J'_m(\alpha_{m,n})}{J_m(\alpha_{m,n})}. \tag{2.24}$$

Later some authors (BRAMBLEY, 2009; BRAMBLEY, 2011; RIENSTRA; DARAU, 2011; RENOU; AURÉGAN, 2011) noted that a very thin boundary layer along an impedance wall might be unstable for certain frequencies and impedance values, leading difficulties for computational simulations in time domain (GABARD; BRAMBLEY, 2014). Some of these instabilities were discussed in details by Rienstra (2003) and Vilenski and Rienstra (2007), which show that the complex behavior of the hydrodynamic field above the liner is different from what is predicted by the Ingard-Myers condition. From a dispersion analysis, Brambley (2009) showed the growth rate[5] can be unbounded as $k\to\infty$, implying that the problem is ill-posed.

Alternatively, the boundary layer effects can be included in the boundary condition, turning into a "corrected" impedance as seen by an acoustic field in the presence of uniform flow. Brambley (2011) proposed a modified Ingard-Myers boundary condition by introducing a small but finite boundary layer δ at the wall, such that the eigenvalue equation is given by

$$\begin{aligned}\mathrm{i}kZ\left[1-(k_{m,n}^2+m^2)\delta I_1\frac{J_m(\alpha_{m,n})}{\alpha_{m,n}J'_m(\alpha_{m,n})}\right]=\\ (k-Mk_{m,n})^2\left[\frac{J'_m(\alpha_{m,n})}{\alpha_{m,n}J_m(\alpha_{m,n})}-\delta I_0\right],\end{aligned} \tag{2.25}$$

where the coefficients δI_0 and δI_1 are given by

$$\begin{aligned}\delta I_0&=\int_0^1 1-\frac{(k-u_0(r)k_{mn})^2}{(k-Mk_{mn})^2}dr,\\ \delta I_1&=\int_0^1 1-\frac{(k-Mk_{mn})^2}{(k-u_0(r)k_{mn})^2}dr.\end{aligned} \tag{2.26}$$

The former may be interpreted as a correction to the impedance as seen by the acoustic field in the presence of uniform flow, while the latter is responsible for the well-posedness of the boundary condition (BRAMBLEY, 2011). The δI_0 term can be understood physically as the mass, momentum and kinetic energy deficit in the boundary layer which causes the effective boundary seen by the acoustic field. So, this term can be rewritten as follows

$$\delta I_0=\frac{1}{(k-Mk_{m,n})^2}[k^2\delta_0-2kk_{m,n}M\delta_1+M^2k_{m,n}^2(\delta_1+\delta_2)], \tag{2.27}$$

[5] For bounded initial conditions, implying $k_{m,n}$ is real, the stability of the subsequent evolution may be characterized by the exponential growth rate $-\mathrm{Im}(k(k_{m,n}))$.

where δ_0 is the "mass" thickness, δ_1 is the displacement thickness of the boundary layer and δ_2 is the momentum thickness. The "mass" thickness is associated with the mean density profile, which should be significant when there is a density profile (e.g. caused by temperature profiles). For the displacement and momentum thicknesses of a boundary layer in a circular duct can be understood as approximations of first order in δ. Since a constant density was assumed across the boundary layer, the displacement thickness is given by

$$\delta_1 = \int_{1-\delta}^{1} 1 - \frac{M(r)}{M_0}. \tag{2.28}$$

Note that the displacement thickness δ_1 can be used to characterize the boundary layer. In terms of the impedance analysis, it can be used to collapse for any mean profile, and the results depend weakly on the shape of the profile (NAYFEH; KAISER; SHAKER, 1974). A detailed review about shear flow effects on the liner impedance is given in the continuation of this Chapter in Section 2.2.3.

2.1.2.2 Shear flow

In the presence of shear flow, the flow velocity is usually assumed zero at the wall, i.e., the flow profile is defined as fully developed (or at least strongly sheared). The boundary condition for hard-walled ducts remains the same (Eq. (2.18)), while for lined ducts the standard definition of impedance can be used,

$$\hat{v}(1) = \frac{\hat{p}(1)}{Z}. \tag{2.29}$$

Note that it is not restrictive to soft-wall in the presence of shear flow, and another approach commonly assumed is Ingard-Myers boundary condition for free-slip cases (i.e., the wall Mach number is not zero) (OPPENEER; RIENSTRA; SIJTSMA, 2016).

One can solve Eq. (2.24) and Eq. (2.25) recursively starting with a well-known value, i.e., the radial wave numbers for hard-walled ducts, given by Eq. (2.19), and take small increments in the impedance until the desired amount is reached. This method is known as the tracking method, and a brief outline of the procedure is given in section 3.2.

By applying the boundary conditions in the linearized Euler equations (Eqs. (2.9) to (2.12)), the eigenvalues and the corresponding eigenfunctions can be found either by a high-order finite difference method (GABARD, 2016) or a spectral method (MARX; AURÉGAN, 2013; BOYD, 2001). Also, these boundary conditions can be applied directly in Pridmore-Brown equation, and it is usually solved by means of a fourth-order Runge-Kutta scheme

(MUNGUR; GLADWELL, 1969; EVERSMAN, 1971). Eversman and Hubbard (1991) discuss that a great advantage of these discretization methods is that the resulting eigenvalue solution spans a complete finite subset of eigenvalues with neither omission nor duplication, provided the discretization is carried out to a high enough level of accuracy.

2.2 FAN NOISE MODELING OVERVIEW

2.2.1 Prediction tools

Several research institutions and engineering sectors of today's leading aviation companies are seeking forecasting methodologies for increasingly accurate estimates of total aircraft noise. In the case of engine noise, specifically for the fan noise component, the estimation tools are usually based on one or more of the approaches described in this section.

Farassat and Casper (2006) proposed to distinguish four different approaches within the current full range of modeling capabilities (specifically derived for airframe noise but in principle applicable to engine noise as well). Later, Bertsch, Simons, and Snellen (2015) added one more important modeling approach to this list. The following five different approaches may be distinguished as (BERTSCH; SIMONS; SNELLEN, 2015):

1. Fully numerical: where the source and propagation are simulated simultaneously in one time-dependent CFD and CAA run. These types of simulations require the computational domain to be large enough for both capturing the sound source regions and the propagation of the sound to the receiver.

2. A CFD step combined with the application of the acoustic solver (i.e., numerical methods or acoustic analogies): the source and propagation are simulated in two different steps. The aerodynamic flow is calculated first for the region where the origins of the sound are expected to be located. Based on post-processing the aerodynamic field results, the sound sources are calculated and then propagated, e.g., using numerical solvers such as ACTRAN/TM and COMSOL commercial codes, which are based on FEM.

3. Fully analytical (also called semi-analytical) methods: this group comprises all approaches where both the flow and acoustic field are derived analytically. The source model is some combination of monopoles, dipoles, and quadrupoles, based on the flow characteristics and object geometry. In the case of engine nacelles, it is commonly modeled by a modal basis and boundary condition assumptions.

4. Semi-empirical (SE) methods: these methods are based on databases containing measured acoustic data, either from component wind-tunnel tests or from full-scale aircraft and for varying operational conditions. For instance, for fan noise, Heidmann's methodology (HEIDMANN, 1979) is commonly used to predict sound level pressure in the far-field and will be further discussed ahead.

5. Fully empirical methods (also called best-practice methods (BERTSCH; GUERIN, et al., 2011)): in this case, the tool is based on databases with measured and standardized noise levels for many aircraft and engine types. As a consequence, only existing aircraft and engine technology can be evaluated with these tools. It is commonly referred to as a non-physics–based approach.

Other hybrid approaches are also considered by many authors, which are based on these key approaches. There is an extensive list of prediction tools for fan noise developed by many companies and research institutions, and it is impracticable to consider all these tools here. Therefore, the fully empirical and numerical methodologies are out of scope of this thesis, and the review will concentrate only analytical and semi-empirical methods.

Envia, Wilson, and Huff (2004) provide as an overview of CAA fan noise tools, presenting the methods and their underlying principles and discussing the relevant results, issues, and conclusions. He also presents an in-depth description of the sources of fan noise and a discussion of the current status of the fan noise prediction methods and their shortcomings.

In order to exemplify these specific characteristics of each modeling approach, some of the most prominent tools based on one or more of these approaches are listed in Table 1. It should be noted that only research institution tools with enough documentation were considered in this review. On the other hand, some of them are commonly referred to as overall aircraft/engine noise simulation tool, which means that their main application are focused on the prediction of the entire engine or aircraft. Also, the approaches listed previously are labelled as "Type" (i.e., following the numbering highlighted previously). In general, the tools based on the CFD step combined with the application of a acoustic solver (i.e., type 2 tools) are focused on: the new aircraft/engine design (in this case, detailed design phase) and the existing aircraft components. The same applications are possible for type 3 tools or fully analytical tools. With tools type 4 or SE methods, applications are expected on the: new aircraft/engine design (in this case, preliminary and conceptual design) and existing aircraft components.

Table 1 – Examples of aircraft/engine noise modeling tools.

Tool	Type	Brief description	Origin	References
ANoPP	4	Aircraft Noise Prediction Program	NASA	Gillian (1982)
ANoPP 2	3,4	Aircraft Noise Prediction Program, the new version	NASA	Lopes and Burley (2011, 2016)
SOPRANO	4	Silencer Common platform for Aircraft Noise calculations	ANOTEC consulting	Oosten and Collin (2014)
IESTA	4	Infrastructure for Evaluating Air Transport Systems Engine noise module: CARMEN	ONERA	Malbéqui, Rozenberg, and Bulté (2011) and Sanders, Malbéqui, and LeGriffon (2016)
SonAIR	4	Model for predicting single flight events to investigate and optimize noise abatement procedures by using either generic data, e.g. cockpit data from real flights	EMPA	Zellmann et al. (2018)
PANAM	3, 4	Aircraft system noise modeling Engine noise module: HEIDI	DLR	Bertsch, Guerin, et al. (2011) and (HEIDI)
PropNoise	3	Modular tool for propulsion noise	DLR	Moreau, Guerin, and Busse (2009)
Piano	2	Computacional Aeroacoustic code	DLR	Caro (2007)
TBIEM 3D	2,3	Thin duct, Boundary Integral Equation Method, three dimensional	NASA	Dunn (1997)
LINFLUX-TURBO	2,3	Computational Aeroacoustic code focused on the fan interaction noise	NASA	Verdon, Montgomery, and Chuang (1999) and Envia (2016)
TFaNS	2	Tone Fan Noise Design/Prediction System	P&W and NASA	Topol and Huff (2003)
elsA-sAbrinA	2,3	Hybrid approach focused on fan interaction noise	ONERA	Polacsek and Burguburu (2005)
PHOENIX	2	Parametric mesHing and analysis of aerOENgine Intakes and eXhausts: CAA code	ISVR and MSC Actran/TM	Mustafi (2013)

Source – Adapted from Bertsch, Simons, and Snellen (2015).

The most prominent example of this group of tools is the Aircraft Noise Prediction Program (ANoPP) developed at NASA. Initially, the tool was developed to predict noise for single flyover events. Engine noise components within ANoPP are modeled as proposed by Krejsa and Stone (2014) for jet noise and Heidmann (1979) for fan noise. Recently, some dedicated studies (ENVIA; TWEEDT, et al., 2008; KREJSA; STONE, 2014; BERTON, 2015) have been published to access NASAs current jet and fan noise prediction capabilities. It has been demonstrated that the implemented methods result in reasonable overall agreement with experimental data. Besides, the airframe noise and other engine noise sources (such as turbine and core noise) can be accounted for with this tool as well. The code is continuously updated, and for fan noise model, for instance, new noise source models have been recently implemented (KONTOS; JANARDAN; GLIEBE, 1996; HERKES; REED, 2005; KREJSA; STONE, 2014). As main limitation, ANoPP is based only on semi-empirical models, which are strongly dependent on the experimental fitting methods and aero-engine configuration (i.e., manufacture details, nacelle design, by-pass ratio, etc).

Recently, NASA has released a new version called ANoPP2. The focus of the latest version lies in a framework that allows the communication with different methodologies (numerical, analytical, etc.) (LOPES; BURLEY, 2011). In some sense, engine/aircraft noise prediction

through ANoPP2 is closer to a hybrid tool than to a parametric one such as its older version. ANoPP2 addresses the problem through the use of acoustic data surfaces (ADS). All acoustic information is stored in ADS, which facilitates and enables communication and acoustic data transfer between prediction methods. According to Lopes and Burley (2016), the ADS can accommodate acoustic data in almost any form, ranging from acoustic pressures, density and velocity history, spectral and integrated metrics. The highest fidelity data surface available within ANOPP2 is the Ffwocs Willians and Hawkings (FW-H) surface proposed by Farassat, Dunn, and Spence (1992). Therefore, there are various source surfaces around the noise components of the aircraft, which are enclosed within an average acoustic surface surrounding the aircraft. The methodology was developed to allow the communication between NASA's main prediction tools such as those listed in Table 1.

The tool proposed by DLR, called the Parametric Aircraft Noise Analysis Module (PANAM), addresses the overall aircraft noise prediction at the conceptual aircraft design stage (BERTSCH; GUERIN, et al., 2011). The tool provides for the noise generated by the aircraft during flight operations (approach, cruise, takeoff, etc.) considering multidisciplinary effects. The platform Infrastructure for Evaluating Air Transport Systems (IESTA) proposed by ONERA (MALBÉQUI; ROZENBERG; BULTÉ, 2011; LEGRIFFON, 2015; SANDERS; MALBÉQUI; LEGRIFFON, 2016) follow similar characteristics of the previous tool. The noise generation of an aircraft is determined by its design, the relative location of the observer, configuration and operating conditions along the flight path. In addition, sound propagation effects under flight conditions need to be taken in account to correct the static noise emission when predicting the aircraft noise during flight. In the IESTA and PANAN tools, the individual noise components are modeled with specific SE and analytical models. In the case of the engine component, the dominant noise sources, i.e., the jet and fan, are modeled separately. Similar to ANoPP, the two standard jet (KREJSA; STONE, 2014) and fan (HEIDMANN, 1979) models were adapted and implemented by DLR and ONERA. Recently, the integration of a model for acoustic treatment modeling improved the accuracy of the results of both tools. For the PANAN tool, the acoustic treatment model is derived from ray theory and based on modal approach, which is described by Moreau, Guerin, and Busse (2009). This approach assumes that the presence of liners does not significantly modify propagation angles or induce mode dispersion. In addition, the implementation of an acoustic treatment attenuation prediction model allows the investigation of the influence of liner length. For the IESTA tool, the analytical model proposed by Eversman (1971) allow the calculation of the propagating and non-propagating modes, as well as their attenuation in dB per material

length. The absorption coefficient or the transmission loss can be derived, and the noise reduction in the far-field due to the liner can be estimated at the inlet and exhaust ducts. The effects of wave diffraction, refraction, reflection and scattering provided by the impedance and mean flow are not modeled in these approaches.

A fourth example is the European tool SOPRANO (Silencer Common Platform for Aircraft Noise Calculus). This tool was developed within the framework of the European aircraft noise research program called SILENCE(R). According to Rolt and Kyprianidis (2010), the latest version can model various noise components of the engine. Thus, similar to other parametric tools, the main engine noise components such as fan and jet noise are modeled with the SE methods (HEIDMANN, 1979; KREJSA; STONE, 2014). Moreover, the tool structure allows pre-processed or measured source noise data to be stored in tables and used in the forecast. Similar to PANAN and IESTA, the SOPRANO tool enables the evaluation of individual sources or the sum of several components to study noise-generating effects, with its main focus being on noise prediction for flight events in a single location or multiple observation locations.

In the fan noise context, as mentioned previously, some of these tools are combined with analytical or numerical approaches to improve the accuracy. In contrast to the SE–based pure tools, hybrid prediction models separate the overall aircraft noise into its major contributions. In general, hybrid models predict the source (fluid-dynamic model) and propagation (acoustic model) independently, based on information and flow.

In the first computational approach coupled with fan noise source predictions, we can cite the code developed by NASA called LINFLUX (VERDON; MONTGOMERY; CHUANG, 1999; CHUANG; VERDON, 1998), which is used to calculate the rotor-OGV interaction tone. This code provides three-dimensional, unsteady modeling of the mean flow, which is based on the Linearized Euler Equation (LEE). In addition, for cases with non-linear mean flow, there is also the possibility of using an in-house auxiliary code called TURBO (ENVIA, 2016), which is based on RANS modeling. For a given mean flow, LINFLUX calculates the acoustic response of the OGV to the incident perturbations (e.g., wakes rotor) which propagate over the flow in a given BPF harmonic. The output results of the LINFLUX is commoly connected with another tool to compute the propagation and radiation of the duct called CDUCT-LaRC (NARK; ENVIA; CASEY, 2009). This code calculates the propagation of a given acoustic source in front of the fan plane or downstream OGV plane in the inlet or exhaust ducts, respectively. Once the in-duct acoustic field is estimated, the code has the ability to calculate the far-field noise radiation, which is based on the application of the FW-H surface.

In addition to NASA approaches, the European community has been developing over the years several hybrid tools used in the prediction of fan noise. Recently, the hybrid tool PropNoise (JARON; MOREAU; GUERIN, 2015; MOREAU; AULICH, et al., 2016) developed by DLR has been used in several research projects. The tool has a modular structure divided into two ways: "RANS-informed" and "autonomous" options (for few geometry inputs). The modular structure allows the generation, propagation, and radiation modeling of noise to be considered individually. Following a similar approach, ONERA has recently developed a hybrid computational procedure to provide a complete numerical simulation of fan tonal noise, including source generation, acoustic propagation in the nacelle, and radiation through the intake or exhaust duct (POLACSEK; BURGUBURU, et al., 2006). By coupling a RANS solver and a 3D high-order LEE solver, the tool allows the simulation of the rotor-OGV sound generation, the propagation in the nacelle and the radiation in the vicinity of the intake (and the exhaust). The acoustic pressure in the near-field is extrapolated to the far-field using a Kirchhoff integral, written in the frequency domain (FARASSAT; DUNN; SPENCE, 1992).

Over time, an extensive literature has developed on commercial tools specialised in analysis of aero-engine intakes and exhausts, and based on FEM and BEM formulations. The hybrid tool called PHOENIX (Parametric mesHing and analysis of aerOENgine Intakes and eXhausts) (MUSTAFI, 2013) is an axisymmetric FE code which automates the procedures for noise prediction in both intake and bypass sections of a turbofan engine. PHOENIX is referred to as a shellcode of commercial code ACTRAN/TM focused on nacelle analysis. Similar to the commercial version, the acoustics solution is based on convected Helmholtz equation (CHE) for the acoustic velocity potential, assuming irrotational flow and appropriate boundary conditions for lined nacelles. On the other hand, The TBIEM 3D (Thin duct, Boundary Integral Equation Method, 3 Dimensional) is based on the boundary integral equation method applied for a finite and unflanged duct, which was proposed by Dunn, Tweed, and Farassat (1996). Later, several studies (DUNN, 1997; DUNN; FARASSAT, 1998; DUNN; TWEED; FARASSAT, 1999) have shown its numerical efficiency for parametric purpose, considering various engine parameters and liner configurations. In this model, the sources are monopoles and dipoles concentrated in single points, and the flow is assumed as unidirecional and uniform. The main limitations of this approach are: the modeling is limited to low Mach numbers ($M < 0.4$), uniform flow (with same Mach number inside and outside the duct), the need to know the strength of the point sources (being related to the torque applied to the fluid), unflanged duct assumption, i.e., phenomena related to thickness of the walls are not taken into account (drag, diffraction, and

scattering effects, etc.).

It should be expected that major aircraft and engine manufacturers run their own confidential noise prediction tools. Due to the lack of information, these tools cannot be detailed and allocated to one specific group. Most likely, the tools are based on each extensive available database produced by these manufacturers, which can be customized for each particular aircraft and engine. Moreover, it can be expected that tools are probably still parametric to some extent to account for different configurations and operational noise generating effects.

In what follows, the attention is switched to different fan noise techniques used in CAA predictions, focusing on numerical and analytical schemes used to model the propagation and radiation from the nacelles.

2.2.2 Techniques and methods in fan noise

In general, the target of noise computation is sound levels in the far field, and a complete noise prediction strategy has to address issues not only of noise generation but also of noise propagation along the intake and bypass ducts and then of radiation to the far field (ENVIA; WILSON; HUFF, 2004).

Over the years, different techniques and methods have been applied to fan noise modeling in order to improve the prediction accuracy of analytical and numerical approaches. In this section, the main focus is on the methods employed to in-duct fan noise modeling, which consider important physics insight about mean flow, acoustic liners, modal decomposition and their effects on the radiation.

Many efforts in the literature detail eigenmode decompositions of duct flows both for the purpose of supporting numerical methods for computational aeroacoustics, and also to better understand the physical behavior of problems in duct acoustics. Ovenden, Eversman, and Rienstra (2004) and Grace et al. (2012) detail different analysis and subsequent numerical methodologies for eigenmode decomposition of duct flows in support of turbomachinery problems. They demonstrate their approach as post-processing tools for the modal decomposition can be used to construct the acoustic field in terms of the reflected and transmitted cut-on modes excited by fan-OGV interaction.

In order to analyze analytically the modal propagation within the engine nacelle, it is necessary to consider the modal scattering (e.g., the transition between rigid and lined sections, and reflections at the duct termination). Other discontinuities may also be considered, such

as varying duct geometry and axially segmented liners (MCALPINE; ASTLEY, et al., 2006; GABARD; ASTLEY, 2008; LAW; DOWLING; CORRAL, 2010; OPPENEER; RIENSTRA; SIJTSMA, 2016). A specific formulation to slowly varying duct can avoid the restriction of a straight duct section, and therefore, it is possible to match the acoustic pressure halfway along the spinner (in the inlet duct) (RIENSTRA, 1999; RIENSTRA; EVERSMAN, 2001). However, at high frequency and for low order mode, it led to some deviations, which is well explained by modal scattering effect (not considered on the slowly varying formulation).

In such cases, a mode matching technique can be employed to predict the entire in-duct acoustic field correctly. McAlpine, Astley, et al. (2006) proposed a mode matching based on a Galerkin formulation considering a matching condition of pressure and axial acoustic velocity conservation at the interface between each section. Also, Law, Dowling, and Corral (2010) and Lafronza et al. (2006) extended this formulation to investigate multimodal propagation and optimum liner impedance. Lafronza et al. (2006) used an approximated evaluation of the Perceived Noise Level (PNL) as a cost function to optimize liners in ducts with uniform cross sections assuming a broadband source. A mode matching method was used to perform acoustic analysis, and Response Surface Modeling (RSM) was used as an optimization tool. Law, Dowling, and Corral (2010) optimized segmented liner (with three liner segments) configurations for broadband source in cylindrical ducts. Later, Gabard and Astley (2008) and Gabard (2010) demonstrated that an improved mode matching technique based on the continuity of mass and momentum could give better results for modes propagating in exhaust by-pass duct, particularly at the liner discontinuities.

In a recent study, the effects of shear refraction inside an exhaust duct have been investigated using a mode matching scheme by Oppeneer et al. (OPPENEER; RIENSTRA; SIJTSMA, 2016). In this case, the PridmoreBrown equations (PRIDMORE-BROWN, 1958) were used to describe modal acoustic waves in straight lined ducts with the radially non-uniform mean flow and mean temperature, which was used to simulate APU operating conditions. Also for exhaust region, the boundary layer effects and different flow profile have been considered by Brooks and McAlpine (BROOKS; MCALPINE, 2007), which used the mode matching scheme with matching conditions of pressure and axial acoustic velocity to calculate the sound transmission in annular ducts. The formulation is based on the McAlpine et al's work (MCALPINE; ASTLEY, et al., 2006) and solutions of the PridmoreBrown equations (PRIDMORE-BROWN, 1958). The authors showed that a linear shear flow profile has significant effects of sound refraction in the resulting acoustic field.

In such cases, the modal radiation directivity is used to link the in-duct modal content to the far-field noise. In this sense, a simplified model of a duct opening surrounded by an infinite baffle (thereby eliminating sharp edge) or by an unflanged edge is usually considered. The sound radiation by an unflanged cylindrical duct was calculated via the Wiener-Hopf technique by Levine and Schwinger (1948) for plane waves and no flow condition. The generalization to high order modes without flow was later proposed by Weinstein (1974) (an approximate solution). Other works that used this technique for high order modes include Homicz and Lordi (1975), which used a Lorentz transform to the solution for the no-flow case, applying it to the pressure and potential velocity equations for the exhaust and intake cases. Munt (1977, 1990) and Rienstra (1984) extended the Wiener-Hopf technique for exhaust flow inside a annular ducts (also computing vortex sheet in the leading edge of the duct). For cylindrical and annular ducts in a baffle, the sound radiation can be calculated by Rayleigh integral approximation (TYLER; SOFRIN, 1962; MORFEY, 1969). Another approach is the Kirchhoff integral approximation, which is useful for intake radiated noise since there is no hypothesis of flanged inlets (LEWY, 2003, 2005). This approximation can be an alternative to Wiener-Hopf methods since it does not require extensive computations and shows accurate results at angles near the maximum lobe (HOCTER, 1999).

With regards to estimating sound radiation into the far-field from engine ducts, Rice (1971) and Rice (1978) established a relationship between the maximum lobe in far-field directivity patterns and cut-off ratio. It was shown that a nearly cut-off mode would radiate predominantly at 90° from the duct axis while the well-propagating modes radiate nearer to the axis. In a follow-on effort, Rice, Heidmann, and Sofrin (1979) have been shown that the radiation directivity with flow (with free-field Mach number equal to in-duct Mach number) includes a convective effect, which shift the maximum lobe away from the inlet axis (i.e., toward the sideline angle). With in-duct flow only, the principle lobe peak beams significantly closer to the inlet axis than for the case of flow everywhere.

At high frequencies where many modes are present, identifying and tracking modes can be very difficult. In such cases, a more straightforward approach such as ray acoustics can be used. When ray acoustics is used, the correct prediction of the diffraction of sound waves around duct edges and corners requires the use of methods, such as the geometric theory of diffraction (GTD) studied by Chapman (1994). Moreover, in nacelles, other effects such as inferences, refraction and specular reflections are expected (see Figure 13), which are produced by the interaction with acoustic treatment at the wall, internal and external mean flow, lip and shape

inlet, etc.

Figure 13 – Mechanisms that modify wave propagation in nacelles intake.

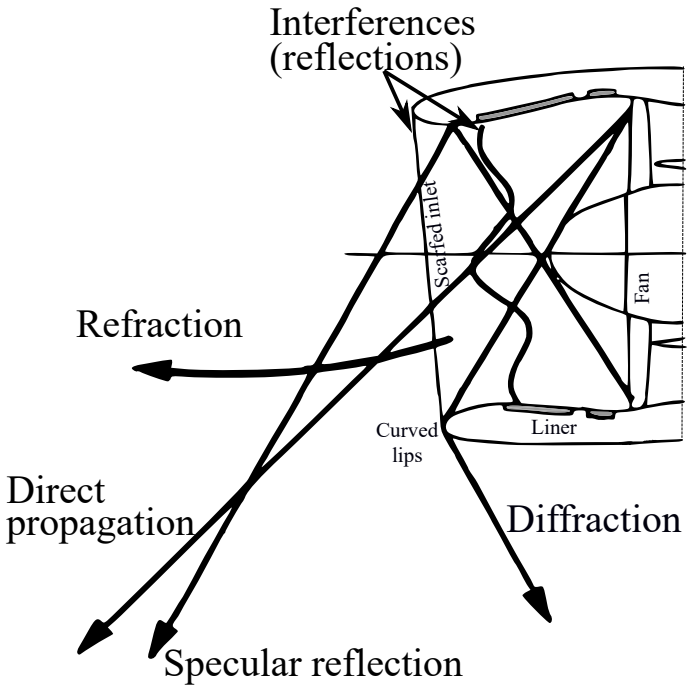

Source – Adapted from Dougherty (1996).

These interactions were observed by Dougherty (1996) and Tester (1973), which studied ray methods in nacelles and lined duct at different operating conditions. The diffracted waves also called creeping waves are generated at the exit of the duct by some acoustic modes, which are used to explain deviations in the results. On the other hand, Lidoine et al. (2001) have used BEM to investigate the diffraction effects in different nacelle inlet lips. The study considered thicker and thin curved lip and scarfed lip. Using Keller's law of edge diffraction proposed by Pierce (1989), the authors explained that the edge acts as a directional source of acoustic energy depending on the relative angle between the incident wave and wedge and the wedge angle. If the wedge angle is zero, the wall thickness ε is infinitely small, and it leads an unflanged duct. The main part of the diffracted field radiates in the Keller cone. These concepts are shown geometrically in Figure 14.

As can be seen in the previous paragraphs, the analytical methods and techniques are placed between the empirical and computational methods. They require an acoustic analogy or modal model assumptions, wherein the aerodynamic pressures are separated from the acoustic pressures. The model equations are mostly based on the wave equations relying on the aerody-

Figure 14 – Local behaviour of the scattered field at a duct lips (thicker curved lip and scarfed lip). χ and σ are incident wave angle and the wedge angle, respectively.

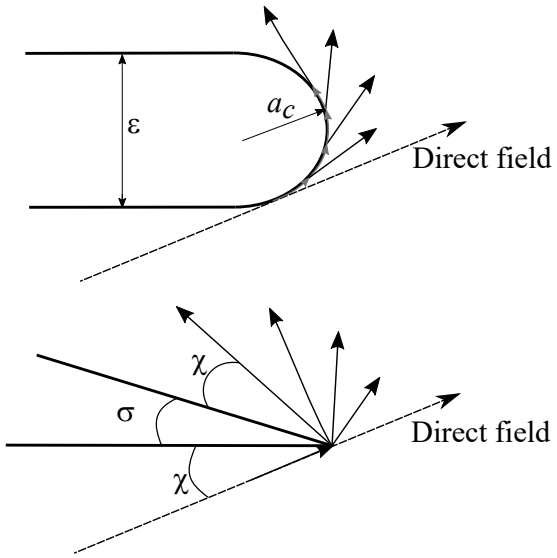

Source – Adapted from Lidoine et al. (2001).

namic loads. Most of these models rely on highly idealized representations of the duct (usually a thin cylindrical duct) and mean flow (usually uniform). If applications require a parametric analysis or a system optimization, long computational times become impractical.

Previous research may be considered a first step towards a more profound understanding of the effect of the boundary layer and flow profile on the intake duct that includes the liner interfaces, especially, when predictions of the radiated noise are required. This approach remains briefly addressed in the literature. Therefore, some of the interesting questions in this context are: How the typical modeling assumptions, such as the uniform flow, can affect the far-field prediction? How the behavior of the acoustic fields close to liner discontinuities between lined and hard surfaces modify these predictions? And for which flight conditions, for intake aero-engines, these effects are more critical?

Another key point in the computational models is how to model the acoustic treatment adequately within the intake, bypass, core and APU ducts. Acoustic liner modeling, therefore, plays a crucial role in the design of low noise engines. The real representation of their acoustic properties has been studied extensively over a year. Almost all techniques and methods described in this section mainly consider representations of the liner as an impedance in the presence of the uniform mean flow. Most of the methods and techniques in fan noise make use of the Ingard-Myers boundary condition (INGARD, 1959; MYERS, 1980). In the next section, the attention is switched to different liner modeling approaches used in analytical and numerical

predictions.

2.2.3 Shear flow effects on the liner impedance

The usual approach is to characterize acoustic liners is by its acoustic impedance, defined as the relation between acoustic pressure $\tilde{p}$ and acoustic velocity $\tilde{v}$ (as defined in Eq. (2.29)). In general, such impedance is assumed to be independent of the acoustic wave incidence angle, the so-called locally reactive impedance, which means that there are no waves propagating within the material. However, the representations of the liner employing a locally reacting acoustic impedance may be not applicable to in the entire nacelle. In fact, real engine acoustic treatment can be non-locally reacting (EATON, 1999). The impedance of the single layer liner (see Fig. 4(a)) is commonly expressed as

$$Z = R + \mathrm{i}\mathcal{X} \tag{2.30}$$

where R and $\mathcal{X}$ are the non-dimensional facing sheet resistance and inertial reactance, respectively. The non-dimensional resistance R of the facing sheet depends on an averaged grazing flow Mach number M_0 over the lined surface and the percentage open area (or porosity). On the other hand, the reactance is commonly related to dissipative effects, which depends on the thickness of the sheet T, the diameter of the holes d and the percentage of open area. Figure 15 shown the typical representation of a acoustic liner by means an array of Helmholtz resonators and the typical representation by means of an effective acoustic impedance.

Besides the liner geometry, as it will be seen, the acoustic impedance also depends on the acoustic wave frequency or wavenumber k, as well as on the temperature, grazing flow velocity, boundary layer effects (thickness, viscosity, etc), and high SPL (SPILLERE, 2017; BODEN et al., 2017).

Figure 15 – Modeling scheme of (a) an array of liner cells and (b) effective acoustic impedance.

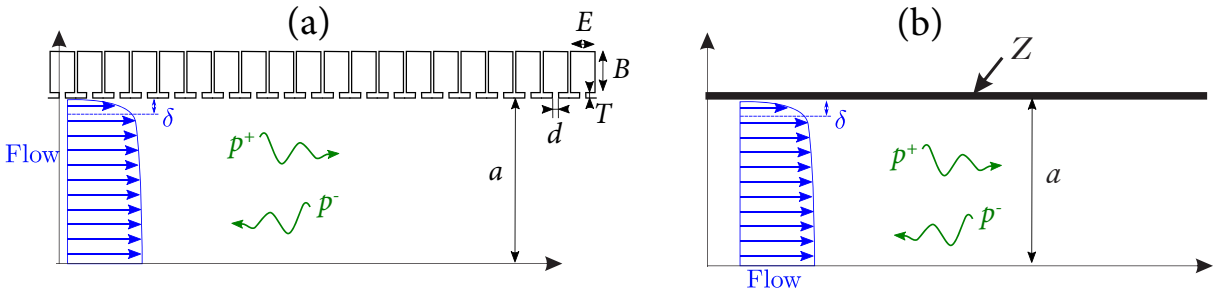

Source – Adapted from Dai and Auregan (2016).

The assumption that a discrete perforated liner (Fig. 15(a)) with grazing flow can be acoustically described as a continuous impedance (Fig. 15(b)) has been investigated by the literature (BODEN et al., 2017; SPILLERE, 2017; DAI; AUREGAN, 2016; RENOU; AURÉGAN, 2011). Usually two different approaches are investigated: one considers the liner as a periodic system and the second approach assumed the liner as homogeneous and described by an impedance. Some authors (BODEN et al., 2017; DAI; AUREGAN, 2016) observed that systematically different results were obtained for upstream and downstream excitation. The main issue is that an equivalent impedance should depend only on the geometry of the problem and possibly on the mean flow characteristics, but should not depend on the direction of the incident waves. Previously, the same characteristics were observed by Renou and Aurégan (2011), who were the first to point this out and attributed it to a failure of the Ingard-Myers boundary condition (INGARD, 1959; MYERS, 1980).

As discussed before, the Ingard-Myers boundary condition leads to an effective impedance as seen by the acoustic field in the presence of the uniform flow. The limitations of this model have been revealed recently, for which it appears that: (1) it is a not a well-posed problem in the time domain (BRAMBLEY, 2009), (2) the boundary condition is not able to correctly predict the instabilities appearing over a liner (RENOU; AURÉGAN, 2011) and (3) it cannot explain the differences that were experimentally observed by many test rigs (BODÉN et al., 2016) when wave propagates in the same direction of flow or in the opposite direction to the flow. However, Bodén et al. (2016) suggested that these models can be used with care depending on the conditions under analysis, but improved models may be necessary if an optimal design is desired. In the frequency domain, far from hydrodynamic instabilities, this boundary condition correctly represents the limit of a vanishingly-thin inviscid boundary layer over the acoustic lining, where this boundary layer needs to be extremely thin for this to be a good approximation.

Over the years, several extensions (RIENSTRA; DARAU, 2011; BRAMBLEY, 2011; KHAMIS; BRAMBLEY, 2016; MASSON et al., 2018; PETRIE; BRAMBLEY, 2018) have been proposed to Ingard-Myers boundary condition and attempt to account for the presence of a boundary layer on top of the liner and the ill-posedness is regularised by considering a non-slipping inviscid mean flow with a finite region of shear (rather than a vortex sheet). The model of Brambley (2011) extended this boundary condition to relax the assumption of low Mach number, with the only remaining premise being that the boundary layer was thin. High-frequency asymptotics of the viscous boundary layer model led to a recovery of the Myers boundary condition (conservation of normal displacement), while low-frequency asymptotics

led to the conservation of mass flux. Rienstra and Darau boundary condition (RIENSTRA; DARAU, 2011) is also considered a first order boundary condition similar to Brambley, which is mainly applied for very thin boundary layers (however, restricted for linear flow profiles). Khamis and Brambley (2016) have demonstrated that the effects of viscosity on the acoustics are of comparable magnitude with the effect of shear, and thus both should be taken into account in the boundary condition. Viscosity effects on the boundary layer have been included in the boundary condition. This approach agrees most closely with results from solving the linearized Navier-Stokes equations for the entire duct.

At fan stage (i.e., between fan and OGV), the swirling flow and high SPL effects are dominating, and also Ingard-Myers boundary condition leads to an non-effective impedance in such cases. To address the swirling flow issue, Masson et al. (2018) developed a generalization of the Ingard-Myers boundary condition in an annular duct with swirl flow, both for the inner wall (hub) and for the outer wall (tip). It has been shown that the Ingard-Myers boundary condition is not the correct limit in the presence of an infinitely thin boundary layer at the walls in the presence of swirl. On the other hand, the high SPL effects were computed by Petrie and Brambley (2018) by using a three-layer formulation on the acoustics within a non-parallel boundary layer flow over an acoustic lining in a cylindrical duct. The formulation combines the influences of the sheared mean flow, viscosity, and non-linearity into a sufficient impedance boundary condition. It was seen that the radial pressure for a given mode does not obey the effective impedance boundary condition due to the amplifying mechanisms within the boundary layer. This means that a single effective impedance boundary condition will not adequately resolve both the linear and the nonlinear acoustics as they have different effective impedance.

For engine applications, where the boundary layer is very thin, Ingard-Myers boundary condition (INGARD, 1959; MYERS, 1980) has been previously assumed be a valid assumption. However, Gabard (2016) has shown that, even for boundary layers of 1% of the duct radius, the Ingard-Myers boundary condition may incorrectly predict the liner attenuation, especially for upstream propagating waves (i.e., engine intake condition). The author performed a detailed parametric study of the effects of the inviscid mean flow boundary layer on sound propagation for downstream and upstream propagating waves. By using normalized absorption rate results calculated from LEE eigenvalue solver or considering Ingard-Myers (INGARD, 1959; MYERS, 1980) and Brambley (BRAMBLEY, 2011) boundary conditions, some important trends associated with the boundary layer: (1) the boundary layer only modifies slightly the downstream attenuation (even for broadband noise propagating, it is not very sensitive to the boundary layer),

(2) the absorption rate depends strongly on the liner resistance, and the two cannot be separated (both variables can actively modify the modal form) and (3) in almost all cases, Brambley boundary condition is a qualitative improvement over the Ingard-Myers condition and the correct trend is captured. Also, Gabard has confirmed Nayfeh's (NAYFEH; KAISER; SHAKER, 1974) observations, in which changing the boundary layer profile, i.e., quadratic, power law, etc., has a small effect on the absorption coefficient, as long as the displacement thickness remains constant, and thus the linear profile was chosen for the sake of simplicity. The same effects in terms of absorption rate were observed in previous studies by Eversman (1971) and Ko (1972) for different frequencies and considering upstream and downstream propagation (i.e., corresponding to the engine intake and exhaust), which led to the conclusion that the boundary layer effects must be carefully included in the design of acoustic linings for turbofan intakes. In addition, for the single mode and equal amplitude assumption for the modal energy distribution analyses, Ko (1972) was observed the maximum attenuation at a given frequency: (1) as Mach number increases, it decreases to the higher frequency side with for the exhaust condition and it increases to the lower frequency side for the inlet condition; (2) as Resistance and reactance increases, it indicates that an optimum resistance and reacting exists for a given situation (and peak attenuation depends on a right set of the mode, frequency, Mach number and boundary layer thickness).

This section points out some of the problems encountered in the extant research. Only a few works in literature demonstrate the application of these boundary conditions such as the Brambley (2011) to model an aero-engine intake. As far as we know, no previous research has investigated a predictive tool to compute the Brambley boundary condition to include shear flow effects at the liner design. Therefore, additional studies to understand more completely the key tenets of this boundary condition in a predictive tool are required. For engine applications, at realistic operating condition, Brambley boundary condition can be compared with Ingard-Myers boundary condition to answer how the uniform flow affect the liner attenuation predictions.

As observed in Ko's work and other studies reviewed in this section, the transmission loss or absorption rate results also depends on the acoustic source characteristics and their behavior along the duct (i.e. single mode or equal amplitude assumption for the modal energy distribution definitions). Their correct modeling allows to represent the sound field to be represented by propagating modes within the duct, which can be expressed in terms of known analytic functions. Therefore, the attention is now switched to sources representation in the modal context.

2.2.4 Modal source representation

2.2.4.1 Rotor-stator modes (Tyler-Sofrin modes)

Tyler and Sofrin (1962) analyzed the mechanisms of propagation and noise generation in axial compressors. After detailing the conditions for acoustic field propagation in terms of cut-on and cut-off modes for rectangular and annular ducts, their article addresses in a phenomenological way the noise generated by the interaction between a rotor and OGV. Tyler and Sofrin's approach is to consider the acoustic field generated by the rotor-OGV interaction as the superposition of rotating modes. Assuming the interaction between the rotor and the OGV composed of a single vane, they express the generated pressure measured at the fan plane and in the reference of the OGV, by a double decomposition in the space of Fourier. Also, the authors consider the following characteristics: (1) a azimuthal grid of V vanes, spaced from $\Delta\varphi_{\text{vane}} = 2\pi/V$, (2) identical B blades equally spaced $\Delta\varphi_{\text{blade}} = 2\pi/B$ and (3) the time taken by a blade rotating from a given position to the next is $\Delta t = \Delta\varphi/\Omega$. By assuming these three statements on the generated pressure at the fan plane in different time steps of a revolution, Tyler and Sofrin have observed that it yields for any azimuthal order m the restriction

$$-\mathrm{i}\mu B\Omega\Delta t + \mathrm{i}m\Delta\varphi = \mathrm{i}2\pi\kappa, \tag{2.31}$$

or

$$m = \kappa V + \mu B \tag{2.32}$$

where κ is any integer, and μ the harmonic of interest. This mode can be identified with a spatial pattern composed of m lobes rotating at angular velocity $\Omega_m = \mu B\Omega/m$. The rotor-OGV interaction generates specific azimuth modes, of which only those with a sufficient rotation speed can propagate. The existence of such patterns can be shown qualitatively with an example involving few blades and vanes illustrated by Bouley (2017). Figure 16 illustrates in the simple diagrams form the interaction of a fan of eight blades (in black, which a blade of reference is blue) with an OGV with six vanes (in red). For $\mu = 1$ (i.e., at first BPF), the Eq. (2.32) predicts the existence of a mode with $8 - 6 = +2$ lobes rotating in the same direction as the fan, with a rotational speed equal to $\Omega_m = 4\Omega$. In the first diagram, the position of the reference pad coincides with that of the paddle to the right, and a similar coincidence exists on the opposite side. These coincidences are represented by the shaded parts of the double-lobed pattern. The

different diagrams show the intermediate positions of the rotor and coincidences when the rotor rotates a quarter of a turn. It can be observed that during this time, the mode has made a complete revolution, illustrating the fact that its rotational speed is four times that of the rotor.

Figure 16 – Representation of the Tyler and Sofrin modes. The red and black lines represent the OGV vanes and the fan blades, respectively, and the blue line indicates the reference blade.

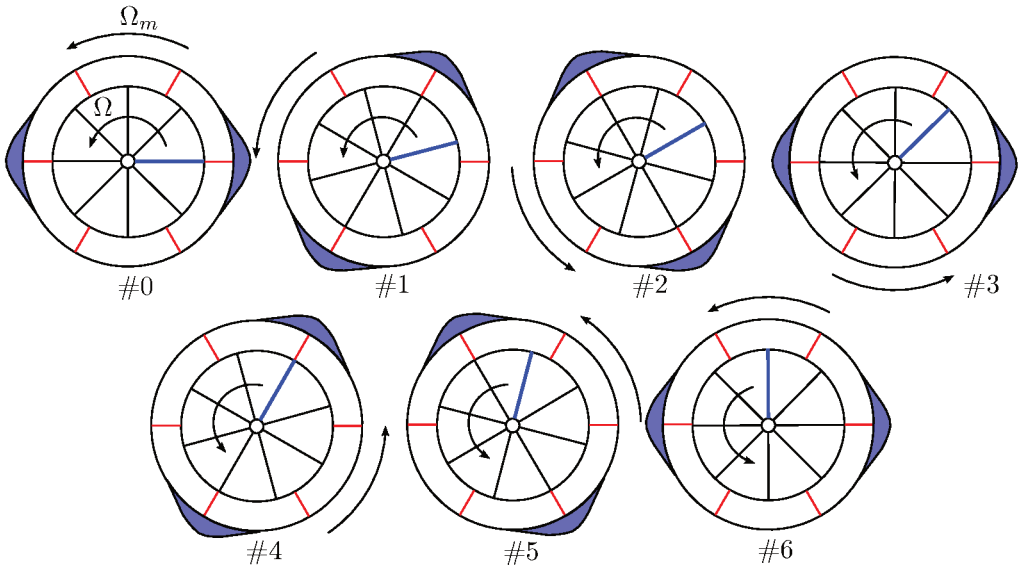

Source – Adapted from Bouley (2017).

By selecting B and V such that the lowest $|m|$ possible is high enough for the harmonic of interest to be cut-off, and this component is effectively absent for a long enough inlet duct (RIENSTRA, 2016a). The rotor-stator modes are dominating at subsonic fan tip speeds, for instance at approach and cruise conditions. The periodic interaction between the wakes from the rotor blades and the OGV produces tones with dominating modal components for each BPF harmonic (MCALPINE; ASTLEY, et al., 2006).

It should be noted that rotor-stator modes are based on the idealization of the perfectly radially symmetric mean flow, and there are no variations on the blades and vanes spacings. All the inlet flow distortion give rise to so-called distortion modes, not satisfying the Tyler-Sofrin formulation in the Eq. (2.32), which mainly contributes to other types of sources such as broadband noise modes and rotor-locked modes (at supersonic Mach number blade tip).

2.2.4.2 Rotor-locked modes

At take-off, rotor-locked tones are the primary source of fan noise. In this case, a simple two-dimensional model of the rotor-alone pressure field, with supersonic flow impinging on the

fan rotor blades was used for McAlpine and Fisher (2001) to explain the rotor-locked tones. For relative Mach number M_{rel}, the pressure field consists of a series of bow shock waves and Prandtl-Meyer expansion fans, as shown in Figure 17. The expansion fans facilitate the turning of the flow onto the suction surface of each rotor blade. The pressure signature in a direction normal to the shock fronts (in direction relative X) will resemble a sawtooth once the shock waves and expansion fans have coalesced into a continuous waveform, which is assumed to occur shortly upstream of the fan.

Figure 17 – Shock-wave generation by a supersonic fan.

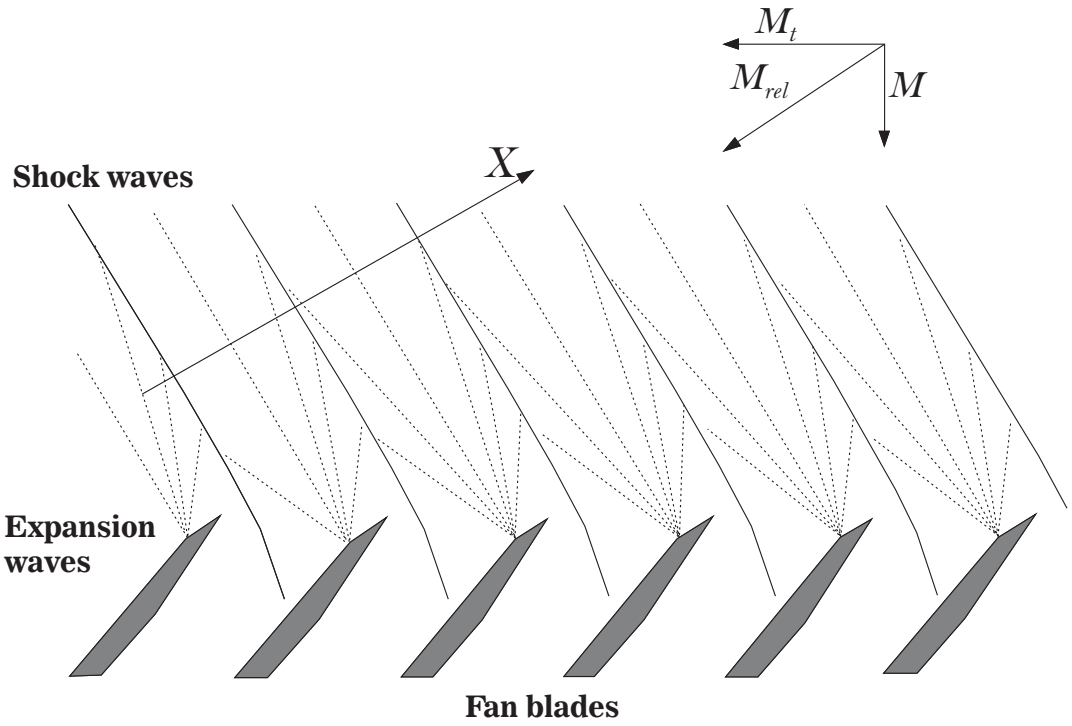

Source – Adapted from McAlpine and Fisher (2001).

All the shocks propagate upstream of the fan at the undisturbed speed of sound relative to the oncoming fluid (weak-shock theory (MCALPINE; FISHER, 2001)), and therefore the blade-to-blade periodicity in the pressure signature is maintained. The energy remains at the BPF harmonics, and the high-pitched tonal noise (predominantly at BPF) is predicted to be radiated from the inlet of an ideal fan. The frequency spectrum of an irregular sawtooth contains energy distributed amongst harmonics based on the engine rotation frequency, called engine orders (EO). The EO harmonics are spinning modes which are all steady in a frame of reference rotating with the fan. Therefore, the dominant propagating modes have the azimuthal mode order equal to the number of fan blades (i.e., $m = B$), and most of the acoustic power is

concentrated on the first radial mode order (MCALPINE; ASTLEY, et al., 2006). Hence, the EO harmonics (including the BPF harmonics) are defined as the "rotor-alone" tones, whereas the "Buzz-saw" tones are defined as the EO harmonics with a frequency less than BPF. This condition is also characterized by high in-duct Mach number and high frequencies, such that the presence of a boundary layer should be relevant (GABARD, 2016). In general, the rotor-locked tones can be the major source of noise at sideline and cut-back operating conditions.

2.2.4.3 Multimode broadband noise

A simple model commonly used as an approximate description of broadband noise in intake and bypass ducts is the uncorrelated modes with equal energy per mode. This can be supported by the fact that each mode at an acoustic frequency is generated by a different harmonic loading. These harmonics are orthogonal (according to Parsevals theorem), and it can be expected that a random acoustic field can be expanded in azimuthal modes m (also called spinning modes) in the same way. There is no similar argument for radial modes n, but it has been experimentally demonstrated by Castres and Joseph (2007) and analytically by Lafronza et al. (2006) that they are incoherent as well. Moreover, in general, they are much less numerous to propagate, and the first radial modes often dominate in a hard-wall duct. The uncorrelated modes with equal energy per mode assumption has also been justified in Lewy's works (LEWY, 2003, 2005, 2008) by averaging the phase ϑ cross product in $\cos(\vartheta_{m,n} - \vartheta_{m',n'})$ over 2π.

The key points on the multimode propagation include (1) the random nature of the sound field, (2) the wide range of frequencies, and (3) the simultaneous presence of all the acoustic modes of the duct. Gabard (2014) has demonstrated a computational method to generate a truly broadband source model within the circular duct. This stochastic source allows computing in a single time-domain simulation the complete spectrum of the broadband multimode sound field, which was tested in the following source assumption: equal incident in-duct power per mode, excitation by incoherent monopoles and axial dipoles uniformly distributed over a duct cross section. The key point in this approach is the cross-correlation between mode amplitudes, which characterizes the stochastic source models that are tailored to radiate a sound field. The author concluded with two fundamental observations (1) the duct mode shape functions represent the ideal basis for constructing the stochastic field, and (2) these shape functions, being independent of frequency, can be used equally in the frequency domain and the time domain.

It should be noted that the multimode broadband noise is outside the scope of this work

(i.e., this thesis is concentrated only on the single mode modeling), however, due to scattering effect present on the formulation studied it is convenient to review these concepts.

3 SEMI-ANALYTICAL MODAL MODELS

In this chapter, the theory outlined in Chapter 2 is applied to the formulation of in-duct propagation and free-field sound radiation models. These analytical predictive models were developed as a low-cost prediction tool for fan noise modeling including acoustic treatment mainly based on the liner geometrical parameters and operating conditions. The main assumptions and limitations of the models are discussed in the continuation of this chapter. Also, the structure of the computer code related to these models, implemented in MATLAB language, is highlighted. The key characteristics of the main codes and an auxiliary code to solve the eigenvalue of the boundary conditions are presented in the last sections.

3.1 MODE MATCHING TECHNIQUE

In general, a single modal basis can only be used to compute the acoustic field in a duct section with constant properties (RIENSTRA, 2016a). Therefore, when rigid and lined sections are connected, it is necessary to couple the modal basis of adjacent segments with a suitable matching condition. Thus, the matching conditions are used to define a continuity across the interfaces. To model the impedance discontinuity, two matching conditions are considered in this work, which are based on the continuity of pressure and axial particle velocity (MCALPINE; ASTLEY, et al., 2006) and continuity of mass and momentum at the interfaces (GABARD; ASTLEY, 2008). Also, details of different matching conditions applied to the mode matching scheme can be found in Gabard (2010).

Figure 18 shows a representation of the scattering effect at the liner interface. Each mode is scattered into a modal spectrum of transmitted and reflected modes N at the segments s and $s+1$. Note that because of circumferential symmetry there is no scattering into other m-modes (i.e., only purely radial modes are considered). The entire field is, therefore, a composition of all the possible cut-on and cut-off modes (i.e., close to the interface).

As discussed before, the solution for the pressure field in a duct can be written by a superposition of FourierBessel modes, defined in Eq. (2.16) for upstream and downstream propagation that can be rewritten as

$$\hat{p}(r,x) = \sum_{m=-\infty}^{\infty} \sum_{n=1}^{\infty} \hat{p}^{+}_{m,n}(r,x) + \hat{p}^{-}_{m,n}(r,x). \tag{3.1}$$

From the momentum conservation equation (Eq. (2.2)), one can find that the axial acoustic

Figure 18 – Incident and scattered field considered in the mode matching scheme.

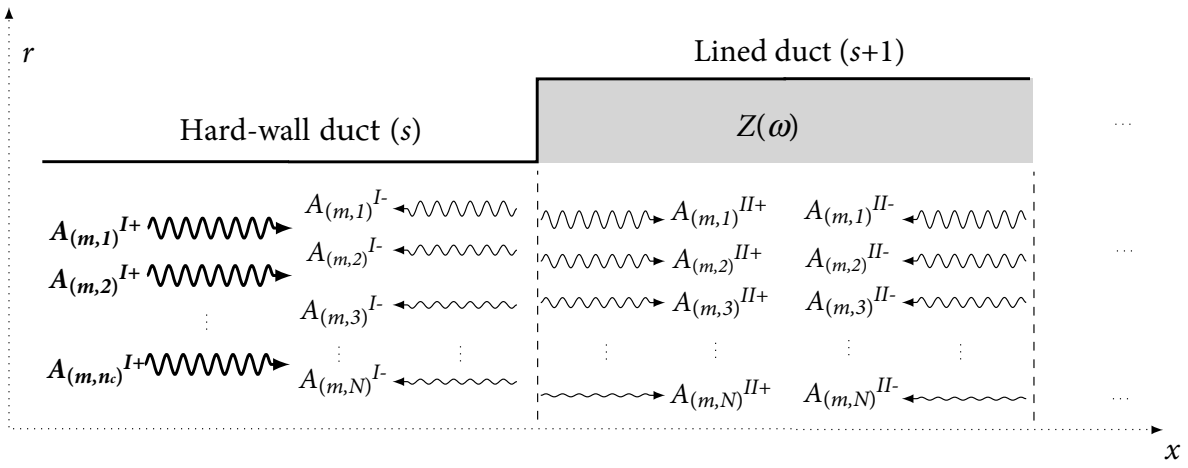

Source – Own authorship.

velocity is given by

$$\hat{u}^{\pm}_{m,n} = \zeta^{\pm}_{m,n}\hat{p}^{\pm}_{m,n} = \frac{k^{\pm}_{m,n}}{k - k^{\pm}_{m,n}M}\hat{p}^{\pm}_{m,n}. \tag{3.2}$$

In this work, the incident and scattered fields are calculated for two liner configurations: uniform and segmented liners (see Figure 19). We consider a single incident mode of azimuthal order m in Section I and no reflection at the duct termination in Section III (uniform liner) or IV (segmented liner), such that the pressure field can be written for each duct segment s as

$$p^{s}_{m}(r,x) = \sum_{n=1}^{N}(A^{s+}_{m,n}\Psi^{s+}_{m,n}(r)e^{-ik^{s+}_{m,n}x} + A^{s-}_{m,n}\Psi^{s-}_{m,n}(r)e^{-ik^{s-}_{m,n}x}), \tag{3.3}$$

where s can be I, II and III (and IV for segmented liner) and also, from Eq. (3.2), the acoustic particle velocity becomes

$$\begin{aligned} u^{s}_{m}(r,x) = \sum_{n=1}^{N}\Bigg(&\zeta^{s+}_{m,n}A^{s+}_{m,n}\Psi^{s+}_{m,n}(r)e^{-ik^{s+}_{m,n}x} \\ &+\zeta^{s-}_{m,n}A^{s-}_{m,n}\Psi^{s-}_{m,n}(r)e^{-ik^{s-}_{m,n}x}\Bigg), \end{aligned} \tag{3.4}$$

and, in case of uniform flow, the radial modal form becomes $\Psi^{\pm s}_{m,n}(r) = J_m(\alpha^{\pm s}_{m,n}r)$. In a rigid-walled duct, $\alpha^{+}_{m,n} = \alpha^{-}_{m,n}$, even when the non-uniform flow is considered[1]. The source amplitude $A^{I+}_{m,n}$ at the fan plane is assumed to be known, and the remaining amplitudes are found by

[1] The radial wavenumber definition does not make sense when considering Pridmore-Brown modes since the dispersion relation is found when assuming uniform flow. However, this variable is useful in the presence of shear flow to order the acoustic modes (GABARD, 2016).

Figure 19 – Inlet duct geometry used on mode-matching technique: (a) uniform and (b) segmented liner.

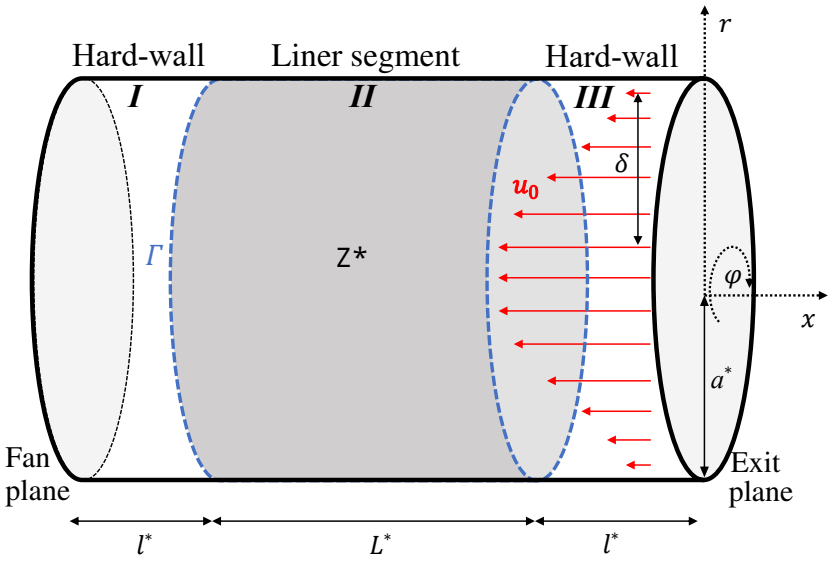

(a)

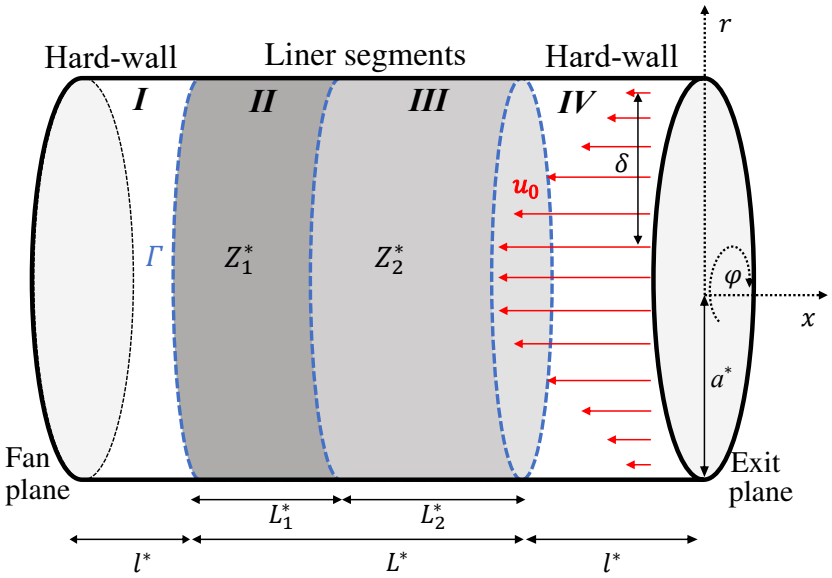

(b)

Source – Own authorship.

means of the Galerkin method of weighted residuals and considering continuity of pressure and axial particle velocity (P-V) at the interfaces ($x = l$ and $x = l + L$), which leads to

$$\begin{aligned} \int_S W_{m,n}(\hat{p}_m^{s+1} - \hat{p}_m^s)dS = 0 \ \text{ and} \\ \int_S W_{m,n}(\hat{u}_m^{s+1} - \hat{u}_m^s)dS = 0, \ \ n = 1 \text{ to } N, \end{aligned} \tag{3.5}$$

where s is the segment number (e.g., at both interfaces, $s = I, II$ or III), and $W_{m,n}$ denotes the trial weighted function, usually defined by the modal basis. Gabard and Astley (2008) also suggest the use of mode shapes of lined ducts $\Psi_{mn}^{II\pm}$ as test functions. This is based on the fact that the mode shapes of hard-walled ducts do not span the complete space of admissible solutions for a lined duct. In this work, we consider the hard-wall mode shapes as trial functions, such that Eq. (3.5) can be rewritten as

$$\begin{aligned} \int_0^1 r\Psi_{m,n}^I(r)(\hat{p}_m^{s+1} - \hat{p}_m^s)dr = 0, \ \ \text{and} \\ \int_0^1 r\Psi_{m,n}^I(r)(\hat{u}_m^{s+1} - \hat{u}_m^s)dr = 0, \ \ n = 1 \text{ to } N. \end{aligned} \tag{3.6}$$

In the presence of an uniform mean flow, the acoustic pressure and acoustic velocity at the rigid-lined wall interface are discontinuous due to the abrupt change of normal acoustic displacement, which induces a singularity in the pressure field in the vicinity of the transition region (GABARD, 2010). To solve this problem, Gabard and Astley (2008) proposed an improved matching condition based on continuity of mass and momentum (M-M). The continuity relation is defined from a variational statement for the field equations and impedance boundary condition over a small transition region between the segments with different impedances. Thus, the formulation of this continuity relation leads to a finite contribution from the contour Γ (see Figure 19) of the transition region to the matching condition, which is written as

$$\begin{aligned} \int_0^1 r\Psi_{m,n}^I(r)(\hat{p}_m^s - \hat{p}_m^{s+1})dr = \\ \frac{\mathrm{i}M^2}{k(1-M^2)} \int_\Gamma \Psi_{m,n}^I(r)\frac{\hat{p}_m^{II}}{Z}d\Gamma, \ \ \text{and} \\ \int_0^1 r\Psi_{m,n}^I(r)(\hat{u}_m^s - \hat{u}_m^{s+1})dr = \\ \frac{\mathrm{i}M}{\rho_0 c_0 k(1-M^2)} \int_\Gamma \Psi_{m,n}^I(r)\frac{\hat{p}_m^{II}}{Z}d\Gamma, \ \ n = 1 \text{ to } N, \end{aligned} \tag{3.7}$$

where Γ is the contour of the cross section at the interface between liner and the hard-wall. Therefore, the match at each interface, considering both matching conditions, is given in matrix

form as

$$\begin{Bmatrix} \mathbf{A}^{\mathbf{s+1+}}_{\mathbf{m,n}} \\ \\ \mathbf{A}^{\mathbf{s-}}_{\mathbf{m,n}} \end{Bmatrix} = \begin{bmatrix} \mathbf{P}^{+}_{\mathbf{s+1}} & -\mathbf{P}^{-}_{\mathbf{s}} \\ \\ \mathbf{M}^{+}_{\mathbf{s+1}} & -\mathbf{M}^{-}_{\mathbf{s}} \end{bmatrix}^{-1} \begin{bmatrix} \mathbf{P}^{+}_{\mathbf{s}} & -\mathbf{P}^{-}_{\mathbf{s+1}} \\ \\ \mathbf{M}^{+}_{\mathbf{s}} & -\mathbf{M}^{-}_{\mathbf{s+1}} \end{bmatrix} \begin{bmatrix} e^{-ik^{s}_{m,n}l} & 0 \\ \\ 0 & e^{-ik^{s+1}_{m,n}(l+L)} \end{bmatrix} \begin{Bmatrix} \mathbf{A}^{\mathbf{s+}}_{\mathbf{m,n}}, \\ \\ \mathbf{A}^{\mathbf{s+1-}}_{\mathbf{m,n}} \end{Bmatrix}, \tag{3.8}$$

where the diagonal matrix (with size $2N \times 2N$) of $e^{-ik_{m,n}x}$ accounts for mode propagation and attenuation. The components of the matrices $\mathbf{P}^{\pm}_{\mathbf{S}}$ and $\mathbf{M}^{\pm}_{\mathbf{S}}$ (with size $N \times N$) depends on the matching condition chosen, which is obtained by the assumption of pressure and velocity continuity as

$$\mathbf{P}^{\pm}_{\mathbf{s,m,n}} = \int_0^1 r\Psi^{I}_{m,n}(r)\Psi^{s\pm}_{m,n}(r)dr, \tag{3.9}$$

$$\mathbf{M}^{\pm}_{\mathbf{s,m,n}} = \int_0^1 r\Psi^{I}_{m,n}(r)\Psi^{s\pm}_{m,n}(r)\left(\frac{k^{\pm}_{m,n}}{k - k^{\pm}_{m,n}M(r)}\right)dr. \tag{3.10}$$

Note that the Mach number can be a function of the radius, and the integral needs to be evaluated numerically. For the continuity of mass and momentum[2], these matrices are given by

$$\mathbf{P}^{\pm}_{\mathbf{s,m,n}} = \frac{k}{k - k^{\pm}_{m,n}M_0}\int_0^1 r\Psi^{I}_{m,n}(r)\Psi^{s\pm}_{m,n}(r)dr, \tag{3.11}$$

$$\begin{aligned}\mathbf{M}^{\pm}_{\mathbf{s,m,n}} = \left[M_0 + \left(\frac{k^{\pm}_{m,n}}{k - k^{\pm}_{m,n}M_0}\right)\right]\int_0^1 r\Psi^{I}_{m,n}(r)\Psi^{s\pm}_{m,n}(r)dr \\ + \frac{iM_0}{Zk(1-M_0^2)}\int_\Gamma r\Psi^{I}_{m,n}(r)\Psi^{s\pm}_{m,n}(r)d\Gamma.\end{aligned} \tag{3.12}$$

In order to solve the system of equations a simple iterative process was used (CUMMINGS, 1999; MCALPINE; ASTLEY, et al., 2006; LAW; DOWLING; CORRAL, 2010) and summarized as follows: (1) all amplitudes are initially zero except the incident one $A^{I+}_{m,n}$, which can be assumed unitary. (2) Eq. (3.8) is evaluated to estimate the values on the left-hand side, which are necessary to evaluate the next interface. (3) Updated values are inserted into Eq. (3.8) as they become available. Convergence is assumed when there is no significant change in the amplitudes.

[2] Note that it is necessary that there is a finite normal acoustic displacement for this formulation to make sense. Therefore, this formulation is only used for uniform flow cases since for sheared flow, we assume a flow profile with the velocity equal zero at the walls.

3.2 BOUNDARY CONDITION SOLVER

One requirement for the mode matching calculation is the correct estimation of the axial wavenumber for a given modal input data, such as (m,n) and k. In the present work, the spectral method was chosen to solve the linearized Euler equations with Ingard-Myers and the standard relation of locally reacting impedance boundary conditions. The system of Eqs. (2.9)-(2.12) is a generalized eigenvalue problem,

$$\mathcal{A}\psi = k_{m,n}\mathcal{B}\psi, \tag{3.13}$$

for a given m and k, where $k_{m,n}$ is the eigenvalue corresponding to the axial wavenumber and ψ is the eigenvector containing pressure and acoustic particle velocity in the axial, radial and azimuthal directions. The matrix $\mathcal{A}$ and $\mathcal{B}$ contain the modal and flow parameters and can be found in Gabard (2016). This system of equations can be solved by a pseudospectral method (BOYD, 2001), together with a Gauss-Lobatto grid point distribution (with N_p points), given by

$$y_i = \cos\left(\frac{\pi i}{N_p}\right), \quad i = 0, 1, ..., N_p \tag{3.14}$$

where $y \in [-1, 1]$. A high number of points are located at both ends of the domain, which is necessary to represent the boundary layer profile correctly. A change of coordinate is made by $r_i = (y_i + 1)/2$, along with the necessary corrections in the differentiation matrix (TREFETHEN, 2000). The Ingard-Myers boundary condition from Eq. (2.23) is applied at the rows corresponding to $r = 1$. Notice that, in the presence of a shear flow, the condition given by Eq. (2.29) is recovered. Parity conditions at the duct center, as outlined by Gabard (2016), are necessary to ensure the correct behavior of the modal solution. The generalized eigenvalue problem from Eq. (3.13) can be solved using the Matlab function eig with a QZ algorithm.

The Brambley boundary condition, Eq. (2.25), is not suitable for this kind of problem since some terms are quadratic in k. For this boundary condition, the tracking method, proposed by Rienstra (2016a) (adapted from Eversman and Hubbard (1991)), is used to find the values of $k_{m,n}$ in a lined duct. These are found by starting from the values in a rigid duct or soft-wall with Ingard-Myers boundary condition, and tracking the values of the $k_{m,n}$ in the complex plane as the acoustic impedance is varied from a high value (rigid wall) to impedance wall Z. The tracking is performed using an initial value problem formulation, and the eigenvalues are refined using the NewtonRaphson method.

3.3 THE MODAL RADIATION PROBLEM

The in-duct modal content described in previous Section can be linked to the far-field noise using the modal radiation directivity. In this sense, some simplified models of a duct opening surrounded by an infinite baffle (thereby eliminating sharp edge), without the baffle or by an unflanged edge are usually considered, which are represented in the Figure 20. In this Section, the governing equations and some physical insights in the sound radiation problem of a cylindrical duct considering integral methods (represented in the Figure 20.a and Figure 20.b) and the Wiener-Hopf technique (illustrated in the Figure 20.c) are presented.

Figure 20 – Geometry of a circular duct ending in an infinite baffle (a), without baffle (b) and with unflanged edge (c) (with edge thickness $\varepsilon \to 0$).

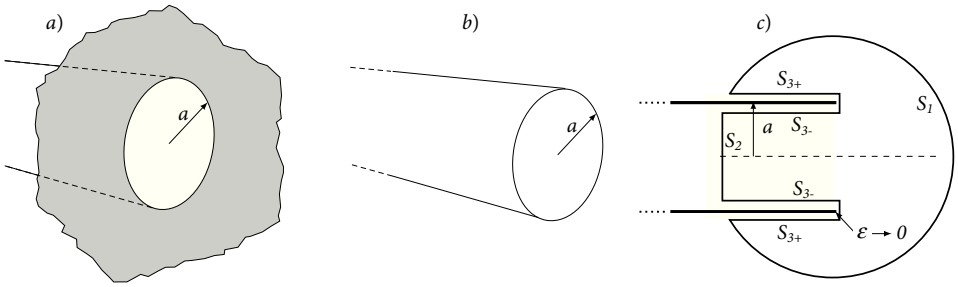

Source – Adapted from Kolbrek (2016).

3.3.1 Integral methods

The sound radiated from the duct termination, in spherical coordinates, is represented in Figure 21. Note that point Q can be in the near-field or far-field, therefore, if we consider any position outside the duct, the sound radiated at a single frequency can be written as the sum of modal contributions, so that

$$p^{\text{rad}}(D,k,\varphi,\theta) = \sum_{m=0}^{\infty}\sum_{n=1}^{\infty} p^{\text{rad}}_{m,n} = \sum_{m=0}^{\infty}\sum_{n=1}^{\infty} A^{exit}_{m,n} F_{m,n}(D,k,\theta,\varphi) \tag{3.15}$$

where $F_{m,n}(k,\theta)$ is the directivity function (and $|F_{m,n}(k,\theta)|$ is the radiation pattern), $D = D^*/a^*$ is the normalized distance from the duct termination and $A^{exit}_{m,n}$ is the modal amplitude at the exit plane. If Rayleigh integral is considered, the classical problem of sound radiation produced by a circular vibrating piston in a baffle, without mean flow, is given by (PIERCE,

Figure 21 – Coordinate system for the computation of sound radiation.

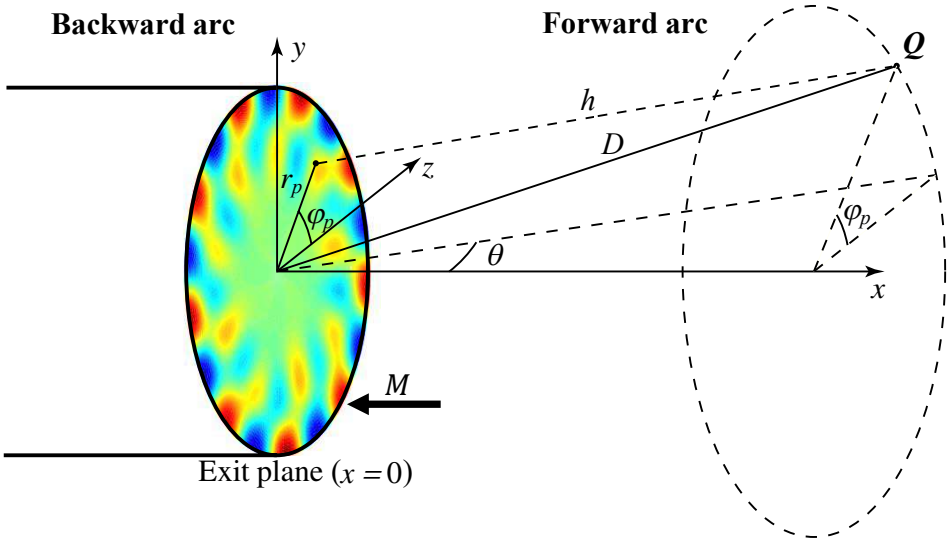

Source – Own authorship.

1989)

$$p^R(D,k,\varphi,\theta) = \frac{\mathrm{i}k}{2\pi}\int_0^1\int_0^{2\pi} \hat{u}(r_p,\varphi_p)\frac{e^{-\mathrm{i}kh(D,\varphi,\theta)}}{h(D,\varphi,\theta)} r_p \mathrm{d}r_p \mathrm{d}\varphi_p, \tag{3.16}$$

where $\hat{u}$ is the acoustic velocity of the piston and $h(D,\varphi,\theta)$ distance from between the point **Q** and a point on surface area of the piston located in the plane $x = 0$, which is defined as

$$h(D,\varphi_p,\theta) = D\sqrt{1+\left(\frac{r_p}{D}\right)^2 - 2\frac{r_p}{D}\sin(\theta)\cos(\varphi-\varphi_p)}. \tag{3.17}$$

Note that the second and third terms (i.e., the second and first-order terms) should be more critical at the vicinity of the piston source, and if $D \to 0$, the near-field solution of the Eq. 3.16 is the own acoustic velocity at piston surface. Since the solution for the acoustic pressure was defined in Eq. (2.16) and the relation between acoustic velocity and pressure is given by the momentum conservation equation (Eq. (2.2)), in the absence of mean flow, it is straightforward to show that

$$\hat{u}(r_p,\varphi_p) = A^{\text{exit}}_{m,n}\frac{k_{m,n}}{k}J_m(\alpha_{m,n}r_p)e^{-\mathrm{i}m\varphi_p}. \tag{3.18}$$

The integral in Eq. 3.16 is solved numerically to obtain the radiated sound pressure at any point in the forward arc (i.e., $0 \geq \theta \geq \pi/2$) for a given mode. In the far-field, for large D (i.e. $a << D$) the distance h is approximately $D - r_p\sin(\theta)\cos(\varphi-\varphi_p)$. Also, the integral over

φ from zero to 2π is exactly the representation of the cylindrical Bessel function of order m argument $k \sin\theta$, and Eq. 3.16 can be written analytically as (TYLER; SOFRIN, 1962)

$$p^R_{m,n}(D,k,\varphi,\theta) = A^{exit}_{m,n} F^R_{mn}(k,\theta) \frac{e^{-\mathrm{i}kD - \mathrm{i}m\varphi}}{D}, \tag{3.19}$$

and the Rayleigh directivity function is given by

$$F^R_{mn}(k,\theta) = \mathrm{i}^{m+1} k_{m,n} J_m(\alpha_{m,n}) \frac{k \sin\theta J'_m(k\sin\theta)}{(\alpha_{m,n})^2 - (k\sin\theta)^2}, \tag{3.20}$$

where $J_m(\cdot)'$ is the the first derivative of the Bessel function of the first kind with respect to its argument. The far-field solution has the following characteristics: (1) modal radiation vanishes as cut-off is approached, i.e. $F_{m,n} \to 0$ as $\eta_{m,n} < 1$; (2) the polar angle of the main radiation lobe occurs near $\theta^{\wedge}_{m,n} = \arcsin 1/\eta_{m,n}$ (as seen before in Section 2.1.2.1); (3) the polar angles of the radiation nulls (i.e. the zeroes) are located at $\theta^{\vee}_{m,n} = \arcsin 1/\eta_{m,j}$, for $j \neq n$.[3] Only first and second far-field characteristics are also applied for near-field solution in Eq. 3.16.

Another integral method is based on Kirchhoff-Helmholtz integral theorem for the same radiation problem in Figure 21. Therefore, the derivation begins assuming the inhomogeneous Helmholtz equation for an isolated piston vibrating surround by unbounded fluid. In comparison with Rayleigh integral, this implies a subtle difference in the solution because the flanged inlet is not considered here. Therefore, considering the Green's second identity solution for the Helmholtz equation (with piston source), which has the surface integral over any surface enclosing the primary source (in this case, we assume a sphere), pressure in any point $\mathbf{Q}$ is given by (PIERCE, 1989)

$$\hat{p}^K(\mathbf{Q}) = -\frac{1}{4\pi}\int_S (G\nabla\hat{p} - \hat{p}\nabla G)\cdot \mathbf{n}\mathrm{d}S, \tag{3.21}$$

where the Green's function solution in the free-space for the axisymmetric case is given by $G(D,\theta,\varphi) = e^{\mathrm{i}kD}/D$. Rewriting the in-duct acoustic field as $J_m(\alpha_{m,n}r)\exp(-\mathrm{i}m\varphi)$ (defined in Section 2.1), we obtain

$$\nabla\hat{p}\cdot\mathbf{n} = \frac{\partial\hat{p}}{\partial x}\Big|_{x=0} = i\omega\hat{v} = -ik_{m,n}A^{\text{exit}}_{m,n}J_m(\alpha_{m,n}r)e^{im\varphi},$$

[3] These zeroes always occur in the forward hemisphere, $\theta < 90°$ and their number is limited by the fact that equation $\theta^{\vee}_{m,n} = \arcsin 1/\eta_{m,j}$ can be satisfied only for those $\alpha_{m,n} < k$. Knowing where the zeroes are, one can then reasonably infer the minor lobes to be roughly midway between them (HOMICZ; LORDI, 1975).

and

$$\nabla G = \frac{D\cos\theta}{h^3}(\mathrm{i}kh - 1)e^{\mathrm{i}kh}.$$

Considering these definitions in Eq. (3.21), the Kirchhoff-Helmholtz integral can be rewritten as follows

$$p^K_{m,n}(D,\varphi,\theta) = \frac{-\mathrm{i}A_{m,n}}{4\pi}\int_0^1\int_0^{2\pi}\left(k_{m,n} + (kh - \mathrm{i})\frac{D\cos\theta}{h^2}\right) J_m(\alpha_{m,n}r)\frac{e^{-im\varphi_p}}{h} r_p \mathrm{d}r_p \mathrm{d}\varphi_p. \tag{3.22}$$

In the presence of in-duct and external mean flow (in same direction), the convective effects modify the Eq. (3.22), which become (LEWY, 2003)

$$p^K_{m,n}(D,\varphi,\theta) = \frac{-\mathrm{i}A_{m,n}}{4\pi}\int_0^1\int_0^{2\pi}\left[\beta^2 k_{m,n} + k\left(\frac{D\cos\theta}{h^2} + M_0\right)\right] J_m(\alpha_{m,n}r)\frac{e^{-\mathrm{i}m\varphi)}}{h} r_p \mathrm{d}r_p \mathrm{d}\varphi_p. \tag{3.23}$$

The distance h becomes

$$h(D, r_p, \varphi_p, \theta) = \sqrt{(\beta_\theta D)^2 - 2\beta^2 r_p D\sin\theta\cos\varphi + (\beta r_p)^2}, \tag{3.24}$$

in which $\beta^2 = 1 - M_0^2$ and $\beta_\theta^2 = 1 - (M_0\sin\theta)^2$ are defined as the Doppler parameters. The far-field approximation for Kirchhoff integral can be determined analytically, as well as, the Rayleigh Integral. If we consider a point **Q** in the far-field ($kD \to \infty$), the sound radiated at a given frequency can be written for any modal contributions, so that

$$p^K_{m,n}(D,k,\varphi,\theta) = A^{\text{exit}}_{m,n}F^K_{m,n}(k,\theta)\frac{e^{-\mathrm{i}m\varphi - \mathrm{i}kD}}{D}, \tag{3.25}$$

where $F^K_{m,n}(k,\theta)$ is the Kirchhoff directivity function is given as follows (HOCTER, 1999)

$$F^K_{m,n}(k,\theta) = (1 + k\cos\theta)\frac{\mathrm{i}^{(m+1)}}{2}\left[\frac{k\sin\theta J'_m(k\sin\theta)}{(\alpha_{m,n})^2 - (k\sin\theta)^2}\right]. \tag{3.26}$$

It is interesting to note that Kirchhoff and Rayleigh directivity functions have a direct correlation in terms of far-field sound radiated. The Kirchhoff directivity function $F^K_{m,n}(k,\theta)$ can be related to the Rayleigh directivity function $F^R_{m,n}(k,\theta)$ by

$$F^R_{m,n}(k,\theta) = \frac{F^K_{m,n}(k,\theta)}{\left(\frac{1}{2} + \frac{k\cos\theta}{2k_{m,n}}\right)}. \tag{3.27}$$

For radiation modeling of modern turbofan, Lewy (2003) observed that the Kirchhoff approximation better simulates actual configurations mainly for lateral radiation (angles closer to $90°$) because there is no hypothesis of the flanged inlet. In comparison with Wiener-Hopf techniques, Hocter (1999) found that the Kirchhoff approximation accurately predicted the main radiation lobe and the zeros of the directivity pattern, but the accuracy of the solution near the sideline was poor. This can be expected when the Kirchhoff approximation is used since the sound radiation in the backward hemisphere cannot be predicted. However, the author found that the usefulness of Kirchhoff approximation may be underestimated for spinning modes (i.e., when $m > 0$). As one changes the governing parameters, such that the number of lobes in the forward arc increases, the overall accuracy of this approximation is improved.

3.3.2 Wiener-Hopf–based method

To this point, we have been concerned with a duct termination neglecting the leading edge (duct wall geometry). In this sense, Wiener-Hopf method can be an alternative, which assumes the discontinuity at the termination and an unflanged end (see Figure 20.c). The essential difference between the intake and exhaust duct problems lies in the different behavior at the duct leading edge, which is conveniently expressed in terms of the radial velocity or radial derivative of the velocity potential. For exhaust problems, the correct behavior at the duct edge is obtained when the Kutta condition is satisfied[4].

This section is a summary of the formulation presented by Homicz and Lordi (1975) for computing the magnitude of the far-field pressure $p^{\text{rad}}(k, \theta)$ radiated from a semi-infinite, hard-walled circular unflanged duct. The governing equations of the sound diffraction problem for an open end duct are not shown in details here. Similar to the Kirchhoff integral, this complex formulation starts with the solution of the velocity potential field using the Green's function on the exit plane at $x = 0$. However, the integration is defined over the composite surface (S_1, S_2, S_3) shown in Figure 20. Due to the Sommerfield radiation condition, the integral over surfaces S_1 and S_2 must be zero as D goes to infinity. The resulting external radiation field may be written in the far-field pressure (assuming the point $\mathbf{Q}$ in Figure 21 far from the source and

[4] It is not shown here, but Kutta condition is essentially applied to edge condition problems such as a hard-soft lining transition, duct termination and to solve the vortex shedding problem. In exhaust radiation problems, the effect of the Kutta condition is significant, but it is particularly large for the plane wave at low frequencies, which implies a smooth streamline at exit plane. In the models proposed by Rienstra (1984) and Gabard and Astley (2006), the Kutta condition can be turned on and off in the current solution, and this capability is used to assess the effect of vortex shedding on noise radiation, which grows exponentially in the streamwise direction.

$kD \gg 1$) as

$$\hat{p}^W_{m,n}(k, \mathbf{Q}) = A^{exit}_{m,n} F^W_{m,n}(k, \theta) \frac{e^{-\mathrm{i}kD - \mathrm{i}m\varphi}}{D}, \tag{3.28}$$

which is equivalent to Eq. (3.19). As the other directivity functions, F^W_{mn} are in general a complex quantity, and directivity pattern $|F^W_{mn}|$, is given by (HOMICZ; LORDI, 1975)

$$|F^W_{m,n}|(k,\theta) = \left| \frac{J_m(\alpha_{m,n}) k_{m,n}}{k\cos\theta - k_{m,n}} \right| \sqrt{\frac{(\alpha_{m,n})^2 - m^2}{\pi \alpha^2_{m,n}} \sin \Upsilon(k \sin\theta)} \sqrt{\prod_{\substack{j=1 \\ j\neq n}}^{n_c} \frac{k_{m,j} + k_{m,n}}{k_{m,j} - k_{m,n}} \prod_{q=1}^{n_c} \frac{k_{m,q} - k\cos\theta}{k_{m,q} + k\cos\theta}} e^{\frac{1}{2}\mathrm{Re}[C(k_{m,n}) - C(k\cos\theta)]}, \tag{3.29}$$

and $\mathrm{Re}[C]$ represent the real part of the function C, which is given by

$$\mathrm{Re}[C(\zeta)] = \frac{1}{\pi} \int_{-1}^{1} \frac{\Upsilon(k\sqrt{1-\nu^2})}{\nu - \zeta} \, \mathrm{d}\nu, \tag{3.30}$$

and

$$\Upsilon(\cdot) = \arctan \frac{Y'_m(\cdot)}{J'_m(\cdot)} \mp \frac{\pi}{2}, \quad \begin{cases} (-), & \text{if} \quad m > 0 \\ (+), & \text{if} \quad m = 0 \end{cases}, \tag{3.31}$$

where $Y_m(\cdot)'$ is the the first derivative of the Bessel function of the second kind. The value n_c represents the order of the highest radial mode that can propagate at k, with $k_{m,n} \in \mathbb{R}$ (and cutoff ratio $\eta > 1$). The Cauchy principal value sense must be used to solve the integral over ν in Eq. (3.30). This integral can be solved by standard methods whenever $\nu \neq \zeta$. In the region $\nu \approx \zeta$, it can be solved by polynomial approximation. Also, for the endpoints ($\zeta = \pm k$), it can be simplified into an easier integral. In Eq. (3.31), the function Υ represents the phase of the Hankel function derivative, where negative m values are not taken account in the numerical calculation. An important condition on the function Υ, not stated explicitly but essential to compute the directivity function in Eq. (3.29), is related to its continuous behavior and must consequently be unwrapped for phase: the singular math problem into the integral need be evaluated carefully (JOSEPH; MORFEY, 1999).

In the presence of in-duct mean flow only, the convective effects can be computed by the dispersion relation between radial wavenumbers $\alpha_{m,n}$, non-dimensional frequency $k/\sqrt{1-M_0^2}$ and axial wavenumbers $k_{m,n}$, as given by Eq. (2.15). For the presence of both in-duct and

external mean flow, the solution to the pressure in the far-field reads (including Rayleigh and Kirchhoff approximations)

$$\hat{p}(D,k,\theta) = \sum_{m,n} A^{exit}_{m,n} F_{m,n}(k,\theta) \frac{e^{-\mathrm{i}kD\mathcal{S}(\theta)}}{D}. \tag{3.32}$$

The factor $\mathcal{S}(\theta)$ accounts for the wavefront stretching or constricting introduced by the ambient mean flow (M_∞) given by

$$\mathcal{S}(\theta) = \frac{\sqrt{1 - M_\infty^2 \sin^2\theta} - M_\infty \cos\theta}{1 - M_\infty^2}, \tag{3.33}$$

where $M_\infty = M_0$. In chapter 6, the effect of flow velocities inside and outside the inlet duct of a turbofan engine is analyzed in detail.

In general, the Wiener-Hopf method is used to couple the sound field inside and outside an unflanged duct in terms of modal reflection and directivity. The reflections at the duct termination can be important in some cases, which lead to a complex computational solution in the presence of mean flow. The reflection coefficients are then defined as $|R_{m,n,\mathfrak{k}}| = A^-_{m,\mathfrak{k}}/A^+_{m,n}$, where the modal amplitudes were defined in Eq. (2.16) and $\mathfrak{k}$ is the radial order reflected at the termination. The typical plot of magnitude $|R_{m,n,\mathfrak{k}}|$ as function of frequency has been evaluated by many authors (LORDI; HOMICZ, 1974; MUNT, 1977; RIENSTRA, 1984; SNAKOWSKA; JURKIEWICZ; GORAZD, 2017). In general, the magnitude of the reflection coefficient for any value of $\mathfrak{k}$ grows asymptotically toward unity near that mode's cut-off frequency. At higher frequencies it decays quickly, exhibiting well-defined dips at the cut-off frequency of each higher mode; this higher mode, of course, is now getting most reflected energy. The behavior for lower azimuthal modes are qualitatively similar.

Due to the high frequency behavior, for low and high order modes (with cut-off ratio $\eta_{m,n}$ above 1) typically found in turbofan engine intakes, the reflections at the duct termination can be, in general, neglected (GABARD; ASTLEY, 2008). On the other hand, cut-off modes are assumed to have little contribution to the far-field sound pressure distribution and are not included in the general formulations. Generally speaking, the radiation models compute the far-field acoustic pressure for cut-on modes on a forward arc (and in such case in backward arc) from an exit plane. This modal far-field content is then used to calculate the complex pressure at the other azimuthal angles including the effect of the relative phase between the modes (i.e., in the case a multi-modal analysis).

3.4 COUPLING THE MODELS

Studies of liner performances are often limited to in-duct propagation and assess the power loss achieved by different liner configurations under shear flow effects (GABARD; ASTLEY, 2008). In some cases, it is essential to characterize these performances in terms of reduction of the noise radiated out of the duct to the far-field. By integrating the mode-matching technique with a radiation model, it is possible to investigate directly how the liner impedance influences the far-field noise.

In order to integrate the radiation model with the mode-matching method, we assume that (1) the duct is not lined at the exit plane, and (2) the effect of the non-developed boundary layer is not considered at the exit plane (assuming a boundary layer with negligible thickness at the duct entrance). Although, it is assumed the modes in a hard-wall section with uniform mean flow, i.e. the simplest eigenvalue solution, which can facilitate the integration with the radiation model. In order to make the integration with the radiation model more simple, a linear combination of the modes (m, n) is assumed.

The solution of the linear systems in Eqs. (3.8) and (3.9) can be rewritten in terms of the scattering matrix $\mathbf{S}$ of the duct defined by the relationship

$$\begin{Bmatrix} \mathbf{A}^- \\ \\ \mathbf{B}^+ \end{Bmatrix} = \mathbf{S} \begin{Bmatrix} \mathbf{A}^+ \\ \\ \mathbf{B}^- \end{Bmatrix}, \tag{3.34}$$

which $\mathbf{A}^{\pm}$ and $\mathbf{B}^{\pm}$ are the global incident and transmitted modes after the liner section (e.g., following our notation, it is equivalent to $s = III$, see Fig. 19a). The scattering matrix is given by

$$\mathbf{S} = \begin{bmatrix} \mathbf{S_{AA}} & \mathbf{S_{AB}} \\ \\ \mathbf{S_{BA}} & \mathbf{S_{BB}} \end{bmatrix}. \tag{3.35}$$

Note that $\mathbf{B}^+$ denote the outgoing mode amplitudes towards the exit plane and, consequently, these modes are radiated to the outside of the duct. Thus, as the sound propagates out of the duct, a part of the acoustic energy is reflected back into the duct ($\mathbf{B}^-$) since there is a change in acoustic impedance at the duct exit plane. As described in Section 3.3, these reflec-

tions depends on the properties of the flow inside and outside the duct and can be described in the matrix form by a reflection matrix $\mathbf{R}$ given by

$$\mathbf{B}^{-} = \mathbf{R}\mathbf{B}^{+}. \tag{3.36}$$

By introducing Eq. (3.36) into Eq. (3.34), it is straightforward to derive

$$\mathbf{B}^{+} = \mathbf{T}\mathbf{A}^{+} = (\mathbf{I} - \mathbf{D}_{\mathbf{BB}}\mathbf{R})^{-1}\mathbf{D}_{\mathbf{BA}}\mathbf{A}^{+}, \tag{3.37}$$

where $\mathbf{T}$ is the transmission matrix of the duct and $\mathbf{I}$ denotes the identity matrix. While the scattering matrix depends solely on the duct properties, the transmission matrix depends also on the ambient flow since it takes the reflections at the plane exit into account. As seen in Section 4.5.2, in practice, the reflections at a intake nacelle at operating conditions are marginal and can be neglected. In this case, the vector with reflected modes $\mathbf{B}^{-}$ is zero, and the Eq. (3.37) can be simplified as

$$\mathbf{B}^{+} = \mathbf{D}_{\mathbf{BA}}\mathbf{A}^{+}, \tag{3.38}$$

which means $\mathbf{T} = \mathbf{D}_{\mathbf{BA}}$. Also, transmission matrix $\mathbf{T}$ can be understood as a transfer matrix in which each term represents the contribution from each source mode independently to the resulting modal amplitudes at the duct exit. For instance, T_{ij} is the modal amplitude of mode (m, i) by injecting only the mode (m, j) of unit amplitude at the source plane.3

Finally, from Eq. (3.19) the sound radiated to the far-field can be rewritten in matrix form as

$$\mathbf{P} = \left(\frac{1}{D}e^{\mathrm{i}kD\mathcal{S}}\right)\mathbf{B}^{+}\mathbf{F}, \tag{3.39}$$

where $\mathbf{P}$ and $\mathbf{F}$ are the far-field pressure matrix and the directivity matrix, respectively. Note that term $e^{\mathrm{i}kD}/D$ is independent of the modal content, which is constant for a given distance from the exit plane. By introducing Eq. (3.38) into Eq. (3.39), the sound radiated from the exit plane is given by

$$\mathbf{P} = \left(\frac{1}{D}e^{\mathrm{i}kD\mathcal{S}}\right)\mathbf{D}_{\mathbf{BA}}\mathbf{A}^{+}\mathbf{F}, \tag{3.40}$$

Note that the Equation 3.40 represents the coupling of the radiation model with the mode-matching method, so that the liner attenuation can be investigated directly in terms of the acoustic far-field (knowing incident modal content $\mathbf{A}^{+}$). Moreover, transmitted, scattered and radiated

modes $\mathbf{B}^+$ depends on the combination of the scattering matrix of the duct with the reflection coefficients (when considered). It is necessary to calculate all terms of the scattering matrix $\mathbf{S}$ by means of the mode matching procedure to assess the transmission matrix $\mathbf{T}$.

3.5 COMPUTER CODES

The theory outlined in Sections 3.1 to 3.4 has been implemented in a MATLAB computer code. The code is referred to as "Liner Discontinuity Code". The theory described in section 3.3, i.e., far-field radiation, has been implemented in a separate MATLAB code, which is named "Free-field radiation code". This code may read the output of the "Liner Discontinuity Code" to obtain the amplitude at exit plane (such as defined in Section 3.4), or the amplitudes can be manually attributed to compute the far- and near-field radiation. The main characteristics of both codes are presented in sections 3.5.1 and 3.5.2.

3.5.1 Liner discontinuity code

The "Liner Discontinuity Code" code was developed as an analysis tool for the design of liners (with segmentation) in the presence of non-uniform flow and is based on the theory presented in Section 3.1. This is mainly focused on nacelle intake modeling (i.e., upstream propagation). The flowchart for the code identifying the main routines is shown in Figure 22.

As a secondary function, the eigenvalue solver presented in Section 3.2 is necessary to compute the wavenumbers for each boundary conditions (hard- and soft-wall) at the cylindrical duct wall. A convergence analysis of this solver is reported in Appendix B.1. The code for the lined duct case follows the same structure of hard-wall one, but it takes a significantly higher amount of computational time to process. Three options were implemented in the first version (1) Ingard-Myers (defined by Eq. (2.24)), (2) Brambley (defined by Eq. (2.25)) and (3) Pridmore-Brown (defined by Eq. (2.29)). The results with all the boundary conditions will be presented later in Chapter 5.

The code can solve the acoustic field inside the duct for particular conditions and configurations. Different cases can be simulated by changing parameters in the input data. The input data can be divided into fluid properties and dimensions, wall properties, modal expansion parameters, and additional data. In the fluid properties and dimensions setup, the inputs are defined by duct radius a^*, number of liner segments N_s[5], hard-wall l^* and liner length L^* (or L_1^* and L_2^*)

[5] Currently, there are only uniform (1 segment) and segmented (2 segments) liner configuration options, as

Figure 22 – Liner Discontinuity code structure.

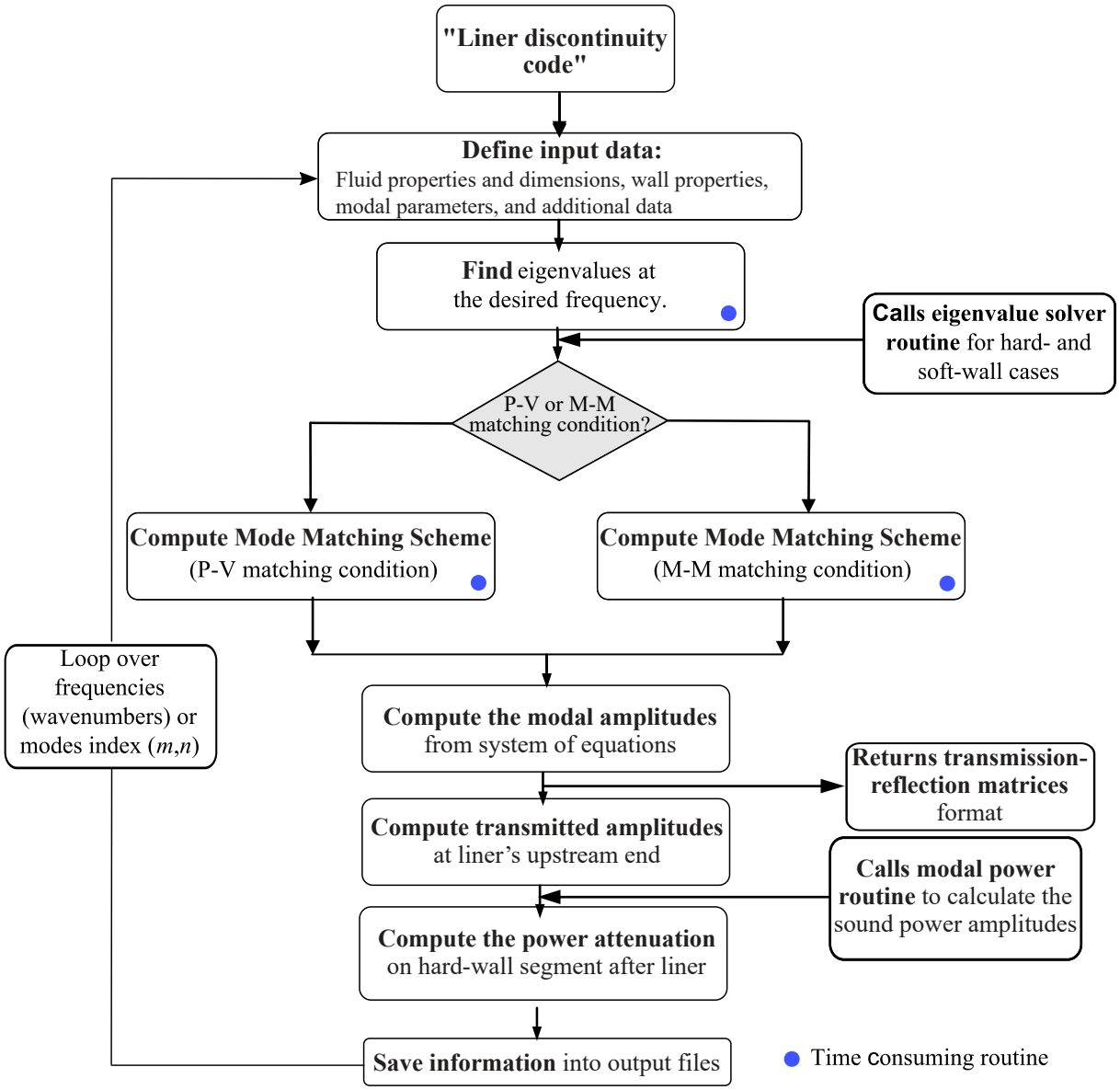

Source – Own authorship.

and fluid properties as Mach number M_0, flow profile $M(r)$, boundary layer thickness δ, fluid density ρ_0^* and speed of sound c_0^*. In the fluid wall properties setup, the acoustic liner impedance Z (or Z_1 and Z_2) and boundary condition are chosen. In modal expansion parameters, the incident mode order (m, n), amplitude $A^+_{m,n}$ (by default it is unitary), and wavenumber k must be defined. The additional input data is the number of modes computed in the mode matching, a number of points on the grid N_p (defined in the Section 3.2) and the print controllers. Typical results of the eigenvalue solver used in the mode-matching scheme are outlined in Appendix B.2.

formulated in Section 3.1.

The scattering and attenuation effects of liner discontinuities are computed by solving the system of equations in Eq. 3.8 (and P-V or M-M matching must be selected). A modal sound power routine is used to compute this amplitude sound power employing the formulation shown in Appendix A. Besides, a new routine to check the behavior of the scattering matrix in terms of transmission-reflection effects has been included.

The output of the "Liner Discontinuity Code" can be used directly as input for "Free-field radiation code". The coupling with the "Liner Discontinuity Code" is described in detail in Section 3.4 and applied in Chapter 6.

An average computation takes about 2 to 4 minutes per mode and per frequency for uniform and segmented liner models on a PC with processor intel core i5 with 2.4 GHz, 8 GB physical RAM and 3G virtual memory, without optimizing the MATLAB code.

It should be pointed out that the segmented liner with two segments is also implemented in this version. However, it is outside the scope of this work to investigate such lined duct configuration.

In the proposed prediction approach, the assumptions can be summarized, as:

1. Source noise is known;
2. Axisymmetric duct is straight and does not have thickness and lips;
3. The formulation is based on the linearized Euler equation solution by means: Pridmore-Brown equation and convective wave equation (CWE);
4. Fully-developed inviscid flow is assumed;
5. Hydrodynamic modes or instability waves produced by the eigenvalue problem are dropped of the solution;
6. The sound diffraction, reflection, and refraction are neglected on the inlet duct;
7. There is a linear combination of the modes (m,n) for coupling of the radiation models and mode matching scheme;

3.5.2 Free-field Radiation code

The major routines used to calculate far- and near-field radiation through the radiation models presented in the Section 3.3 are shown in Figure 23. In contrast with the "Liner Discontinuity Code", this tool was developed to compute the modal radiated sound outside the duct at

any point in the free-field, based on the modal theory presented in Chapter 2 and on the radiation models described in this Chapter. Furthermore, this code considers only the radiation effect at forward hemisphere, assuming upstream propagation. Therefore, depending on the source, and geometric characteristics as the wavenumber k and the distance from the exit plane D, it defines the far- or near-field solutions. Then, Rayleigh and Kirchhoff radiation models (referred in Fig. 23 as flanged and no-flanged duct models, respectively) may compute the radiated sound by using Eqs. (3.16) or (3.19) and Eqs. (3.23) or (3.25), respectively. On the other side, the Wiener-Hopf–based method computes only the far-field prediction.

Figure 23 – Far-field Radiation code structure.

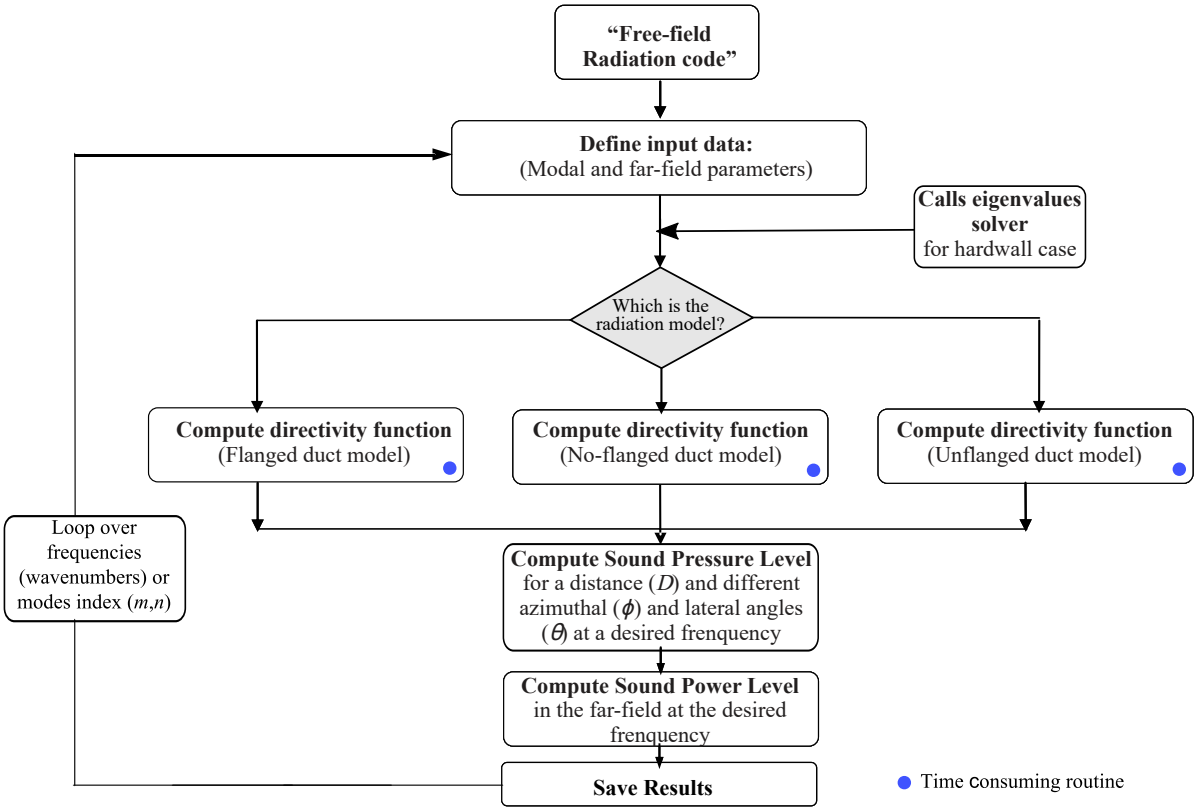

Source – Own authorship.

The input data can be easily divided into two types: far-field parameters and modal expansion parameters. The far-field parameters are defined as the duct radius a^*, the distance from exit plane to the listening point D^*, lateral θ and azimuthal φ angles range and the fluid properties as Mach number M_0 (the ambient mean flow can be turned on and off in the current solution), fluid density ρ_0^* and speed of sound c_0^*. In modal expansion parameters, the incident mode order must be defined m, n and amplitude $A_{m,n}^+$ (i.e., it may be linked with the output amplitude of the "Liner Discontinuity Code" by means the integration formulated in Section 3.4) and wavenum-

ber k. In addition, the eigenvalue solver presented in Section 3.2 is used here to compute the wavenumbers for hard-wall boundary conditions ($\alpha_{m,n}$ and $k_{m,n}$) of the cylindrical duct, which is defined by Eq. (2.20). As output data, the code returns the radiated sound outside the duct in terms of SPL as a function of the lateral θ and azimuthal φ angles range and the PWL for a given frequency (defined in Appendix A).

In terms of computational time, the models take about 3 to 5 minutes per mode and per frequency for Rayleigh/Kirchhoff integrals and Wiener-Hopf–based method on a PC with processor intel core i5 with 2.4 GHz, 8 GB physical RAM and 3G virtual memory, without optimizing the MATLAB code. The far-field approximation solutions are faster than the integral ones and it take a half minute on the same computer configuration.

4 ASSESSMENT AND VALIDATION OF THE SEMI-ANALYTICAL MODELS

In this chapter, the mode-matching scheme and the radiation models are benchmarked for acoustic propagation in turbofan intake problems. The main objective of this chapter is to explore the accuracy and efficiency of the semi-analytical methods for simulating intake propagation and radiation at relevant frequencies and flow condition by comparing results with the FE code. Both acoustic and mean flow fields in the inlet duct (i.e., nacelle intake) have been simulated using specialized FE software called ACTRAN/TM, whose acoustic tool for turbomachinery noise prediction is based on a hybrid approach of finite/infinite element method and includes a CFD code for potencial flow analysis.

4.1 MODELING THE MEAN FLOW

The assessment of the mean flow effect on the acoustic propagation requires the discretization of the acoustic waves in moving media. For large problems such as those considered in aeronautics, the common methods are generally based on a hybrid approach that consists of dissociating aerodynamic and acoustic problems. The mean flow then serves as a support for writing the acoustic propagation operator and must be determined prior to the acoustic computation. Figure 24 shows schematically both computational domains typically considered to solve intake nacelle radiation problem separately.

The CFD approach considered in this work is based on a compressible potential flow model[1], for which a systematic decoupling between a mean flow and sound waves is rigorously valid (RIENSTRA; EVERSMAN, 2001). The fluid is assumed as inviscid, irrotational, isentropic, perfect gas. It can be described by the Euler equations (2.1) - (2.3), which can be used to write the steady irrotational compressible flow (ANTWERPEN et al., 2008). As assumed in Eq. (2.5), the acoustic disturbances in the mean flow can be described by decomposing the potential field in fluctuation (acoustic) and the steady-state velocity potential, which is given by

$$\phi = \phi_0 + \tilde{\phi}, \tag{4.1}$$

[1] The potential flow model is not necessarily restrictive for hybrid tools such as ACTRAN, and other mean flow models can also be used. Rarata (RARATA, 2014) has shown the influence of other types of mean flow on the intake nacelles with non-symmetric lips by using other approaches such as RANS solver. The author observed that the effects of refraction due to the mean flow distortion play an important role in shaping the sound field inside and outside the nacelle.

Figure 24 – Representation of the computational domains for mean flow (top) and acoustic propagation (bottom) modeling.

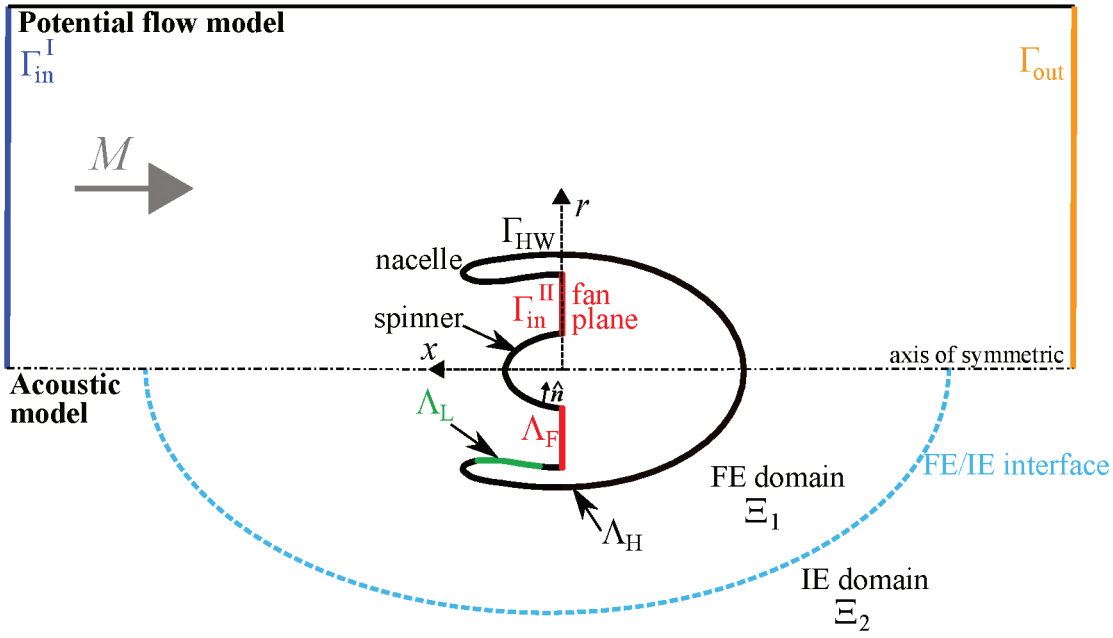

Source – Own authorship.

where it is assumed that $\phi_0 >> \tilde{\phi}$. The velocity vector $\mathbf{u}_0$ may be expressed in terms of a velocity potential such as $\mathbf{u}_0 = \nabla\phi_0$ (i.e. corresponding to a potential flow). The flow field boundary condition is specified in terms of Mach number at the fan plane (Γ_{in}^{I}) and the ambient flow Mach number (Γ_{in}^{II}). These conditions can also be specified in the model in terms of mass flow rate. The boundary conditions on rigid surfaces correspond to zero normal velocity condition at walls ($\mathbf{u}_0 \cdot \mathbf{n} = 0$ on Γ_{HW}), and the velocity potential is specified at outlet boundary (Γ_{out}).

Assuming a potential flow (i.e. isentropic and irrotational), the momentum equation may be integrated into a compressible flow variant of Bernoullis equation. Thus, the mean flow field may be calculated by following a set of equations given by (RIENSTRA; EVERSMAN, 2001)

$$\begin{aligned} \nabla \cdot (\rho_0 \mathbf{u}_0) &= 0, \\ \frac{1}{2}\mathbf{u}_0^2 + \frac{c_0}{1-\gamma} &= E, \\ c_0 = \gamma\frac{p_0}{\rho_0} &= \rho_0^{\gamma-1}, \end{aligned} \tag{4.2}$$

where E is a constant and $\gamma = 1.4$ is the ratio of specific heats at constant pressure and volume for air. The subsonic mean flow is determined by conditions of uniformity upstream, the constant E, and a constant axial mass flux. A numerical model for mean flow is based on a

finite-element discretization of the steady flow field equation. Second order and quadratic finite elements are used to perform this calculation. The mean flow solution is then interpolated on the acoustic mesh.

4.2 ACOUSTIC FIELD MODELING

Assuming a harmonic acoustic excitation on the form of $\tilde{\phi}(\mathbf{x},t) = \hat{\phi}(\mathbf{x})\exp\{(\mathrm{i}\omega t)\}$ and combining the Euler equations, $\hat{\phi}$ is found by solving the convected Helmholtz equation (Eq. (2.14)) in terms of the velocity potential. The FEM is based on a weak variational statement constructed by multiplying Eq. (2.14) by weight function $\delta\hat{\phi}$, and integrating over the acoustic domain Ξ_1 (see Figure 24):

$$\begin{aligned}\int_{\Xi_1}\rho\left[\nabla\hat{\phi}\cdot\nabla\delta\hat{\phi}-\left(\frac{\mathbf{u_0}}{c_0}\cdot\nabla\hat{\phi}\right)\left(\frac{\mathbf{u_0}}{c_0}\cdot\nabla\delta\hat{\phi}\right)\right]\,d\Xi_1\\ +i\omega\int_{\Xi_1}\frac{\rho}{c_0^2}\left[\nabla\hat{\phi}(\mathbf{u_0}\cdot\nabla\delta\hat{\phi})\right]\,d\Xi_1-\omega^2\int_{\Xi_1}\frac{\rho}{c_0^2}\hat{\phi}\delta\hat{\phi}\,d\Xi_1\\ =\int_{\Lambda}\delta\hat{\phi}\left[\rho_0\nabla\hat{\phi}-\frac{\rho}{c_0^2}(i\omega\hat{\phi}-\mathbf{u_0}\cdot\nabla\hat{\phi})\mathbf{u_0}\right],\end{aligned} \tag{4.3}$$

where $\Lambda=\Lambda_F\cup\Lambda_L\cup\Lambda_H$ is the bounding surface of the computational domain (e.g. the surfaces represented in Figure 24). The surface integral right hand side of Eq. (4.3) can be simplified because it is assumed that on Λ the mean flow is tangent to the boundary surface, so $\mathbf{u_0}\cdot\mathbf{n}=0$. In addition, for a hard wall boundary (Λ_H), both $\mathbf{u_0}\cdot\mathbf{n}$ and $\hat{\phi}\cdot\mathbf{n}$ are equal to zero (MCALPINE; WRIGHT, 2006). The right hand side of Eq. (4.3) is then zero. For a lined wall (Λ_L) however, only $\mathbf{u_0}\cdot\mathbf{n}$ is zero and any impedance boundary condition can be defined for $\hat{\phi}\cdot\mathbf{n}$. The surface integral Λ_L is then calculated by using the impedance boundary condition originally derived by Ingard-Myers (INGARD, 1959; MYERS, 1980) and implemented for FEM formulation by Eversman (2001) as

$$\mathrm{i}\omega\hat{u}=[\mathrm{i}\omega+\mathbf{u_0}\cdot\nabla-\mathbf{n}\cdot(\mathbf{n}\nabla\mathbf{u_0})]\left(\frac{\hat{p}}{Z}\right),\quad\text{on}\quad\Lambda_\mathrm{L}, \tag{4.4}$$

which is equivalent to Eq. (2.23). In general, the acoustic domain Ξ is divided into an inner and outer domain (MCALPINE; WRIGHT, 2006) (see Figure 24). Infinite elements[2] are used for the outer domain (Ξ_2), which is restricted to sound radiation analysis. The inner domain (Ξ_1)

[2] The infinite element method implemented in the ACTRAN is an extension of a variable order Legendre polynomial formulation whose numerical performances have been extensively studied in the past. Details about this domain formulation is discussed in Astley (2009) and Astley, Sugimoto, and Mustafi (2011).

is required for the propagation simulation, where the source and/or exit planes (i.e., Λ_F) of the ductare defined and, $\hat{\phi} \cdot \mathbf{n}$ is prescribed in terms of duct modes.

The conventional Galerkin FEM is used to discretize the acoustic domain, which is divided into a number of sub-domains called finite elements (and nodes are defined at the element vertices). Therefore, Equation 4.4 is calculated at each node and a summation of the volume and surface integrals is performed for each element in the entire domain Ξ_1. The solution for velocity potential $\hat{\phi}$ within the entire computational domain can be expressed as

$$\hat{\phi}(\mathbf{x}) = \sum_{j=1}^{J} \hat{\phi}_j N_j(\mathbf{x}), \tag{4.5}$$

where J is the total number of nodes, N is a vector containing the global interpolation functions (or shape functions), and N_j and ϕ_j are the local shape function and velocity potential. More details of the FE procedure are discussed by McAlpine and Wright and Antwerpen et al. (2008) and can also be found in the ACTRAN user manual (ACTRAN/TM, 2016).

4.3 MESH REQUIREMENTS

The mesh density is governed by the demands of the acoustic problem and is substantially more refined than the one required for the mean flow analysis for the frequencies of interest. The acoustic mesh is then locally refined in order to correctly catch the local wavelength as

$$\lambda = \frac{2\pi(1-M)}{k\left(\sqrt{1-\frac{\gamma-1}{2}M^2}-M\right)}, \tag{4.6}$$

for plane waves, which can be usually simplified to

$$\lambda = \frac{2\pi(1-M)}{k}, \tag{4.7}$$

and the element size $\mathcal{H}$ needs to be at least

$$\mathcal{H} \leq \frac{\lambda}{\text{PPW}}, \tag{4.8}$$

where PPW is points (or nodes) per wavelength, which has been defined by many authors and summarized as follows. Ozyoruk, Alpman, et al. (2004) and Ozyoruk and Long (1996) has shown that a structured mesh grid resolution of 12 to 15 PPW gave results without significant dispersion and dissipation for modal radiation from nacelles. McAlpine and Wright (2006) defined that the axial resolution of 10 PPW is sufficient for an unstructured mesh of in-duct model

with spliced liner. From a convergence analysis, Gabard and Astley (2008) assessed the accuracy of the in-duct model for a positive mode and a negative mode (i.e. negative azimuthal order) propagation, where a mesh resolution of 17.4 PPW to 22 PPW showed good results. For the unflanged duct case, Chen et al. (2004) has shown that a minimum 7 PPW can be used for the majority of the propagation area, but around the duct edge a high resolution of PPW > 15 should be adopted. Moreover, the convective effect on the λ implies that locally higher velocity areas need to be refined. For high order modes, it is necessary to take into account the cut-on mode with maximum radial order to determine the local wavelength, i.e., (ACTRAN/TM, 2016)

$$\lambda = \frac{2\pi(1-M)}{k\, n_c}. \tag{4.9}$$

The mesh refinement needs to take into account the fact that mode shapes of higher order modes are more complex and less accurately resolved in FE meshes with poor resolution. On the other hand, Gabard and Astley (2008) observed that with structured meshes the numerical error can vary significantly from one mode to the next. This is due to the fact that for some modes the azimuthal symmetry of the mesh matches that of the mode, and this effect is less pronounced with unstructured meshes.

4.4 TEST CASES – COMPARISON WITH SPECIALIZED FE SOFTWARE

A model-scale problem is used to simulate realistic subsonic fan operating conditions. The aim being to preserve most of the physics of the full-scale problem. The engine nacelle geometry was inspired in the Advanced Ducted Propulsor (ADP) fan rig developed by NASA and Pratt and Whitney, which has similar dimensions to the original test rig. In order to assess different physical behavior through the FE models, the numerical models of this nacelle are separated in terms of the in-duct field and near-field/far-field modeling.

The scattering and transmission of sound in the lined nacelle inlet duct are modeled using two inlet duct geometries shown in Fig. 25. Note that the straight duct model (Fig. 25.(a)) is equivalent to the analytical approach considered in this work, which is based on the mode matching scheme. The second model (Fig. 25.(b)) has more realistic characteristics considering the regions of non-uniform duct geometry, such as the section variation and spinner. Moreover, the sound radiation effects of inlet duct are considered in the entire domain (near-field) and surround the nacelle exit plane as shown in Fig. 26. In such cases, flanged duct, no-flange duct and unflanged duct models (Fig. 26.(a)-(c)) are equivalent to analytical radiation models

Figure 25 – Representation of the FE models of the in-duct domain: (a) straight duct and (b) real nacelle.

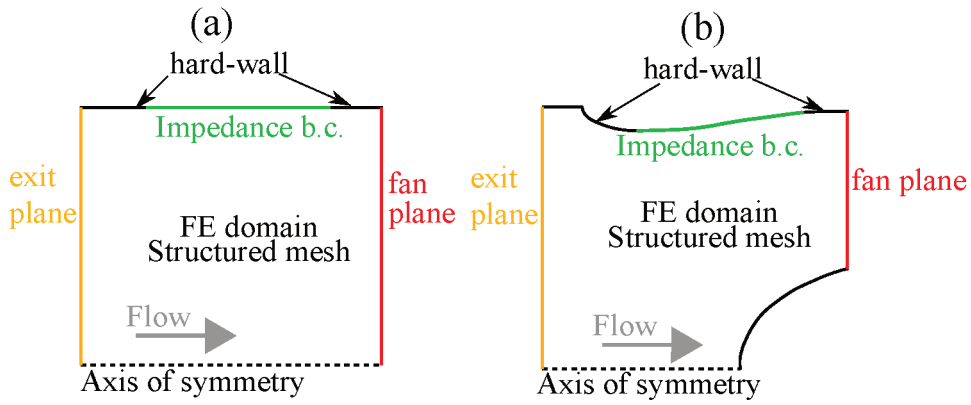

Source – Own authorship.

Figure 26 – Representation of the FE models of the near-field close to inlet duct: (a) flanged duct, (b) no-flanged duct, (c) unflanged duct and (d) real nacelle.

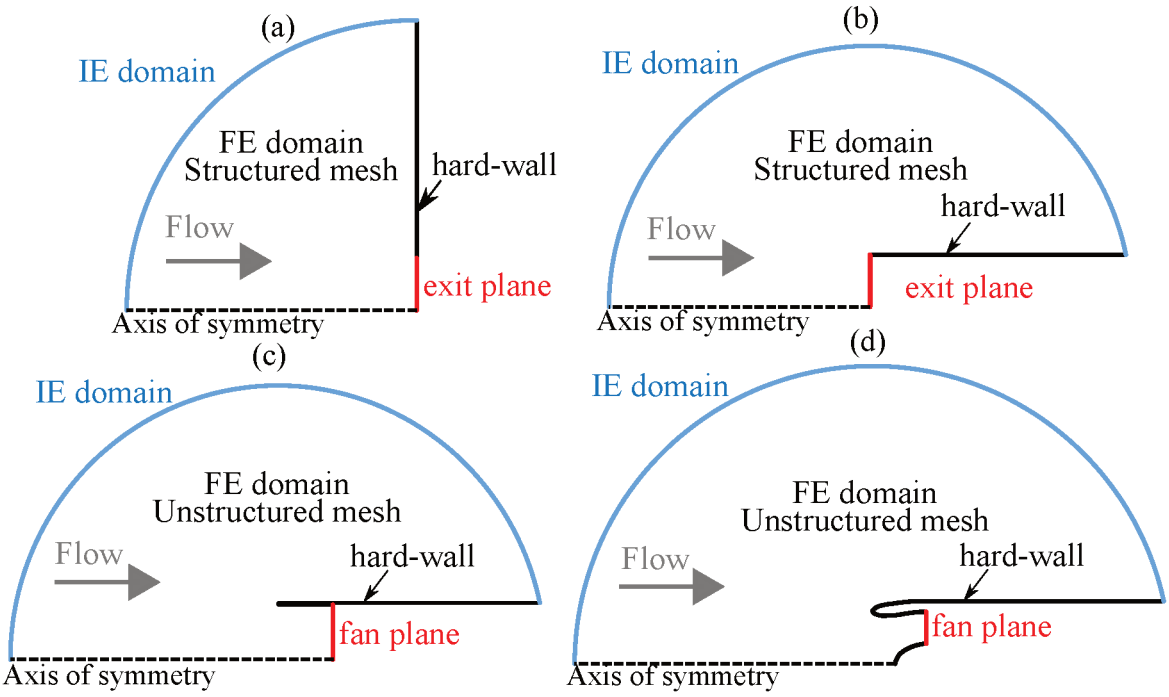

Source – Own authorship.

such as Rayleigh, Kirchhoff, and Wiener-Hopf–based methods, respectively. The values of the parameters used in these analyses are the duct length $L^* + 2l^* = 0{,}29\,\mathrm{m}$, the outer radius $a^*_{\mathrm{out}} = 0{,}28\,\mathrm{m}$ and inner radius $a^*_{\mathrm{in}} = 0{,}11\,\mathrm{m}$ at fan plane and the liner length $L^* = 0{,}18\,\mathrm{m}$. For the radiation models, the sideline angles were limited to an arc from $0°$ to $90°$ and a distance from the duct of $5\,\mathrm{m}$ (approximately $D = 18a$), which is defined in Section 4.5.2. All cases are assumed as two-dimensional axisymmetric models.

Table 2 – Operational parameters considered in this study.

Fan operating condition parameters	
azimuthal order, m	0, 4 , 8, 12, 16, 20, 24
Frequency, f^*	5422.8 Hz
Wavenumber, k	28
Mach number, M	0.4
Liner impedance, Z	2-1i

Source – Own authorship.

The in-duct acoustic field is obtained for each incident mode applied at the fan plane (or exit plane depending on the model) at a given frequency. On the fan and exit planes, the natural boundary conditions can be used to introduce the noise source and non-reflecting boundary conditions. Therefore, the numerical model consists of three main boundary conditions: modal basis, impedance, and non-reflection. Outside the duct, the acoustic field is radiated for each transmitted mode that is propagating at the near-field region to IE/FE interface and then propagates on the external region model using infinite elements, at the far-field region, which works naturally as a non-reflecting boundary condition. And the numerical model consists of two main boundary conditions: modal basis and non-reflection (generated artificially by IE domain).

The number of quadratic elements in the radial direction is decided in such a way that the elements are square-shaped at the fan plane. A mesh resolution of 18 PPW is used to discretize the FE domain (based on the review in section 4.3). Moreover, depending on the model, the structured mesh is preferred instead of an unstructured one based on the ease of construction of the mesh grid.

The parametric verification analysis was performed considering the boundary effects of each model on the modal propagation and radiation. Table 2 lists the details of the operating condition used in this analysis. Note that the test cases were defined with fixed liner length and impedance, the radius of the duct, Mach number and the wavenumber. Only the first radial order of the propagating modes will be considered, which has cut-off ratio $\eta_{m,n}$ ranging from 1.15 to 5.75 (or cut-off parameter $\xi_{m,n}$ varying from 0.03 to 0.74). In view of the symmetry, only positive values of m and $\alpha_{m,n}$ are to be considered here.

As variations of the circumferential mode number m yield the biggest effect, these parameters are varied as indicated, and the values are chosen such that they are representative of aircraft engines. Therefore, the results from the different radial eigenvalue or cut-off ratio are compared regarding each FE model in terms of in-duct propagation and free field radiation.

This will allow capturing the modal effects, in term of modal scattering, sound transmission and reflection and directivity patterns, comparing each FE model with analytical approaches. On the other hand, the acoustic impedance would always vary with frequency, it was restricted to two wall impedances ($Z = \infty$ for hard-wall, and $Z = 2 - 1\mathrm{i}$ for lined duct). Other values have been experimented but they did not seem to produce essentially different conclusions. Similarly, it has been considered, only, a mean flow of Mach number 0.4. The issues about a parametric study in terms of Mach number (and without flow), impedance and frequency was extensively discussed in the past by several authors such as Rienstra and Eversman (2001) and Ovenden, Eversman, and Rienstra (2004).

4.5 RESULTS

4.5.1 In-duct acoustic field

The test cases used in this verification assume a cylindrical duct composed of three segments as presented in Section 4.4. For a real nacelle case, the fan plane is annular due to spinner presence, and the modes have an eigenvalue solution quite different than that of the cylindrical duct, which is more critical for low order modes and higher radius ratio $a_{\text{in}}/a_{\text{out}}$. To evaluate this effect on the FE prediction, an additional model without spinner was examined.

The analytical methods used in this work have been converged and verified as follows: (1) The uniform flow eigenvalue solver using the methodology presented in section 3.2 is converged for a high number of points on the radius (see Appendix B.1); (2) The uniform flow mode-matching solver is validated by comparison with the FE commercial code. In the next section, a mode matching convergence is analyzed and the number of cut-off modes necessary for a better relationship between computational fidelity and cost is defined. For the analysis proposed in this section 50 modes are included in the mode matching schemes.

First, the mode matching schemes are used to predict the transmission loss (i.e. the acoustic power absorbed and reflected by the liner), which is generally the quantity of practical interest for liners design. For each incident mode assumed at the fan plane, Figure 27(a) shows the transmission loss given by the analytical solutions (dash lines) and by the FE models (solid lines). As expected, the real nacelle FE model has a deviation on the order of $20\,\mathrm{dB}$ for higher modes, while the nacelle without spinner FE model is closer to a straight duct model, which means that the reflections provided by the section variation have slight influence on the transmission loss (see Fig. 27(b)). The greater discrepancies observed between analytical models and

nacelle FE model for higher order modes can be understood as a consequence of the eigenvalue solution for annular duct (at fan plane) and the higher gradients in the mean flow velocity along the nacelle, which have effective lower Mach numbers than the other numerical and analytical models. Nevertheless, the mode matching with two matching conditions have a reasonable agreement with numerical models. The difference between the straight duct FE model and the M-M matching scheme (black lines) yields good results with an error below half a decibel for all the modes, and the P-V matching condition (red lines) exhibit relatively higher error around $4\,\mathrm{dB}$, especially for the higher order modes.

The liner attenuation is also clearly illustrated by comparing the pressure amplitude along the duct wall as shown in Figure 28. Note that the interfaces between the liner and hard-wall segments are located approximately at $x/L_{\text{total}} = 0.18$ and 0.84. In terms of acoustic field, it has been observed that agreement between mode matching schemes increase with azimuthal order (see Fig. 28(a-e)), which can be explained due to pressure distribution of the mode strongly concentrated close to the wall, and the spinner's reflections having less influence. The reflected and transmitted modes have a complex behavior (and it depends on the cut-off ratio and number of cut-on modes), which have, in general, greater deviations in the second and third segments. Moreover, the gradient of mean flow close to the wall produces variations on the convective effect, such that it strongly influences the acoustic field. The same issue with the nacelle FE model is observed here (see Fig. 28(f)), where the higher order mode ($m = 24$) has a strong attenuation. Again, it is observed that there is a higher variation in the pressure at the wall, which is better captured by the M-M matching scheme, especially in the vicinity of the interfaces (i.e. where the impedance discontinuity at the wall induces a singular pressure field).

Generically speaking, one can summarize the possible modeling discrepancies between FEM and mode matching with different matching schemes as following:

1. The geometry plays an important role. The transmission loss does not only depend on the acoustic impedance (strictly speaking in dissipation), but the net reduction may benefit from reflections at discontinuities in the duct (hard/soft walls and varying cross-section).

2. The modal scattering provided by the varying cross section depends on the local cut-off ratio (i.e. due Mach number gradient), and consequently on the number of the cut-on modes. Moreover, it may be more important since an attenuated mode does not produce a significant reflection (RIENSTRA; EVERSMAN, 2001).

Figure 27 – Predicted sound power transmission loss:(a) for each FE model (—) and analytical solution with the matching of P-V and the matching of M-M (− − −).(b) Absolute error on the transmission loss between mode matching solutions (red lines: matching of P-V and black lines: matching of M-M) and nacelle FE solution (solid lines) and straight duct FE solution (dash lines).

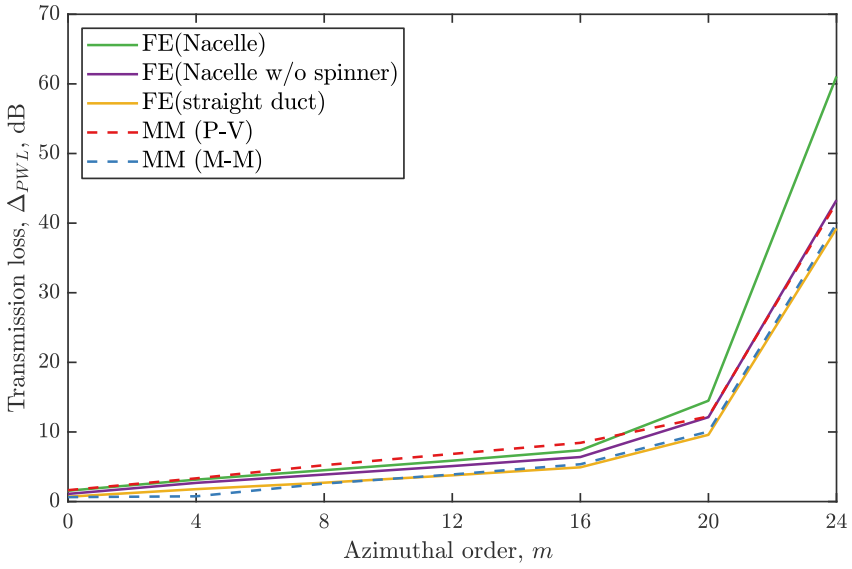

(a)

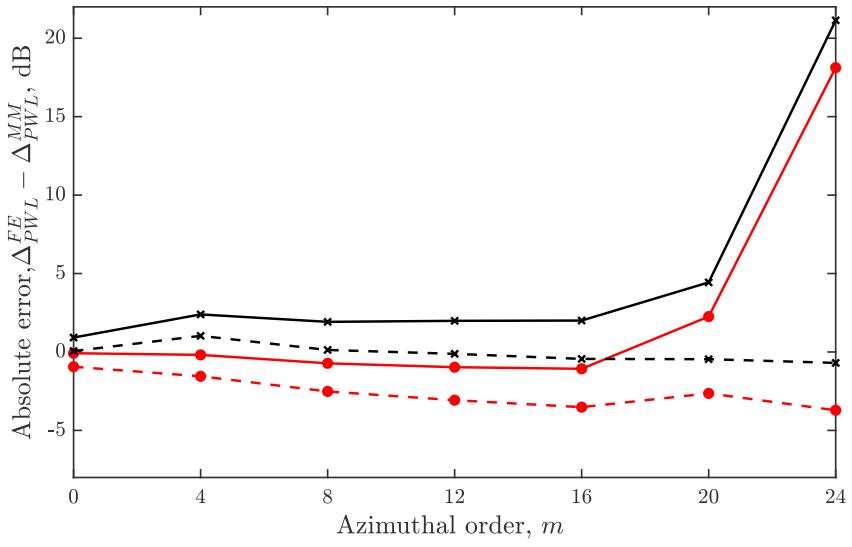

(b)

Source – Own authorship.

Figure 28 – Sound pressure level at the duct wall ($r = a$) with the uniform flow for different azimuthal order. Comparison of the analytical solution with the matching of P-V and matching of M-M ($- - -$) and FE solutions (—).

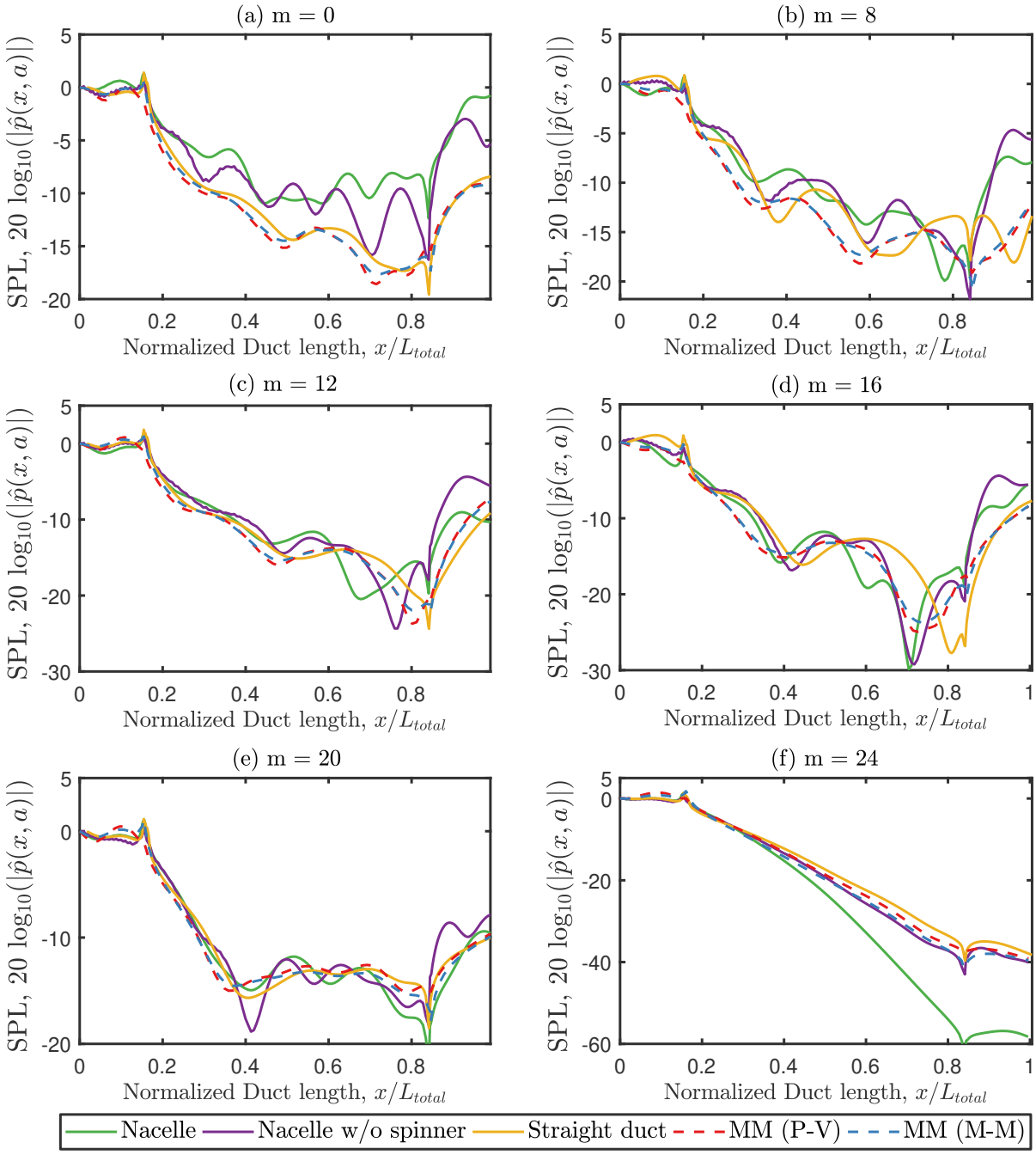

Source – Own authorship.

Figure 29 – Contour of the in-duct mean flow velocity (u_0^*) calculated from FE models: (a) Nacelle without spinner and (b) Entire nacelle.

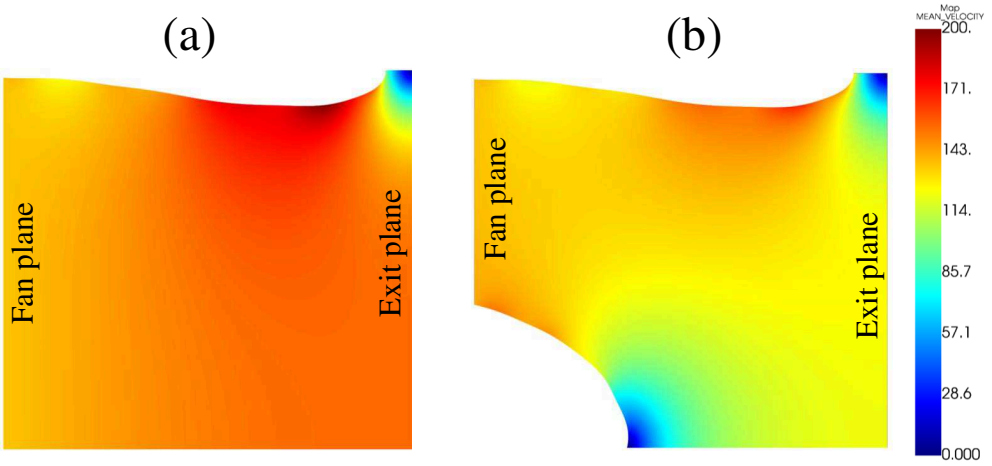

Source – Own authorship.

3. The annular duct may be important in some cases (for nacelle FE model). It yields an eigenvalue solution quite different than cylindrical ducts, especially for low order modes (see Figs. 28(a) and 28(b)).

4. In regions with a high variation on the mean flow, especially in the nacelle FE case, the propagating modes have an effective cut-off ratio smaller than the cut-off ratio used in the analytical approach and the straight duct FE model, what affects the liner attenuation (see Figure 29). In addition, the axial variation of the mean flow near the outer radius modify significantly the behavior of the modal absorption rate along the duct.

In order to illustrate some of these issues, the contours of the pressure field (Re($\hat{p}$)) obtained numerically and analytically are shown in Figures 30 and 31, respectively. The low order modes are represented by mode (0,1) (plane wave) and the high order by mode (20,1). Note that the phase of waves propagating in Fig. 31 are shifted in approximately π regarding the results in the Fig. 30. For the cases of the high order mode (see Fig. 30 (b)(d)(f) and Fig. 30(c)(d)) the agreement of pressure contours is reasonably good, where these cases share the characteristic of high attenuation and wave propagation. Even in the nacelle FE model, the acoustic field is slightly affected. In the plane wave cases (Figs. 30 (a)(c)(e) and 30(a)(b)) almost no attenuation is given for either the mode matching or FEM results. As noted previously, the presence of the spinner produces the noticeable change in the acoustic field. Further modified mean flow field (see Figure 29), a considerable number of scattered cut-on modes play a role in this case. Some

Figure 30 – In-duct pressure field calculated from mode matching scheme with matching condition of P-V (a,c) and M-M (b,d) for azimuthal orders $m = 0$ (a,b) and $m = 20$ (c,d).

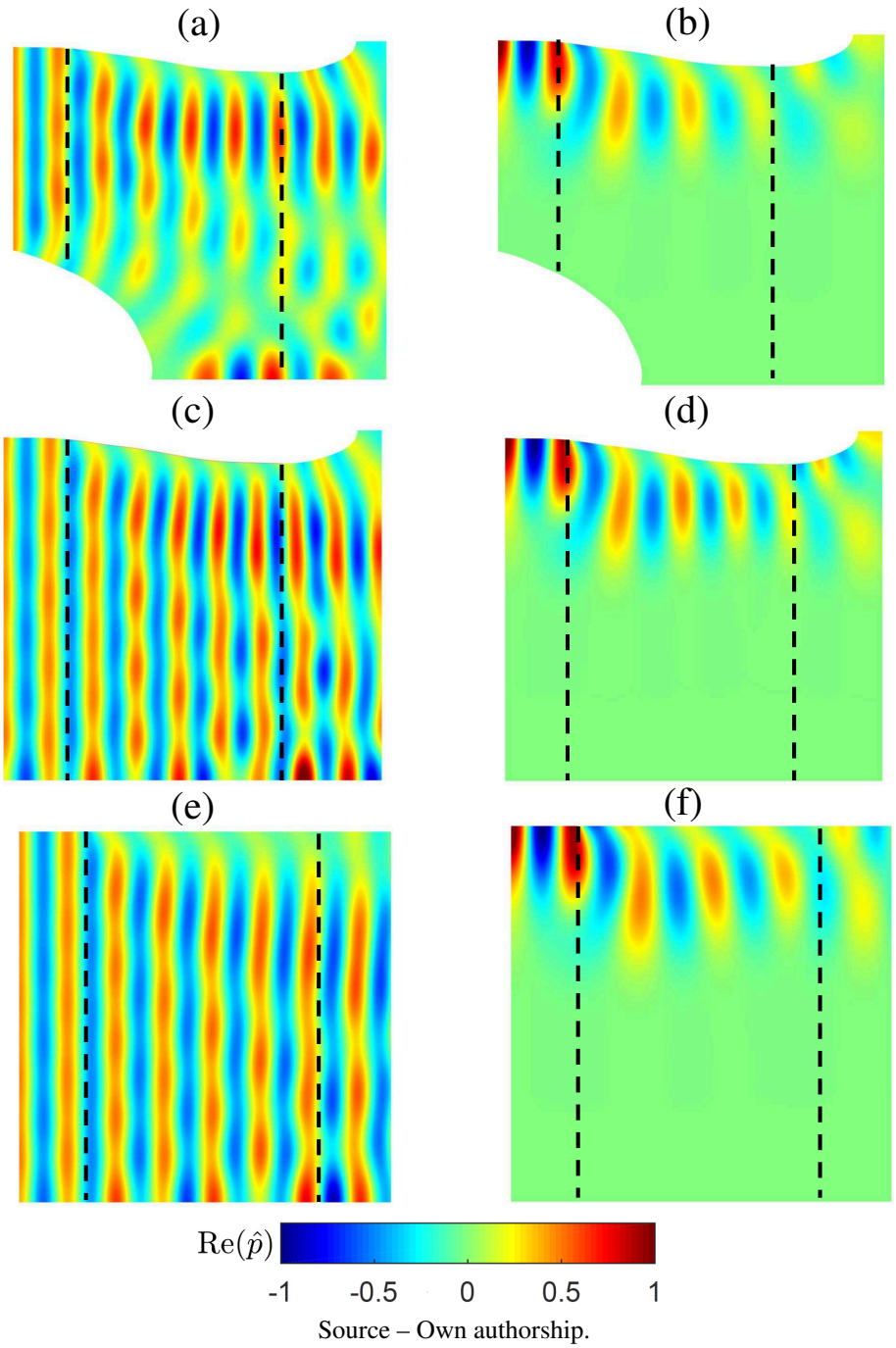

Source – Own authorship.

discrepancies are visible in the other FE and mode matching solutions, where the average trend, however, does not seem affected.

The general information about the cases studied in this section in terms of the sound power transmission loss (defined in Appendix A) and reflection[3] afforded by liner impedance is

[3] The sound power reflection has a similar definition regarding the sound power transmission loss in the Eq. (A.9).

Figure 31 – Contour of the in-duct pressure field calculated from FE models for azimuthal orders $m = 0$ (a,c,e) and $m = 20$ (b,d,f): Nacelle (a,b), Nacelle without spinner (c,d) and straight duct (e,f).

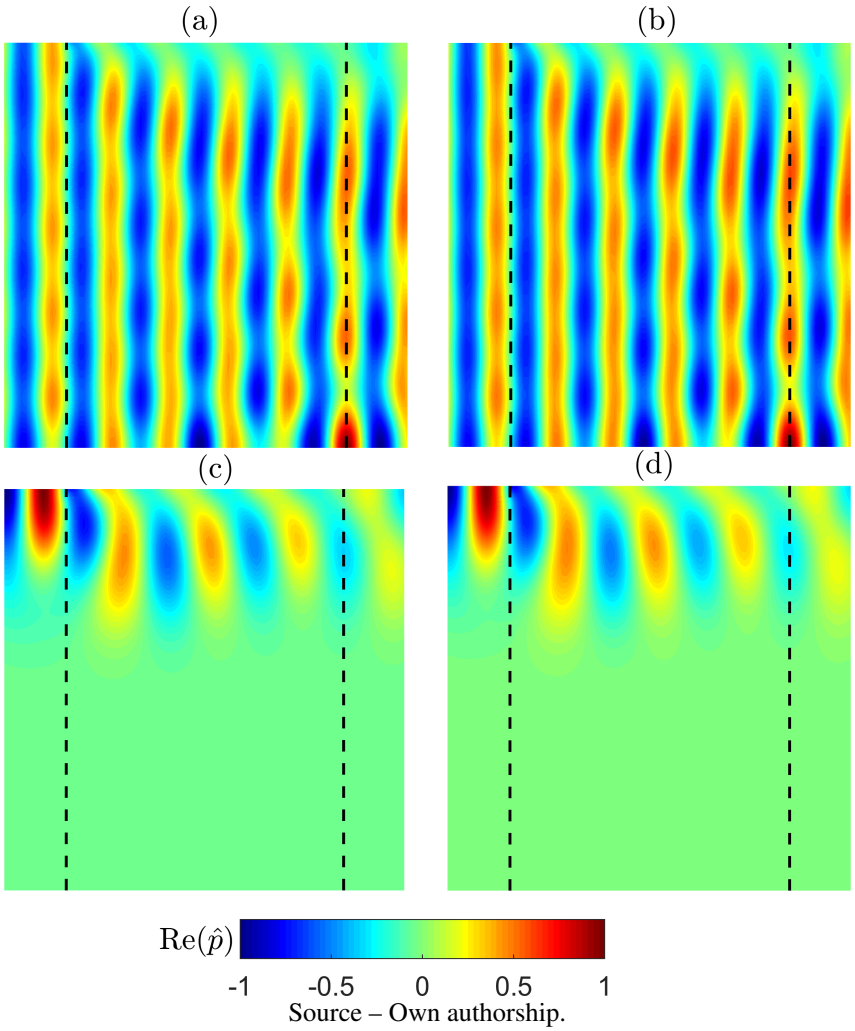

Source – Own authorship.

given in Table 3. In addition, Table 3 gives the number of hard-wall cut-on modes at the source plane and the cut-off ratio of the respective incident mode[4]. Note that important features such as (1) interference of incident and reflected modes (associated with the cut-off ratio and the number of cut-on modes) creates the bumps in absolute pressure implying a complex behaviour on the propagating wave; (2) the sound power reflection for high frequency follows the opposite behaviour of the transmission loss.

However, it is calculated for opposite direction and considering the sign "−" in the Eq. (A.4).

[4] Note that the number cut-on modes at the source plane and the cut-off ratio for annular duct is quite different.

Table 3 – Summary of observed attenuation and reflection provided by liner impedance, including the number of hard-wall cut-on modes (n_c) and the cut-off ratio ($\eta_{m,n}$) of the incident mode.

m	**Sound power transmission loss (dB)\reflection (dB)**					n_c	$\eta_{m,n}$
	FE, Nacelle	**FE, w/o spinner**	**FE, straight duct**	**MM, P-V**	**MM, M-M**		
0	1.6 \21.9	1.1 \22.4	0.7 \29.6	1.6 \30.1	0.6\26.6	10	∞
4	3.2 \23.0	2.7 \21.6	1.8 \26.5	3.3 \24.1	0.8 \25.5	8	5.8
8	4.5 \19.5	3.9 \20.5	2.7 \26.7	5.3 \22.6	2.6 \23.5	6	3.2
12	5.9 \19.5	5.1 \19.6	3.8 \21.3	6.8 \21.4	3.9 \22.3	5	2.2
16	7.4 \17.4	6.4 \18.9	4.9 \18.9	8.4 \20.4	5.4 \21.4	3	1.7
20	14.5 \18.6	12.1 \21.7	9.6 \20.9	12.2 \18.8	10.1 \19.8	2	1.4
24	61.0 \17.5	43.3 \18.7	39.2\19.1	42.9 \18.5	39.9 \18.1	1	1.15

Source – Own authorship.

4.5.2 Duct external acoustic field

The problem of the free field sound radiation has its own important features, especially in the presence of mean flow. For the sake of brevity, the same velocity is taken throughout the free-field for the analytical radiation models. In Section 6.1, the effect of flow mismatch in terms far-field solution is carried out. In addition, possible reflections of incident acoustic waves on the duct exit are neglected.

An important issue about the acoustic field outside the duct is the definition of near-field and far-field for high order modes. In the general acoustics, once in the far-field, the pressure and acoustic velocity must be in phase, and wave-fronts are nearly parallel, which extend outward to infinity. For each doubling of distance away from the source, the sound pressure will drop $6\,\mathrm{dB}$ in the far field (PIERCE, 1989).

Both regions were formulated analytically in the Section 3.3 considering Rayleigh and Kirchhoff integrals, which can be useful for a first analysis of the acoustic pressure in the far-field and near-field regions. Figure 32(a) shows a comparison of the Sound Pressure Level at a single position (φ, θ), $k = 28$ and $M = 0.4$ between near-field and far-field solutions for varying distance. Kirchhoff exact and approximation integral solutions were used on this analysis. The low order modes are represented by mode (0,1) (plane wave) and the high order by mode (20,1). At the mentioned conditions, it can be observed that the low order mode needs a greater distance to be in the far-field region, which can be used to establish this region for all other modes. As defined previously in Section 4.4, a distance greater than or equal to $18a$ seems sufficient. Figure 32(b) is a comparison of directivity patterns between the near-field solution

of Eq. (3.23) and the far-field solution of Eq. (3.25) for mode (0,1). Note that the directivity solution is symmetrical for both formulations.

In order to analyze the agreement of the radiation models formulated for the far-field region in Section 3.3, this section is focused on the modeling of the radiation from an open-ended waveguide. Again these analytical approaches are compared with FE models. The ability to compute the far-field sound radiation for higher values of m might be of importance in cases where coupling occurs between modes with different azimuthal dependence (i.e. multi-modal analysis). The parametric study has been undertaken with the same characteristics presented in Section 4.5.1 and follows the four FE models presented in Figure 26.

Figure 33 presents the results of these FE models and analytical approaches in terms of the far-field sound radiation directivity for each mode. This shows the normalized sound pressure level in the forward arc (0 to $90°$). A unitary amplitude is assumed for each incident mode at the fan plane. The radiation models based on Rayleigh, Kirchhoff, and Wiener-Hopf are represented directly by flanged, no-flanged and unflanged FE models (also called here as representative FE models), respectively. In this sense, a quantitative and qualitative agreement is naturally expected between these analytical and numerical methods. On the worst case at $\theta^{\wedge}_{m,n}$, the absolute deviation is around $5{,}1\,\mathrm{dB}$ between the flanged duct solutions, $1\,\mathrm{dB}$ for no-flanged duct solutions and $2{,}5\,\mathrm{dB}$ for unflanged duct solutions. It has been observed that these deviations at the main lobe angle vary slightly when all modes are considered. One can expect the higher deviation found between flanged analytical and numerical models, which may be understood as a first-order approximation on the Rayleigh integral (assuming $a << D$ as a simplification of the general formulation (TYLER; SOFRIN, 1962)).

The analytical and representative FE models follow reasonably the general trend of the real nacelle FE model in the case of very high order modes. The mentioned trend due to the lip influence seems to be still observed, but careful attention must be paid to the inherent error committed in the vicinity of the lip and close to the sideline angles ($\theta > 70\,\mathrm{degree}$) (LIDOINE et al., 2001). With accelerating Mach number on the wall, strong discontinuities in the velocity field have to be considered in addition to the scattering effects (also observed on the previous Section). Therefore, in the cases with high Mach number, these characteristics may be important in the prediction. However, such effect of flow in the vicinity of the lip are outside the scope of this work.

The absolute error between the analytical approach and its numerical representation is shown in Figure 34. The differences between the representative FE models and the respective

Figure 32 – Comparison between Kirchhoff integral solution for azimuthal orders $m = 0$ (red lines) and $m = 20$ (blue lines): Exact (dash-dotted line) and approximation (solid line) solution.

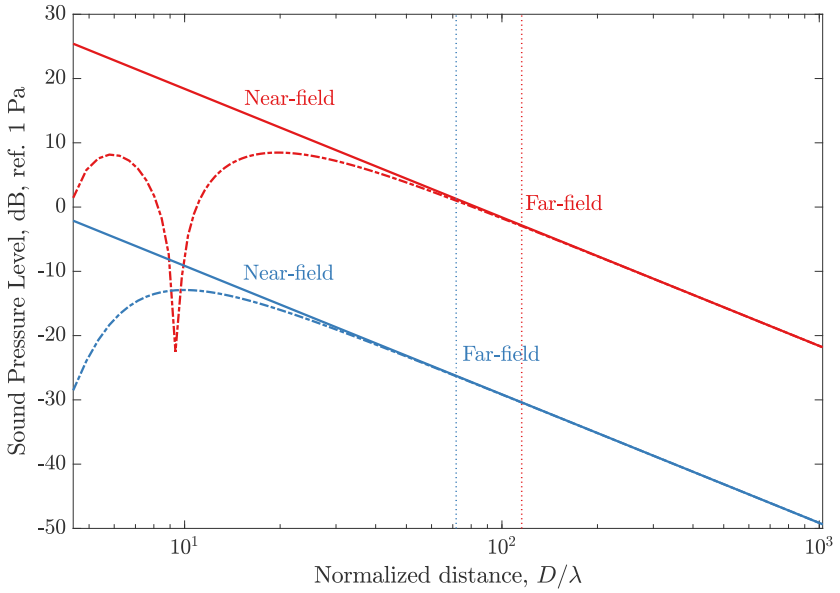

(a) SPL variation at one position on (φ, θ) with dimensionless distance.

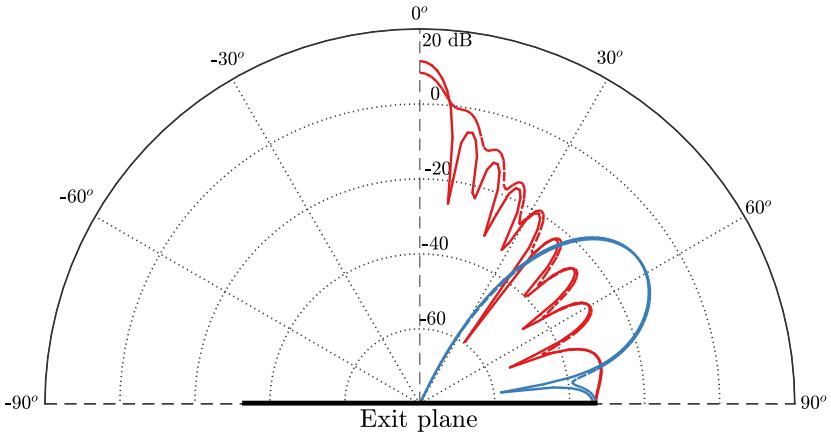

(b) Directivity function of each mode.

Source – Own authorship.

Figure 33 – Predicted far-field directivity pattern in terms of sound pressure level for several modes radiated from a cylindrical duct. Comparison of the analytical solution based on integrals approximation (– – –) and FE solutions (—).

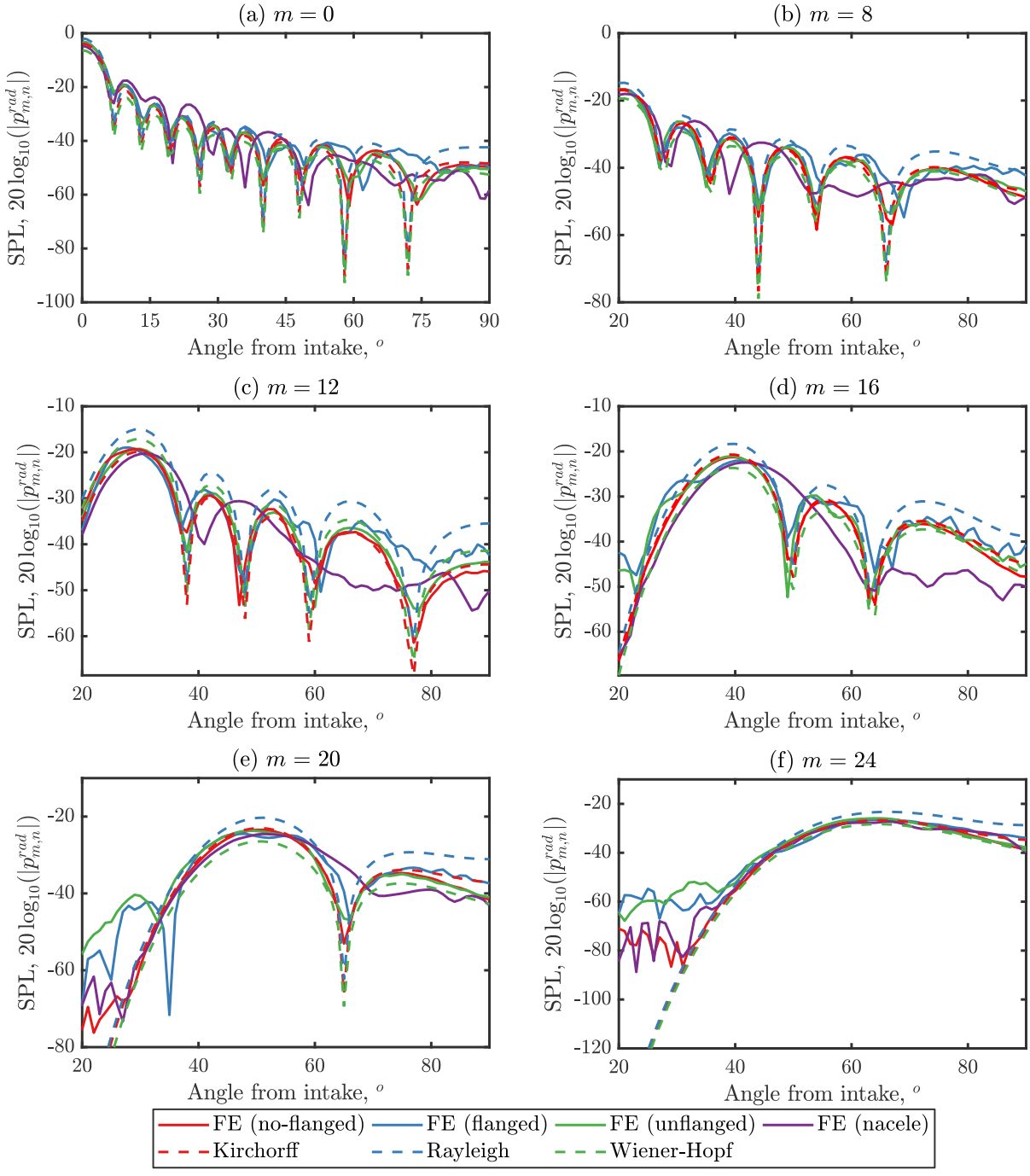

Source – Own authorship.

Figure 34 – Absolute error of the predicted far-field SPL between the analytical approach and its numerical representation: Flanged duct (blue), no-flanged (red) and unflanged (green). The main lobe is highlighted by a dash line.

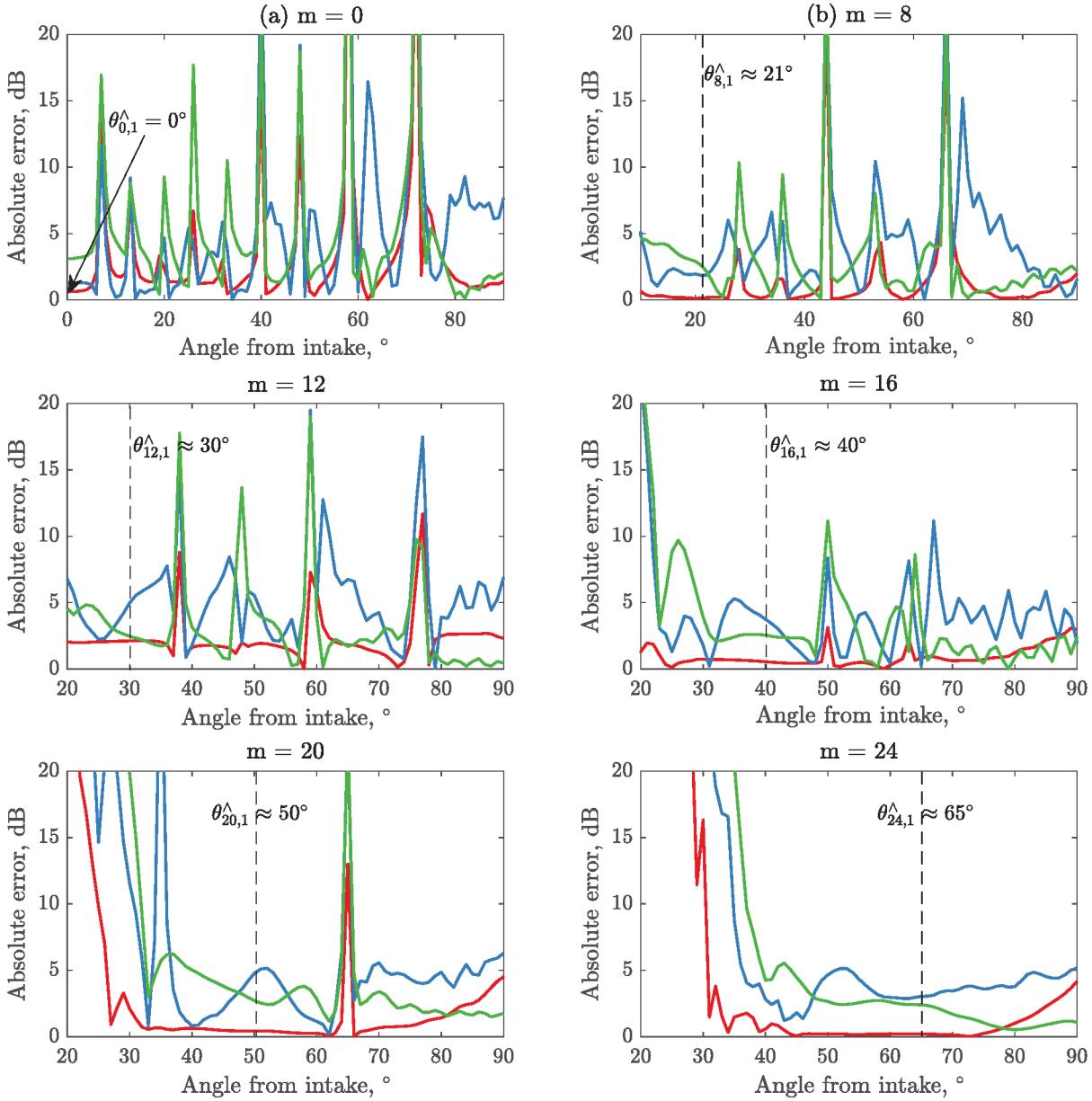

Source – Own authorship.

analytical model yield reasonable results with an error remaining below some decibels for the region near the main lobe, and for regions near the angles of the radiation nulls it exhibits relatively higher error greater than 15 dB, especially for cases of high cut-off ratio (i.e. cases with great number of the cut-on modes). Therefore, it is observed that the local pressure minima $\theta^{\vee}_{,n_c}$ are found instead of pressure-nulls and they are proportional to the number of the cut-on modes.

In term of the main lobe angle, all analytical and numerical approaches have a similar

Figure 35 – Main lobe angle as function of modal content (in-terms of the azimuthal order and cut-off ratio) for study condition considered here: $M = 0.4$ and $k = 28$.

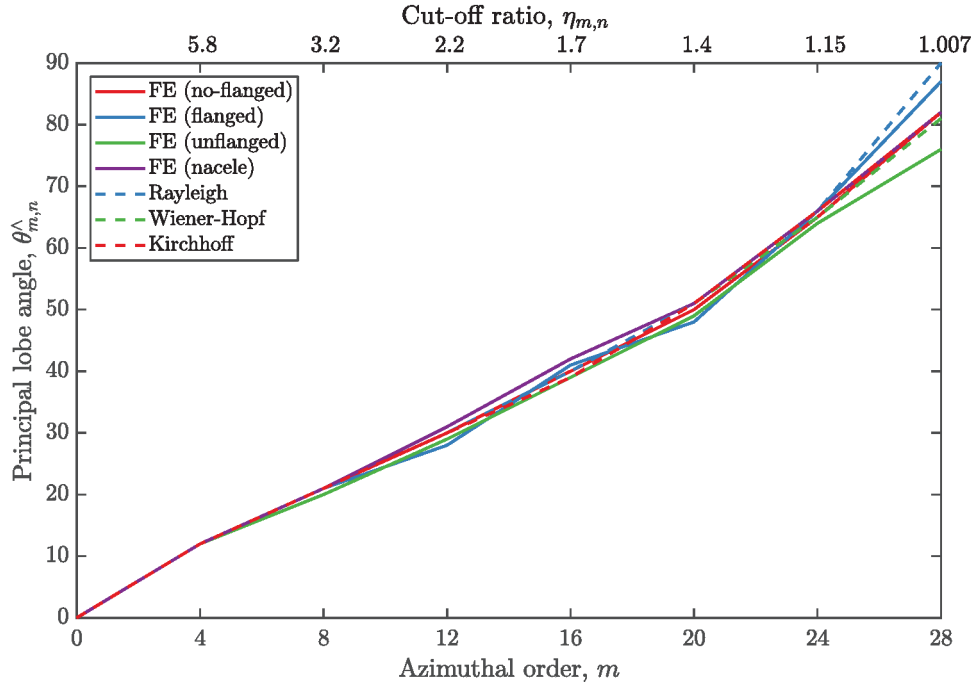

Source – Own authorship.

result. Even when all cut-on modes are used, this is the case as shown in Figure 35. This agreement could be expected here, since input modal base at a given frequency and free-field Mach number is the same, and the diffraction effects may be negligible. On the other hand, it is possible to observe the effect of the "infinite" baffle required by flanged models implies a deviation for modes radiating mainly above 70° (i.e. nearly cut-on modes). Moreover, the unflanged FE model overestimates the effects of the diffraction on the lip, and provide a small reduction these main lobe angles around 6° with relation to the real nacelle model when nearly cut-on modes are propagating.

Of particular relevance for the turbofan application, the reflection on the exit plane is usually neglected when the analytical approach is assumed (GABARD; ASTLEY, 2008; LEWY, 2003). In order to assess the real impact of this assumption, reflections on the exit plane were calculated by FE models in terms of the sound power, which is defined as $10\log_{10}(\mathcal{P}^{in}/\mathcal{P}^{rad})$. Figure 36 shows the key difference between the sound power reflection as a function of the all cut-on modes for real nacelle and straight duct FE models (selected for natural reasons). At high frequency, when nearly cut-off modes propagate ($\eta \approx 1$ and $\theta^{\wedge}_{m,n} \approx 90°$) is expected a higher reflection energy. This trend is easily observed for both FE models, which has low reflection energy for the most part of modal content and an exponential growth when it radiates near 90°

Figure 36 – Sound power reflection as function of modal content (same of Fig. 35) for real nacelle (black line) and straight duct (red line) FE model.

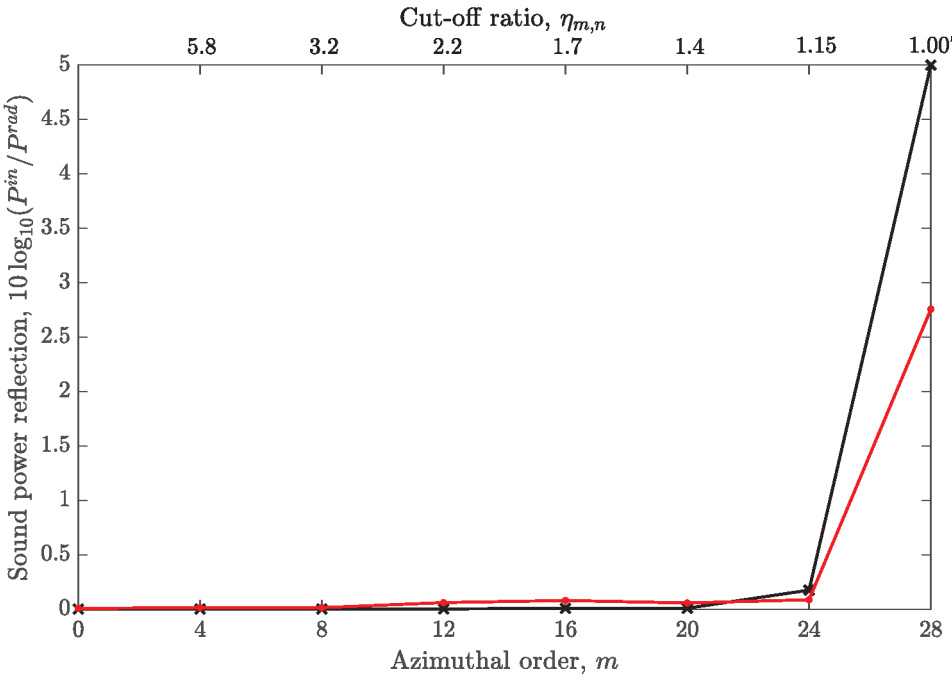

Source – Own authorship.

(see Figure 36). The numerical discrepancies between the FE models may be explained by the variation of the flow field next to the lips wall, which has higher Mach number values for the nacelle FE model.

Finally, the significant effects are caused by the presence of lip discontinuities and a mean flow lead to some numerical discrepancies between the analytical radiation model and FE modes, which may be mainly summarized as:

1. The lip geometry plays an important role. It is not investigated here, but on the main lobe of the directivity pattern, it is expected that SPL increases with increasing lip thickness, whereas sideline radiation decreases ($\approx 90°$) (LIDOINE et al., 2001). It is not happening here due to the reflections at the exit plane and on the in-duct section variation. At this point, this seems more important for modes near to the cut-off frequency of the duct.

2. Thickness and curvature of the inlet lip have a significant influence on the modal directivity patterns. In some studies using ray tracing method in nacelles (DOUGHERTY, 1996), it is observed that the mechanism of diffraction around inlet lip is different for curved (or nacelles) and discontinuous (or unflanged duct) lips and this scattered field vanishes at high frequencies.

3. Combined convection and relative frequency shift modify the modal directivity patterns. It has been observed that the presence of mean flow involves only problem convection effects on the frequency for analytical methods (i.e. based on a simple Prandtl-Glauert transformation that allows the problem to reformulate). The FE models without finite lips (flanged and no-flanged models) follow closely this simplification. But for the FE models with thick or finite lips, simulating a mean flow leads to a change of the physical modeling.

Another conclusion of this study is that the validity of the flanged, no-flanged and unflanged approaches follow closely to the real nacelle results, which depends on three significant factors: frequency (fixed and approximated of the typical engines operating conditions), modal content (typically high order modes are well cut-on and dominate) and mean flow (it involves an equivalent increase of the frequency which allows some cut-off modes to become cut-on).

In comparison with the representative FE models, the analytical method shows a good approximation for far-field directivity pattern, even when the reflection is neglected. However, in the vicinity of the cut-off frequencies, the analytical radiation models are affected by some discrepancies (i.e. reflection and diffraction issues may be important). Nevertheless, the methods may be able to describe reasonably well the behavior of a nearly cut-off mode.

5 EFFECTS OF THE SHEAR FLOW ON THE SOUND TRANSMISSION

This chapter explores the effect of the shear flow on the in-duct propagation considering liner discontinuities by using the mode matching scheme. The key point on this analysis is to understand the behavior of the liner impedance on the presence of the inviscid and homoentropic flow at different operating conditions. The effect of the boundary layer thickness over Brambley boundary condition is explored and compared with the Pridmore-Brown solution. Futhermore, a parametric impedance study is conducted to verify if the effects are also observed for other conditions.

5.1 FLOW PROFILE ALONG THE NACELLE

The particular case of the nacelle intake with the acoustic liner presence is considered here. From the modal approach, we assume that only the modes propagating against the flow from the fan plane are present. At real engine nacelles, the boundary layer is constantly changing (at some conditions, the section variation may retard or reset the boundary layer development), and it is usually assumed thinner at intake lip and thicker closer to the fan plane. Since the boundary layer thickness varies reasonably, this refraction effect is not constant along the in-duct propagation. In the present work, we focus on propagating modes within the subsonic sheared flow with particular emphasis on the role of lined walls.

The main issue about boundary layer thickness in the in-duct nacelles is related to the question: what is a representative value at a given operating condition? It is not a straightforward task to find the right answer to this question. The boundary layer growth within the nacelle can be affected in different ways: (1) by the angle of attack of the nacelle, (2) by turbulence ingestion, (3) by the turbulent boundary layer of the nacelle (and interaction of inflow with a perforated plate of the liner). Therefore, the real flow profile in nacelles and its boundary layer thickness are also relative to these variations. In the presence of a strongly inhomogeneous shear layer, such as a viscous boundary-layer near the wall, dissipative effects on the propagating wave are expected (VILENSKI; RIENSTRA, 2007). Therefore, a distinction must be made between the refractive effect of a laminar boundary layer and a turbulent boundary layer on acoustic propagation. The refractive effect of a turbulent boundary layer on the sound attenuation is out of scope in this work, which is discussed in details by Weng (2015) for hard-walled duct.

In reality, the mean flow gradients is caused by viscosity effects. For the aero-engine intake, these mechanisms are considered insignificant for the acoustic perturbations (BRAMBLEY, 2011). As assumed in Section 2.1.2.2, we considered a fully-developed shear flow with zero axial velocity component at the wall (no-slip condition). Here the boundary layer thickness δ is defined as the distance from the wall to the radial position, where the local velocity is equal to 99% of the free stream in-duct velocity M_0. Moreover, the boundary layer thickness δ is a percentage value of the total duct radius, with the rest of the mean flow being virtually uniform.

In order to analyze the boundary condition of the uniform flow compared to the others boundary conditions, a flow profile $M(r)$ describes by the Mach number in the duct, and it must be included in the mean flow. In this sense, some profiles have been used in previous studies to assess the impedance boundary conditions (NAYFEH; KAISER; SHAKER, 1974). In terms of liner attenuation analysis, it is desirable to have an analytic form of the velocity profile, which has a minimum impact on sound attenuation rate provided by the acoustic impedance, and its derivative to be infinite at the wall (i.e., $M'(1)$). For purposes of calculating attenuation rates, Nayfeh, Kaiser, and Shaker (1974) observed that the details of the flow profile has little effect on sound absorption, and, in general, it is sufficient to rely on parameters such as the displacement thickness and shape factor to characterize the boundary layer impact on the liner attenuation. This assumption is confirmed later by Gabard (2013, 2016) with different boundary conditions modeling. Also, he observed that since the same boundary layer thickness is used for all profiles, it can be seen that some differences are visible, especially in the upstream propagation.

The flow profiles such as the polynomial (MARX; AURÉGAN, 2013), parabolic (GABARD, 2013), linear (GABARD, 2016), sinusoidal (EVERSMAN, 1971) and hyperbolic tangent (tanh) (VILENSKI; RIENSTRA, 2007; BRAMBLEY, 2011) profiles have been used for calculating liner attenuation rates. For flow profile such as the $1/N$ power law, Eversman (1972) has been shown that its derivative is singular at the wall, and the numerical solution (in this case, Runge-Kutta procedure) of Pridmore-Brown equation can be affected in the wall vicinity. The only exception to this occurs if the walls are rigid, in which case the zero pressure derivative boundary condition eliminates the singular behavior if appropriate special care is used in the numerical procedure.

The boundary conditions implemented on the numerical solver studied in this work are able to handle an arbitrary flow profile, and the hyperbolic tangent profile has been selected due

to its infinite derivative at the wall, which is given by (VILENSKI; RIENSTRA, 2007)

$$M(r) = M_0 \Bigg\{ \tanh\left(\frac{1-r}{\delta}\right) + [1-r]\left[1-\tanh\left(\delta^{-1}\right)\right] \left[\frac{1+\tanh(\delta^{-1})}{\delta} r + (1+r)\right] \Bigg\}, \tag{5.1}$$

where $M(r)$ is practically constant in r except for a boundary layer of thickness δ. On the other hand, the boundary layer thickness δ is characterised by $M(1-\delta) \simeq 0.76 M_0$, and a displacement thickness (defined in Eq. 2.28) given by $\delta_1 \simeq \delta - \delta \ln[\cosh(1)] + \mathcal{O}(\delta^2) \simeq 0.56\delta + \mathcal{O}(\delta^2)$. Given that this flow profile is not very realistic, it should have little impact on the sound attenuation compared to other profiles (VILENSKI; RIENSTRA, 2007). As explained before, if one assumes the same boundary layer displacement thickness for any arbitrary flow profile, the results remain the same (GABARD, 2013). Moreover, at engine intake, the boundary layer thickness is constantly growing until the fan plane and, in general, δ values of less than 2% are expected (GABARD, 2016). The range of boundary layer profiles from 0.1% to 3% used in this chapter are shown in Fig. 37.

Figure 37 – Tanh flow profile for (a) different values of boundary layer thickness, and (b) detail at the boundary layer close to the wall.

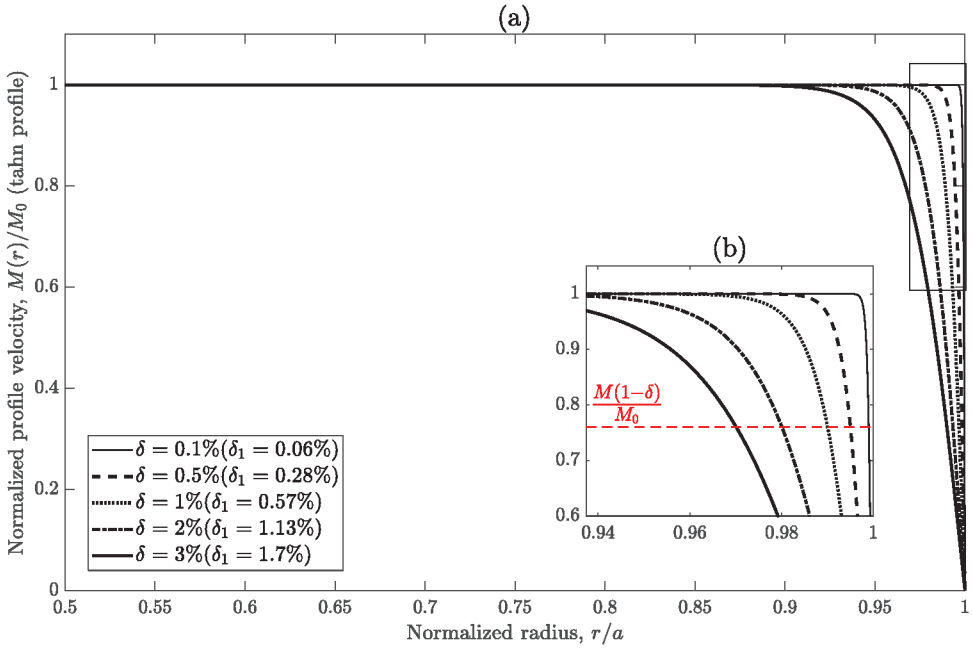

Source – Own authorship.

.

Table 4 – Typical turbofan engine operating conditions considered in this work.

Operating conditions	**Mach No,** M	**Wave-number,** k	**Azimuthal order,** m	**Cut-off ratio,** $\eta_{m,1}$	**Impedance,** Z
Sideline	0.5	31	24	1.36	3-0.5i
Cutback	0.4	26.6	24	1.1	2-1i
Approach	0.288	16.67	9	1.63	2-1i

Source – Own authorship based on the results of the McAlpine, Astley, et al. (2006) and McAlpine and Wright (2006).

5.2 APPLICATION TO INTAKE FAN NOISE - CASE STUDY

In order to better understand the impact of uniform and shear flows on the in-duct noise prediction, three different flight conditions were considered based on typical operating conditions (MCALPINE; ASTLEY, et al., 2006; MCALPINE; WRIGHT, 2006), which are shown in Table 4. For sideline and cutback conditions, we assume a supersonic fan tip speed, and therefore a dominant rotor-locked mode (see Section 2.2.4.2). For approach condition, a subsonic fan tip speed is assumed, such that the dominant azimuthal mode order is calculated by the Tyler-Sofrin rule (TYLER; SOFRIN, 1962), as described in Section 2.2.4.1. Notice that the cut-off ratio is close to 1, especially for cutback condition, indicating that the propagating mode is nearly cut-off. The impedance values presented in Table 4 have been chosen to be representative of a typical intake liner.

For the mode matching technique, typical dimensions of a turbofan engine and liner length are used in this work, and the geometric parameters are the same as those used by McAlpine, Astley, et al. (2006). In this case, following the coordinate system from Fig. 7, the duct radius is $a^* = 1\,\mathrm{m}$, the duct length is $L^*_{\text{total}} = L^* + 2l^* = 1{,}1\,\mathrm{m}$, and the lined length is $L^* = 0{,}8\,\mathrm{m}$. For the radiation model, the sideline angles were limited to an arc from $0°$ to $90°$ and a distance from the duct of $5\,\mathrm{m}$.

The flow profiles used in this work are based on the tanh profile, as given by Eq. (5.1), with δ varying from 0.1% to 2% for sideline and cutback conditions and from 0.5% to 3% for approach condition (see Fig. 37).

5.3 IN-DUCT RESULTS

In this section, we are concerned with the in-duct propagation, particularly the modal absorption rate along the duct, transmission loss, and scattering effects. The accuracy of the mode matching schemes used in this work was assessed in the previous chapter by using the

commercial finite element (FE) code ACTRAN/TM. Moreover, for the sideline operating condition, McAlpine, Astley, et al. (2006) and Braga, Cordioli, and Reis (2018) have shown that, without flow, the solutions considering the mode-matching method and FE exhibit excellent agreement. On the other hand, when the mean flow was included, the agreement was slightly affected, especially near the interfaces. Nevertheless, the transmission loss results were still in good agreement, with differences smaller than $1{,}8\,\mathrm{dB}$.

The same behavior is observed here in terms of SPL, as shown in Figure 38. In regions far from the liner discontinuities, the deviations on the results follow the same trend observed by other authors (GABARD; ASTLEY, 2008; GABARD, 2010; BROOKS; MCALPINE, 2007), with a relative error of less than $2{,}5\,\mathrm{dB}$ for cutback and $1\,\mathrm{dB}$ for other conditions. Also, the error in transmission loss remains smaller than $2{,}5\,\mathrm{dB}$ for all cases considered. In this validation and for all conditions 30 cut-off modes were included and the matching condition of P-V on the mode matching solutions was considered. Since there no significant deviation between the matching condition of P-V and M-M was observed in Chapter 4 for high order modes, for simplicity, the matching condition of P-V was preferred here.

Figure 38 – Acoustic pressure at the duct wall with uniform flow: approach (green), cutback (red) and sideline (blue) conditions. Mode matching ($\cdots$) and FE (—) solutions.

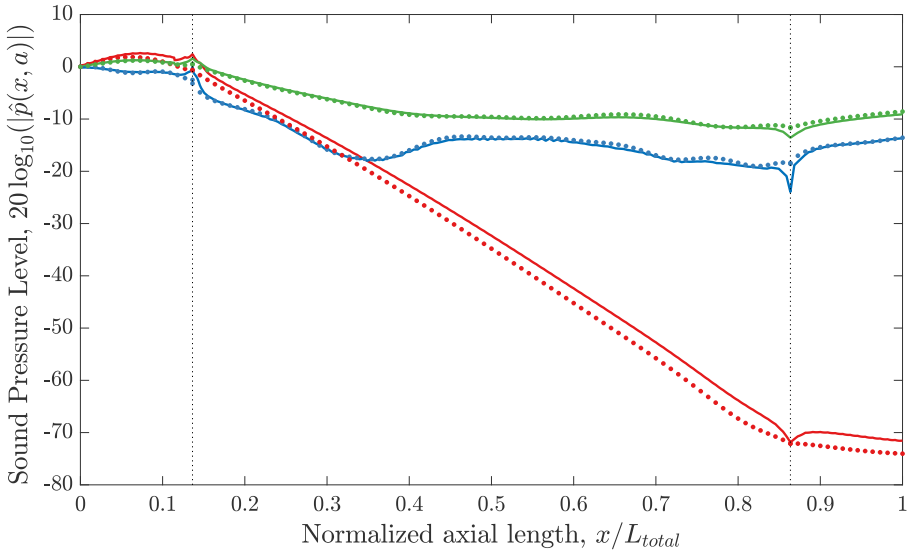

Source – Own authorship.

As a matter of fact, the mode matching accuracy could be improved if more cut-off modes were included. Figure 39 shows how the number of modes affects the in-duct content for uniform and shear flow at transitions, with emphasis on the sideline condition. It can be observed that increasing the number of radial modes modifies the acoustic field only at distances close

to the interfaces. Since most of these modes are well cut-off, their influence is limited to the vicinity of the interface, and therefore their contribution to other locations is negligible. A convergence analysis has been performed by other authors and summarized as follows. McAlpine, Astley, et al. (2006) concluded that, for $n_c = 2$, a total of 20 radial modes was sufficient for convergence. Law, Dowling, and Corral (2010) demonstrated that, for seven cut-on modes with azimuthal order $m = 0$, it was reasonable to use 30 radial modes. For $n_c = 5$, Gabard (2010) included 80 radial modes to represent accurately the solution near the liner interface.

Figure 39 – Variation of the mode matching solution for sideline condition with the number of radial modes included.

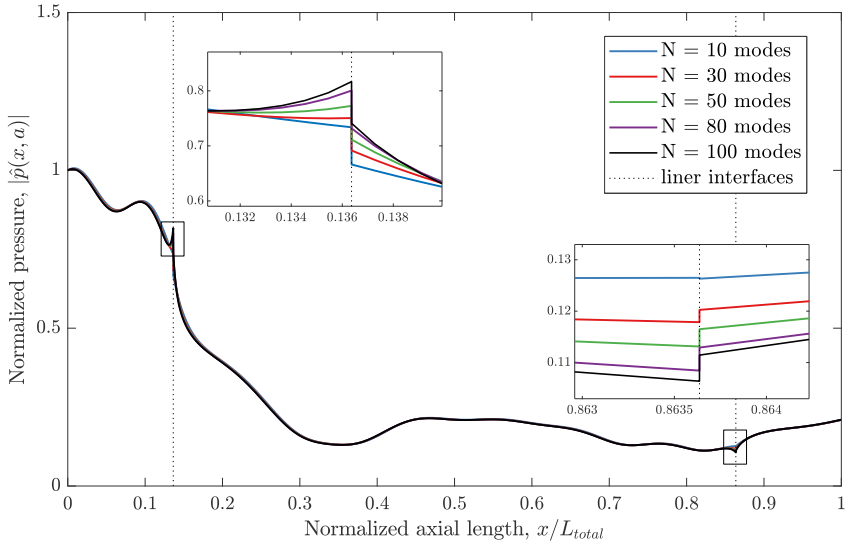

(a) Uniform flow with Ingard-Myers boundary condition

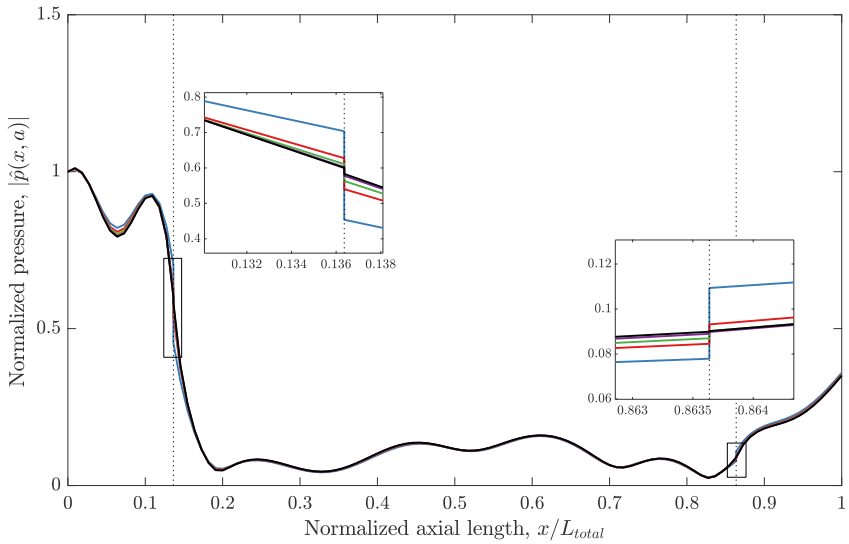

(b) Shear flow for $\delta = 2\%$ considering the Pridmore-Brown equation

Source – Own authorship.

The discontinuity at the interfaces is not observed when considering shear flow in terms of

the acoustic pressure, as shown in Figure 39b. In this case, a better convergence at the interfaces is achieved when a greater number of modes is considered. It follows directly from the no-slip condition at the wall, which provides better agreement for matching condition considered here. When considering the Ingard-Myers boundary condition, the acoustic power is not conserved across the interface due to the presence of a vortex sheet on the liner surface, such that the standard matching assumption of pressure and axial particle velocity is incorrect (EVERSMAN, 2001; GABARD, 2010), which can explain the mismatching at the interfaces.

To estimate the error of the matching at the interface as function of the number of radial modes N, one can use the mean squared error function ϵ_m, defined as (LAW; DOWLING; CORRAL, 2010)

$$\epsilon_m(N) = \frac{\int_0^1 |\hat{p}_m^{s+1}(r,N) - \hat{p}_m^{s}(r,N)|^2 \, dr}{\int_0^1 |\hat{p}_m^{s+1}(r,N)|^2 \, dr}, \tag{5.2}$$

and shown in Figure 40 for the interface at $x = l$ and sideline condition. Since the computational cost scales with the matrix size in Eq. (3.8), it is important to define a maximum number of radial modes that guarantees a satisfactory level of accuracy for all conditions. In this work, we consider 30 cut-off modes, which should be sufficient for computing the transmission loss, even in the presence of a sheared flow. In addition, a convergence analysis of the wavenumber solver used in the the mode matching scheme is outlined in Appendix B.1.

Figure 40 – Variation of the error function at sideline condition with the number of radial modes included: Ingard-Myers (black) and Pridmore-Brown (red) solutions.

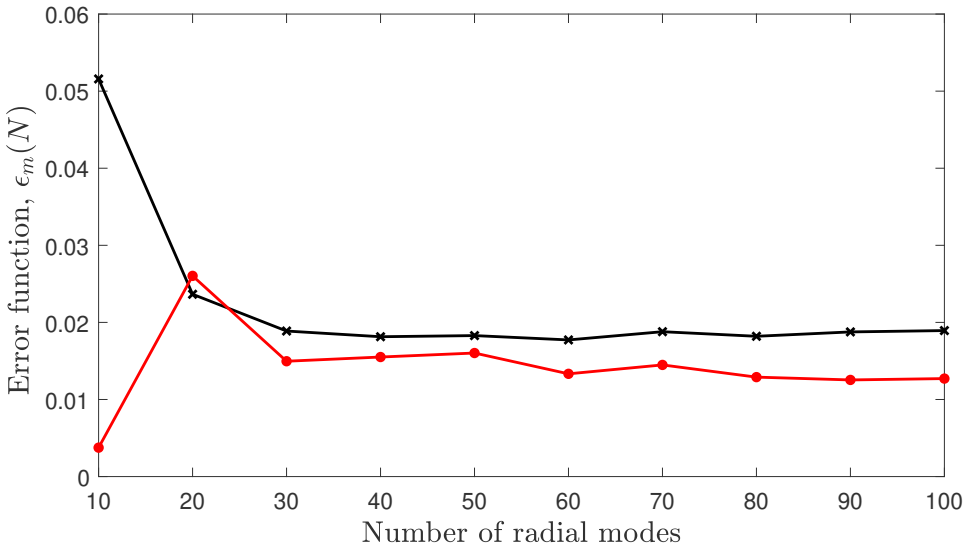

Source – Own authorship.

To assess boundary layer effects, the solution of the Pridmore-Brown equation and convected Helmholtz equation with Brambley boundary condition were considered for rigid and

lined sections. The procedure to find the wavenumbers was different for each case. The Pridmore-Brown equation was solved using a spectral method, as outlined in Section 3.2, in the form of a generalized eigenvalue problem. The Brambley boundary condition is not suitable for this kind of problem since some terms are quadratic in k, and therefore the tracking method proposed by Eversman and Hubbard (1991) was used in this case for each mode. For this reason, the time to compute the Pridmore-Brown solution is much faster than the Brambley formulation. The mode matching prediction for both formulations are shown in Figures 41 to 43 for all operating conditions. The results with uniform flow and Ingard-Myers boundary condition are used as reference, and a parametric study with four different boundary layer thicknesses was considered for this comparison.

A first observation is that increasing the boundary layer thickness leads to a reduction on liner attenuation, which is more prominent for higher Mach numbers. For the sideline condition, the acoustic field in the lined section is significantly modified when compared to the uniform mean flow case. In fact, at some locations, the difference between assuming uniform and shear flow with $\delta = 2\%$ is above $10\,\mathrm{dB}$ for both Pridmore-Brown solution and convected wave equation with Brambley boundary condition. Although it is not clear in Figures 41a and 41b, assuming Brambley boundary condition results in a slightly overpredicted attenuation, which is in line with the results shown by Gabard (2016). Nevertheless, it is a more conservative choice when compared to Ingard-Myers boundary condition. It should be noted that scattering occurs pre-dominantly at the start of a each interface.

For cutback condition, only one radial mode is cut-on in the hard-walled duct and the cut-off ratio is close to 1. Therefore, this mode is well absorbed in the lined section in the presence of uniform flow, as seen in Figures 42a and 42b. The presence of a boundary layer leads to a significant reduction in total attenuation, although the mode remains well attenuated. In Figure 42b when considering Brambley boundary condition, this reduction is about $20\,\mathrm{dB}$ for $\delta = 2\%$ at the duct termination. On the other hand, this boundary condition underpredicts the liner attenuation when compared to the Pridmore-Brown solution in less than $2{,}5\,\mathrm{dB}$.

For approach condition, the lower Mach number leads to a liner attenuation barely affected by the presence of a boundary layer. When comparing to the uniform flow case, even a thicker boundary layer of 3% results in a reduction of only $1{,}3\,\mathrm{dB}$ in the Pridmore-Brown solution, and $1{,}6\,\mathrm{dB}$ in the convected wave equation with Brambley boundary condition. Since most of the acoustic power in this mode is quite distanced from the duct wall when compared with the mode $(24, 1)$, it is expected less attenuation due to liner impedance. This is consistent with

complex plane analysis outlined in the Appendix B.2, which shows at each operating condition that the higher spacing from real axis (i.e. corresponding a higher modal attenuation) happens for upstream propagation for thin boundary layer.

In addition, the pressure of a mode in the lined section decreases like $\exp[-\mathrm{Im}(k_{m,n}x)]$, which is linear in a sound level as can be found for cutback condition (see Figure 42), but not in the two other cases (Figures 41 and 43). This can be explained by two distinct mechanisms: (1) due to the reflected wave at low attenuation and (2) the presence of radial modes propagating. The last one will be analyzed in Section 6.2.1.

The change in the transmission loss associated with the presence of a boundary layer is shown in Figure 44 for each operating condition. It is clear that the effect of the boundary layer becomes important as the Mach number increases. Considering $\delta = 2\%$ and comparing to results with uniform flow, a difference of approximately $0{,}5\,\mathrm{dB}$ is found for approach condition, $24\,\mathrm{dB}$ for cutback condition and $9{,}5\,\mathrm{dB}$ for sideline condition. The results with Brambley boundary condition closely follow the trends observed in the Pridmore-Brown solution when considering this range of boundary layer thickness. Moreover, comparing the Brambley boundary condition with the Pridmore-Brown solution, it can be seen that it slightly overpredicts the attenuation at sideline and approach conditions, whereas at cutback condition it underpredicts.

An interesting behavior is that the presence of a boundary layer increases the attenuation when $0\% \leq \delta \leq 0.1\%$ at sideline and cutback conditions and $0\% \leq \delta \leq 0.5\%$ at approach condition, which is not explained by the refraction effect. This indicates that the interaction between the liner and the boundary layer is actually more complex (GABARD, 2016). In fact, it is possible that the increase in sound attenuation with the boundary layer thickness may be linked to the liner impedance reaching its optimum value (SPILLERE; CORDIOLI, 2019). For larger values of δ, the trend is a reduction in attenuation, which has been observed by Gabard (2016) in terms of absorption rate. From the analysis presented here, the mean flow assumption together with Ingard-Myers boundary condition can lead to erroneous results of the transmission loss, specially in sideline and cutback conditions, which may result in inaccurate predictions of the far-field radiated noise.

5.4 PARAMETRIC IMPEDANCE STUDY: IN-DUCT PROPAGATION

To extend the analysis to other liner configurations, a brief parametric study of the acoustic impedance is carried out to identify general trends at the sound power transmission loss in

Figure 41 – Prediction of acoustic pressure at the duct wall with uniform and shear flow for sideline condition.

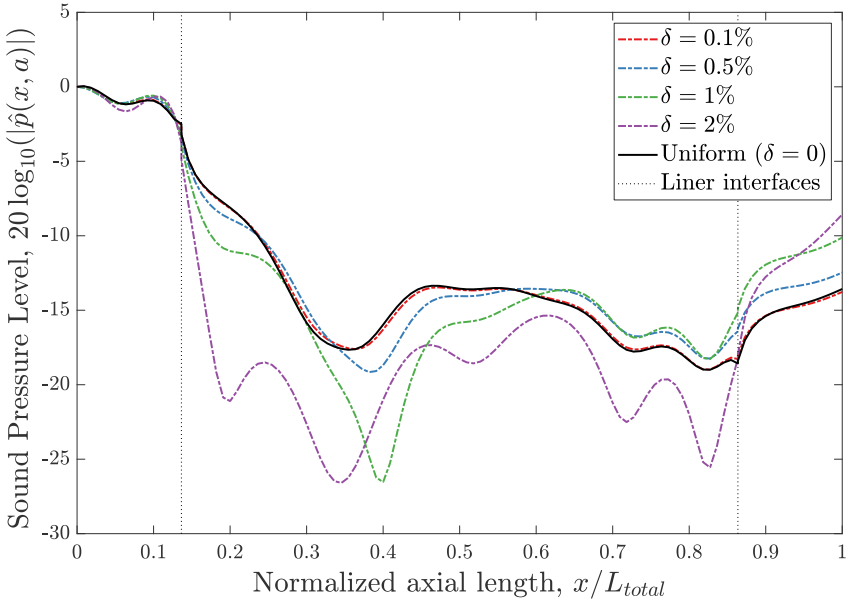

(a) Pridmore-Brown solution

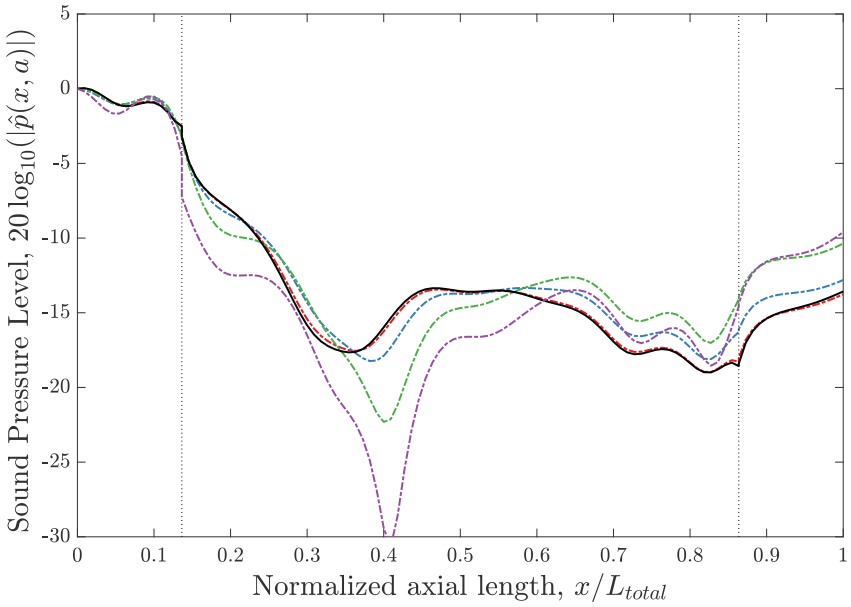

(b) CHE with Brambley boundary condition

Source – Own authorship.

Figure 42 – Prediction of acoustic pressure at the duct wall with uniform and shear flow for cutback condition.

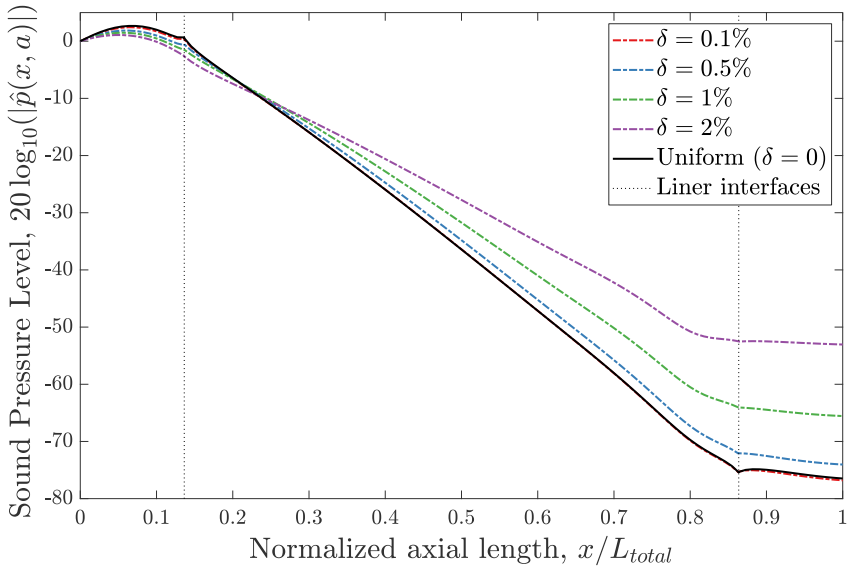

(a) Pridmore-Brown solution

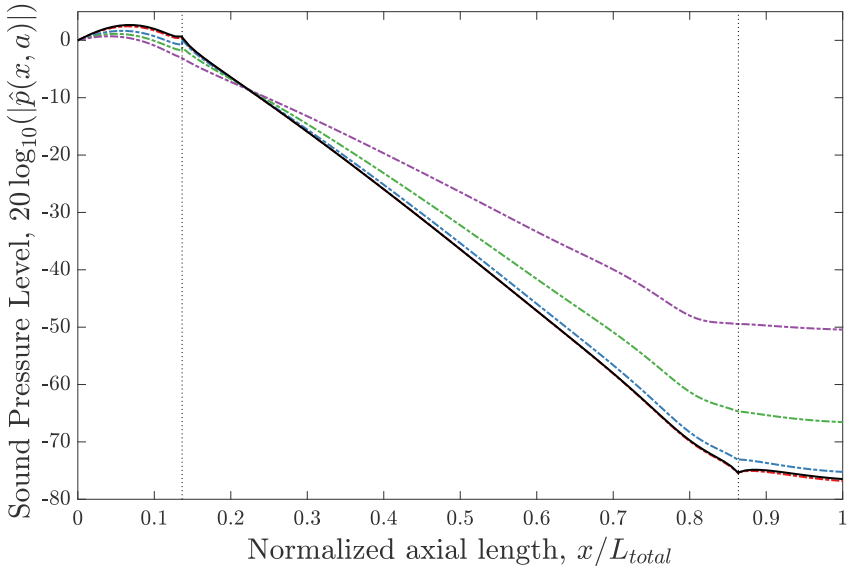

(b) CHE with Brambley boundary condition

Source – Own authorship.

Figure 43 – Prediction of acoustic pressure at the duct wall with uniform and shear flow for approach condition.

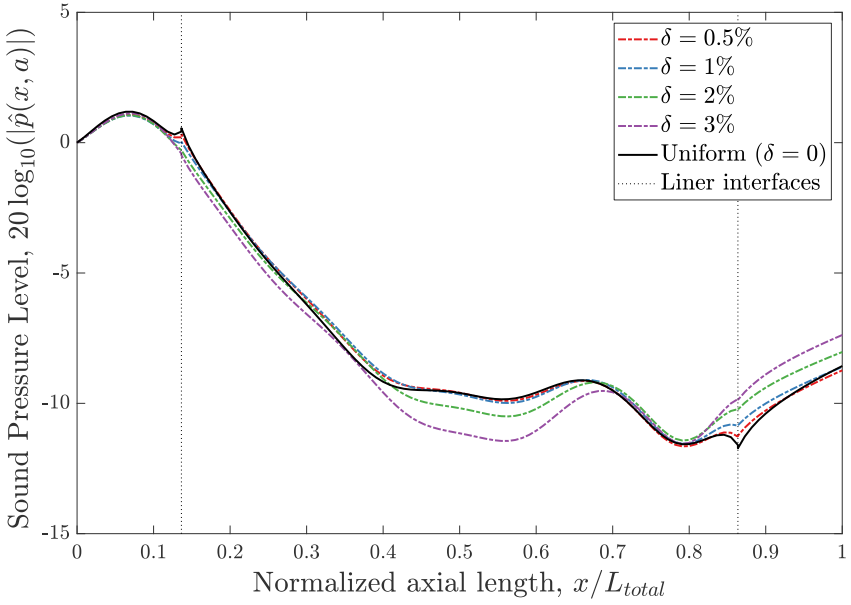

(a) Pridmore-Brown solution

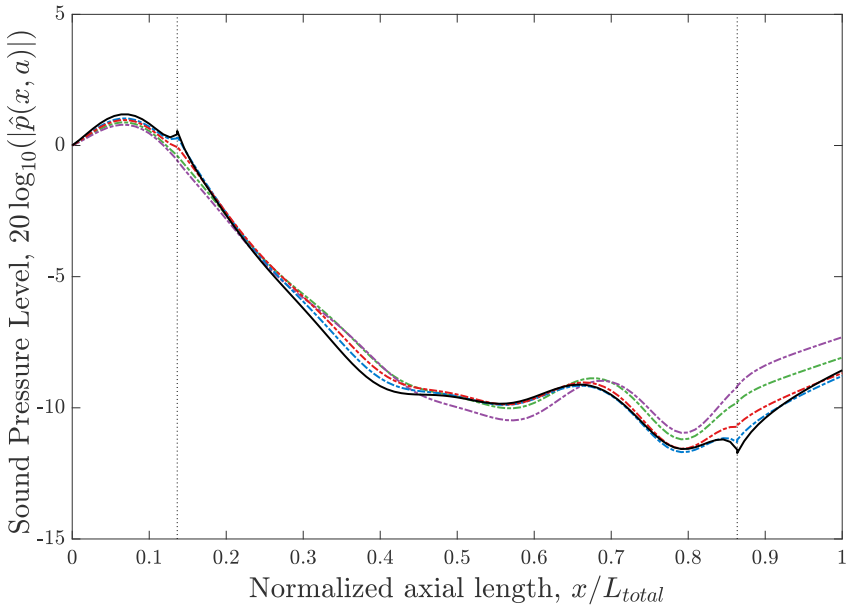

(b) CHE with Brambley boundary condition

Source – Own authorship.

Figure 44 – Predicted sound power transmission loss for boundary layer thickness growth considering Pridmore-Brown solution (Black) and Brambley solution (red): a) Sideline, b) Cutback and c) Approach.

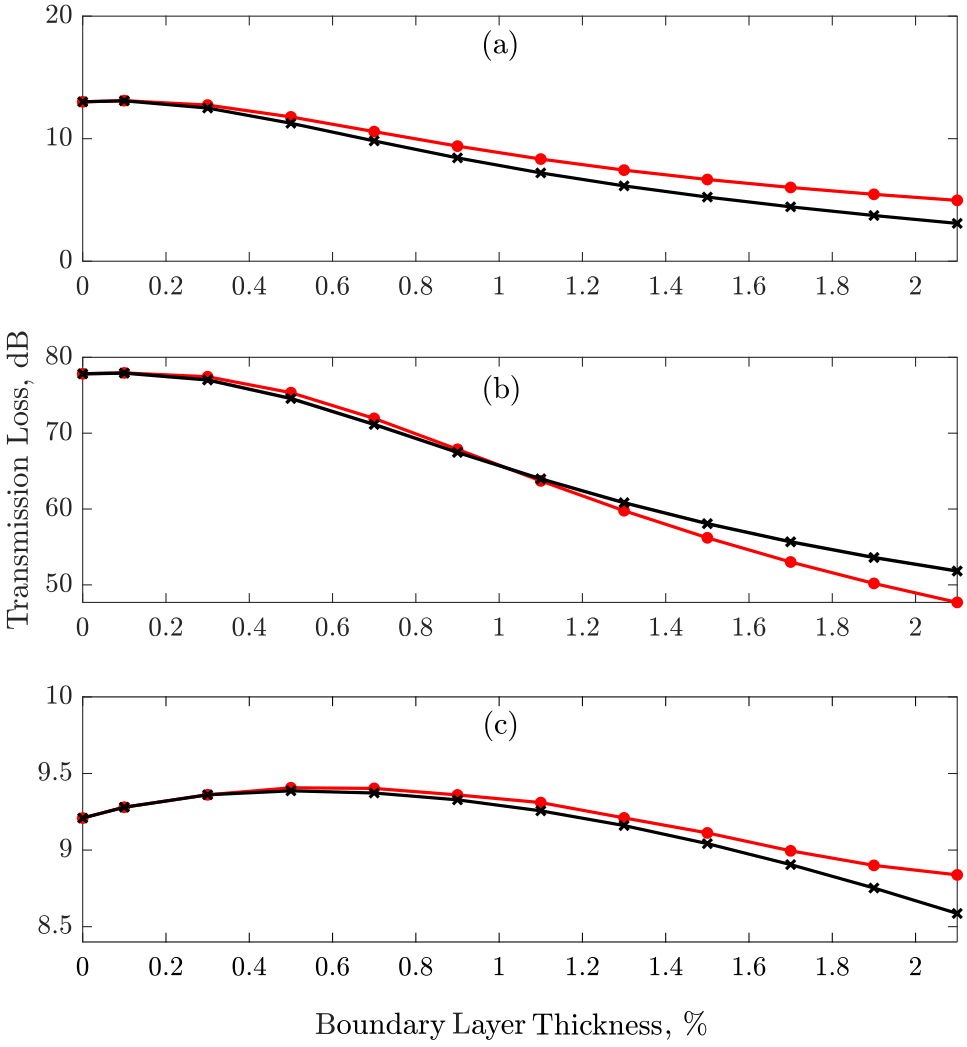

Source – Own authorship.

terms of the liner impedance for the operating conditions studied here. The non-dimensional specific acoustic impedance of the lining was defined in Eq. (2.30), which is commonly rewritten by a simple impedance model for a single-degree-of-freedom (SDOF) as (EVERSMAN; HUBBARD, 1991)

$$Z = R + \mathrm{i}\mathcal{X} = \frac{0.3M_0}{\varrho} + \mathrm{i}(k\varpi - \cot(kB)), \tag{5.3}$$

where B is the depth of the liner, ϱ is the $\%$ porosity (or the percentage open area) and ϖ is the mass inertance. This mass ϖ of the facing sheet is determined by

$$\varpi = \frac{[T + \mathcal{E}(\varrho)d]}{\varrho}, \tag{5.4}$$

where $\mathcal{E}$ is the dimensionless end correction, which depends on porosity ϱ and the grazing flow effects. Note that the dimensionless end correction is always less than unity $(\mathcal{E} < 1)$. On the other hand, the resistance R in the Eq. (5.3) is taken to be independent of the frequency directly. However, it depends on an averaged grazing flow Mach number M_0 (which is related to speed rotation) over the lined surface and the percentage open area.

In order to limit the upper and lower values of the variables within feasible values, the values suggested by Spillere (2017) were used[1]. Therefore, the realistic values of R and $\mathcal{X}$ are specified. Figure 45 shown acoustic impedance curves for two parametric studies proposed in this section. In the first case, in Figure 45.(a), the liner resistance was varied around typical values of liner configurations, which is applicable for liner design at low and high frequencies. For the second parametric analysis, the liner reactance was also varied around typical values following results of the Eqs. (5.3) and (5.4). Note that the black dash line highlighted wavenumbers of the operating condition studied in this chapter. Therefore, the liner resistance values used in this section, vary from 2 to 4 for sideline condition. For approach condition, a lower variation is observed in terms of liner resistance, with values from 1 to 3. Regarding the impedance values for cutback condition, it follows the intermediate trend observed for the previous condition, which can vary from 1 to 2.5. The same range was also considered for variable liner reactance case.

Firstly, the resistance is analyzed. Figure 46 presents the results for the transmission loss for parametric study of variable liner resistance, which was investigated for assigned values of the Table 4. In this case, the liner resistance was varied around typical values for each condition, which is applicable for liner design at low and high frequencies. Only results for the Pridmore-Brown solution are shown here since results with Brambley boundary condition are very similar. In terms of transmission loss, different behaviors can be observed for this parameter in terms of the boundary layer thickness when the resistance is varied. The attenuation maximum lobe is a function of the liner impedance, and this may be linked to the relation between optimal impedance and refraction effects within the boundary layer (SPILLERE; CORDIOLI, 2019).

[1] Some of these bounds were defined empirically while care was taken not to overly limit the possible curves that can be generated by Eqs. (5.3) and (5.4)

Figure 45 – Impedance curves as function of the non-dimensional frequency in terms of the liner resistance and reactance: (a) varying the non-dimensional resistance R of the facing sheet and (b) varying the non-dimensional reactance $\mathcal{X}$ (gray filled areas). Fixed reactance and resistance values are solid black lines, respectively.

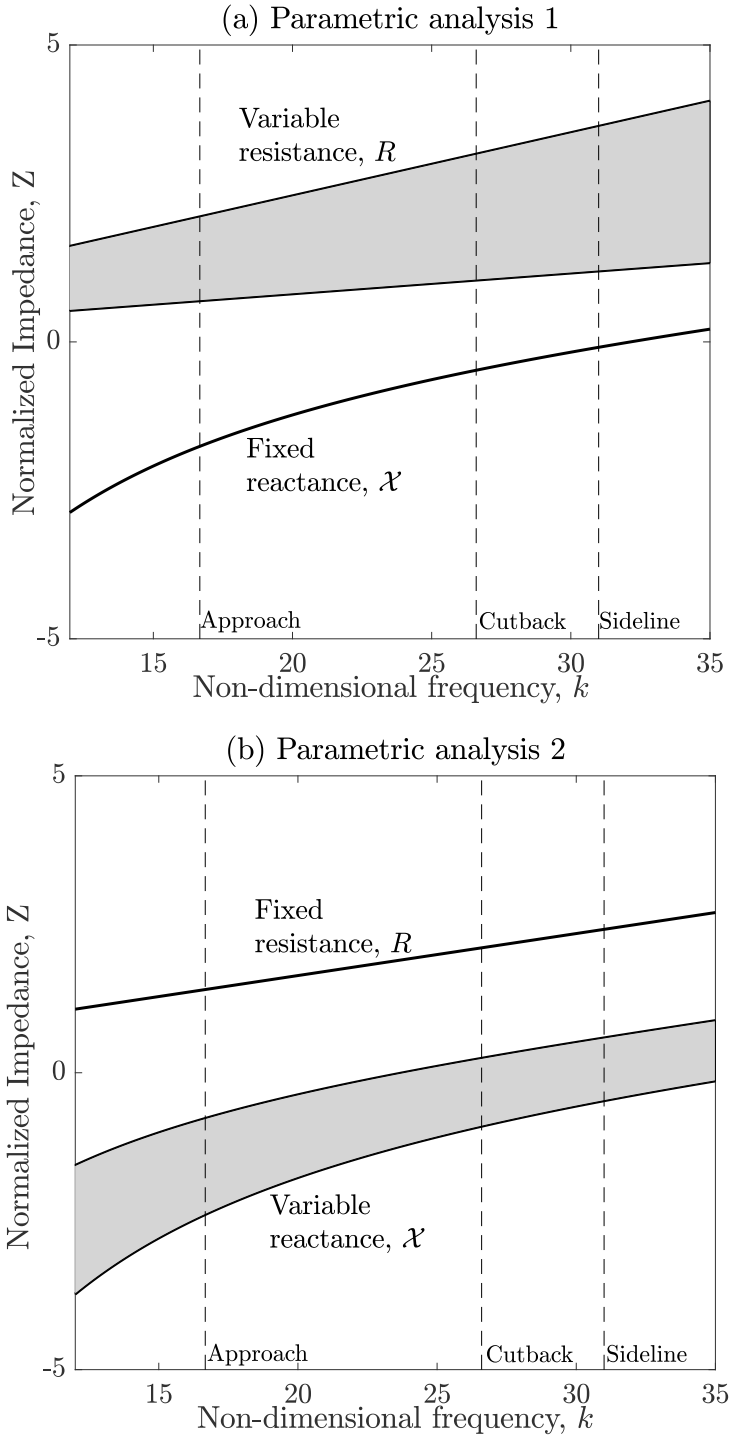

Source – Own authorship.

Depending on the liner resistance, especially at approach (Fig. 46a) and cutback (Fig. 46b) conditions, larger values of δ can lead to an increase of the attenuation, which goes against the common sense associated with refraction effects. At sideline condition (Fig. 46c), the behavior of the attenuation is less affected by the liner resistance, with only a small impact in the maximum attenuation for lower values of δ (closer to the uniform flow condition).

As can be seen in Figure 47, the presence of a boundary layer in a lined duct considering different reactance values have a strong influence in the transmission loss results. It modifies both the maximum attainable attenuation (similar to offset in the curves) and shifts the boundary layer thickness of peak attenuation shifts towards its lower value with a moderate change in the level of peak attenuation (as the imaginary part of the impedance increases), for all operating conditions. This characteristic is mainly seen in Figures 47a and 47b. Again, this trend indicates that an optimum acoustic reactance exists for a given situation. For cutback (Fig. 47b) and approach conditions (Fig. 47c) (where the mean flow M_0 is smaller), the behavior of the curves is similar, where the peak attenuation is slightly shifted and the boundary layer thickness has smaller influence on transmission loss results (i.e., it is approximately constant for any boundary layer thickness).

These results demonstrate why efforts should be concentrated in the impedance values, especially in improving the values towards liner optimization for BPF tones. While liner resistance was vigorously explored in terms of the attenuation rate by several previous authors (EVERSMAN, 1971; KO, 1972; NAYFEH; KAISER; SHAKER, 1974; GABARD, 2016), as can been in this section, the liner reactance also plays a hole on the liner attenuation – the curves in Fig. 47 provide much more information about its importance for the liner design process, which is far from simple. The trends shown in results are very different depending on the operating condition (i.e., it can be generalized in terms of the modal parameters). It is therefore not a straightforward task to find a liner impedance value that provides a large attenuation at all operational conditions, and, in general, liners are optimized for a specific condition.

Figure 46 – Predicted sound power transmission loss considering the Pridmore-Brown solution for different values of boundary layer thickness and liner resistance: (a) Sideline, (b) Cutback, and (c) Approach. Black solid line: reference curve (same as Figure 44). Colored dot-dashed line: varying resistance for fixed reactance (following the values in Table 4).

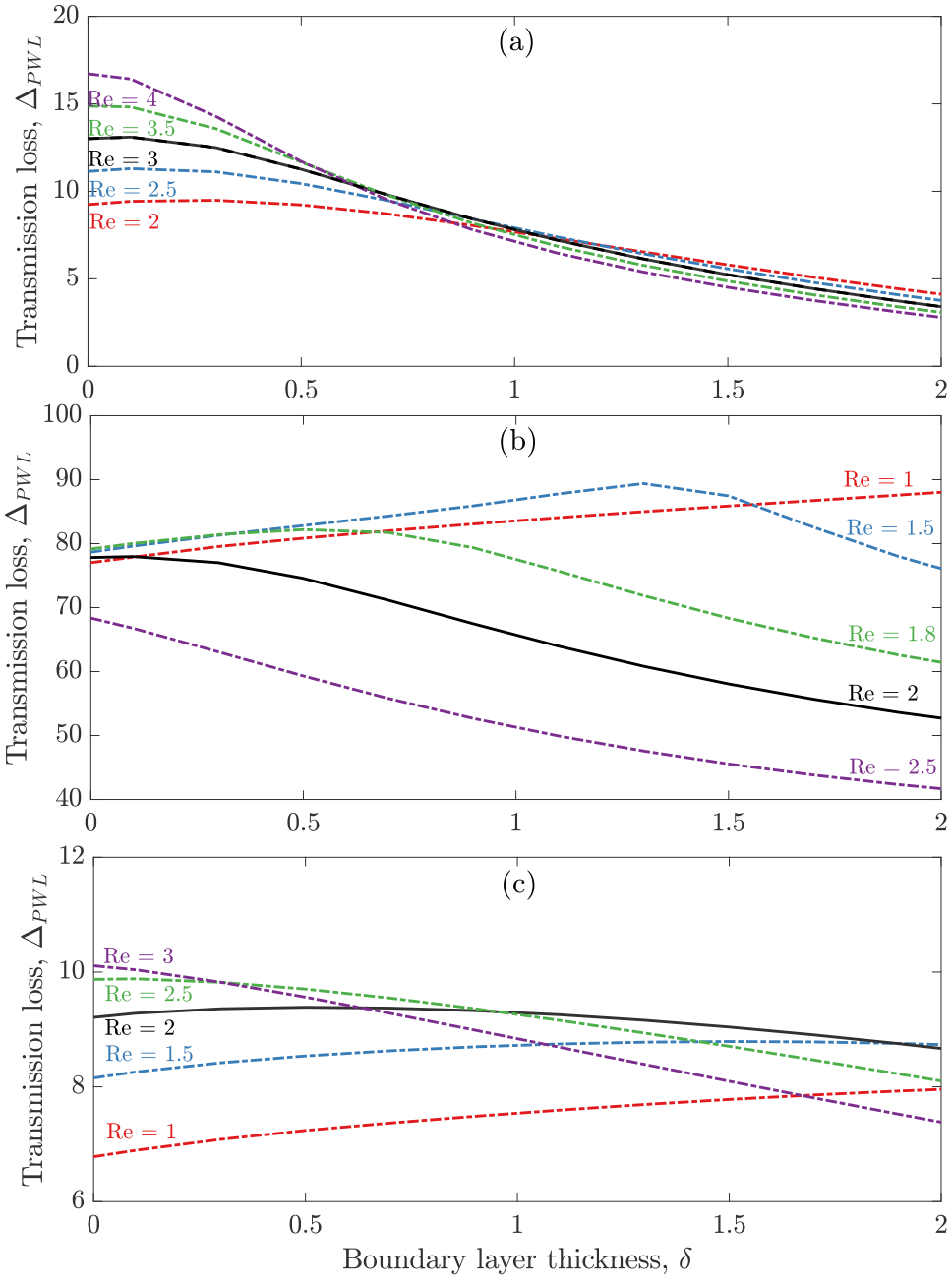

Source – Own authorship.

Figure 47 – Predicted sound power transmission loss considering the Pridmore-Brown solution for different values of boundary layer thickness and liner reactance: (a) Sideline, (b) Cutback, and (c) Approach. Black solid line: reference curve (same as Figure 44). Colored dot-dashed line: varying reactance for fixed resistance (following the values in Table 4).

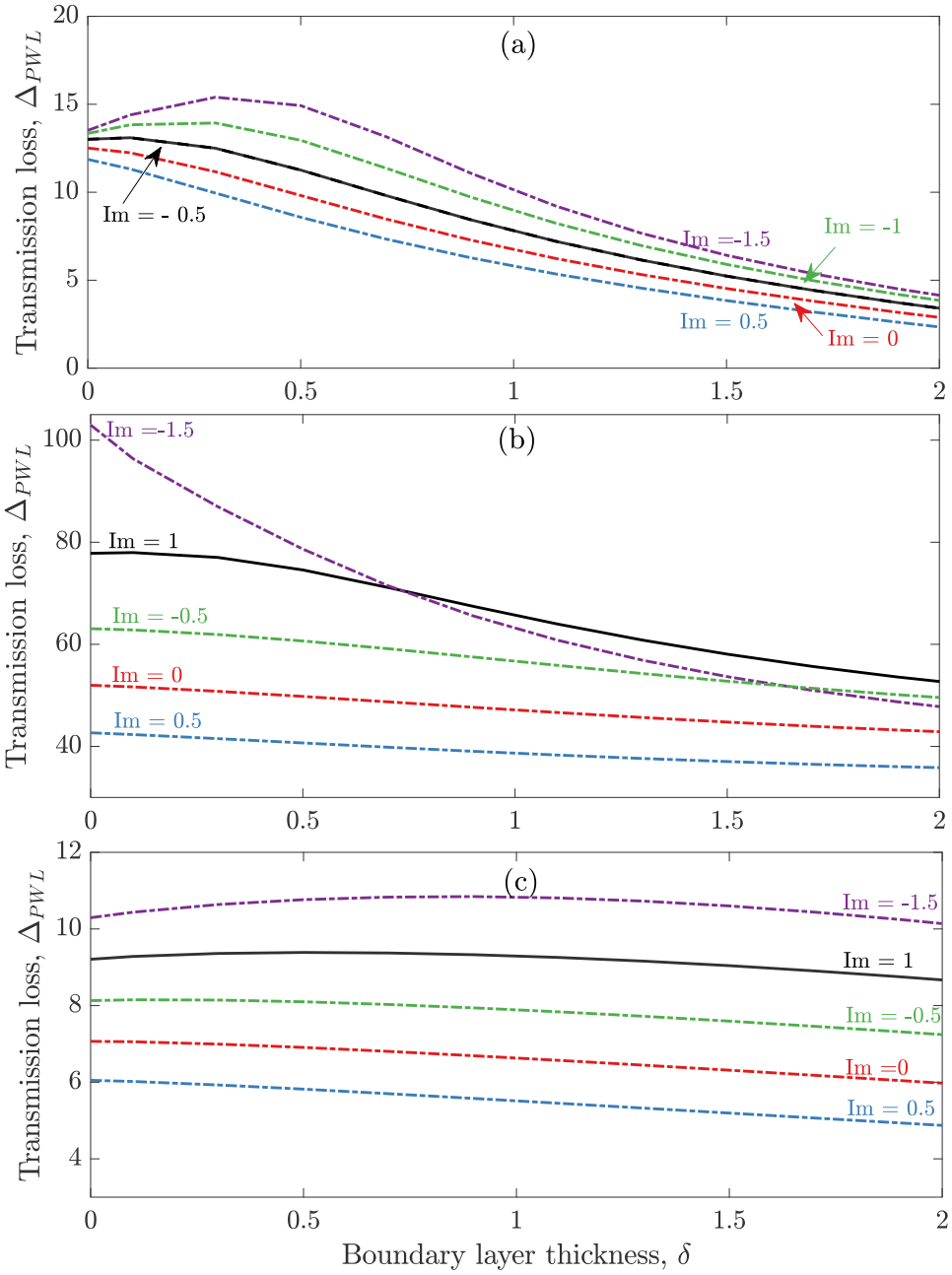

Source – Own authorship.

6 EFFECT OF THE FLOW ON THE NOISE RADIATED TO THE FAR-FIELD

In this chapter, the attention is switched to the effect of the mean flow in terms of the far-field prediction. First, the effect of the in-duct and external flows will be analytically evaluated by using the radiation models, where the key issues about flow presence are investigated. Second, the equations for the integration of the radiation model with the mode-matching method is described in detail. Then, the hybrid tool (based on the "in-duct eigenmode + analytic radiation" models) is used to predict the far-field radiation patterns for the asymmetric intake ducts at different frequencies and mean flow conditions (uniform and non-uniform) of practical interest.

6.1 EFFECT OF THE EXTERNAL FLOW ON THE FAR-FIELD RADIATION

Previous far-field radiation theories applicable to engine inlets have dealt with the special cases of zero Mach number or uniform Mach number inside and outside the duct (RICE; HEIDMANN; SOFRIN, 1979). The external flow that may be present due to the aircraft movement (also called in-flight effect) can modify significantly the far-field noise radiation pattern depending on the operating condition. Also, in the case of a static engine test, when the external flow is zero (also called duct flow alone), the in-duct Mach number plays a hole in the modal propagation. Therefore, in the presence of mean flow, two main effects are expected: (1) the noise radiation pattern is shifted as Mach number is varied and (2) its overall sound level pressure trend increases for upstream propagation and decreases for downstream propagation.

In such cases, the concept that the far-field radiation pattern is a function of the modal cut-off ratio can be useful for acoustic linear design purposes. By using this definition, the location of the maximum peak or lobe of each mode can be approximated, which also depends on the relation of the in-duct M_0 and external M_∞ Mach numbers. In the past, Rice (1978) has shown that the angle of maximum lobe in far-field radiation is perhaps a more basic parameter such that the cut-off ratio for multimode calculations. When the flow velocity inside and outside the duct is the same (i.e., avoiding any flow mismatch), an expression can be written from results of **a**s

$$\cos\theta^{\wedge}_{m,n}\bigg|_{M_\infty=M_0} = \sqrt{1-M_0^2}\left[\frac{1-\eta_{m,n}^{-2}}{1-M_0^2(1-\eta_{m,n}^{-2})}\right]^{1/2}, \tag{6.1}$$

which is a generalized case of the $\theta^{\wedge}_{m,n}$ defined in Section 3.3.1, and it is equivalent to the factor $\mathcal{S}(\theta)$ given by Eq. (3.33). Note that for $M_0 = 0$, the zero Mach number case of Eq.

(6.1) leads to $\theta^{\wedge}_{m,n} = \cos^{-1}\sqrt{1-\eta^{-2}_{m,n}} = \sin^{-1} 1/\eta_{m,n}$. The flow velocity in the far-field equal to the duct (also called flow everywhere (RICE; HEIDMANN; SOFRIN, 1979; HEIDMANN; SAULE; MCARDLE, 1980)) can cause relatively small angular displacements toward the axis. Rice, Heidmann, and Sofrin (1979) extended the work of Homicz and Lordi (1975) to handle the case of radiation from a duct with an in-duct Mach number different from the free-field Mach number, and showed the main lobe $\theta^{\wedge}_{m,n}$ as function of both external and internal Mach number so that

$$\begin{aligned}\cos\theta^{\wedge}_{m,n}\Big|_{M_\infty\neq M_0} &= \left[M_\infty - M_0 + (1-M_0M_\infty)\sqrt{1-\eta^{-2}_{m,n}}\right] / \\ &\left\{\left[1 - M_0\sqrt{1-\eta^{-2}_{m,n}}\right][1 + M_\infty(M_\infty + 2M_0)\right. \\ &\left.\left. +(2M_\infty - M_0 - M_0M^2_\infty)\sqrt{1-\eta^{-2}_{m,n}}\right]\right\}^{1/2}.\end{aligned} \tag{6.2}$$

Note that when $M_\infty = M_0$, Eq. (6.2) reduces to Eq. (6.1). An special case of Eq. (6.2) is that of $M_\infty = 0$ which is applicable for static engine tests. Eq. (6.2) then reduces to

$$\cos\theta^{\wedge}_{m,n}\Big|_{M_\infty=0} = \frac{-M_0 + \sqrt{1-\eta^{-2}_{m,n}}}{1 - M_0\sqrt{1-\eta^{-2}_{m,n}}} \tag{6.3}$$

As discussed by Rice, Heidmann, and Sofrin (1979), the radiation directivity with flow inside and outside the duct includes a convective effect in the far-field. For the duct flow alone, the principle lobe peak beams significantly closer to the inlet axis than for the case of flow everywhere. Therefore, the change of cut-off ratio (i.e., in the modal content) or Mach number, of course, modifies the estimated main lobe directly. It should be noted that the theory was developed by Rice, Heidmann, and Sofrin (1979) using approximations for sound propagation and ray tracing and in the circular duct may deviate when it is compared with predicted and measured radiation patterns as observed by Heidmann, Saule, and McArdle (1980). Despite the limitations, these are valuable in light of the concepts behind angle transformations as can be seen in Figures 48 and 49, which is applied for operating conditions defined in the last chapter. The three radiation models studied in this work were used here.

For the results in Figure 48, the effect of the in-duct Mach number is assumed to be uniform, and it is solved by dispersion relationship between the wavenumbers of Eq. (2.15) for radiation models (colored solid lines), while the Eq. (6.3) is used to calculate the duct flow

alone angle for each operating condition (black dash line). On the other hand, for the results in Figure 49, the factor $\mathcal{S}(\theta)$ (Eq. (3.33)) with external Mach number values is used in addition with dispersion relationship for the in-duct Mach number at each operating condition. The main characteristics of the operating conditions are listed in Table 4.

Figure 48 – Convective effect upon far-field radiation main lobe angle for inlet under Static test ($M_\infty = 0$) at different operating conditions. Comparison between Rayleigh (blue), Kirchhoff (red) and Wiener-Hopf (green) radiation models with solution of the Eq. (6.3) (black).

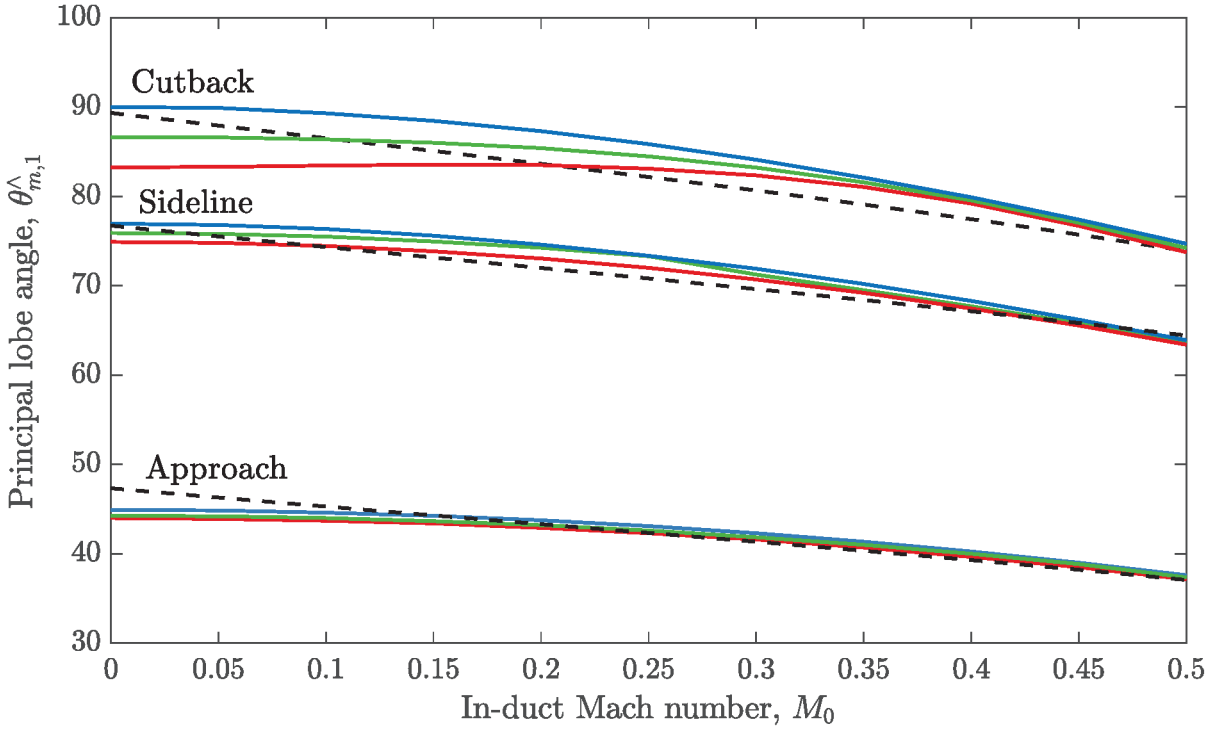

Source – Own authorship.

For static test configuration, in Figure 48, as in-duct Mach number increases, the main lobe in the radiation pattern is shifted considerably toward the inlet axis when compared to zero Mach number radiation theory (i.e., $\theta^{\wedge}_{m,n} = \sin^{-1} 1/\eta_{m,n}$). On the other hand, as the external Mach number is increased (see Figure 49) the noise radiation pattern is shifted away from the inlet axis (i.e., toward the sideline angle). The results in Figs. 48 and 49 show some deviations from Rice's theory, but they corroborated qualitatively with it.

The radiation directivities for the operating conditions are shown Figure 50. Since a similar behavior is observed for radiation models, the Kirchhoff solution is used to exemplify the tendency in terms of the directivity pattern. Also, the present solution produces a main lobe in a similar range of Figure 49. Note that the directivities show a monotonic fall-off at small angles, which is a characteristic of the high order modes. For the mean flow $M_0 \leq M_\infty$, most

Figure 49 – Effect of the external and in-duct flow velocities on the far-field main lobe angle at different operating conditions. Comparison between Rayleigh (blue), Kirchhoff (red) and Wiener-Hopf (green) radiation models with solution of the Eq. (6.2) (black).

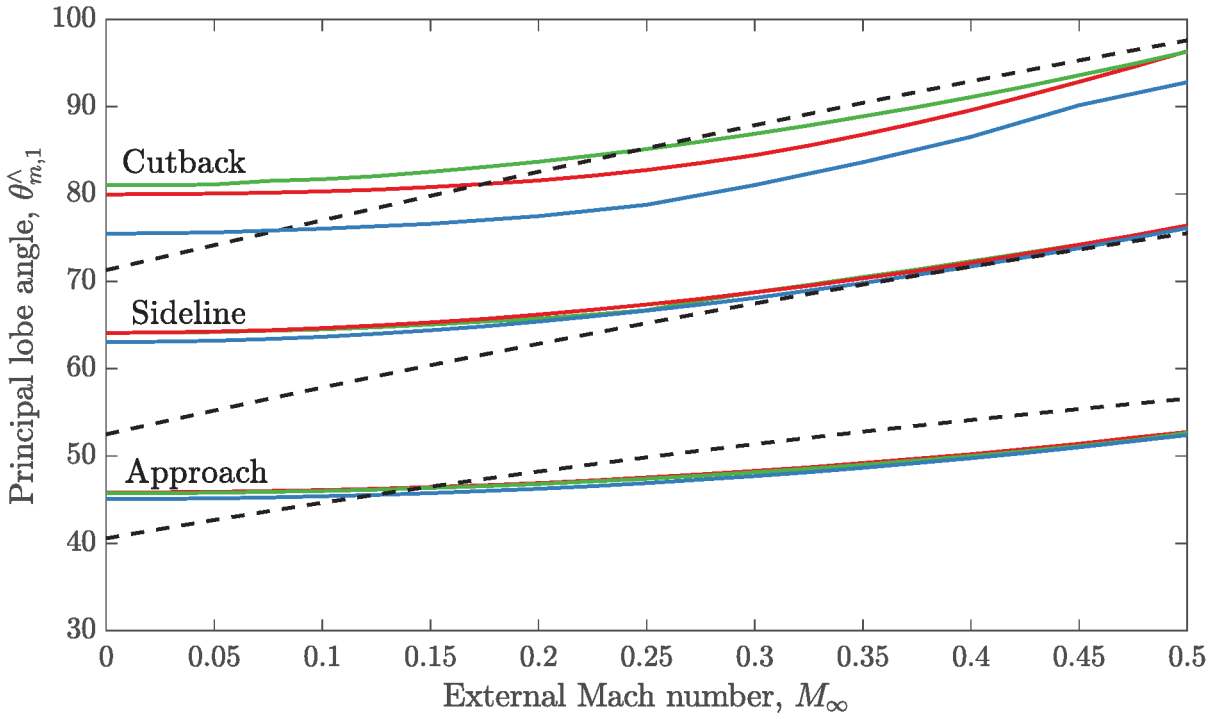

Source – Own authorship.

of the radiation content is confined on the angles around $50°$, $71°$ and $42°$ at sideline, cutback and approach conditions, respectively. However, for duct flow alone ($M_\infty = 0$) the variations around 3 to $10°$ are observed for these conditions. Therefore, even small variations of the velocity can imply erroneous estimation of the far-field directivity pattern, which implies that the Mach number outside and inside of the duct needs to be carefully estimated. For cutback and approach conditions, the inclusion of an external flow modifies the far-field directivity pattern slightly due to the small variation on the cut-ratio. In contrast, at sideline condition, the shape of the far-field directivity has been modified due to a great variation on the cut-ratio, which is more affected by higher Mach number. Moreover, the flow effect implies in a reasonable variation of the magnitude values, which is also attributed to the external convective effect, as observed by Lewy (2003).

Figure 50 – Far-field directivity variation with external Mach number for Kirchhoff approximation in different operating conditions.

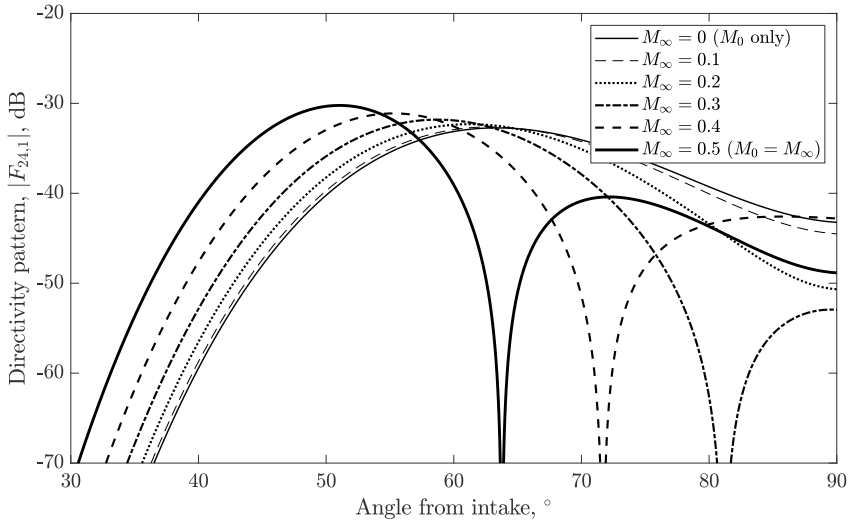

(a) Sideline condition

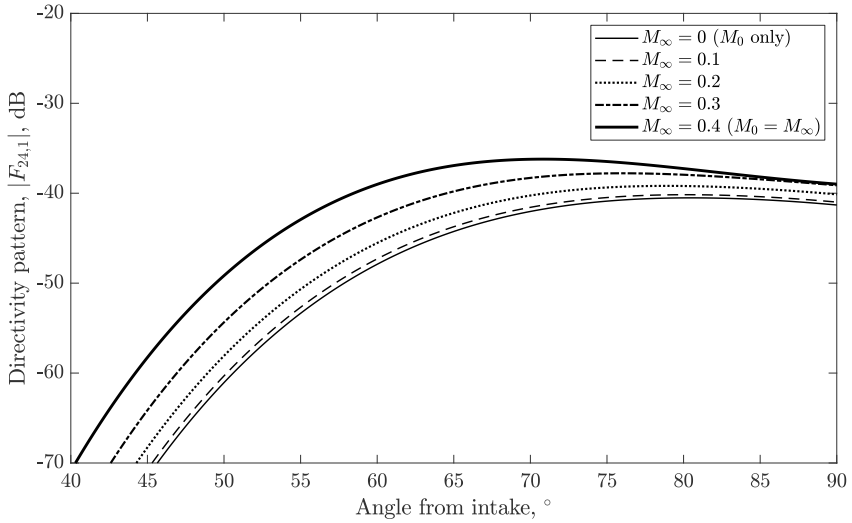

(b) Cutback condition

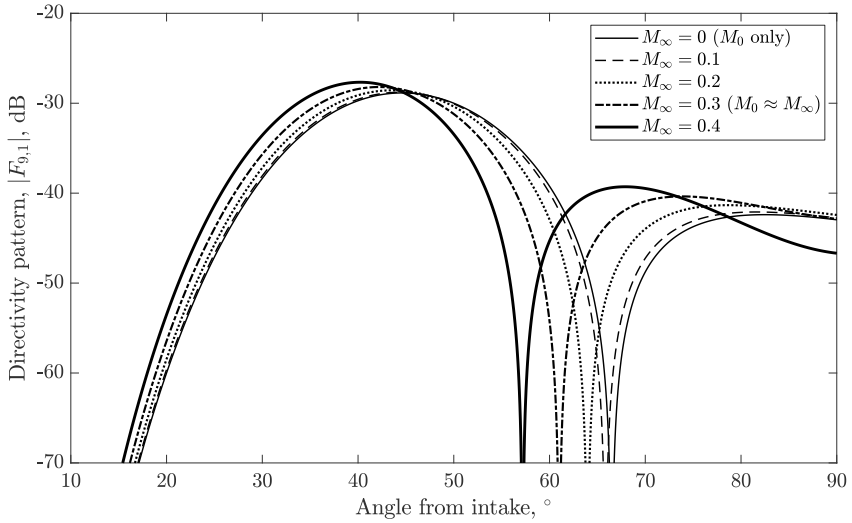

(c) Approach condition

Source – Own authorship.

6.2 EFFECT OF THE LINER IN FAR-FIELD PREDICTIONS

6.2.1 Output amplitudes modes at the exit section

The procedure outlined in the Section 3.4 is implemented to predict the far-field noise levels by using mode matching method with analytic radiation model. This involves the following steps: (1) Predict the modal amplitudes of the transmitted modes $\mathbf{B}^+$ at the duct exit by using the mode matching scheme (for instance, assuming unitary incident amplitude $\mathbf{A}^+$), as discussed in Chapter 5); (2) identify the transmitted amplitudes $\mathbf{B}^+$ yield by scattering effect (i.e. the cut-on radial modes for a particular azimuthal mode m); (3) define the proper radiation model (i.e., defined by the directivity matrix $\mathbf{F}$) and operating characteristics; and (4) determine the radiated sound pressures of all the azimuthal mode orders at different lateral angles in a correlated manner to obtain the total far-field solution.

In the single mode analysis, this procedure needs to be done once for a given azimuthal mode cut-on at the fan plane. In the case of the multimodal analysis, it is necessary to execute these steps for each azimuthal mode cut-on at the fan plane.

In the previous chapter, the mode matching scheme was used to compute the transmitted modes, which is necessary for the solution of the sound radiation into the far-field, and their levels. As it was observed, the sideline and approach conditions yield scattered and transmitted modes at the exit plane, which depends on the solution obtained for each boundary layer thickness. For the sake of brevity, the results with Brambley boundary condition are omitted, and we will focus only on Ingard-Myers boundary condition and Pridmore-Brown solution. The results of the transmitted modal amplitudes at the exit plane for unitary incident amplitude are presented in Figure 51. It should be pointed out that the incident mode is scattered to all modes considered in the mode matching solution, even the cut-off modes (in these cases, with $n > 2$) that are not considered on the transmitted modes array $\mathbf{B}^+$. In Figures 51a and 51b, mode $(24, 1)$ and $(9, 1)$ are incident. The cases considering different boundary layers were defined in Figures 41 and 43. The scattered modes are distributed approximately symmetrical into two cut-on modes, where it is observed an important change of the energy between the modes is outlined at approach condition (see Figure 51b). In this case, the change in the modal amplitudes associated with the presence of a boundary layer is significant. Considering $\delta = 3\%$ and comparing to results with the uniform flow (i.e., $\delta = 0\%$), the second cut-on mode is greater than first one. It is interesting to note that the presence of the boundary layer also modify the modal scattering since the energy exchange is quite different in each case, which is directly

related to the performance of the liner, which will be reduced by the presence of boundary layer thickness.

Figure 51 – Transmitted modal amplitudes at exit plane for approach and sideline conditions based on results of the mode matching scheme in Section 5.3.

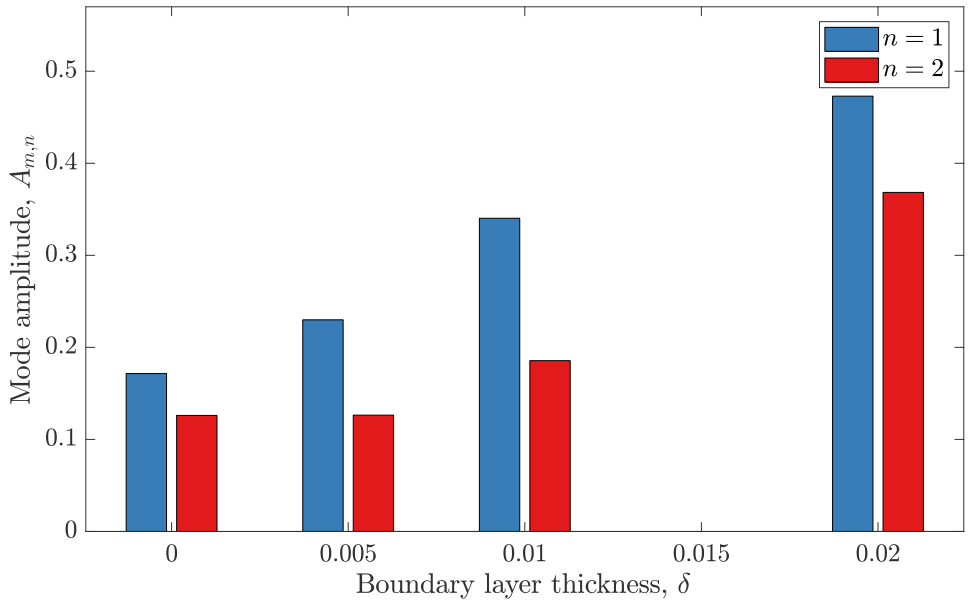

(a) Sideline condition

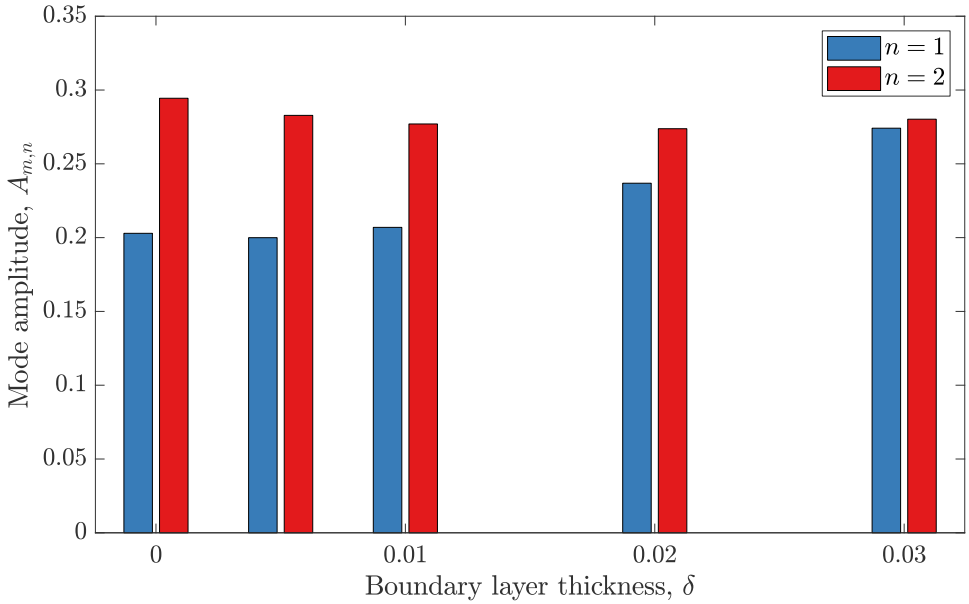

(b) Approach condition

Source – Own authorship.

6.2.2 Sound radiation pattern

The far-field sound radiation model was previously validated using the commercial finite element ACTRAN/TM in Chapter 4. In this case, the results are very accurate near the principal lobes and zeros, but the agreement is poor near angles of $90°$. The best results were observed when there is only one radiating mode. In this section, we assume that only in-duct convective effects modify the modal directivity pattern, which had the main issues explored in Section 6.1. Therefore, the external flow that may be present due to the aircraft movement (also called in-flight effect) is neglected, as in the case of a static engine test. Moreover, the attention can be concentrate on the investigation of the sound attenuation prediction in the far-field, due to the presence of shear flow in the in-duct propagation. Also, since the results of the radiation models have been similar to the forward arc, only Kirchhoff approximation is considered here.

Figures 52 to 54 present the far-field predictions considering different in-duct boundary layer thicknesses for each operating condition. Again, the results with Brambley boundary condition are omitted, and only Ingard-Myers boundary condition and Pridmore-Brown solution are presented. The far-field prediction in the presence of hard-wall (HW) was calculated directly by the formulation presented in Section 3.3.

At sideline condition (Figure 52), the main lobe of the directivity is located at approximately $63°$ and $84°$ for the two cut-on modes. The inclusion of a lined wall modifies the far-field directivity pattern slightly due to the small redistribution of acoustic energy into the two first cut-on radial modes. This redistribution does not change when the boundary layer is included. On the other hand, the presence of a boundary layer reduces liner attenuation in approximately $6\,\mathrm{dB}$ for $\delta = 1\%$, for instance.

At cutback condition, a substantial attenuation is observed in Figure 53 for both uniform and shear flow cases. The main lobe is concentrated at approximately $81°$ for mode $(24, 1)$. The far-field directivity pattern is only slightly shifted from hard wall prediction, and the boundary layer thickness clearly reduces the liner attenuation, even for a thin boundary layer.

At approach condition, the first radial mode $(9, 1)$ has two lobes concentrated at approximately $45°$ and $83°$, as seen in Figure 54 for the hard wall prediction. On the other hand, the second radial mode $(9, 2)$ has the maximum lobe at $66{,}5°$. In this case, the presence of a lined wall modifies the far-field directivity pattern due to the redistribution of the acoustic energy to other cut-on radial modes. This modal redistribution causes these modes to have approximately the same amplitude and almost the same radiated energy. The notch observed on the red line (at

approximately $66°$) is a result of the directivity pattern of the mode $(9, 1)$, and the maximum of the mode $(9, 2)$ is at $66{,}5°$. Due to scattering effects provided by liner, the second radial mode receives significant energy, and its maximum lobe covers the zero of mode $(9, 1)$. The inclusion of the boundary layer does not only modify this scattering effect (also observed in Fig. 51b), but it also slightly reduces the liner attenuation. In other words, the uniform mean flow prediction may be sufficiently accurate to estimate liner attenuation effect in the far-field for this condition.

Figure 52 – Predicted sound pressure level in the far-field for different boundary layer thickness at sideline condition.

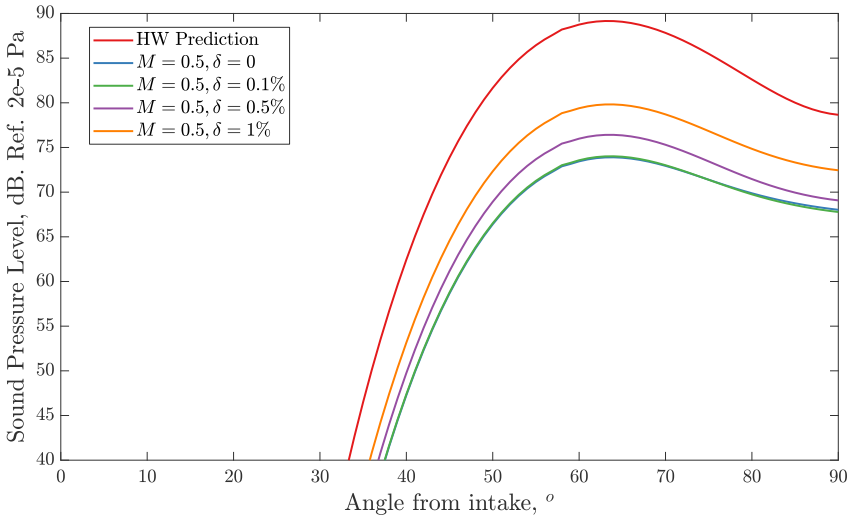

Source – Own authorship.

Figure 53 – Predicted sound pressure level in the far-field for different boundary layer thickness at cutback condition.

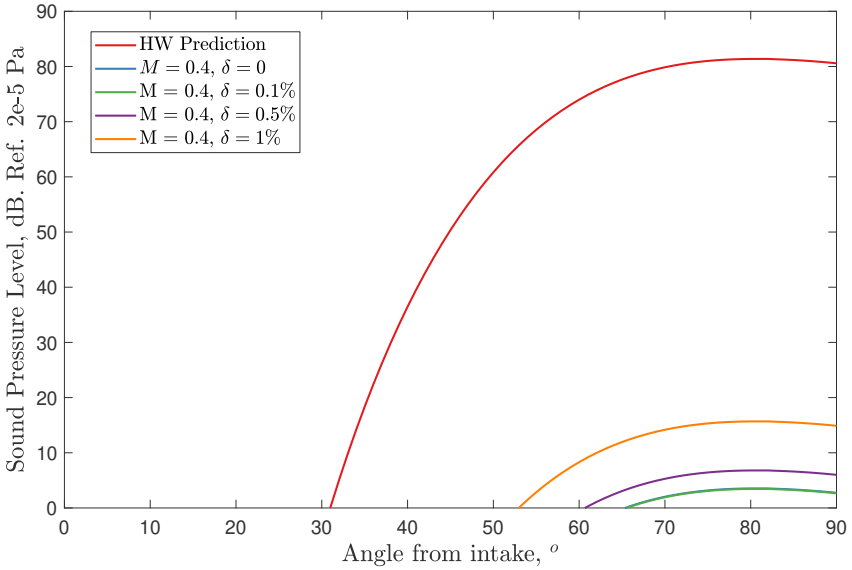

Source – Own authorship.

Figure 54 – Predicted sound pressure level in the far-field for different boundary layer thickness at approach condition.

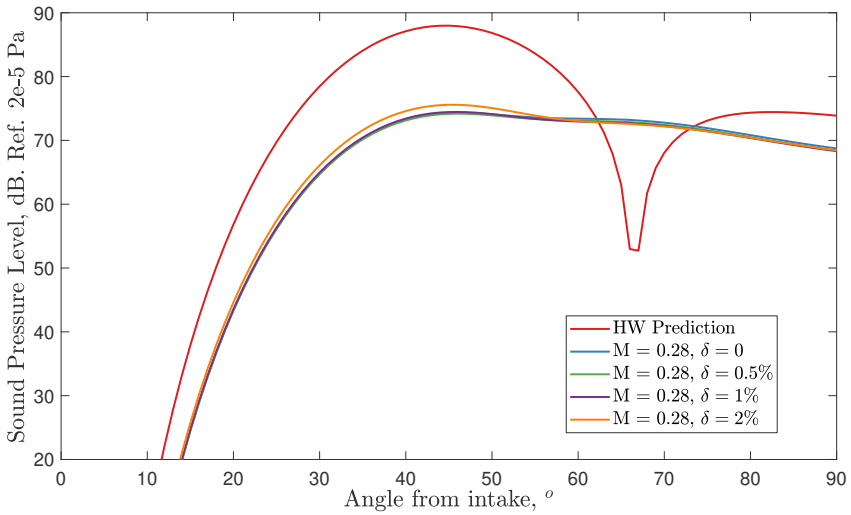

Source – Own authorship.

In summary, with the shear flow and impedance liner combination, the far-field sound radiation at certain operating conditions can be strongly affected in terms of the magnitude and shape. This is why these effects need to be taken account and predicted carefully for the design of acoustic linings for inlet applications. The combined effect with external flow leads to a significant issue that modifies the overall sound pressure computed for the fan noise component.

6.3 IMPEDANCE PARAMETRIC STUDY: FAR-FIELD RADIATION

This section can be understood as a continuation of the impedance parametric analysis carried out in Section 5.4. The keypoint, therefore, is to verify if the effects observed in the course of the Chapter 5 in terms of induct attenuation are also presented for the far-field radiation. The results on modal content considering the liner resistance and reactance varied around typical values for each operating condition are extrapolated in terms of far-field radiated noise. It comprehended the same process to determinate the modal amplitude outlined in Section 6.2.1. For the sake of brevity, only Kirchhoff approximation is considered here.

In Figures 55a, 55b, 55c, similar tendencies were observed to those seen for the transmission loss (see Fig. 46). The liner resistance variations impose modifications to the far-field sound pressure levels and the shape of the far-field pattern. The dash lines show the limits of the far-field sound pressure level for different values of liner resistance, while the solid line represents the mean value. In general, the bound limits are the results for the higher and lower

liner resistance at each condition. In agreement with section 6.2.2, the general tendency of the results depends mainly on the scattering effect (in the cases where there are two cut-on modes) and the modal attenuation provided by the liner impedance. The variation of the impedance resistance does not only modify the scattering behavior, but it also influences the liner attenuation, which decreases for thicker boundary layers. The most significant changes in the sound radiation pattern were associated with approach and sideline conditions, whereas the cutback condition produced the highest variations of the far-field sound pressure level. Depending on the liner resistance, this behavior can be easily understood from the combined effect of modal attenuation and scattering of each mode transmitted to far-field. In addition, at approach and sideline conditions, the resultant main lobe angle has varied quite differently (i.e., a consequence of modal amplitudes combination).

The reactance results for the acoustic far-field have also shown a significant impact in the attenuation and shape of the sound pressure levels as can be seen in Figure 56. In comparison with liner resistance results, the impact of the liner reactance variations may be considerably more significant for the condition studied here. Moreover, it follows the transmission loss results presented in the Section 5.4, which also modifies both the attenuation and the general shape of the curves, especially for lower Mach numbers and greater boundary layer thickness. At approach conditions (Figs. 56b), the second radial mode can be more critical than the first one. This trend was observed previously for the same operating condition in Fig. 51b, whereas the amplitude associated with the second cut-on mode may be higher than the first one. The resultant main lobe angle is almost the same for all cases.

As can be seen, the variation in the liner resistance and reactance for uniform flow and shear flow may be completely different at some operating condition. In the presence of shear flow with a thin boundary layer thickness (e.g., 0.5%), the far-field radiation is clearly affected. Also, the main lobe is affected, which may be modified for the case with more cut-on modes. This analysis can be extended to different boundary layer thicknesses, which would lead to different values of the magnitude of SPL and shape (i.e., as can be seen by the SPL variations in dash lines).

It must be noted that the previous section is based on a finite lined duct with a constant boundary layer thickness – the overall picture changes for aero-engines, as discussed in Section 5.1. First, duct radius is not constant, and neither Mach number inside the duct nor boundary layer thickness. Secondly, the high SPL also varies along the lined wall, and as consequence the liner impedance may be modified. Thus, the previous analysis provides some insight into liner

Figure 55 – Predicted far-field sound radiation considering the Pridmore-Brown solution for different values of boundary layer thickness and liner resistance: (a) Sideline,(b) Cutback (c) Approach. Colored solid line: mean value of the far-field sound radiation considering impedance variation. Colored dash lines: limits considering different liner resistances (corresponding to same values defined in Fig. 46).

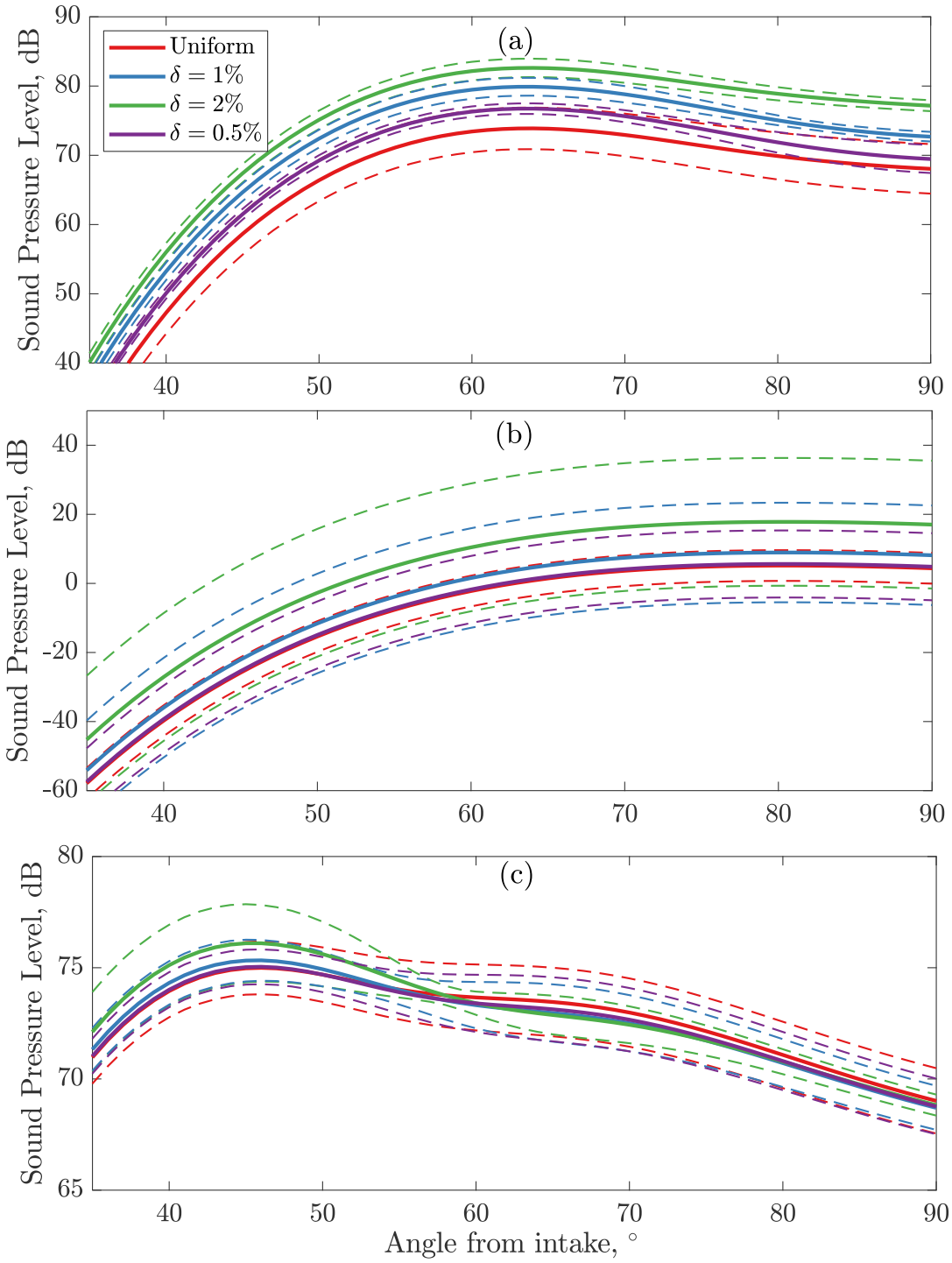

Source – Own authorship.

Figure 56 – Predicted far-field sound radiation considering the Pridmore-Brown solution for different values of boundary layer thickness and liner reactance: (a) Sideline,(b) Cutback (c) Approach. Colored solid line: mean value of the far-field sound radiation considering impedance variation. Colored dash lines: limits considering different liner reactances (corresponding to same values defined in Fig. 47).

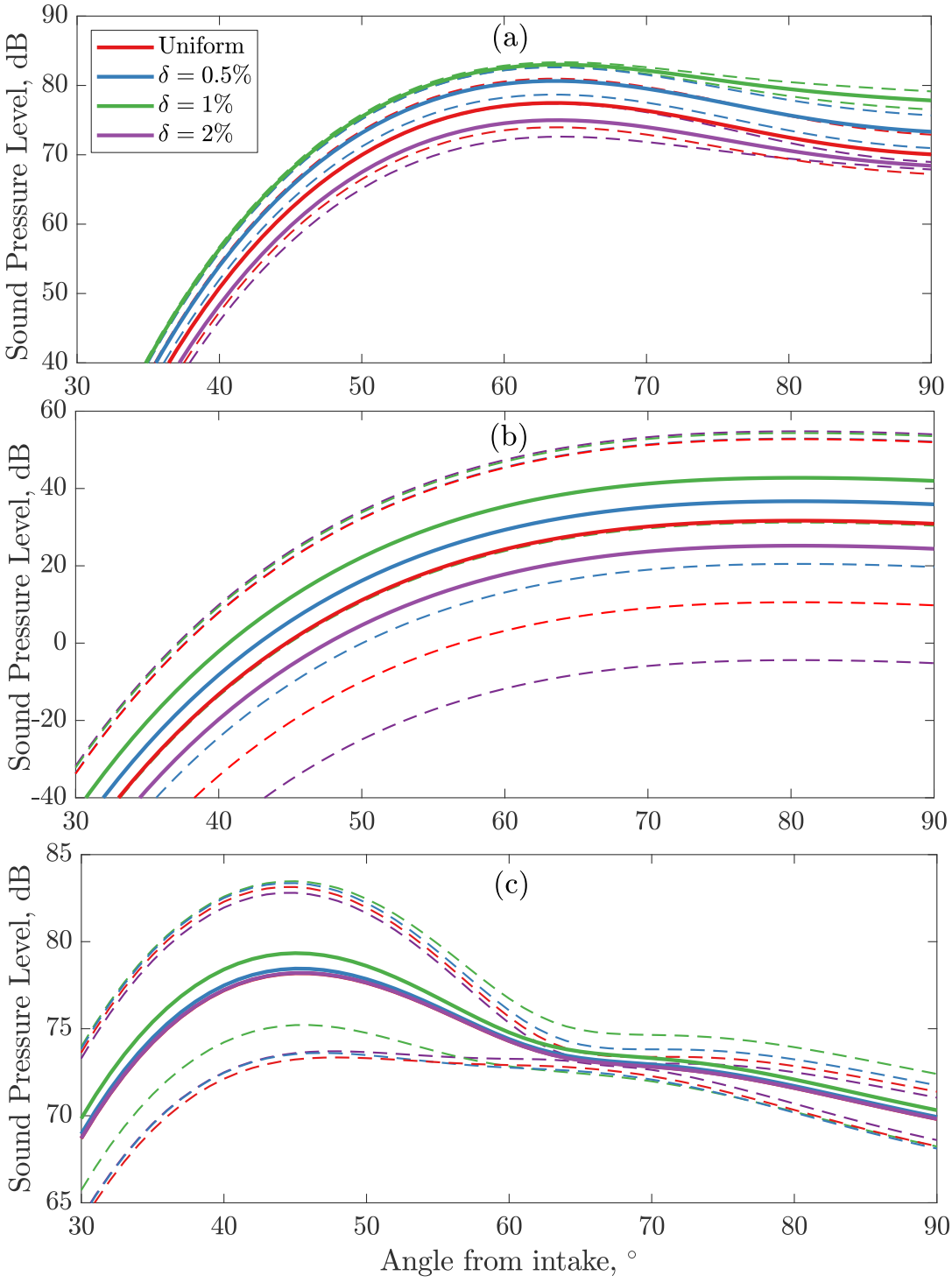

Source – Own authorship.

performance under shear flow effects at different conditions in terms of far-field radiation and in-duct propagation, but a more detailed analysis may be also required.

7 CONCLUSIONS AND FUTURE WORK

7.1 OVERALL CONCLUSIONS

Fan noise reduction remains a key technology in the context of the turbofan aero-engines. However, due to the complex environment to which fan noise is exposed, it remains a challenge to predict sound attenuation in different conditions correctly. The presence of flow gradients and liner impedance at different operating condition play a fundamental role in the sound propagation behavior. The work presented in this thesis is motivated by the need to better understand this complex scenario and properly predict the performance of acoustic liners in modern turbofan intakes to reduce community noise. In this sense, a predictive tool concept was proposed regarding fan noise attenuation by the acoustic liner. The main physical parameters of the acoustic field inside and outside of the nacelle (i.e., represented here as a straight duct) are considered. Then, the concept of attenuation provided by impedance for circular ducts with the shear flow, considering liner discontinuities (therefore, for a given finite liner) is investigated. Of particular interest are boundary layer effects, so both uniform and shear flows are analyzed inside and outside of the duct. On the following, the main conclusions from each chapter are summarized.

Chapter 3 reviews the formulation of the intake sound propagation and radiation available in the literature. These formulations were structured in two wireframe codes referred to "Liner Discontinuity Code" and "Free-field radiation code". The key point in the "Liner Discontinuity Code" is the presence of a sub-routine to determine duct eigenvalues, which depends extremely on the initial inputs and the numerical discretization of the duct radius (i.e., inherent to spectral method (TREFETHEN, 2000)). The numerical eigenvalue solver can be used to obtain the eigenvalues and radial form of the modes in the lined or hard-wall sections with uniform or shear flow. Moreover, the mode-matching scheme routine is presented in two versions (depending on the solution near the transition between rigid and lined surfaces): matching of P-V and M-M. "Liner Discontinuity Code" also offers the option for segmented liner solution, which was not exploited in this thesis, but it has important insights to increase the attenuation of fan tones at high engine powers. "Free-field radiation" code may read the output of the "Liner Discontinuity Code" to obtain the amplitude at exit plane. This code is simpler than "Liner Discontinuity" because it uses the modal solution in a hard-wall section only. Three different radiation models can be used in this code, based on Rayleigh, Kirchhoff approximations and Wiener-Hopf method. Several assumptions were taken to estimate the modal amplitudes asso-

ciated with the fan noise source (required by the code) to investigate tone noise components. It was observed that the liner performance can be sensitive to the modal content of the disturbance.

Chapter 4 presents a validation of the code developed in Chapter 3 by means of typical conditions for turbofan engines for the in-duct and radiation models, where the methods were compared with specialized FE software. At specific frequency and Mach number, different modes were used in this verification. The transmission loss does not only depend on the dissipation due to the acoustic impedance (strictly speaking in dissipation), but also may benefit from reflections at discontinuities in the duct (hard/soft walls and varying cross-section). The modal scattering provided by spinner presence can also become significant in such cases, which can be more critical for an attenuated mode that does not produce a significant reflection (RIENSTRA; EVERSMAN, 2001). Also, it has been observed that regions with a high variation on the mean flow (e.g., in the nacelle FE case) the propagating modes have an effective cut-off ratio less than the cut-off ratio used in the analytical approach and the straight duct FE model.

Another discussion arises from differences between the FE and the analytical solutions in terms of the far-field radiation. The lip geometry may play a role. This seems more important for modes near to the cut-off frequency of the duct. Thickness and curvature of the inlet lip have a significant influence on the modal directivity patterns. In some studies using ray tracing method in nacelles (DOUGHERTY, 1996), it is observed that the mechanism of diffraction around inlet lip is different for curved (or nacelles) and discontinuous (or unflanged duct) lips. Moreover, this scattered field vanishes at high frequencies.

The combined convection and relative frequency shift modify the modal directivity patterns. And, the presence of mean flow produce only convection effect on the frequency propagation for analytical methods. The FE models without finite lips (flanged and no-flanged models) follow this simplification closely. However, for the FE models with thick or finite lips, simulating a mean flow leads to a change of the physical modeling. Therefore, despite some discrepancies, the mode matching and radiation models implemented deal more accurately with well cut-on modes and display a reasonable agreement with FE models.

Chapter 5 analyzes the sound transmission considering the effects of the shear flow in lined ducts. In order to verify the boundary condition of the uniform flow compared to the other boundary conditions, a flow profile $M(r)$ was included in the mean flow. Three typical turbofan engine operating conditions were considered in this work: sideline, cutback, and approach. In order to investigate boundary layer effects over liner attenuation, a modified Ingard-Myers boundary condition proposed by Brambley (2011) was implemented and compared to

the Pridmore-Brown solution (PRIDMORE-BROWN, 1958). In the presence of thin boundary layers up to $\delta = 0.5\%$, the boundary condition by Brambley (2011) shows a good agreement with the Pridmore-Brown solution. For thicker boundary layers, some deviations were observed between them for the sideline condition. The same tendency was observed for the transmission loss prediction when increasing the boundary layer thickness, which displayed differences up to $0{,}5\,\mathrm{dB}$ for approach condition, $24\,\mathrm{dB}$ for cutback condition and $9{,}5\,\mathrm{dB}$ for sideline condition in comparison with uniform mean flow. Therefore, analyses based on Ingard-Myers boundary condition can lead to a significant error in transmission loss, especially for sideline and cutback conditions. From a parametric impedance study, it was observed that the acoustic field interaction with the boundary layer in the presence of the liner is also a function of the liner reactance and resistance. It has been suggested that this behavior may be linked to the refraction effects and the liner impedance approaching or getting away from its optimum value (SPILLERE; CORDIOLI, 2019), which can explain maximum attenuation lobes in the transmission loss results.

Chapter 6 focuses on the prediction of far-field sound radiation, considering the effect of the external and in-duct flow. Also, the liner attenuation in the presence of in-duct shear flow was considered here. The effects of flow velocity inside and outside of the duct are first investigated. It has been observed that as in-duct Mach number increases, the main lobe in the radiation pattern is shifted considerably toward the inlet axis when compared to zero Mach number radiation theory (i.e., $\theta^{\wedge}_{m,n} = \sin^{-1} 1/\eta_{m,n}$). On the other hand, as the external Mach number is increased, the noise radiation pattern is shifted away from the inlet axis (i.e., toward the sideline angle). However, this study considers only a direct solution of the radiation models (i.e., applied to the hard-wall solution). Then, by using a formulation to integrate a radiation model with the mode-matching method is possible to characterize the liner performances in terms of reduction of the noise to the far-field. The far-field noise prediction showed that the influence of liner impedance on the far-field directivity is far from simple, and the modal scattering at the liner discontinuities can result in complex behavior in terms of noise radiation, as observed for the approach condition. Also, the influence of the boundary layer thickness can lead to a reduction of liner attenuation, which is more prominent at higher Mach numbers, and even when different liner impedance is considered. Finally, from a parametric impedance study, it was observed that the variation in the liner resistance and reactance for uniform flow and shear flow might be completely different at some operating condition.

Finally, it should be pointed out that the analysis presented in this thesis is limited to

straight ducts with constant boundary layer thickness, which is not the case in aero-engines but should provide a first estimate of liner performance in terms of the in-duct transmission loss and far-field directivity pattern. On the other hand, the results obtained by the numeral methods are computationally expensive (e.g., FE and CFD methodologies)and still cannot account for more complex boundary conditions that include the boundary layer thickness. Then, the analytical modal expansion approach not only provides a reliable solution, but it is also computationally efficient. To better represent typical turbofan aero-engines, the effects of slowly varying duct radius and impedance transition should be investigated. Also, viscous effects and turbulent mixing have been neglected in this work, but they may also play a role in sound attenuation, and consequently in liner design. Last but not the least, the study also indicates the importance of considering shear flow effects on the propagation studies (especially for high Mach numbers) in the prediction to accurately calculate the liner transmission loss and the noise radiation to the far field at high fan speeds.

7.2 SUGGESTIONS FOR FUTURE WORK

This section summarizes the different research topics that can arise from the work in this thesis. Based on the work conclusions and the suggested recommendations given in the previous sections, the following future tasks are proposed:

- In order to be able to have clear information about the propagation of a single mode in the lined duct, it is proposed to run simple experiments with a few modes present. The results from these experiments can be used to validate the mode matching models for modes that are essentially cut-off or attenuate rapidly.

- The increased attenuation at high engine powers provided by this segmented liners could be investigated considering realistic flow profile. Also, the concept of a two-section axially segmented liner will be extended to a multi-section axially segmented liner. The aim is to analyze a single-mode at a given frequency, the optimum number of lined duct sections to improve the attenuation in this scenario.

- The shear flow effects employing Brambley boundary condition and Pridmore-Brown solution could be extended to include multiple-frequency and multi-modal analysis. Therefore, the same characteristics explored in Chapters 5 and 6 could be observed in terms of

a range of modes for a given frequency (e.g., assuming uncorrelated modes with equal energy per mode).

- Following the similar issues of the previous topic, the liner optimization could be performed concerning single layer liner construction characterized by liner resistance and reactance for tone and broadband source modeling. Also, the sound attenuation prediction affected by the presence of the boundary layer can be included to check whether trends found in this work are still valid. For instance, the use of response surface method (LAFRONZA et al., 2006) could be considered as an option for optimization studies when more design parameters are included.

- In order to extend the model used here for aft-fan radiation, the model has to be modified for annular geometry. Also, it is necessary to analytically and experimentally investigate the combination of liners impedance (inner radius and outer) in this sector of the engine to obtain an improved noise abatement device.

- By adapting the boundary condition solver for the linearized Navier-Stokes equation, the mode matching scheme will be able to explore the effect of the viscosity in the transmission loss. It will be challenging to investigate the effect of the sound propagation and radiation from the inlet of a turbofan by considering a turbulent flow profile.

- The model presented in this thesis does not account for the reflection of energy at the exit plane and source generation modeling at the fan stage. It will be challenging to investigate the effect of the complete modeling of fan noise each step by considering the whole propagation circuit (i.e., the noise propagated inside the duct and radiated out of the duct to the far field) as the sound source. A preliminary attempt at such an approach is the framework reported in Appendix C.

- An inverse methodology will be used to predict modes and their amplitudes radiated by a duct from far-field numerical and experimental data. The proposed method will be assessed during the model engine fan tests, which will include both in-duct modal analyses and free-field acoustic measurements. The main goal is to deduce the modal structure generated by the acoustic sources from free-field measurements without requiring any in-duct modal analysis.

- Most of the mathematical formulation in this work is valid for infinitely long straight ducts. In order to better represent typical turbofan aero-engines, effects of slowly varying (also called multiple-scales solution) duct radius transition should be investigated for modal sound transmission with the mean flow and acoustic lining. Ultimately, numerical simulations and experimental data can be used to validate this implementation.

REFERENCES

ACTRAN/TM. **Actran 17 Users Guide - Volume 1: Installation, Operations, Theory and Utilities**. English. Version Actran 17. Mont-Saint-Guibert, Belgium, 2016. 768 pp.

ANTWERPEN, B. V. et al. New advances in the use of Actran/TM for nacelle simulations. In: 14TH AIAA/CEAS Aeroacoustics Conference. Vancouver, Canada: AIAA No. 2008-2827, May 2008.

ASTLEY, R. J. Numerical methods for noise propagation in moving flows, with application to turbofan engines. **Acoustical Science and Technology**, v. 30, n. 4, p. 227–239, July 2009.

ASTLEY, R.; SUGIMOTO, R.; MUSTAFI, P. Computational aero-acoustics for fan duct propagation and radiation. Current status and application to turbofan liner optimisation. **Journal of Sound and Vibration**, v. 330, p. 3832–3845, 2011.

BERTON, J. System Noise Prediction of the DGEN 380 Turbofan Engine. In: 21ST AIAA/CEAS Aeroacoustics Conference. Texas, USA: No. AIAA 2015-2516, 22-26 June 2015.

BERTSCH, L.; GUERIN, S., et al. The Parametric Aircraft Noise Analysis Module - status overview and recent applications. In: 17TH AIAA/CEAS Aeroacoustics Conference (32nd AIAA Aeroacoustics Conference). Portland, Oregon: AIAA No. 2011-2855, June 2011.

BERTSCH, L.; SIMONS, D.; SNELLEN, M. **Aircraft Noise: The major sources, modelling capabilities, and reduction possibilities**. DLR IB 224-2015 A 110, 2015.

BODÉN, H. et al. On the effect of flow direction on impedance eduction results. In: 22ND AIAA/CEAS Aeroacoustics Conference. Lyon, France: No. AIAA 2016-2727, May 2016.

BODEN, H. et al. Comparison of the effect of flow direction on liner impedance using different measurement methods. In: 23RD AIAA/CEAS Aeroacoustics Conference. Denver, Colarado, US: No. AIAA 2017-3184, June 2017.

BOULEY, S. **Modélisations analytiques du bruit tonal dinteraction rotor/stator par la technique de raccordement modal**. 2017. Ph.D. Thesis.

BOYD, J. **Chebyshev and Fourier Spectral Methods: Second Revised Edition**. New York, USA: Dover Publications, 2001. (Dover Books on Mathematics).

BRAGA, D.; CORDIOLI, J. A.; REIS, D. Effect of uniform flow on liner attenuation prediction in aero-engine. In: XXVIII Encontro da Sociedade Brasileira de Acústica. Rio Grande do Sul, Brasil: Galoa, Outubro 3-5 2018.

BRAMBLEY, E. Well-posed boundary condition for acoustic liners in straight ducts with flow. **AIAA Journal**, v. 49, n. 6, p. 1272–1282, 2011.

BRAMBLEY, E. J. Fundamental problems with the model of uniform flow over acoustic linings. **Journal of Sound and Vibration**, v. 322, n. 4, p. 1026–1037, 2009.

BROOKS, J. C.; MCALPINE, A. Sound transmission in ducts with sheared mean flow. In: 13TH AIAA/CEAS Aeroacoustics Conference (28th AIAA Aeroacoustics Conference). Rome, Italy: AIAA No. 2007-3545, 2007.

CADOT-BURILLET, D. et al. Technology Evaluator: a global way of assessing low noise technologies. In: 28TH AIAA Aeroacoustics Conferences. Rome, Italy: AIAA No. 2007-3669, 21-23 may 2007.

CARO, S. CEAS-ASC highlights 2006. **Journal of Sound and Vibration**, Elsevier BV, v. 304, n. 3-5, p. 421–449, July 2007.

CASALINO, D.; HAZIR, A.; MANN, A. Turbofan Broadband Noise Prediction using the Lattice Boltzmann Method. In: 22ND AIAA/CEAS Aeroacoustics Conference. Lyon, France: No. AIAA 2016-2945, 30 May - 1 June 2016.

CASTRES, F. O.; JOSEPH, P. F. Mode detection in turbofan inlets from near field sensor arrays. **The Journal of the Acoustical Society of America**, v. 121, n. 2, p. 796–807, 2007.

CHAPMAN, C. J. Sound radiation from a cylindrical duct. Part 1. Ray structure of the duct modes and of the external field. **Journal of Fluid Mechanics**, Cambridge University Press, v. 281, p. 293–311, 1994.

CHEN, X. et al. A numerical method for computation of sound radiation from an unflanged duct. **Journal of Sound and Vibration**, Elsevier BV, v. 270, n. 3, p. 573–586, Feb. 2004.

CHUANG, H. A.; VERDON, J. M. **A Numerical Simulator for Three-Dimensional Flows Through Vibrating Blade Rows**. NASA CR-208511, 1998.

CUMMINGS, A. High Frequency Ray Acoustics Models for Duct Silencers. **Journal of Sound and Vibration**, v. 221, n. 4, p. 681–708, 1999.

DAI, X.; AUREGAN, Y. Acoustic of a perforated liner with grazing flow: Floquet-Bloch periodical approach versus impedance continuous approach. **The Journal of the Acoustical Society of America**, v. 140, n. 3, p. 2047–2055, 2016.

DOUGHERTY, R. Nacelle acoustic design by ray tracing in three dimensions. In: 2ND Aeroacoustics Conference. State College, USA: AIAA No. 1996-1773, May 1996.

DUNN, M. H. **TBIEM3D - A Computer Program for Predicting Ducted Fan Engine Noise (Version 1.1)**. NASA CR-206232, 1997.

DUNN, M. H.; TWEED, J.; FARASSAT, F. The Prediction of Ducted Fan Engine Noise Via a Boundary Integral Equation Method. In: 2ND AIAA Aeroacoustics Conference. State College, USA: AIAA No. 1996-1770, June 1996.

DUNN, M.; FARASSAT, F. Liner optimization studies using the ducted fan noise prediction code TBIEM3D. In: 4TH AIAA/CEAS Aeroacoustics Conference. AIAA No. 1998-2310, June 1998.

DUNN, M.; TWEED, J.; FARASSAT, F. The Application Of A Boundary Integral Equation Method To The Prediction Of Ducted Fan Engine Noise. **Journal of Sound and Vibration**, v. 227, n. 5, p. 1019–1048, 1999.

EATON, J. A. The influence of drainage slots on locally reacting acoustic panels. In: 5TH AIAA/CEAS Aeroacoustics Conference. Bellevue, WA: No. AIAA 99-1949, May 1999.

ENVIA, E.; TWEEDT, D. L., et al. **An Assessment of Current Fan Noise Prediction Capability**. NASA CR-215415, 2008.

ENVIA, E. Prediction of model scale turbofan exhaust tone noise. **International Journal of Aeroacoustics**, v. 15, n. 4-5, p. 395–429, 2016.

ENVIA, E.; WILSON, A. G.; HUFF, D. L. Fan Noise: A Challenge to CAA. **International Journal of Computational Fluid Dynamics**, v. 18, n. 6, p. 471–480, 2004.

EVERSMAN, W. Representation of a power law boundary layer in the sheared flow acoustic transmission problem. **Journal of Sound and Vibration**, Elsevier BV, v. 24, n. 4, p. 459–469, Oct. 1972.

EVERSMAN, W. The boundary condition at an impedance wall in a non-uniform duct with potential mean flow. **Journal of Sound and Vibration**, v. 246, n. 1, p. 63–69, 2001.

EVERSMAN, W.; HUBBARD, H. **Theoretical models for duct acoustics propagation and radiation. in Aeroacoustics of flight vehicles: Theory and practice**. NASA Langley Research Center, United States: NASA-RP-1258-VOL-2, 1991.

EVERSMAN, W. Effect of Boundary Layer on the Transmission and Attenuation. **The Journal of the Acoustical Society of America**, v. 49, n. 5, 1971.

FARASSAT, F.; CASPER, J. Towards an Airframe Noise Prediction Methodology: Survey of Current Approaches. In: 44TH AIAA Aerospace Sciences Meeting and Exhibit. AIAA No. 2006-210, Jan. 2006.

FARASSAT, F.; DUNN, M. H.; SPENCE, P. L. Advanced Propeller Noise Prediction in the Time Domain. **AIAA Journal**, v. 30, n. 9, p. 2337–2340, 1992.

GABARD, G. A comparison of impedance boundary conditions for flow acoustics. **Journal of Sound and Vibration**, v. 332, n. 4, p. 714–724, 2013.

GABARD, G. Boundary layer effects on liners for aircraft engines. **Journal of Sound and Vibration**, v. 381, p. 30–47, 2016.

GABARD, G. Noise Sources for Duct Acoustics Simulations: Broadband Noise and Tones. **AIAA Journal**, American Institute of Aeronautics and Astronautics (AIAA), v. 52, n. 9, p. 1994–2006, Sept. 2014.

GABARD, G.; ASTLEY, R. J. Theoretical model for sound radiation from annular jet pipes: far-field and near-field solutions. **Journal of Fluid Mechanics**, v. 549, p. 315, 2006.

GABARD, G.; ASTLEY, R. A computational mode-matching approach for sound propagation in three-dimensional ducts with flow. **Journal of Sound and Vibration**, v. 315, n. 4, p. 1103–1124, 2008.

GABARD, G.; BRAMBLEY, E. A full discrete dispersion analysis of time-domain simulations of acoustic liners with flow. **Journal of Computational Physics**, v. 273, p. 310–326, 2014.

GABARD, G. Mode-Matching Techniques for Sound Propagation in Lined Ducts with Flow. In: 16TH AIAA/CEAS Aeroacoustics Conference. Stockholm, Sweden: AIAA 2010-3940, June 2010.

GABARD, G.; DAZEL, O. A discontinuous Galerkin method with plane waves for sound absorbing materials. **International Journal for Numerical Methods in Engineering**, v. 104, May 2015.

GILLIAN, R. E. **Aircraft Noise Prediction Program: Users Manual**. NASA TM 84486, 1982.

GRACE, S. et al. Fan Broadband Interaction Noise Modeling. In: 18TH AIAA/CEAS Aeroacoustics Conference. Colorado, USA: No. AIAA 2012-2269, 2012.

HEIDMANN, M. **Interim prediction method for fan and compressor source noise**. NASA TM X-71763, 1979.

HEIDMANN, M.; SAULE, A.; MCARDLE, J. Predicted and Observed Modal Radiation Patterns from JT15D Engine with Inlet Rods. **Journal of Aircraft**, American Institute of Aeronautics and Astronautics (AIAA), v. 17, n. 7, p. 493–499, July 1980.

HERKES, W. H.; REED, D. H. **Modular Engine Noise Component Prediciton System (MCP): Technical Description and Assessment Document**. NASA CR 213526, 2005.

HOCTER, S. T. Exact and approximate directivity patterns of the sound radiated from a cylindrical duct. **Journal of sound and vibration**, v. 227, n. 2, p. 397–407, 1999.

HOMICZ, G.; LORDI, J. Note on the radiative directivity patterns of duct acoustic modes. **Journal of Sound and Vibration**, v. 41, p. 283–290, 1975.

INGARD, U. Influence of Fluid Motion Past a Plane Boundary on Sound Reflection, Absorption, and Transmission. **The Journal of the Acoustical Society of America**, v. 31, n. 7, p. 1035–1036, 1959.

JARON, R.; MOREAU, A.; GUERIN, S. Extrapolation of RANS flow data for improved analytical fan tone prediction. In: 21ST AIAA/CEAS Aeroacoustics Conference. Texas, USA: No. AIAA 2015-2515, 22-26 June 2015.

JOSEPH, P.; MORFEY, C. L. Multimode radiation from an unflanged, semi-infinite circular duct. **The Journal of the Acoustical Society of America**, v. 105, n. 5, p. 2590–2600, 1999.

KHAMIS, D.; BRAMBLEY, E. J. Viscous effects on the acoustics and stability of a shear layer over an impedance wall. **Journal of Fluid Mechanics**, Cambridge University Press (CUP), v. 810, p. 489–534, Dec. 2016.

KO, S.-H. Sound attenuation in acoustically lined circular ducts in the presence of uniform flow and shear flow. **Journal of Sound and Vibration**, v. 22, n. 2, p. 193–210, 1972.

KOLBREK, B. **Extensions to the Mode Matching Method for Horn Loudspeaker Simulation**. 2016. Ph.D. Thesis.

KONTOS, K. B.; JANARDAN, B. A.; GLIEBE, P. R. **Improved NASA-ANOPP Noise Prediction Computer Code for Advanced Subsonic Propulsion Systems**. NASA CR 195480, 1996.

KREJSA, E.; STONE, J. R. **Enhanced Fan Noise Modeling for Turbofan Engines**. NASA CR 218421, 2014.

LAFRONZA, L. et al. Response Surface Method Optimization of Uniform and Axially Segmented Duct Acoustics Liners. **Journal of Aircraft**, American Institute of Aeronautics and Astronautics, v. 43, n. 4, p. 1089–1102, July 2006.

LAW, T.; DOWLING, A.; CORRAL, R. Optimisation of axially segmented liners for aeroengine broadband noise. **Journal of Sound and Vibration**, v. 329, n. 21, p. 4367–4379, 2010.

LEGRIFFON, I. Aircraft noise modelling and assessment in the IESTA program with focus on engine noise. In: 22TH International Congress on Sound and Vibration. Florence, Italy: International Institute of Acoustics and Vibration (IIAV), Dec. 2015.

LEONARD, T. et al. Large Eddy Simulation of a scale-model turbofan for fan noise source diagnostic. In: 22ND AIAA/CEAS Aeroacoustics Conference. Lyon, France: AIAA No. 2016-3000, May 2016.

LEVINE, H.; SCHWINGER, J. On the Radiation of Sound from an Unflanged Circular Pipe. **Phys. Rev.**, v. 73, p. 383–406, 4 1948.

LEWY, S. Computation of Broadband Noise Radiated by a Ducted Fan in a Uniform Flow. **International Journal of Acoustics and Vibration**, v. 8, n. 4, p. 211–218, 2003.

LEWY, S. Inverse method predicting spinning modes radiated by a ducted fan from free-field measurements. **The Journal of the Acoustical Society of America**, v. 117, n. 2, p. 744–750, 2005.

LEWY, S. Numerical inverse method predicting acoustic spinning modes radiated by a ducted fan from free-field test data. **The Journal of the Acoustical Society of America**, v. 124, n. 1, p. 247–256, 2008.

LEWY, S. Overview on fan noise prediction. In: KOLLOQUIUM fur Fluid-und Thermodynamik. Siegen, Allemagne: Universitat Siegen, June 2002.

LEYLEKIAN, L.; LEBRUN, M.; LEMPEREUR, P. An Overview of Aircraft Noise Reduction Technologies. **AerospaceLab Journal**, v. 1, p. 1–15, 7 2014.

LIDOINE, S. et al. Acoustic radiation modelling of aeroengine intake comparison between analytical and numerical methods. In: 7TH AIAA/CEAS Aeroacoustics Conference. Masstricht, Netherlands: No. AIAA 2001-2140, 28-30 May 2001.

LOPES, L. V.; BURLEY, C. L. **ANOPP2 Users Manual: Version 1.2**. NASA TM 219342, 2016.

LOPES, L. V.; BURLEY, C. L. Design of the Next Generation Aircraft Noise Prediction Program: ANOPP2. In: 17TH AIAA/CEAS Aeroacoustics Conference. Portland, Oregon: No. AIAA 2011-2854, 2011.

LORDI, J.; HOMICZ, G. Effects of finite duct length and blade chord on noise generation bya rotating blade row. In: 7TH AIAA Fluid and Plasma dynamics conference. California, USA: AIAA No. 1974-555, June 1974.

MALBÉQUI, P.; ROZENBERG, Y.; BULTÉ, J. Aircraft Noise Prediction in the Iesta Program. In: INTER-NOISE 2011. Osaka, Japan, Apr. 2011.

MANCINI, S. et al. Boundary element formulation for wave propagation in weakly non-uniform potential flows. In: 22ND AIAA/CEAS Aeroacoustics Conference. Lyon, France: AIAA No. 2016-2713, May 2016.

MARX, D.; AURÉGAN, Y. Effect of turbulent eddy viscosity on the unstable surface mode above an acoustic liner. **Journal of Sound and Vibration**, v. 332, n. 15, p. 3803–3820, 2013.

MASSON, V. et al. The impedance boundary condition for acoustics in swirling ducted flow. **Journal of Fluid Mechanics**, Cambridge University Press (CUP), v. 849, p. 645–675, June 2018.

MCALPINE, A.; ASTLEY, R., et al. Acoustic scattering by an axially-segmented turbofan inlet duct liner at supersonic fan speeds. **Journal of Sound and Vibration**, v. 294, n. 4, p. 780–806, 2006.

MCALPINE, A.; FISHER, M. On the prediction of buzz-saw noise in aero-engine inlet ducts. **Journal of Sound and Vibration**, Elsevier BV, v. 248, n. 1, p. 123–149, 2001.

MCALPINE, A.; WRIGHT, M. Acoustic scattering by a spliced turbofan inlet duct liner at supersonic fan speeds. **Journal of Sound and Vibration**, v. 292, n. 3, p. 911–934, 2006.

MÖHRING, W. Energy flux in duct flow. **Journal of Sound and Vibration**, v. 18, n. 1, p. 101–109, 1971.

MOREAU, A.; GUERIN, S.; BUSSE, S. A method based on the ray structure of acoustic modes for predicting the liner performance in annular ducts with flow. In: NAG/DAGA International Conference on Acoustics. Rotterdam, Netherland: NAG/DAGA, 23 - 26 March 2009.

MOREAU, A.; AULICH, A.-L., et al. Optimization of casing contours in an aero-engine fan stage with emphasis on rotor-stator interaction noise. In: INTERNATIONAL Symposium on Transport Phenomena and Dynamics of Rotating Machinery. Hawaii, Honolulu: Pacific Center of Thermal-Fluids Engineering, Apr. 2016.

MORFEY, C. L. A note on the radiation efficiency of acoustic duct modes. **Journal of Sound and Vibration**, v. 9, n. 3, p. 367–372, 1969.

MORFEY, C. Acoustic energy in non-uniform flows. **Journal of Sound and Vibration**, v. 14, n. 2, p. 159–170, 1971.

MORFEY, C. Sound transmission and generation in ducts with flow. **Journal of Sound and Vibration**, v. 14, n. 1, p. 37–55, 1971.

MUNGUR, P.; GLADWELL, G. Acoustic wave propagation in a sheared fluid contained in a duct. **Journal of Sound and Vibration**, v. 9, n. 1, p. 28–48, 1969.

MUNT, R. M. The interaction of sound with a subsonic jet issuing from a semi-infinite cylindrical pipe. **Journal of Fluid Mechanics**, v. 83, n. 4, p. 609–640, 1977.

MUNT, R. Acoustic transmission properties of a jet pipe with subsonic jet flow: I. The cold jet reflection coefficient. **Journal of Sound and Vibration**, v. 142, n. 3, p. 413–436, 1990.

MUSTAFI, P. **Improved turbofan intake liner design and optimization**. 2013. Ph. D. Thesis – University of Southampton.

MYERS, M. K. On the Acoustic Boundary Condition in the Presence of Flow. **Journal of Sound and Vibration**, v. 71, n. 3, p. 429–434, 1980.

NARK, D. M.; ENVIA, E.; CASEY, B. L. Fan Noise Prediction with Applications to Aircraft System Noise Assessment. In: 15TH AIAA/CEAS Aeroacoustics Conference. Florida, United States: AIAA No. 2009-3291, Nov. 2009.

NAYFEH, A.; KAISER, J.; SHAKER, B. Effect of mean-velocity profile shapes on sound transmission through two-dimensional ducts. **Journal of Sound and Vibration**, v. 34, n. 3, p. 413–423, 1974.

OOSTEN, N. V.; COLLIN, D. NINHA: Noise Impact of aircraft with Novel engine configurations in mid- to High Altitude operations. In: INTER-NOISE 2014. Melboune, Australia: International Institute of Noise Control Engineering, Nov. 2014.

OPPENEER, M.; RIENSTRA, S. W.; SIJTSMA, P. Efficient Mode Matching Based on Closed-Form Integrals of Pridmore-Brown Modes. **AIAA Journal**, v. 54, n. 1, p. 266–279, Feb. 2016.

OVENDEN, N.; EVERSMAN, W.; RIENSTRA, S. Cut-on Cut-off Transition in Flow Ducts: Comparing Multiple-scales and Finite-element Solutions. In: 10TH AIAA/CEAS Aeroacoustics Conference. Manchester, Great Britain: AIAA No. 2004-2945, May 2004.

OVENDEN, N.; RIENSTRA, S. Mode-matching strategies in slowly varying engine ducts. **AIAA Journal**, v. 42, n. 9, p. 1832–1840, 2004.

OZYORUK, Y.; ALPMAN, E., et al. Frequency-domain prediction of turbofan noise radiation. **Journal of Sound and Vibration**, v. 270, n. 4, p. 933–950, 2004.

OZYORUK, Y.; LONG, L. N. Computation of sound radiating from engine inlets. **AIAA Journal**, American Institute of Aeronautics and Astronautics (AIAA), v. 34, n. 5, p. 894–901, 1996.

PETRIE, O.; BRAMBLEY, E. J. Nonlinear Acoustics in a Non-Parallel Boundary Layer over an Acoustic Lining. In: 2018 AIAA/CEAS Aeroacoustics Conference. AIAA No. 2018-3607, June 2018.

PIERCE, A. **Acoustics: An Introduction to Its Physical Principles and Applications**. Springer International Publishing, June 1989. v. 34.

POLACSEK, C.; BURGUBURU, S. Fan interaction noise predictions using RANS-BEM coupling. **International Journal of Aeroacoustics**, v. 4, n. 1, p. 153–168, 2005.

POLACSEK, C.; BURGUBURU, S., et al. Numerical simulations of fan interaction noise using a hybrid approach. **AIAA Journal**, v. 44, n. 6, p. 1188+1196, 2006.

PRIDMORE-BROWN, D. C. Sound Propagation in a Fluid Flowing Through an Attenuating Duct. **Journal of Fluid Mechanics**, v. 4, p. 393–406, 1958.

RARATA, Z. Application and assessment of time-domain DGM for intake acoustics using 3D linearized Euler equations. Aug. 2014.

RENOU, Y.; AURÉGAN, Y. Failure of the IngardMyers boundary condition for a lined duct: An experimental investigation. **The Journal of the Acoustical Society of America**, v. 130, n. 1, p. 52–60, 2011.

RICE, E. J. **A Model for the Acoustic Impedance of Perforated Plate Liner with Multiple Frequency Excitation**. NASA TM X-67950, 1971.

RICE, E.; HEIDMANN, M.; SOFRIN, T. Modal propagation angles in a cylindrical duct with flow and their relation to sound radiation. In: 17TH Aerospace Sciences Meeting. New Orleans, USA: American Institute of Aeronautics and Astronautics, Jan. 1979.

RICE, E. A. P. Multimodal Far-Field Acoustic Radiation Pattern Using Mode Cutoff Ratio. **AIAA Journal**, v. 16, n. 9, p. 906–911, Sept. 1978.

RIENSTRA, S. W. Acoustic radiation from a semi-infinite annular duct in a uniform subsonic mean flow. **Journal of Sound and Vibration**, v. 94, p. 267–288, 1984.

RIENSTRA, S. W. Sound transmission in slowly varying circular and annular lined ducts with flow. **Journal of Fluid Mechanics**, Cambridge University Press (CUP), v. 380, p. 279–296, Feb. 1999.

RIENSTRA, S. W. Sound Propagation In Slowly Varying Lined Flow Ducts Of Arbitrary Cross Section. **Journal of Fluid Mechanics**, v. 495, p. 157–173, 2003.

RIENSTRA, S. W.; DARAU, M. Boundary-layer thickness effects of the hydrodynamic instability along an impedance wall. **Journal of Fluid Mechanics**, Cambridge University Press, v. 671, p. 559–573, 2011.

RIENSTRA, S. **Fundamentals of Duct Acoustics**. Eindhoven, Netherlands: Von Karman Institute Lecture Notes, 2016.

RIENSTRA, S.; HIRSCHBERG, A. **An Introduction to Acoustics**. Eindhoven, Netherlands: TR-IWDE-92-06, Technische Universiteit Eindhoven, 2015.

RIENSTRA, S. Sound Propagation in Slowly Varying 2D Duct with Shear Flow. In: 22ND AIAA/CEAS Aeroacoustics Conference. American Institute of Aeronautics and Astronautics, May 2016.

RIENSTRA, S. w.; EVERSMAN, W. A numerical comparison between the multiple-scales and finite-element solution for sound propagation in lined flow ducts. **Journal of Fluid Mechanics**, Cambridge University Press, v. 437, p. 367–384, 2001.

ROLT, A. M.; KYPRIANIDIS, K. G. Assessment of new aeroengine core concepts and technologies in the EU framework 6 NEWAC programme. In: 27TH International Congress of the Aeronautical Sciences (ICAS 2010). Nice, France: International Astronautical Federation, Sept. 2010.

SANDERS, L.; MALBÉQUI, P.; LEGRIFFON, I. Capabilities of iesta-carmen to predict aircraft Noise. In: 23RD International Congress on Sound and Vibration. Athens, Greece: International Institute of Acoustics and Vibration (IIAV), Oct. 2016.

SHUR, M. et al. Effect of Inlet Distortions on Ducted Fan Noise. In: 22ND AIAA/CEAS Aeroacoustics Conference. Lyon, France: No. AIAA 2016-2819, 30 May - 1 June 2016.

SMITH, M. J. **Aircraft Noise**. Cambridge, England: Cambridge University Press, 2004.

SNAKOWSKA, A.; JURKIEWICZ, J.; GORAZD, L. A hybrid method for determination of the acoustic impedance of an unflanged cylindrical duct for multimode wave. **Journal of Sound and Vibration**, v. 396, p. 325–339, 2017.

SPILLERE, A. **Towards optimal design of acoustic liners in turbofan aero-engines**. 2017. Masters Thesis – Universidade Federal de Santa Catarina.

SPILLERE, A. M.; CORDIOLI, J. A. Optimum acoustic impedance in circular ducts with inviscid sheared flow: Application to turbofan engine intake. **Journal of Sound and Vibration**, v. 443, p. 502–519, 2019.

TESTER, B. Ray models for sound propagation and attenuation in ducts, in the absence of mean flow. **Journal of Sound and Vibration**, Elsevier BV, v. 27, n. 4, p. 515–531, Apr. 1973.

TOPOL, D. A.; HUFF, D. L. **TFaNS-Tone Fan Noise Design/Prediction System: Users' Manual TFaNS Version 1.5**. NASA CR-212380, 2003.

TREFETHEN, L. **Spectral Methods in MATLAB**. Pennsylvania, USA: Society for Industrial and Applied Mathematics (SIAM), 2000.

TYLER, J. M.; SOFRIN, T. G. Axial flow compressor noise studies. **Transactions of the society of automotive engineers**, v. 70, p. 309–332, 1962.

VERDON, J. M.; MONTGOMERY, M. D.; CHUANG, H. A. **Development of a Linearized Unsteady Euler Analysis with Application to Wake/Blade-Row Interactions**. NASA CR-208879, 1999.

VILENSKI, G.; RIENSTRA, S. W. On hydrodynamic and acoustic modes in a ducted shear flow with wall lining. **Journal of Fluid Mechanics**, Cambridge University Press, v. 583, p. 45–70, 2007.

WEINSTEIN, L. **The Theory of Diffraction and the Factorization Method**. Colorado, USA: Golem Press, 1974.

WENG, C. **Theoretical and numerical studies of sound propagation in low-Mach-number duct flows**. 2015. Ph.D. Thesis – KTH, Linné Flow Center, FLOW.

ZELLMANN, C. et al. Aircraft Noise Emission Model Accounting for Aircraft Flight Parameters. **Journal of Aircraft**, American Institute of Aeronautics and Astronautics (AIAA), v. 55, n. 2, p. 682–695, 2018.

ZHANG, Q.; BODONY, D. J. Numerical investigation of a honeycomb liner grazed by laminar and turbulent boundary layers. **Journal of Fluid Mechanics**, Cambridge University Press, v. 792, p. 936–980, 2016.

APPENDIX A – SOUND POWER TRANSMISSION

A.1 MODAL ACOUSTIC POWER

In some cases, a basic assessment of the validity of the computations consists of checking that sound powers inside the duct and the radiated to the far-field are equal. Morfey (1971a) defined that the sound power, as the surface integral, extends the continuity property of sound power for homo-entropic and irrational flows. Thus, the acoustic power of a given mode in the presence of mean flow is calculated by integrating the axial acoustic intensity over the duct cross-section, expressed by Morfey (1971a,b) as

$$\mathcal{P} = 2\pi \int_0^1 I_x(r)\, dr \tag{A.1}$$

where the (non-dimensional) axial acoustic intensity $I_x(r)$ is

$$I_x(r) = \frac{1}{2}\mathrm{Re}\{(\hat{p} + M_0\hat{u})(\overline{\hat{u} + M_0\hat{p}})\}, \tag{A.2}$$

where Re denotes real part, and the overline symbol is the complex conjugate. In the rigid duct sections, the sound power is the sum of the power in all the cut-on modes (i.e., each mode can be summed because the mode shapes are orthogonal). The modal axial sound intensity can be given by (MORFEY, 1971a)

$$I^{\pm}_{x,m,n}(r) = \frac{1}{2}\mathrm{Re}\left[(1 - M_0^2)p^{\pm}_{m,n}\overline{u^{\pm}_{m,n}} + M_0|p^{\pm}_{m,n}|^2 + M_0|u^{\pm}_{m,n}|^2\right], \tag{A.3}$$

and by using acoustic pressure (Eq. (2.16)) and velocity (Eq. (2.17)) definitions, it is straightforward to show that

$$I^{\pm}_{x,m,n}(r) = \frac{1}{2}\mathrm{Re}\left[|A^{\pm}_{m,n}|^2 J_m(\alpha_{m,n}r)^2 \left(\frac{k}{(k - k^{\pm}_{m,n}M_0)^2}\right) \left(kM_0 + k^{\pm}_{m,n}(1 - M_0^2)\right)\right]. \tag{A.4}$$

On the other hand, Möhring (1971) defined an equivalent acoustic intensity expression for shear flows, which leads to an acoustic intensity given as

$$I^{\pm}_{x,m,n}(r) = \frac{1}{2}\mathrm{Re}\left\{|A_{m,n}|^2 \left(\frac{k}{k - k^{\pm}_{m,n}M}\right) \left[\frac{-k}{2(k - k^{\pm}_{m,n}M)}\frac{dM}{dr} \frac{d|\Psi_{m,n}(r)|^2}{dr} + (kM + k^{\pm}_{m,n}(1 - M^2))\right]\right\}. \tag{A.5}$$

Note that "cross-terms" were neglected in the Eq. (A.5) from the original equation, which computes the interactions between different modes and their coherence. It has been found that the contribution of the "cross-terms" is small (BROOKS; MCALPINE, 2007). This assumption implies that one can use an incoherent sum of the individual sound power in the case of non-uniform flow as well.

The sound power in free field is also deduced from the integration of the axial component of the time-averaged sound intensity (Eq. (A.2)) computed on a sphere of radius D and the same velocity is taken throughout the space to avoid any flow mismatch in the exit plane ($M_0 = M_\infty$). Thus applying the axial component of acoustic velocity $\hat{u}$ and pressure $\hat{p}$ definition and following the notation in Figure 21, the sound intensity (non-dimensional) in a uniform flow of velocity is given as

$$I_x^{\text{rad}} = \frac{1}{2}\text{Re}\Big[(1 - M_0^2\cos\theta)p^{\text{rad}}u^{\text{rad}} + M_0\cos\theta(p^{\text{rad}})^2 + M_0\cos\theta(u^{\text{rad}})^2\Big]. \tag{A.6}$$

Again the momentum equation links $\hat{u}$ to $\hat{p}$, and this relation can be written as $u^{\text{rad}} = p^{\text{rad}}/\sqrt{1 - M_0^2\sin^2\theta}$ (neglecting the second order term (LEWY, 2002)) and Eq. (A.6) becomes

$$I_x^{\text{rad}} = \frac{1}{2}\text{Re}\left[\frac{1 - M_0^2\cos\theta}{\sqrt{1 - M_0^2\sin^2\theta}} + \left(1 + \frac{1}{\sqrt{1 - M_0^2\sin^2\theta}}\right) M_0\cos\theta\right](p^{\text{rad}})^2. \tag{A.7}$$

Finally, the sound power radiated in the half-space $0 < \theta < \pi/2$, i.e., for the intake region, is given by

$$\mathcal{P}^{\text{rad}} = 2\pi D^2 \int_0^{\pi/2} I_x^{\text{rad}}\sin\theta\, d\theta, \tag{A.8}$$

which can be evaluated from the traditional integration methods (e.g. trapezoidal, rectangular, Simpson methods etc.).

A.2 TRANSMISSION LOSS

To assess the sound power transmitted by the modal pressure field, it assumes that all incident acoustic energy is concentrated on the first radial mode[1]. Therefore, the transmission loss can be expressed as a relation between cut-on mode amplitudes, in terms of the sound power, before and after the lined duct, given by

$$\Delta_{\text{PWL}} = 10 \log_{10} \frac{\mathcal{P}_{m,1}^{I+}}{\sum_{n=1}^{n_c} \mathcal{P}_{m,n}^{N_s+}} \tag{A.9}$$

where n_c is the total number of cut-on modes for a given azimuthal mode order m, as defined by Eq. (2.21). $\mathcal{P}_{m,1}^{I+}$ is the power associated with the single incoming mode at the fan plane (in segment I), and $\mathcal{P}_{m,n}^{III+}$ (or $\mathcal{P}_{m,n}^{IV+}$ for segmented liner) is the power of the propagating (scattered) mode of order (m, n_c) at the exit plane (in last segment N_s). The summation is performed over all of the propagating modes. Also, it is convenient to define the transmission loss in terms of SPL as

$$\Delta_{\text{SPL}} = 20 \log_{10} \frac{A_{m,1}^{I+}}{\sum_{n=1}^{n_c} A_{m,n}^{N_s+}}, \tag{A.10}$$

which implies that the sound pressure spectrum, for the lined duct, can be found by subtracting directly the values of Δ_{SPL} from the sound pressure spectrum for the hard-walled duct.

[1] Even if there are more cut-on modes, one can easily assume the propagation of a single mode. In other words, the modal amplitude of higher order radial modes is negligible when compared to the first radial mode. It is a common assumption made to evaluate results without dependence on the phasing of the multiple incident mode. Lafronza et al. (2006) and Law, Dowling, and Corral (2010) have shown that phasing between the incident modes has a small effect on transmitted power.

APPENDIX B – VALIDATION OF THE WAVENUMBER SOLVER

B.1 CONVERGENCE ANALYSIS

In this appendix, the necessary number of grid points for convergence of the wavenumber is investigated. Therefore, one can defined the error function as (MARX; AURÉGAN, 2013)

$$\gamma_{m,n}(N_p) = \max\left(\left|\frac{\text{Re}\,(k_{m,n}(N_p) - k_{m,n}^{ref})}{\text{Re}\,(k_{m,n}^{ref})}\right|, \left|\frac{\text{Im}\,(k_{m,n}(N_p) - k_{m,n}^{ref})}{\text{Im}\,(k_{m,n}^{ref})}\right|\right). \tag{B.1}$$

The reference value $k_{m,n}^{ref}$ is given by the best resolution available, in this work $N_p = 500$. Higher resolutions were also tested and no significant change in the results were observed.

For support the chapter 5, we consider as reference case the sideline condition ($k = 31$, $M = 0.5$ and $m = 24$) and boundary layer thickness of $\delta = 0.1\%$ and 2%. Figure 57 shows the error as function of the number of grid points for high order radial modes ($n = 10$, 20 and 30) which are necessary for the mode matching scheme, in both upstream and downstream directions. For uniform flow, high accuracy is achieved even for a small number of grid points. For shear flow, more grid points are necessary, specially for thin boundary layers, and a relatively small error of 10^{-10} is achieved with $N_p = 400$.

B.2 TRAJECTORIES OF AXIAL WAVENUMBER

The axial wavenumber can vary significantly for each boundary layer thickness in the operating conditions considered in this work. The trajectory of these wavenumbers in the complex plane (also called k-plane) can give valuable insights about in-duct acoustic behavior and transmission loss prediction using the mode-matching technique. Thus, to illustrate this behavior, the trajectories are shown in Figure 58. The results are based on an exact solution to the Pridmore-Brown equation, as outlined in the previous sections, and include both hard and soft wall boundary conditions. The boundary layer thickness varies from 0.1% to 2%. It can be observed that the upstream propagating modes are mostly affected by the presence of a boundary layer in all conditions. Moreover, in most cases, the imaginary part of the axial wavenumber of cut-on modes is reduced as boundary layer thickness increases, which is associated with the reduction in transmission loss predictions.

It has been pointed out that Figure 58 is consistent with Fig. 44, which in the k-plane shows at each operating condition that the higher spacing from the real axis (i.e., corresponding

Figure 57 – Convergence of the wavenumber as function of the number of grid points N_p for (a) uniform flow and (b) shear flow with $\delta = 0.1\%$ and (c) shear flow with $\delta = 2\%$. High order radial modes considered $n = 10$ (blue), 20 (red) and 30 (green) in upstream (——) and downstream ($- - -$) directions.

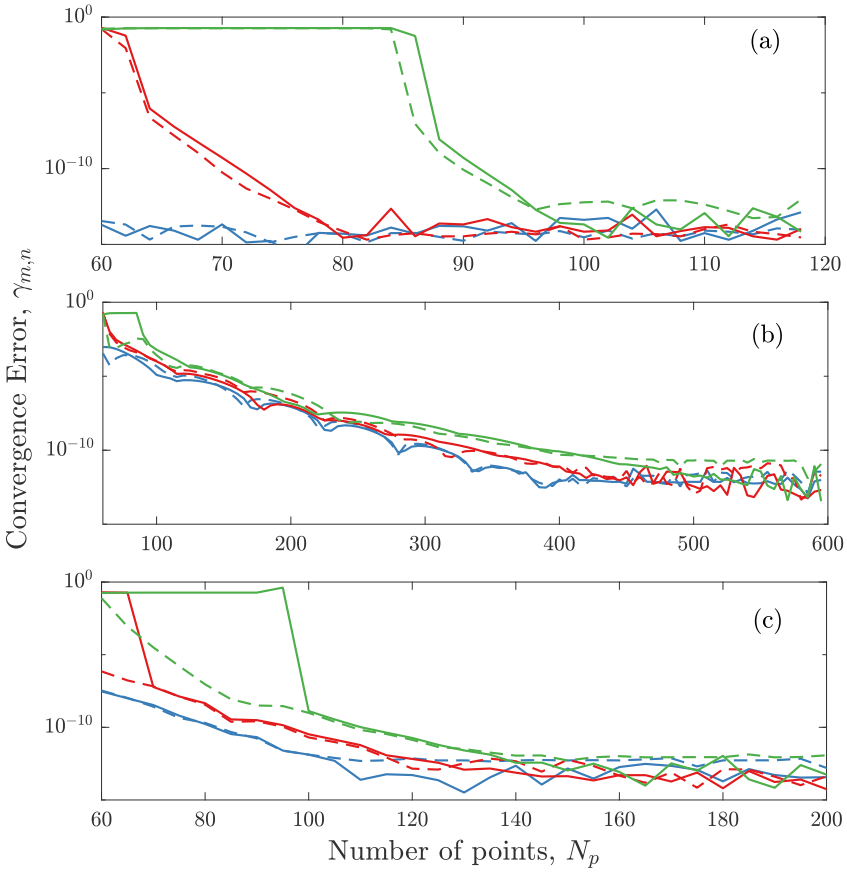

Source – Own authorship.

a higher modal attenuation) happens for upstream propagation for thin boundary layer, and the pressure of a mode in the lined section decreases theoretically like $\exp[-\mathrm{Im}(k_{m,n})x]$.

Figure 58 – Trajectories of the axial wavenumbers k_{mn} for upstream (red) and downstream (black) propagation at sideline condition varying with δ. Hard wall and (left) soft wall (right) solutions. Symbol • represents the final value of δ in analysis.

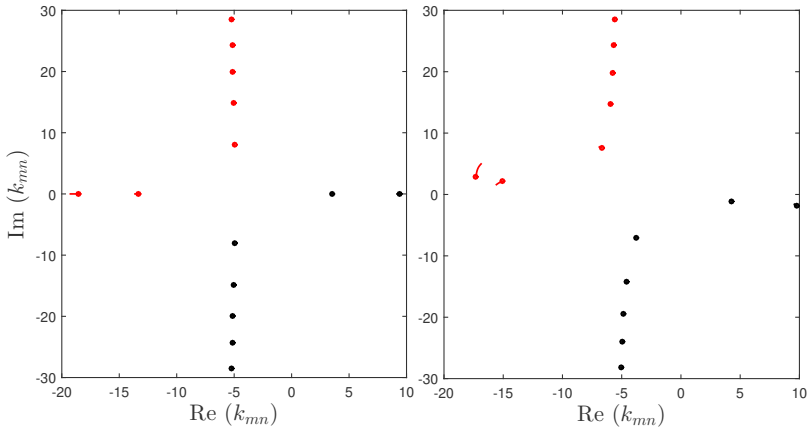

(a) Approach condition.

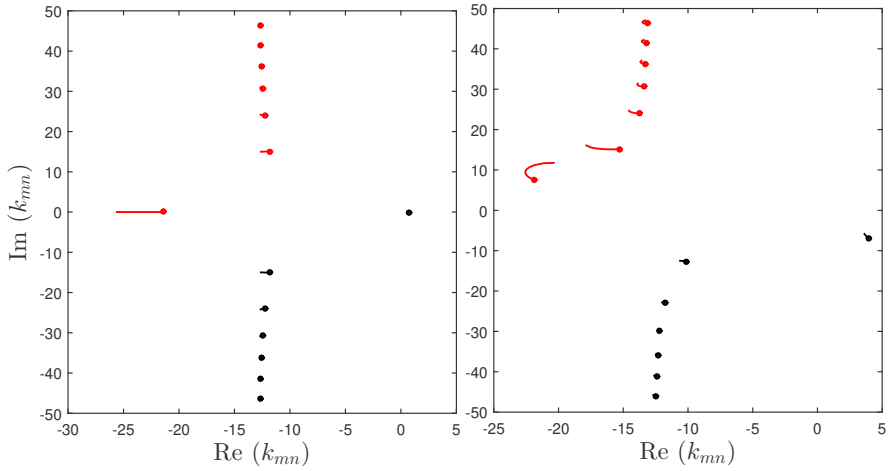

(b) Cutback condition

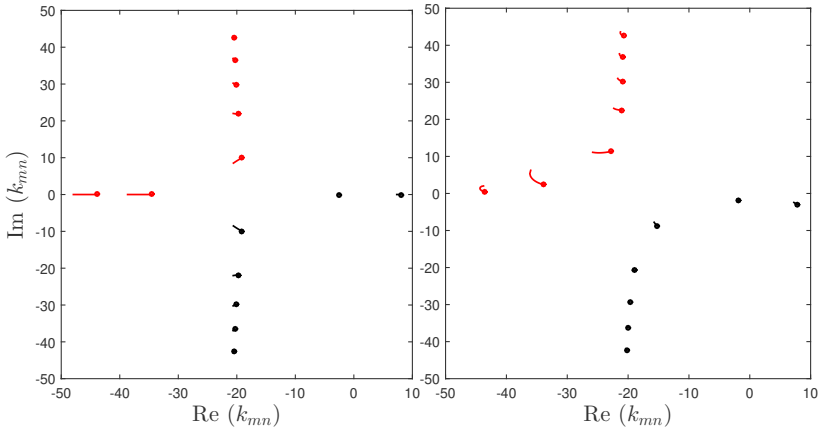

(c) Sideline condition

Source – Own authorship.

APPENDIX C – COMPUTATIONAL TOOL - MODAL2FAN

This appendix describes briefly a computational tool in the modular form with the fidelity and flexibility necessary to predict the aero-engine fan noise in different flight conditions, named here as MODular ALgorithm to FAn Noise (MODAL2FAN). The implementations described in this thesis (i.e., in Chapter 3) are part of this current tool. The simulation framework has been planned for a mathematical language capable of connecting the different modules through a modal approach. This approach was chosen because it is a complete and simple base for any solution (even in conditions with more complex behavior in terms of mean flow and acoustic field). Therefore, the sound generation, propagation, and radiation solution steps can be written by modal solutions, which would allow their integration. Then, different methods can be compared by MODAL2FAN, where the user can choose from a range of possibilities for predictions based on the fidelity requested at execution speed.

The structure of the tool proposed is similar to the architecture of ANOPP2, IESTA, and PANAN described in Section 2.2.1. On the current parametric tool, the input data can be more straightforward with the operation, geometry (engine and acoustics parameters), modal amplitudes and acoustic metrics or, in the case of hybrid tools, more involved with geometric definitions in CAD or mesh. As output data, the code will always address the SPL spectra and total SPL directivity, in the required metric and the distance from the source, as well as the modal and total attenuation obtained with the acoustic treatment.

The Data-flow diagram (DFD) of the MODAL2FAN tool is shown in Figure 59. The red boxes and their line connections are the auxiliary functions considered in the scope of this thesis. Initially, the input parameters are required by the command platform in two different ways: engine/acoustic characteristics and geometry file. In this diagram, the numbered boxes are the auxiliary functions that will be connected to the four main modules (preprocessing, generate the source, propagate the modes, calculate the radiation). The key idea is to select the individual models (analytical, numerical, experimental, or SE) for a given stage of fan noise prediction. The databases represent numerical solutions obtained by external software or the input of the experimental data.

Figure 59 – Data-flow diagram of the Framework and functional modules of the MODAL2FAN. The Highlighted red boxes represent the functions considered in this work.

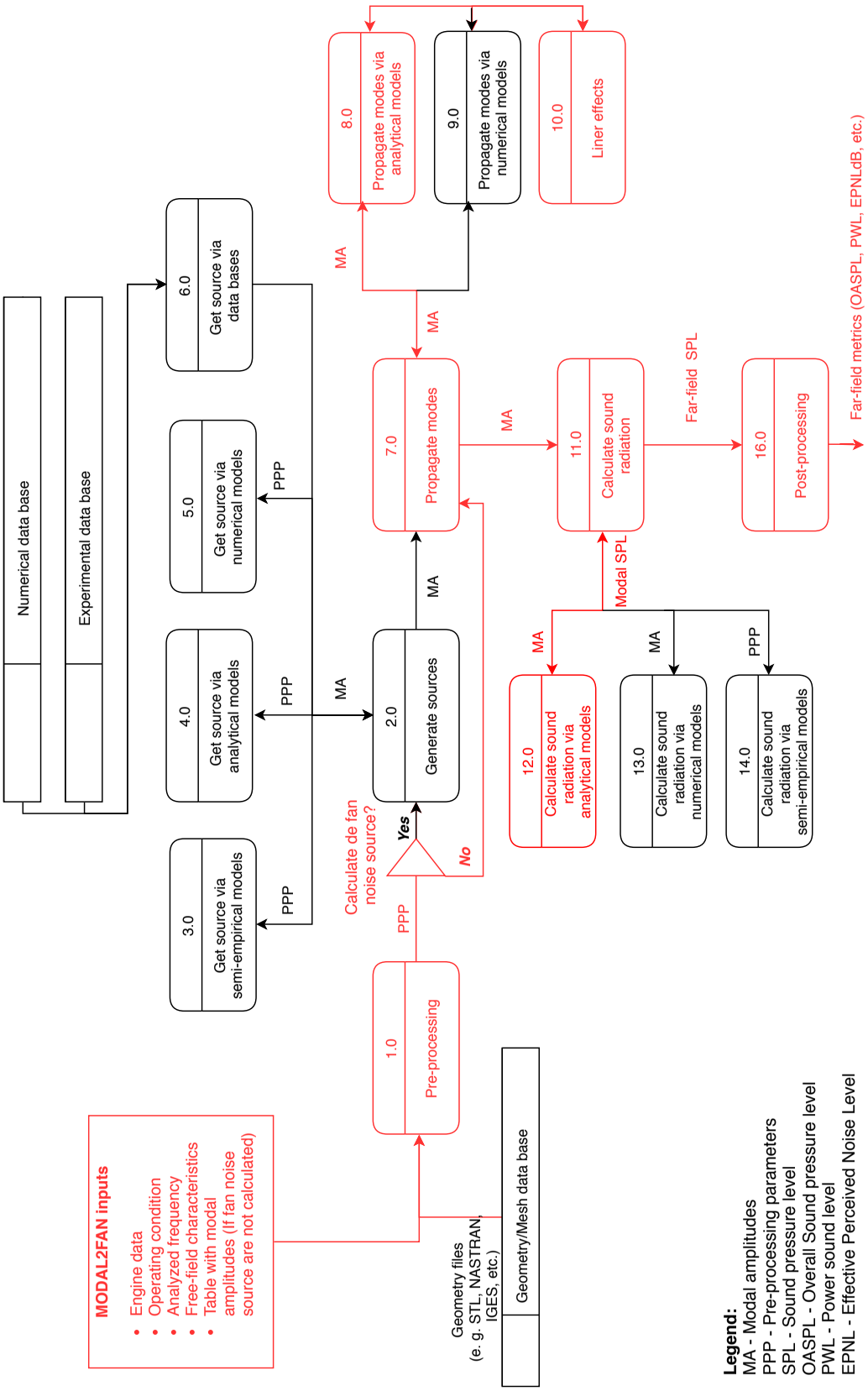

Source – Own authorship.

APPENDIX D – LIST OF PAPERS

D.1 JOURNAL PAPERS

BRAGA, D.; SPILLERE, A. M. N.; DA SILVA, A. R.; CORDIOLI, J. A.; REIS, D. C. Intake fan noise attenuation due to liners considering uniform and shear flows. **American Institute of Aeronautics and Astronautics (AIAA) Journal**, vol. 57:8, pp. 3480-3492, 2019.

D.2 CONFERENCE PAPERS

BRAGA, D.; SPILLERE, A. M. N.; DA SILVA, A. R.; CORDIOLI, J. A.; REIS, D. C. On the prediction of far-field fan noise attenuation due to liners considering uniform and shear flows. In: 24th AIAA/CEAS Aeroacoustics Conference. Atlanta, USA: No. AIAA 2018-2898, 2529 June 2018.

BRAGA, D.; CORDIOLI, J. A.; REIS, D. Effect of uniform flow on liner attenuation prediction in aero-engine. In: XXVIII Encontro da Sociedade Brasileira de Acústica. Rio Grandedo Sul, Brasil, Outubro 35, 2018.

SPILLERE, A.; BRAGA, D.; SEKI, L.; BONOMO, L. A.; CORDIOLI, J. A.; MARTINEZ, B.; GRECO, P. C.; REIS, D. C.; COELHO, E. L. Inlet liner design for a fan noise test rig. In: 25th AIAA/CEAS Aeroacoustics Conference. Delft, Netherlands: AIAA No. 2019-2724, 2023 May 2019.

D.3 OTHER PAPERS

The following papers are not directly linked to this thesis, but also they were essential for the overall research:

NETO SANTANA, J. P.; BRAGA, D.; DA SILVA, A. R.; CORDIOLI, J. A. Predictions of the far-field noise due to vortex-shedding using a lattice boltzmann scheme and an acoustic analogy. In: 22nd International Congress on Acoustics.Buenos Aires, Argentina: ICA2016-802, September 59, 2016.

BRAGA, D.; NETO SANTANA, J. P.; DA SILVA, A. R.; CORDIOLI, J. A.;. Assessment of the far-field sound radiation of ducts using the lattice boltzmann method and a two-dimensional ffwocs williams and hawkings formulation. In: 22nd International Congress on Acoustics. Buenos Aires, Argentina: ICA2016-802, September 59, 2016.

NETO SANTANA, J. P.; BRAGA, D.; DA SILVA, A. R.; CORDIOLI, J. A. Numerical investigation of normal mode radiation properties of ducts with low mach number incoming flow. In: Meeting of the Acoustical Society of America, Acoustical Society of America (ASA), v. 141, n. 5, p. 39583958, May 2017.

BRAGA, D.; CORDIOLI, J. A.; REIS, D. Predição via modelos semi-empíricos do ruído de fan gerado por motores aeronáuticos. In: XXVII Encontro da Sociedade Brasileira de Acústica. Brasilia, Brasil, Maio 2831, 2017.